

AD-A259 445



AFWAL-TR-86-3030
VOLUME II

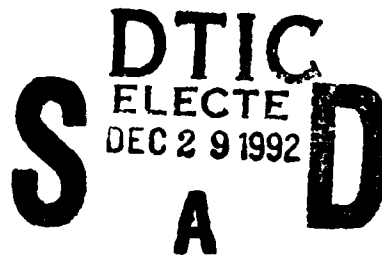


2

FATIGUE CRACK GROWTH AND RETARDATION DUE TO OVERLOADS IN METAL-MATRIX COMPOSITES

Volume II - Finite Element Analysis of Cracks in
Metal-Matrix Composites

C. T. Sun, J. F. Doyle and A. R. Leewood
School of Aeronautics and Astronautics
Purdue University
West Lafayette, IN 47907



August 1986

Final Report for June 1982 to December 1985

Approved for public release; distribution unlimited

FLIGHT DYNAMICS LABORATORY
AIR FORCE WRIGHT AERONAUTICAL LABORATORIES
AIR FORCE SYSTEMS COMMAND
WRIGHT-PATTERSON AIR FORCE BASE, OHIO 45433-6553

92-32874

NOTICE

WHEN GOVERNMENT DRAWINGS, SPECIFICATIONS, OR OTHER DATA ARE USED FOR ANY PURPOSE OTHER THAN IN CONNECTION WITH A DEFINITELY GOVERNMENT-RELATED PROCUREMENT, THE UNITED STATES GOVERNMENT INCURS NO RESPONSIBILITY OR ANY OBLIGATION WHATSOEVER. THE FACT THAT THE GOVERNMENT MAY HAVE FORMULATED OR IN ANY WAY SUPPLIED THE SAID DRAWINGS, SPECIFICATIONS, OR OTHER DATA, IS NOT TO BE REGARDED BY IMPLICATION, OR OTHERWISE IN ANY MANNER CONSTRUED, AS LICENSING THE HOLDER, OR ANY OTHER PERSON OR CORPORATION; OR AS CONVEYING ANY RIGHTS OR PERMISSION TO MANUFACTURE, USE, OR SELL ANY PATENTED INVENTION THAT MAY IN ANY WAY BE RELATED THERETO.

THIS REPORT HAS BEEN REVIEWED BY THE OFFICE OF PUBLIC AFFAIRS (ASD/PA) AND IS RELEASABLE TO THE NATIONAL TECHNICAL INFORMATION SERVICE (NTIS). AT NTIS IT WILL BE AVAILABLE TO THE GENERAL PUBLIC INCLUDING FOREIGN NATIONS.

THIS TECHNICAL REPORT HAS BEEN REVIEWED AND IS APPROVED FOR PUBLICATION.



GEORGE P. SENDECKYJ, Aero Engr
Fatigue, Fracture & Reliability Grp
Structural Integrity Branch



KEVIN L. BOYD, Actg Tech Mgr
Fatigue, Fracture & Reliability Grp
Structural Integrity Branch

FOR THE COMMANDER



JAMES L. RUDD, Chief
Structural Integrity Branch
Structures Division

IF YOUR ADDRESS HAS CHANGED, IF YOU WISH TO BE REMOVED FROM OUR MAILING LIST, OR IF THE ADDRESSEE IS NO LONGER EMPLOYED BY YOUR ORGANIZATION PLEASE NOTIFY WL/FIBEC, WRIGHT-PATTERSON AFB, OH 45433-6553 TO HELP MAINTAIN A CURRENT MAILING LIST.

COPIES OF THIS REPORT SHOULD NOT BE RETURNED UNLESS RETURN IS REQUIRED BY SECURITY CONSIDERATIONS, CONTRACTUAL OBLIGATIONS, OR NOTICE ON A SPECIFIC DOCUMENT.

UNCLASSIFIED

SECURITY CLASSIFICATION OF THIS PAGE

REPORT DOCUMENTATION PAGE

1a. REPORT SECURITY CLASSIFICATION UNCLASSIFIED			1b. RESTRICTIVE MARKINGS N/A	
2a. SECURITY CLASSIFICATION AUTHORITY N/A			3. DISTRIBUTION/AVAILABILITY OF REPORT APPROVED FOR PUBLIC RELEASE; DISTRIBUTION UNLIMITED	
2b. DECLASSIFICATION/DOWNGRADING SCHEDULE N/A				
4. PERFORMING ORGANIZATION REPORT NUMBER(S)			5. MONITORING ORGANIZATION REPORT NUMBER(S) AFWAL-TR-86-3030, Vol. II	
6a. NAME OF PERFORMING ORGANIZATION Purdue University		6b. OFFICE SYMBOL (If applicable) AFWAL/FIBEC	7a. NAME OF MONITORING ORGANIZATION Air Force Wright Aeronautical Laboratories Flight Dynamics Laboratory AFWAL/FIBEC	
6c. ADDRESS (City, State and ZIP Code) West Lafayette, IN 47907			7b. ADDRESS (City, State and ZIP Code) W-PAFB, OH 45433-6553	
8a. NAME OF FUNDING/SPONSORING ORGANIZATION Flight Dynamics Laboratory		8b. OFFICE SYMBOL (If applicable) AFWAL/FIBEC	9. PROCUREMENT INSTRUMENT IDENTIFICATION NUMBER F33615-82-K-3218	
8c. ADDRESS (City, State and ZIP Code) AFWAL/FIBEC W-PAFB, OH 45433-6553			10. SOURCE OF FUNDING NOS.	
			PROGRAM ELEMENT NO. 61102F	TASK NO. N1
			PROJECT NO. 2307	WORK UNIT NO. 20
11. TITLE (Include Security Classification) see block 16				
12. PERSONAL AUTHOR(S) C.T. Sun, J.F. Doyle and A.R. Leewood				
13a. TYPE OF REPORT FINAL		13b. TIME COVERED FROM June 82 to Dec 85		14. DATE OF REPORT (Yr., Mo., Day) August 1986
15. PAGE COUNT 237				
16. SUPPLEMENTARY NOTATION FATIGUE CRACK GROWTH AND RETARDATION DUE TO OVERLOADS IN METAL-MATRIX COMPOSITES. Vol. 2 - FINITE ELEMENT ANALYSIS OF CRACKS IN METAL MATRIX COMPOSITES				
17. COSAT CODES			18. SUBJECT TERMS (Continue on reverse if necessary and identify by block number)	
FIELD	GROUP	SUB GR	METAL-MATRIX COMPOSITES, BORON-ALUMINUM, ELASTOPLASTIC BEHAVIOR, ORTHOTROPIC MATERIAL, PLASTIC ZONES, CRACKS, FINITE ELEMENT ANALYSIS	
1L	04			
19. ABSTRACT (Continue on reverse if necessary and identify by block number) The general three dimensional flow rule for anisotropic plasticity is derived and explicitly defined for the special case of plane stress. Parametric studies of orthotropic elastoplastic behavior and the corresponding yield surfaces are investigated. A finite element program, ANPLAST, is developed to analyze non-linear orthotropic elastic-plastic problems. An in depth elastoplastic study of a sheet with a circular hole is conducted. A detailed investigation of the elastoplastic response of center and edge cracked panels is thoroughly addressed. The anisotropic plasticity formulation is extended to multi-layer laminates and implemented in ANPLAST. It was found that the isoparametric quadrilateral and constant strain triangle finite elements both performed adequately with neither element demonstrating any significant advantages in efficiency or accuracy. Analysis of the sheet with a circular hole and the cracked panels demonstrated the strong influence of anisotropy on plastic zone growth. The character of residual stress distributions due to unloading was not affected by plastic anisotropy. The effect of transverse remote loading on plastic zone growth was also shown to be significant. The advantages of an incremental plasticity formulation for problems consisting of complex loading paths were clearly demonstrated. Elastoplastic laminates displayed complex distortions of their initial yield surface during plastic work-hardening. Analysis of a laminated sheet with a circular hole demonstrated vastly different plastic zone growth within each layer.				
20. DISTRIBUTION/AVAILABILITY OF ABSTRACT UNCLASSIFIED/UNLIMITED <input checked="" type="checkbox"/> SAME AS RPT. <input checked="" type="checkbox"/> DTIC USERS <input type="checkbox"/>			21. ABSTRACT SECURITY CLASSIFICATION UNCLASSIFIED	
22a. NAME OF RESPONSIBLE INDIVIDUAL GEORGE P. SENDECKYJ			22b. TELEPHONE NUMBER (Include Area Code) (513) 255-6104	22c. OFFICE SYMBOL AFWAL/FIBEC

FOREWORD

This report was prepared in the School of Aeronautics and Astronautics, Purdue University, West Lafayette, Indiana. The work was performed under Contract No. F33615-82-K-3218.

The work reported herein was performed during the period June 1982 to December 1985. Dr. C.T. Sun and Dr. J.F. Doyle are professors and A.R. Leewood is a former graduate student, all from the School of Aeronautics and Astronautics at Purdue University.

Accession For	
NTIS CRA&I	<input checked="checked" type="checkbox"/>
DTIC TAB	<input type="checkbox"/>
Unannounced	<input type="checkbox"/>
Justification	
By	
Distribution /	
Availability Codes	
Dist	Avail and/or Special
A-1	

1123

TABLE OF CONTENTS

	Page
SECTION 1: INTRODUCTION	1
SECTION 2: FUNDAMENTALS OF ORTHOTROPIC PLASTICITY	3
INTRODUCTION	3
BASICS OF ELASTICITY	3
PLASTICITY FORMULATION	6
Three Dimensional Anisotropic Flow Rule	6
Reduction to Two Dimensional Plane Stress	8
Definition of Effective Stress and Strain	9
Layered Elastoplastic Materials	11
ORTHOTROPIC BEHAVIOR UNDER UNIAXIAL STRESS	15
Interpretation of the Plasticity Coefficients	15
Parametric Study of the Plasticity Coefficients	17
Interrelation of Work-hardening and the Plasticity Coefficients.	18
YIELD CRITERION UNDER MULTIAXIAL LOADING	27
Parametric Study of the Plasticity Coefficients	27
Isotropic Behavior.	28
Effect of Work-hardening on the Yield Surface	31
LOAD PATH DEPENDENCE OF ACCUMULATED STRAIN	34
Deformation Theory.	34
Unloading and Cyclic Loading.	36
Some Particular Complex Loading Paths	39
SECTION 3: FORMULATION OF COMPUTATIONAL TOOLS	42
INTRODUCTION	42
OVERALL VIEW OF PROGRAM ANPLAST.	42
Program Structure and Philosophy.	42
Comparison of Solution Algorithms	45
Program Re-start Capabilities	45

TABLE OF CONTENTS (Continued)

	Page
Numerical Form of the Incremental Constitutive Relations.	46
Numerical Implementation of Loading and Unloading.	48
FORMULATION OF THE CONSTANT STRAIN TRIANGLE	49
The Strain-Nodal Displacement Relations.	49
Element Stiffness Matrix Formulation	51
FORMULATION OF THE ISOPARAMETRIC ELEMENT.	52
The Strain-Nodal Displacement Relations.	52
Element Stiffness Matrix Formulation	57
Numerical Integration of Element Matrices.	58
PRE-PROCESSING AND POST-PROCESSING FEATURES	59
Mesh Generation and Plotting Features.	59
Bandwidth Optimization by Nodal Sweeping	59
Nodal Averaging of Stresses and Strains.	61
Presentation of Results by Contour Plotting.	61
NUMERICAL EXTENSION OF LAMINATION THEORY.	62
LAMINATE Computer Program.	62
Modifications to ANPLAST	63
COMPUTER PROGRAM PORTABILITY.	63
SECTION 4: ELASTOPLASTIC STUDY OF A SHEET WITH A CIRCULAR HOLE.	65
INTRODUCTION.	65
SHEET WITH ISOTROPIC MATERIAL PROPERTIES.	65
Elastic Loading: Comparison with Theoretical Solution . . .	65
ANPLAST Replication of Ramberg-Osgood Stress-Strain Behavior	72
Elastoplastic Response	74
Comparison of the Isoparametric Quadralateral and Constant Strain Triangle Elements.	79
SHEET WITH ORTHOTROPIC MATERIAL PROPERTIES.	87
Elastic Loading: Comparison with Theoretical Solution . . .	87
A Study of the Plasticity Coefficients Effect on Plastic Zone Growth.	90
A Study of Unloading and the Resulting Residual Stresses	98
A COMPLEX LOADING PATH.	99
Discussion of Plastic Zone Growth.	103
Comparison of Permanent Deformation at the Final Loading Level.	106
COMPARISON TO EXPERIMENTAL RESULTS FOR A CONTINUOUS FIBER REINFORCED METAL MATRIX COMPOSITE	109

TABLE OF CONTENTS (Continued)

	Page
SECTION 5: ELASTOPLASTIC STUDY OF CRACKED PANELS.	119
INTRODUCTION	119
ELASTIC ANALYSIS OF CENTER CRACKED PANELS.	119
Comparison of Stress Distribution with Theory	119
Philosophy of Finite Element Mesh Design.	126
Comparison of Constant Strain Triangle and Isoparametric Quadralateral Elements.	130
ELASTIC ANALYSIS OF AN EDGE CRACKED PANEL.	134
Effect of Anisotropy on Stress Distribution	134
Stress Intensity Determination by an Energy Technique	135
Stress Intensity Determination by Extrapolation of the Stresses.	142
ISOTROPIC ELASTIC-PLASTIC ANALYSIS OF AN EDGE CRACK.	148
A Study of Plastic Zone Growth.	148
The Effect of a Remotely Applied Transverse Stress.	154
A Study of Unloading and the Resulting Residual Stresses.	158
ORTHOTROPIC ELASTIC-PLASTIC ANALYSIS OF AN EDGE CRACK.	159
The Effect of Anisotropy on Plastic Zone Growth	159
The Effect of a Remotely Applied Transverse Stress.	164
A Study of Unloading and the Resulting Residual Stresses.	169
A Look at the Crack Opening Profile	169
Comparison to Experimental Results for a Continuous Fiber Reinforced Metal Matrix Composite	173
SECTION 6: STUDY OF LAMINATED ELASTOPLASTIC MATERIALS	177
INTRODUCTION	177
ELASTIC-PLASTIC LAMINATE BEHAVIOR: ISOTROPIC LAYERS	177
Global Response Due to Uniaxial Loading and Unloading	178
Laminate Response Due to Cyclic Loading	183
A Study of the Laminate Yield Surface	187
Path Dependency Due to Multiaxial Loading	190
ELASTIC-PLASTIC LAMINATE BEHAVIOR: ORTHOTROPIC LAYERS	190
Global Response Due to Uniaxial Loading and Unloading	192
Laminate Response Due to Cyclic Loading	195
A Study of the Laminate Yield Surface	198
Path Dependency Due to Multiaxial Loading	200
ANALYSIS OF A LAMINATED SHEET WITH A CIRCULAR HOLE: ISOTROPIC LAYERS	202

TABLE OF CONTENTS (Concluded)

	Page
A Study of Plastic Zone Growth Within Each Layer.	202
A Study of Residual Stresses and Strains Due to Unloading	205
ANALYSIS OF A LAMINATED SHEET WITH A CIRCULAR HOLE: ORTHOTROPIC LAYERS	205
A Study of Plastic Zone Growth Within Each Layer.	205
A Study of Residual Stresses and Strains Due to Unloading	213
SECTION 7: CONCLUSIONS	215
LIST OF REFERENCES	218
General References	220

LIST OF FIGURES

Figure	Page
2.1 Illustration of an N-layered laminate along with a typical deformed geometry	13
2.2 Illustration of a uniaxial specimen cut at an arbitrary angle to the principal material directions.	16
2.3 Uniaxial elastoplastic response of an isotropic material.	19
2.4 Uniaxial elastoplastic response of a material in which the plasticity coefficient r_{11} is varied.	20
2.5 Uniaxial elastoplastic response of a material in which the plasticity coefficient r_{12} is varied.	22
2.6 Uniaxial elastoplastic response of a material in which the plasticity coefficient r_{66} is varied.	24
2.7 Illustration of the yield surface in σ_{11} , σ_{22} , σ_{12} stress space for different values of the plasticity coefficients.	29
2.8 Uniaxial elastoplastic response of a material in which the plasticity coefficients are constrained to non-typical isotropic values	32
2.9 Illustration of isotropic hardening of an anisotropic yield surface	33
2.10 Illustration of anisotropic hardening of an initially isotropic yield surface	35
2.11 Uniaxial elastoplastic response of an isotropic material which is loaded, unloaded, then reloaded.	37
2.12 Uniaxial elastoplastic response of an isotropic material under cyclic loading	38

LIST OF FIGURES (Continued)

	Page
2.13 Elastoplastic deformation of an isotropic material for three complex loading paths involving both normal stress components.	40
2.14 Elastoplastic deformation response of an isotropic material for three complex loading paths involving a normal and a shear stress component	41
3.1 Flow Diagram of the ANPLAST finite element program.	44
3.2 Dimensions and assumed displacements of a constant strain triangle finite element.	50
3.3 Flow Diagram of an alternate version of ANPLAST which utilizes an isoparametric quadrilateral element	53
3.4 Subroutine description for the isoparametric element version of ANPLAST.	54
3.5 Local coordinate system for the 8-node isoparametric quadrilateral element	56
3.6 A collage of finite element meshes created by the ANPLAST pre-processors. Each mesh design demonstrates biasing of element density	60
4.1 Finite element mesh of a sheet with a circular hole subjected to a uniaxial remote load with fixed grip end conditions	66
4.2 Local and global coordinate systems for a sheet with a circular hole.	68
4.3 Comparison of ANPLAST nodal stresses with the ELLPLAS theoretical solution for a sheet with a circular hole and isotropic material properties	69
4.4 Comparison of ANPLAST effective stress distribution with the ELLPLAS theoretical solution for an isotropic sheet with a circular hole.	70
4.5 Effective stress contour for the sheet with isotropic material properties subjected to elastic loading	71
4.6 Comparison of uniaxial Ramberg-Osgood stress-strain response with the ANPLAST replication of this behavior.	75

LIST OF FIGURES (Continued)

	Page
4.7 Plastic zone growth for an isotropic sheet subjected to elastic-plastic loading.	77
4.8 Plastic zone growth experimentally detained by Theocaris and Marietos [21] using a birefringent coating on an isotropic sheet, then subjected to elastic-plastic loading	78
4.9 Comparison of ANPLAST nodal stresses with the Budiansky-Vidensek [20] theoretical solution for an isotropic sheet with a circular hole subjected to elastic-plastic loading.	80
4.10 Comparison of ANPLAST effective stresses with the Budiansky-Vidensek [20] solution for an isotropic sheet with a circular hole subjected to elastic-plastic loading	81
4.11 Comparison of ANPLAST stresses with an experimental photoplasticity solution by Frocht and Thomson [22] for the isotropic sheet with a circular hole subjected to elastic-plastic loading.	82
4.12 Finite element mesh of the sheet with a circular hole utilizing the 8-noded isoparametric quadralateral element	84
4.13 Isoparametric quadralateral stress distribution for an isotropic sheet with a circular hole subjected to elastic loading.	85
4.14 Comparison of plastic zone growth for the isoparametric quadralateral and CST elements for an isotropic sheet subjected to elastic-plastic loading	86
4.15 Comparison of the ANPLAST stress distribution with the ELLPLAS theoretical solution for a mildly orthotropic (B-A1) sheet with a circular hole subjected to elastic loading	88
4.16 Comparison of the ANPLAST stress distribution with the ELLPLAS theoretical solution for a strongly orthotropic (G-Ep) sheet with a circular hole subjected to elastic loading.	89
4.17 Plastic zone growth for an orthotropic sheet subjected to elastic-plastic loading. The strong material direction is oriented perpendicular to the remote load	92

LIST OF FIGURES (Continued)

	Page
4.18 Plastic zone growth for an orthotropic sheet subjected to elastic-plastic loading. The strong material direction is oriented parallel to the remote load.	93
4.19 Effective stress contours for three orthotropic sheets at the onset of yielding.	94
4.20 Effective stress contours for three orthotropic sheets after considerable plastic flow has occurred	95
4.21 Plastic zone growth for an orthotropic sheet ($r_{66} = 3.0$) under elastic-plastic loading. The orientation of the principal material directions does not affect this illustration.	97
4.22 ANPLAST residual stress distribution after unloading from a remote stress which was twice that necessary to initiate yielding.	100
4.23 Finite element mesh of a sheet with a circular hole for analysis of complex loading paths	102
4.24 Plastic zone growth for an isotropic sheet subjected to non-proportional remote loading (Case I)	104
4.25 Plastic zone growth for an isotropic sheet subjected to non-proportional remote loading (Case II).	105
4.26 Plastic zone growth for an isotropic sheet subjected to a simultaneous biaxial remote loading (Case III)	107
4.27 Effective plastic strain contour for the isotropic sheet at the final deformation state	108
4.28 Geometry of test specimen used by Rizzi [24] for experimental determination of the stress-strain behavior of a Boron-Aluminum metal matrix composite	110
4.29 Comparison of ANPLAST strains with the experimental results of Rizzi [24] for a B-Al sheet with a circular hole subjected to uniaxial elastic loading	111

LIST OF FIGURES (Continued)

	Page
4.30 ANPLAST incremental loading path for analysis of the B-A1 strip with a circular hole.	113
4.31 Plastic zone growth for the B-A1 strip subjected to elastic-plastic loading	114
4.32 Comparison of ANPLAST strains with experimental results of Rizzi [24] for the B-A1 strip with a circular hole subjected to elastic-plastic loading	116
4.33 Comparison of ANPLAST lateral strains with the experimental results of Rizzi [24] presented on an expanded scale.	117
4.34 Comparison of ANPLAST longitudinal strain with the experimental results of Rizzi [24] for the complete load-history of the test. The strain gage is located at the innermost position along the horizontal symmetry line	118
5.1 Finite element mesh of a center cracked panel with a uniaxial remote load and fixed grip end conditions	120
5.2 Illustration of the local and global coordinate systems for a cracked panel.	121
5.3 Comparison of the ANPLAST stress distribution with the ELLPLAS theoretical solution for an isotropic panel with a center crack subjected to elastic loading	122
5.4 Comparison of the ANPLAST stress distribution with the ELLPLAS theoretical solution for a weakly orthotropic (B-A1) panel with a center crack subjected to elastic loading	123
5.5 Comparison of the ANPLAST stress distribution with the ELLPLAS theoretical solution for a strongly orthotropic (G-Ep) panel with a center crack subjected to elastic loading	124
5.6 Finite element mesh of a center cracked panel which utilizes a rectangular grid design in the vicinity of the crack tip.	127
5.7 Comparison of ANPLAST stress distribution for the radial and rectangular mesh designs for an isotropic center cracked panel subjected to elastic loading.	128

LIST OF FIGURES (Continued)

	Page
5.8 Finite element mesh of the center cracked panel utilizing 8-nodes isoparametric elements.	131
5.9' Comparison of the isoparametric element results with the ELLPLAS solution for the center cracked panel subjected to elastic loading.	132
5.10 Finite element mesh of a transverse edge cracked panel with a uniaxial remote load and fixed grip end conditions.	136
5.11 Mises stress contour of a isotropic edge cracked panel subjected to elastic loading.	137
5.12 Mises stress contour of a weakly orthotropic (B-A1) edge cracked panel subjected to elastic loading	138
5.13 Mises stress contour of a strongly orthotropic (G-Ep) edge cracked panel subjected to elastic loading	139
5.14 Stress Intensity Factor (K_I) chart for the edge cracked panel containing the isotropic handbook solution and that obtained by ANPLAST for B-A1.	143
5.15 Stress distribution along 19 radial lines emanating from the crack tip of the transverse edge cracked panel.	145
5.16 Stress Intensity Factor calibration plot. A least squares curve fit of $K_I F_{ij}(\theta)$ vs the 19 radial intercept values ($\sigma_{ij}\sqrt{r}$)	147
5.17 Plastic zone growth for an isotropic edge-cracked panel subjected to elastic-plastic loading.	149
5.18 Effective stress contour of an isotropic edge-cracked panel at the onset of yielding.	150
5.19 A finite element mesh of an oblique edge-cracked panel subjected to uniaxial loading and fixed grip end conditions	151
5.20 Plastic zone growth for an isotropic oblique edge-cracked panel subjected to elastic-plastic loading	152

LIST OF FIGURES (Continued)

	Page
5.21 Effective stress contours for the oblique edge-cracked panel at the onset of yielding.	153
5.22 Plastic zone progression for an isotropic transverse edge-cracked panel subjected to proportional biaxial remote loading.	155
5.23 ANPLAST residual stress distribution following unloading for an isotropic transverse edge cracked panel.	160
5.24 Plastic zone growth for an orthotropic B-Al transverse edge-cracked panel subjected to elastic-plastic loading.	161
5.25 Effective stress contours of an orthotropic B-Al transverse edge-cracked panel at the onset of yielding	163
5.26 Plastic zone growth for an orthotropic B-Al oblique edge-cracked panel subjected to elastic-plastic loading.	165
5.27 Plastic zone growth for an orthotropic B-Al transverse edge-cracked panel subjected to proportional biaxial remote loading.	166
5.28 ANPLAST residual stress distribution following unloading for an orthotropic B-Al transverse edge-cracked panel	170
5.29 Crack opening profiles for a transverse edge-cracked panel under uniaxial remote loading. Note that the displacements are normalized by the outer edge displacement.	172
5.30 Geometry of edge cracked test specimens used by Kenaga [12] for the experimental determination of the stress-strain behavior of a B-Al metal matrix composite	174
5.31 Comparison of ANPLAST strains with the experimental results of Kenaga [12] and Rizzi [24] for a B-Al panel with a transverse and oblique edge crack	175
6.1 Uniaxial load-deformation response of an isotropic laminate (Laminate #1)	179
6.2 Uniaxial load-deformation response of an isotropic laminate (Laminate #2)	181

LIST OF FIGURES (Continued)

	Page
6.3 Axial and transverse layer stress distribution during uniaxial loading of an isotropic laminate.	182
6.4 Stress-strain response of an isotropic laminate cycled between fixed load limits.	184
6.5 Layer stress-strain response of an isotropic laminate cycled between fixed load limits	186
6.6 Illustration of the yield surface for an isotropic laminate during uniaxial cyclic loading between fixed load limits	188
6.7 Illustration of the yield surface for an isotropic laminate during a multiaxial non-proportional loading path.	189
6.8 Deformation response of an isotropic laminate due to different complex loading paths.	191
6.9 Uniaxial load-deformation response of an orthotropic B-Al laminate $[0^\circ/90^\circ]_5$	193
6.10 Axial and transverse layer stress distribution during monotonic uniaxial loading of the B-Al laminate.	194
6.11 Stress-strain response of the B-Al laminate cycled between fixed load limits.	196
6.12 Layer stress-strain response of the B-Al laminate cycled between fixed load limits.	197
6.13 Illustration of the yield surface for the B-Al laminate during uniaxial cyclic loading between fixed load limits	199
6.14 Deformation response of the B-Al laminate due to different complex loading paths	201
6.15 Plastic zone growth in each layer of an isotropic laminated sheet subjected to elastic-plastic loading	203
6.16 Effective stress contours in each layer for the isotropic laminated sheet subjected to elastic-plastic loading	206

LIST OF FIGURES (Concluded)

	Page
6.17 ANPLAST residual stresses in each layer for the isotropic laminated sheet with a circular hole subjected to elastic unloading.	207
6.18 Plastic zone growth in each ply for the B-A1 laminated sheet $[0^\circ/90^\circ]_s$ with a circular hole subjected to elastic-plastic loading.	208
6.19 Effective stress contours in each ply for the B-A1 laminated sheet subjected to elastic-plastic loading	211
6.20 Plastic zone growth calculated by Dvorak [33] for an orthotropic FP-A1 laminated sheet $[0^\circ/90^\circ]$ with a circular hole subjected to elastic-plastic loading	212
6.21 ANPLAST residual stresses in each ply for the B-A1 laminated sheet with a circular hole subjected to elastic unloading	214

SECTION 1

INTRODUCTION

When studying the deformation of metallic solids due to applied external loads, it is common to assume the material will behave in an isotropic manner [1]. Typically, this assumption is extended to both the elastic and elastic-plastic response [2]. In many cases, the particular manufacturing process, such as rolling, introduces anisotropy into the material, giving directionally sensitive elastoplastic mechanical behavior [3].

There are two categories of problems involving anisotropic behavior. One is the induction of anisotropy into an initially isotropic bulk material [4], most commonly observed during metal forming operations. The second category involves those materials which are initially anisotropic. An example is the behavior of some metal-matrix composites. Both categories of problems are pertinent to this research and a finite element program ANPLAST is developed to this end. This program implements a properly formulated anisotropic plasticity theory in a convenient form to use for numerical purposes.

The anisotropic elastoplasticity of sheet materials is often studied from two perspectives. The first takes into consideration the transverse or through-thickness anisotropy while assuming planar isotropy. Most of the research to date has concentrated on this subject [3,5] because this is the usual case incurred in rolling. While the problem of planar anisotropy has been investigated from a

theoretical perspective [4,6,7], very few examples of its applications can be found in the literature. Consequently, this research will concentrate exclusively on planar anisotropy and its influence on some practical problems of interest.

Specifically, a thin sheet with a circular hole and a panel with a crack will be studied. The differences between the isotropic and anisotropic solutions are elaborated. The elastoplastic analysis is extended to layered (or laminated) structures with a particular application to the sheet with a circular hole. The present numerical solutions of these problems are confirmed by comparison with experimental results. Some comparisons are also made with the available theoretical solutions.

SECTION 2 FUNDAMENTALS OF ORTHOTROPIC PLASTICITY

INTRODUCTION

This section will review the fundamentals of elasticity of orthotropic materials. A similar approach will then be used to derive the orthotropic plasticity flow rule. The meaning of the coefficients that appear in the theory will be demonstrated for uniaxial response of the material. A discussion of the path dependency associated with plastic flow necessarily entails a comparison of incremental deformation theories of plasticity and this is also covered in this section. In anticipation of the later applications to laminated composites, formulation of the elastoplastic response of a multilayered laminate is included.

BASICS OF ELASTICITY

For an elastic body, the current stress state depends only on the current deformation state. This can be expressed as [1]

$$e_{ij} = \frac{\partial w}{\partial \sigma_{ij}} \quad (2.1)$$

where

σ_{ij} = stress tensor

e_{kl} = strain tensor

w = energy density function

For linear elasticity, W is assumed quadratic in the stress as

$$W = C_{ijkl} \sigma_{ij} \sigma_{kl} \quad (2.2)$$

Equation 2.1 then becomes

$$e_{ij} = C_{ijkl} \sigma_{kl}$$

The tensor of elastic constants C_{ijkl} is independent of stress and strain and exhibits the following symmetric behavior

$$C_{ijkl} = C_{jikl}; C_{ijkl} = C_{ijlk}; C_{ijkl} = C_{klij}$$

The matrix $[C_{ijkl}]$ has a maximum of 21 independent constants, which can be written in contracted notation as

$$\begin{Bmatrix} e_{11} \\ e_{22} \\ e_{33} \\ e_{23} \\ e_{13} \\ e_{12} \end{Bmatrix} = \begin{bmatrix} C_{11} & C_{12} & C_{13} & \cdots & C_{16} \\ & C_{22} & & & \\ & & \text{Symmetric} & & \\ & & & & C_{66} \end{bmatrix} \begin{Bmatrix} \sigma_{11} \\ \sigma_{22} \\ \sigma_{33} \\ \sigma_{23} \\ \sigma_{13} \\ \sigma_{12} \end{Bmatrix}$$

If the material has three mutually perpendicular planes of symmetry, it is considered orthotropic and the stress-strain relation reduces to

having 9 independent constants as,

$$\begin{Bmatrix} e_{11} \\ e_{22} \\ e_{33} \\ e_{23} \\ e_{13} \\ e_{12} \end{Bmatrix} = \begin{bmatrix} C_{11} & C_{12} & C_{13} & 0 & 0 & 0 \\ C_{12} & C_{22} & C_{23} & 0 & 0 & 0 \\ C_{13} & C_{23} & C_{33} & 0 & 0 & 0 \\ 0 & 0 & 0 & C_{44} & 0 & 0 \\ 0 & 0 & 0 & 0 & C_{55} & 0 \\ 0 & 0 & 0 & 0 & 0 & C_{66} \end{bmatrix} \begin{Bmatrix} \sigma_{11} \\ \sigma_{22} \\ \sigma_{33} \\ \sigma_{23} \\ \sigma_{13} \\ \sigma_{12} \end{Bmatrix}$$

When analyzing thin sheets of material, the through-thickness stress can be neglected as well as the corresponding shear stresses, resulting in a state of plane stress. The constitutive equation now becomes

$$\begin{Bmatrix} e_{11} \\ e_{22} \\ 2e_{12} \end{Bmatrix} = \begin{bmatrix} C_{11} & C_{12} & 0 \\ C_{12} & C_{22} & 0 \\ 0 & 0 & C_{66} \end{bmatrix} \begin{Bmatrix} \sigma_{11} \\ \sigma_{22} \\ \sigma_{12} \end{Bmatrix} \quad (2.3)$$

A total of 4 independent constants describe the planar problem. The through thickness strain e_{33} could be obtained from knowledge of C_{13} and C_{23} . The coefficients in Eq. 2.3 can be represented in the more common engineering form as

$$\begin{aligned} C_{11} &= \frac{1}{E_1} & C_{12} &= C_{21} = \frac{-\nu_{12}}{E_2} \\ C_{22} &= \frac{1}{E_2} & C_{66} &= \frac{1}{G_{12}} \end{aligned}$$

where

E_1, E_2 = elastic moduli

ν_{12} = Poisson ratio

G_{12} = shear modulus

and subscripts 1, 2 denote the corresponding principal material directions.

Since the material coefficients are constants, the incremental constitutive relation for the plane orthotropic case simply becomes

$$\begin{Bmatrix} d\epsilon_{11} \\ d\epsilon_{22} \\ d\epsilon_{12} \end{Bmatrix} = [c] \begin{Bmatrix} d\sigma_{11} \\ d\sigma_{22} \\ d\sigma_{12} \end{Bmatrix} \quad (2.4)$$

where $[c]$ has the same meaning as Eq. 2.3.

The incremental load deformation response of an elastic material is completely defined by Eq. 2.4.

PLASTICITY FORMULATION

The approach taken to the plasticity formulation is to use a flow rule that is quadratic in the stresses. This gives sufficient flexibility to describe orthotropic plasticity [2].

Three Dimensional Anisotropic Flow Rule

The incremental plastic strains can be written in terms of a plastic potential [8] as

$$de_{ij}^p = \frac{\partial g}{\partial \sigma_{ij}} d\lambda^* \quad (2.5)$$

where the superscript "p" denotes plasticity. For an anisotropic body, Kachanov [8] suggested that g take the quadratic form

$$g = C_{ijkl} \sigma_{ij} \sigma_{kl} \quad (2.6)$$

It is interesting to note that a number of authors [9,10,11] have investigated non-quadratic potential functions, but a quadratic function is deemed sufficient for the purposes of this research. Taking advantage of the symmetric properties of C_{ijkl}^p , Eq. 2.5 is contracted and rewritten (as in the elastic case) as

$$\begin{Bmatrix} de_{11} \\ de_{22} \\ de_{33} \\ de_{23} \\ de_{13} \\ de_{12} \end{Bmatrix}^p = \begin{bmatrix} C_{11} & C_{12} & C_{13} & \dots & C_{16} \\ & C_{22} & & & \\ & & \text{Symmetric} & & \\ & & & & C_{66} \end{bmatrix}^p \begin{Bmatrix} \sigma_{11} \\ \sigma_{22} \\ \sigma_{33} \\ \sigma_{23} \\ \sigma_{13} \\ \sigma_{12} \end{Bmatrix} d\lambda^*$$

The matrix $[C_{ij}]^p$ contains 21 independent coefficients. If the material contains three mutually perpendicular planes of symmetry, then the plastic coefficient matrix takes the form

$$[C]^P = \begin{bmatrix} C_{11} & C_{12} & C_{13} & 0 & 0 & 0 \\ C_{12} & C_{22} & C_{23} & 0 & 0 & 0 \\ C_{13} & C_{23} & C_{33} & 0 & 0 & 0 \\ 0 & 0 & 0 & C_{44} & 0 & 0 \\ 0 & 0 & 0 & 0 & C_{55} & 0 \\ 0 & 0 & 0 & 0 & 0 & C_{66} \end{bmatrix}$$

Thus, to describe three dimensional orthotropic plastic flow requires only nine independent coefficients.

Reduction to Two Dimensional Plane Stress

When dealing with plane stress, the plastic flow relations simplify further since $\sigma_{33} = 0$, $\sigma_{13} = 0$, $\sigma_{23} = 0$, giving

$$\begin{Bmatrix} de_{11} \\ de_{22} \\ de_{12} \end{Bmatrix}^P = \begin{bmatrix} C_{11} & C_{12} & 0 \\ C_{12} & C_{22} & 0 \\ 0 & 0 & C_{66} \end{bmatrix}^P \begin{Bmatrix} \sigma_{11} \\ \sigma_{22} \\ \sigma_{12} \end{Bmatrix} d\lambda^* \quad (2.7)$$

The above system of equations are over-specified with four C-values and $d\lambda^*$. Normalize these equations by introducing the following definitions

$$\begin{aligned} r_{11} &= C_{11}^P / C_{22}^P \\ r_{66} &= C_{66}^P / C_{22}^P & d\lambda &= C_{22}^P d\lambda^* \\ r_{12} &= C_{12}^P / C_{22}^P \end{aligned}$$

Then, the incremental expressions for plane stress become

$$\begin{Bmatrix} de_{11} \\ de_{22} \\ de_{12} \end{Bmatrix}^p = \begin{bmatrix} r_{11} & r_{12} & 0 \\ r_{12} & 1 & 0 \\ 0 & 0 & r_{66} \end{bmatrix} \begin{Bmatrix} \sigma_{11} \\ \sigma_{22} \\ \sigma_{12} \end{Bmatrix} d\lambda \quad (2.8)$$

It is clear from this equation that the incremental plastic strains are orthotropic with respect to the stresses, i.e., the normal components of incremental strain are uncoupled from the shear stress. This relation reduces to isotropic plastic flow when the r's have the values [12]

$$r_{11} = 1.0 \quad r_{12} = -.50 \quad r_{66} = 1.50$$

The factor of proportionality $d\lambda$ is solved from work considerations. Parenthetically, the plane stress orthotropic flow rule could have been derived directly by taking the potential function g as

$$g = \frac{1}{2} [r_{11}\sigma_{11}^2 + \sigma_{22}^2 + 2r_{66}\sigma_{12}^2 + 2r_{12}\sigma_{11}\sigma_{22}]$$

Definition of Effective Stress and Strain

In general, the plastic work increment can be written as

$$dW^p = \sigma_{ij} de_{ij}^p$$

which for plane stress expands to

$$dW^P = \sigma_{11} de_{11}^P + \sigma_{22} de_{22}^P + 2\sigma_{12} de_{12}^P$$

The plastic strain increments previously defined in Eq. 2.8 can be substituted into the above relation resulting in

$$dW^P = \{r_{11}\sigma_{11}^2 + \sigma_{22}^2 + 2r_{66}\sigma_{12}^2 + 2r_{12}\sigma_{11}\sigma_{22}\} d\lambda = 2gd\lambda \quad (2.9)$$

Let the effective stress and strain be defined such that

$$\bar{\sigma} d\bar{\epsilon}^P = dW^P = 2gd\lambda \quad (2.10)$$

Further, the effective stress can be defined as

$$\frac{2}{3} \bar{\sigma}^2 = r_{11}\sigma_{11}^2 + \sigma_{22}^2 + 2r_{66}\sigma_{12}^2 + 2r_{12}\sigma_{11}\sigma_{22} = 2g \quad (2.11)$$

Therefore,

$$d\lambda = \frac{3}{2} (d\bar{\epsilon}^P / \bar{\sigma}) = \frac{3}{2} (d\bar{\epsilon}^P / d\bar{\sigma}) (d\bar{\sigma} / \bar{\sigma}) \quad (2.12)$$

and the effective plastic strain can be written as [12]

$$\begin{aligned} [d\bar{\epsilon}^P]^2 &= \frac{2}{3} [de_{11}^P{}^2 + r_{11}de_{22}^P{}^2 - 2r_{12}de_{11}^P de_{22}^P \\ &\quad + 2(r_{11} - r_{12}^2) de_{12}^P{}^2 / r_{66}] / [r_{11} - r_{12}^2] \end{aligned} \quad (2.13)$$

Substituting the above expression for $d\lambda$ into Eq. 2.8, the plane stress orthotropic plastic flow equations become

$$\begin{Bmatrix} de_{11} \\ de_{22} \\ 2de_{12} \end{Bmatrix}^p = \begin{bmatrix} r_{11} & r_{12} & 0 \\ r_{12} & 1 & 0 \\ 0 & 0 & 2r_{66} \end{bmatrix} \begin{Bmatrix} \sigma_{11} \\ \sigma_{22} \\ \sigma_{12} \end{Bmatrix} \frac{3}{2} \left(\frac{d\bar{e}^p}{d\bar{\sigma}} \right) \left(\frac{d\bar{\sigma}}{\bar{\sigma}} \right) \quad (2.14)$$

No assumption of constant volume deformation or incompressibility was made during the development of these plastic flow equations. To consider volumetric changes or thickness changes in the 2-D case would require additional coefficients.

Layered Elastoplastic Materials

A laminate is defined as two or more laminas bonded together to act as an integral structural element. Let the laminate consist of thin layers, each exhibiting plane stress behavior. Due to the potential for plastic flow in each layer, all stress-strain relations will be written in incremental form. The elastic and plastic incremental constitutive relations can be written in matrix form as

$$\begin{aligned} \{d\sigma\}_k &= [\bar{Q}]_k^e \{de^e\}_k \\ \{d\sigma\}_k &= [\bar{Q}]_k^p \{de^p\}_k \end{aligned} \quad (2.15)$$

where $[\bar{Q}]^e$ and $[\bar{Q}]^p$ are the transformed inverse of matrices of Eqns. 2.4 and 2.14, respectively for the k^{th} layer of a multilayered laminate.

The total stress-strain relation is obtained by adding the elastic and plastic responses to give

$$\{d\sigma\}_k = [\bar{Q}]_k \{de_k\} \quad (2.16)$$

where

$$[\bar{Q}] = [\bar{Q}]^e + [\bar{Q}]^p$$

It should be noted that $[\bar{Q}]$ will be stress dependent when plastic deformation occurs through the contribution of $[\bar{Q}]^p$.

Knowledge of the variation of stress and strain through the laminate thickness is essential to the extensional stiffness of a laminate. For the purposes of this research, bending stiffness and deformation will be ignored and only the first order extensional behavior considered. The laminate is assumed to consist of perfectly bonded laminae with displacements continuous across the lamina boundaries so that no lamina can slip relative to another. These are the usual type of assumptions made in laminate theory [13].

A typical laminate is pictured in Fig. 2.1 along with its deformed shape. It is quite clear that the deformation and strain in the plane of each layer is the same. The incremental stress-strain relations for each lamina can be expressed as

$$\{d\sigma\}_k = [\bar{Q}]_k \{de_o\} \quad (2.17)$$

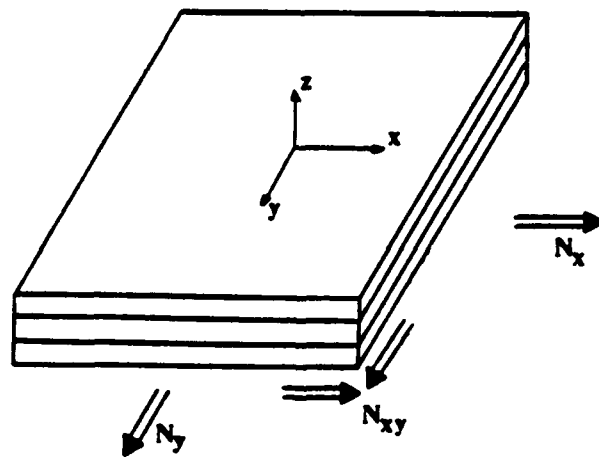
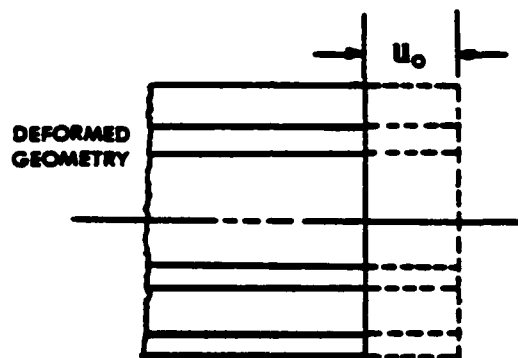
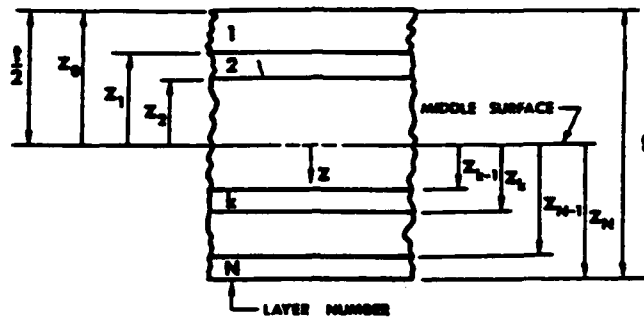


Figure 21 Illustration of an N-layered laminate along with a typical deformed geometry.

where $\{de_0\}$ is the laminate strain increment.

The resultant laminate forces per unit width are obtained by integrating the stress components of each lamina through the total thickness of the laminate. They will take the following form

$$\begin{Bmatrix} dN_x \\ dN_y \\ dN_{xy} \end{Bmatrix} = \int_{-t/2}^{t/2} \begin{Bmatrix} d\sigma_{xx} \\ d\sigma_{yy} \\ d\sigma_{xy} \end{Bmatrix} dz$$

Since the stresses are constant through the thickness of each lamina, then this becomes

$$\begin{Bmatrix} dN_x \\ dN_y \\ dN_{xy} \end{Bmatrix} = \sum_{k=1}^N \begin{Bmatrix} d\sigma_{xx} \\ d\sigma_{yy} \\ d\sigma_{xy} \end{Bmatrix} (z_k - z_{k-1})$$

Replacing the incremental lamina stresses with those from Eq. 2.17, results in the incremental laminate load-deformation equations taking the form

$$\begin{Bmatrix} dN_x \\ dN_y \\ dN_{xy} \end{Bmatrix} = \sum_{k=1}^N [\bar{Q}]_k (z_k - z_{k-1}) \begin{Bmatrix} de_{xx}^0 \\ de_{yy}^0 \\ d_{xy}^0 \end{Bmatrix} \quad (2.18)$$

The global response of the laminate will be affected by each layer's stiffness contribution $[\bar{Q}]_k$. During elastoplastic deformation, each layer accounts for its particular plastic stiffness through $[\bar{Q}]_k^p$.

ORTHOTROPIC BEHAVIOR UNDER UNIAXIAL STRESS

The effect of the plasticity coefficients appearing in the previous constitutive relations can best be understood by analyzing a uniaxial stress state.

Interpretation of the Plasticity Coefficients

For a uniaxial specimen cut from an orthotropic material at an arbitrary direction to the principle axes as illustrated in Fig. 2.2, the state of stress with respect to the material directions are as follows

$$\sigma_{11} = \sigma_{\theta} \cos^2 \theta$$

$$\sigma_{22} = \sigma_{\theta} \sin^2 \theta$$

$$\sigma_{12} = \sigma_{\theta} \sin \theta \cos \theta$$

The incremental strains in the loading direction and in the transverse direction are

$$de_{\theta_L}^p = [r_{11} \cos^4 \theta + 2r_{12} \cos^2 \theta \sin^2 \theta + \sin^4 \theta + 2r_{66} \sin^2 \theta \cos^2 \theta] d\lambda$$

$$de_{\theta_T}^p = [r_{11} + 1 - 2r_{66}) \sin^2 \theta \cos^2 \theta + r_{12} (\sin^4 \theta + \cos^4 \theta)] d\lambda$$

(2.19)

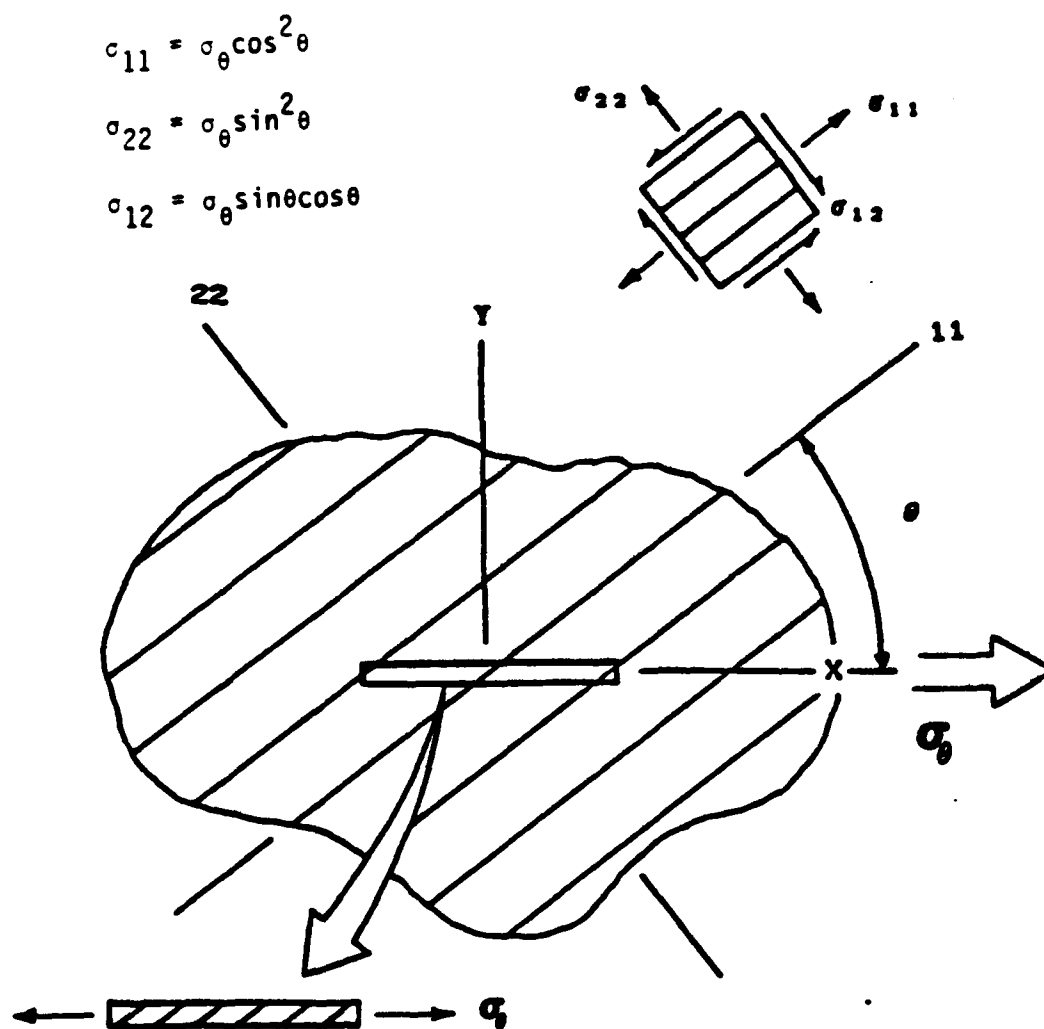


Figure 2.2 Illustration of a uniaxial specimen cut at an arbitrary angle to the principal material directions.

The ratio of transverse to longitudinal strain increments can be viewed as a plastic Poisson ratio and is written

$$-\nu_{\theta}^p = \frac{de_{\theta T}^p}{de_{\theta L}^p} = \frac{(r_{11} + 1 - 2r_{66})\sin^2\theta\cos^2\theta + r_{12}(\sin^4\theta + \cos^4\theta)}{r_{11}\cos^4\theta + \sin^4\theta + 2(r_{12} + r_{66})\sin^2\theta\cos^2\theta} \quad (2.20)$$

Note that for various orientations the sine and cosine terms are zero, and the above expression simplifies, i.e.

$$\begin{aligned} \theta = 0^\circ : -\nu_{00}^p &= r_{12}/r_{11} \\ \theta = 90^\circ : -\nu_{90}^p &= r_{12} \\ \theta = 45^\circ : -\nu_{45}^p &= \frac{r_{12} - 2r_{66} + 2r_{12} + 1}{r_{11} + 2r_{66} + 2r_{12} + 1} \end{aligned} \quad (2.21)$$

Thus, it seems that the plasticity coefficients behave similarly to Poisson ratio's. If the isotropic values of the r 's are substituted into the above equation, the plastic Poisson ratio is $\frac{1}{2}$ for all orientations. Otherwise, if the plasticity coefficients are varied from their isotropic values, anisotropy will be induced into the plastic flow.

Parametric Study of the Plasticity Coefficients

Additional insight can be obtained by conducting a simple parametric study of the three plasticity coefficients. The axial and transverse loading-deformation behavior of an arbitrarily oriented uniaxial specimen will be studied. The elastic behavior of the

material will be assumed to be isotropic so that the anisotropy of the plastic flow can be highlighted.

A FORTRAN computer program MULTIAX was developed for the purpose of predicting the load-deformation behavior of an ideal element under multiaxial loading. This program calculates the incremental strains during each load increment and sums them to obtain the total strain. The program can handle any loading path.

The plasticity parameter r_{11} is studied first. Figure 2.3 illustrates the load-deformation behavior with assumed isotropic properties. As expected, the global stress-strain response is not a function of θ . The isotropic example will be used as the base response for comparison. Changing the value of r_{11} to .8 and then .4 as shown in Fig. 2.4, highlights the global stress-strain dependence on θ . It is quite evident that the more r_{11} deviates from unity, the stronger the induced anisotropy. It is obvious that yield does not occur at a common value for all orientations. This is because the yield is a function of the r 's.

Figure 2.5 depicts the uniaxial load-deformation as r_{12} is changed from its isotropic value of -0.5. Figure 2.6 shows the effect as r_{66} is changed from its isotropic value of 2.5. The departure of either of these plasticity coefficients from their isotropic value also induces anisotropy into the uniaxial yield.

These studies show that each parameter can affect the anisotropy of material behavior.

Interrelation of Work-hardening and the Plasticity Coefficients

Plasticity coefficients play an important role in determining the unique relationship between effective stress ($\bar{\sigma}$) and the effective

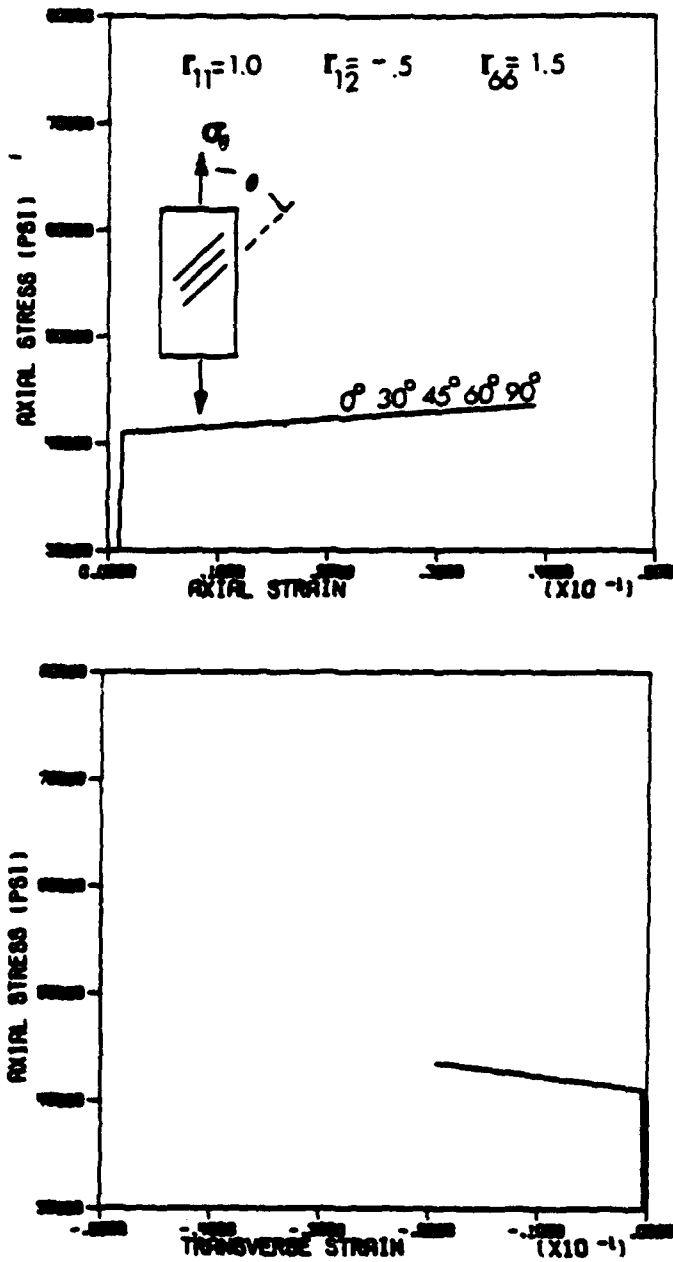


Figure 2.3 Uniaxial elastoplastic response of an isotropic material.

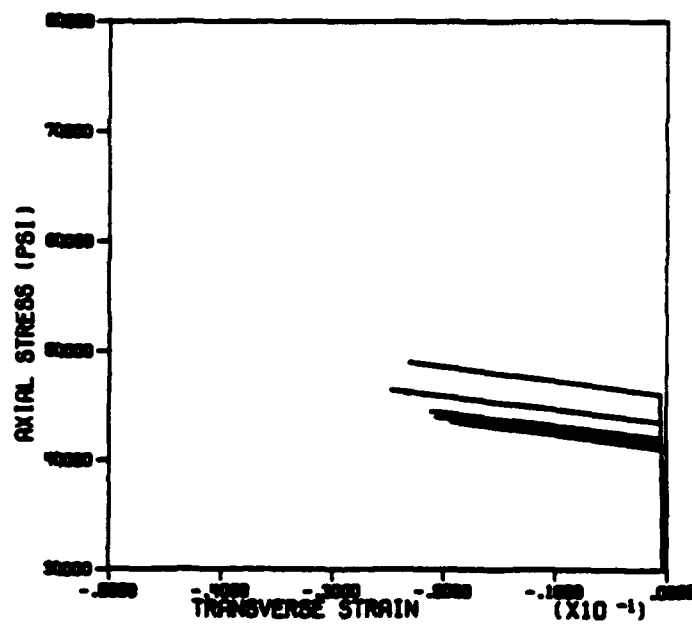
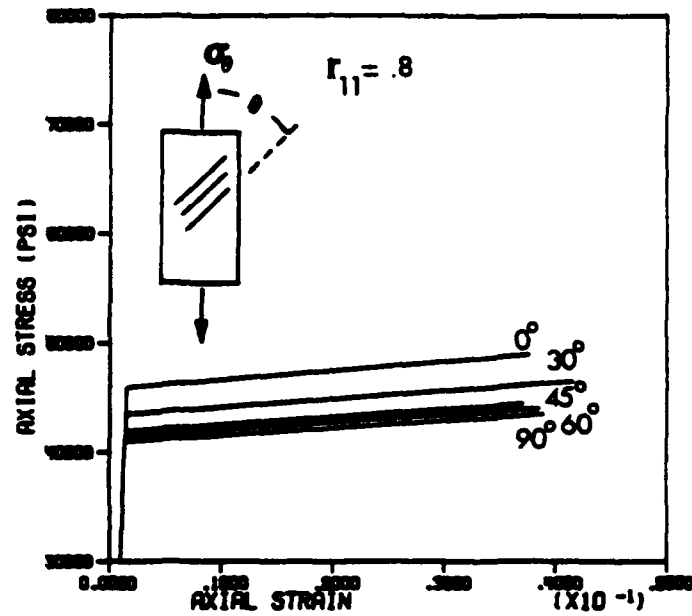


Figure 2.4 Uniaxial elastoplastic response of a material in which the plasticity coefficient r_{11} is varied.

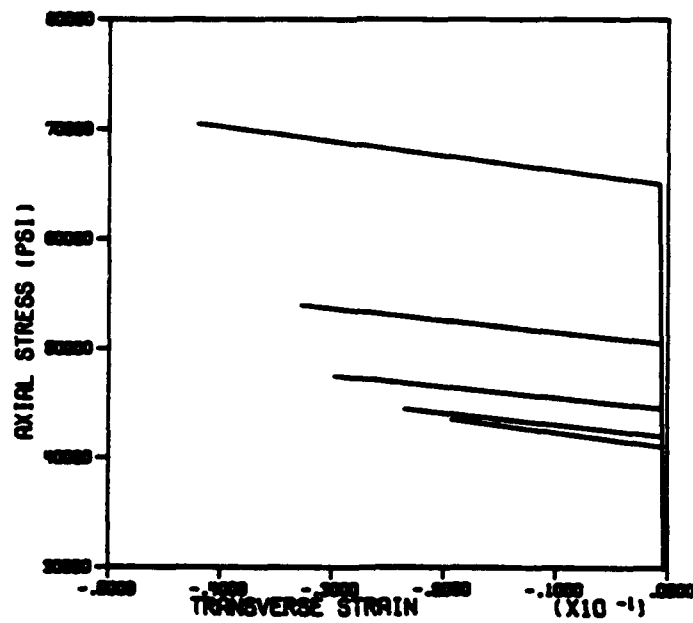
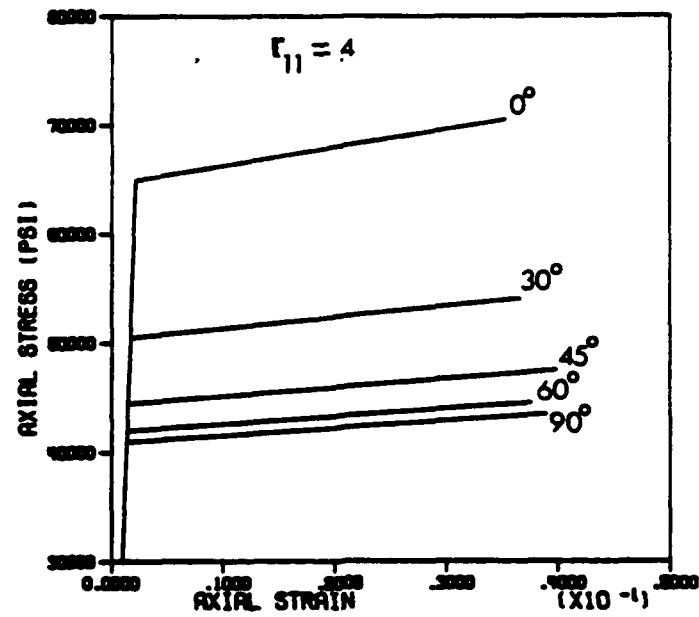


Figure 2.4 continued

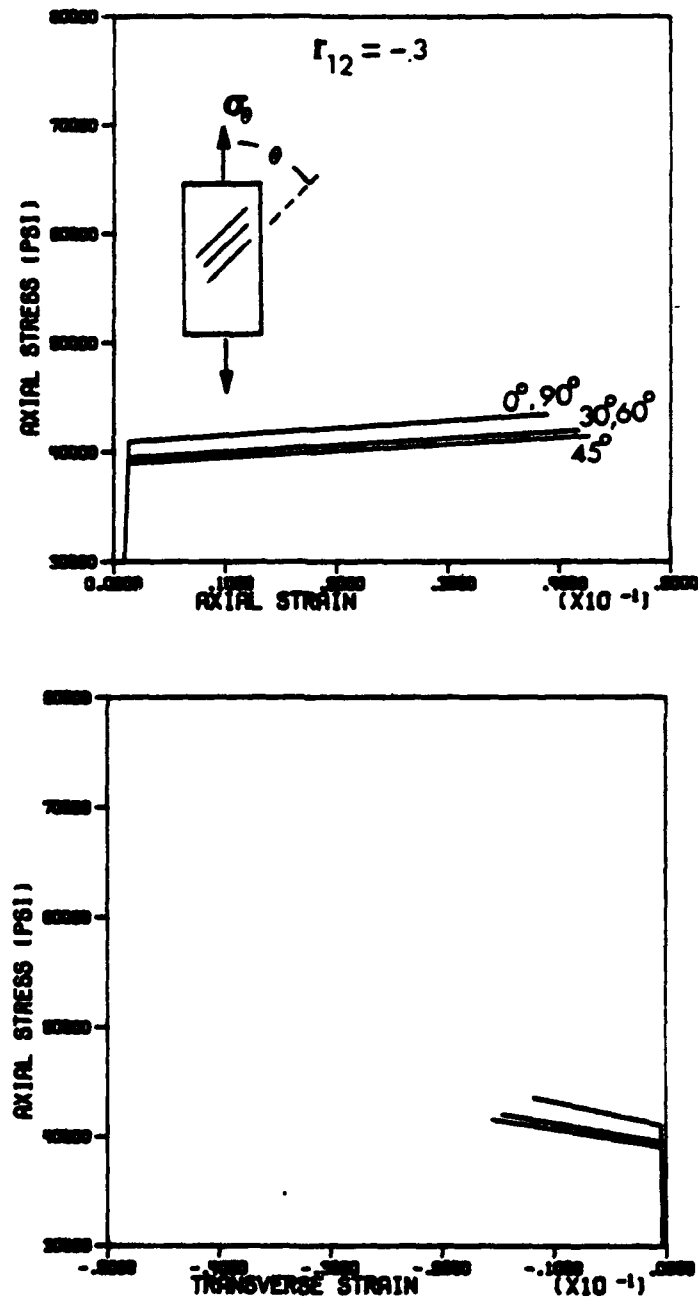


Figure 2.5 Uniaxial elastoplastic response of a material in which the plasticity coefficient r_{12} is varied.

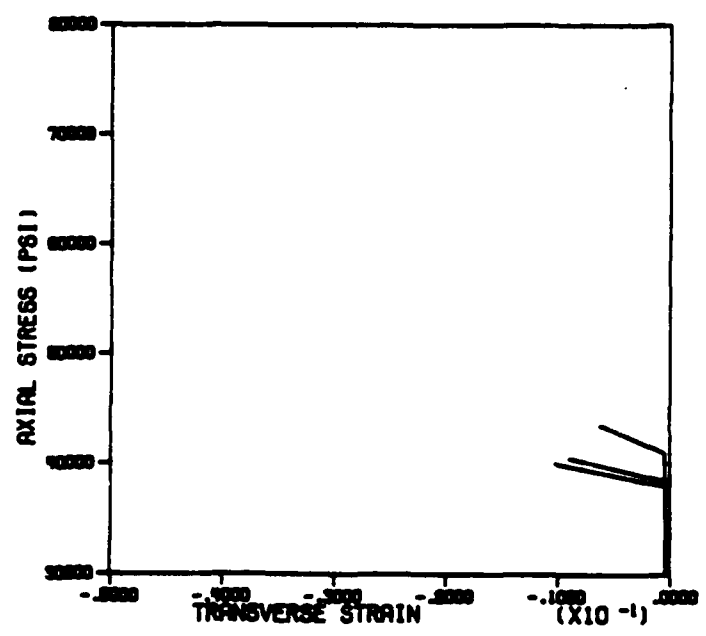
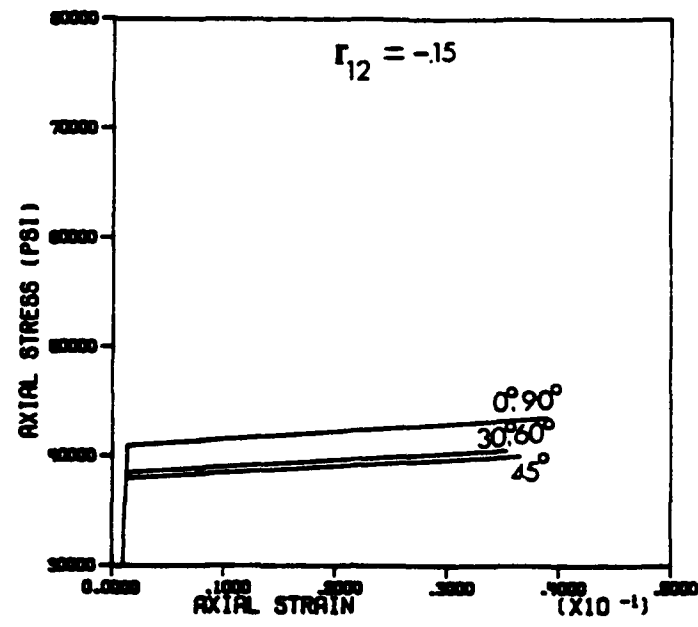


Figure 2.5 continued

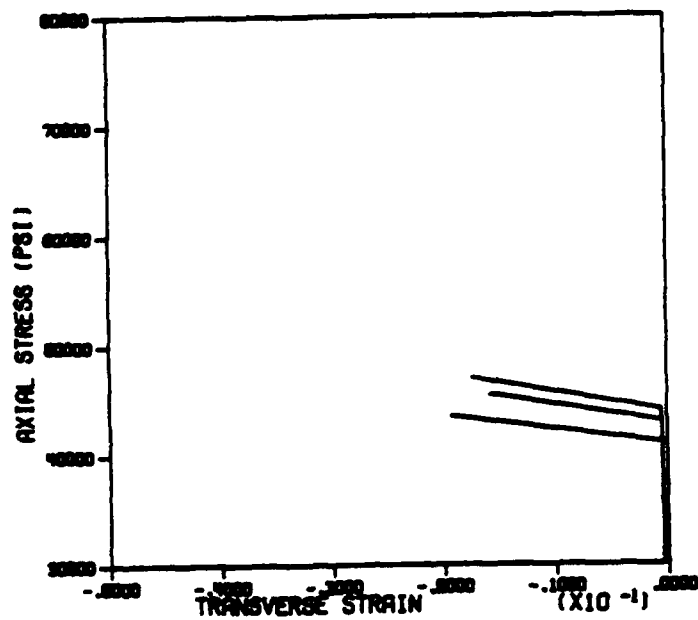
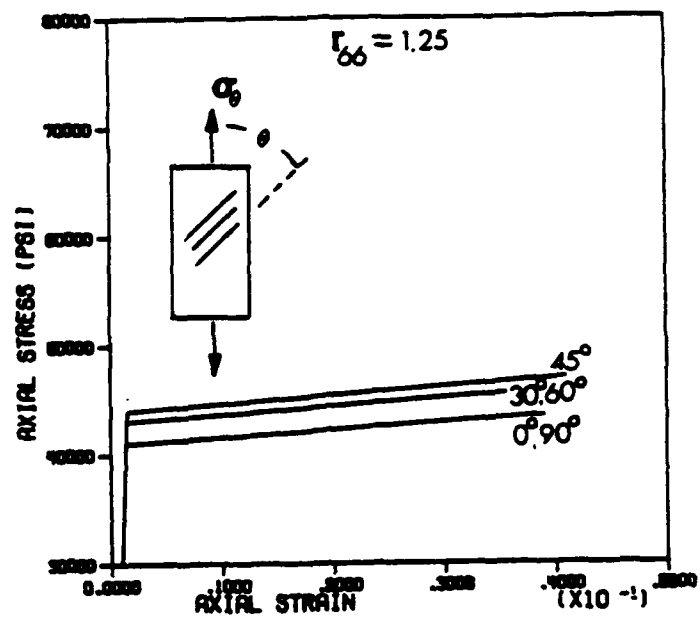


Figure 2.6 Uniaxial elastoplastic response of a material in which the plasticity coefficient r_{66} is varied.

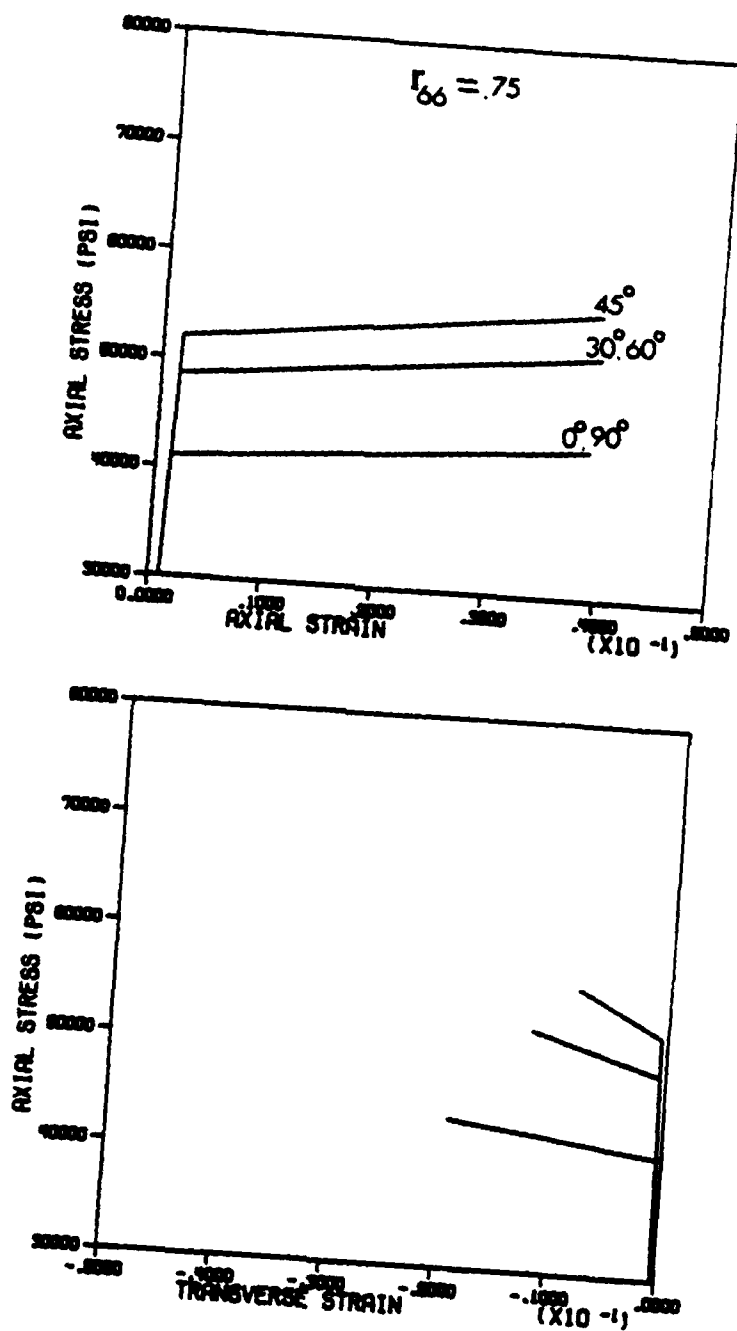


Figure 2.6 continued

plastic strain (\bar{e}^p). These coefficients allow the stress-strain curves obtained at different angles to be collapsed into a single master curve. With this in mind, the work-hardening relationship for any arbitrary orientation of a uniaxial specimen can be written as

$$\bar{\sigma} = h(\bar{e}^p) \quad (2.22)$$

where

$$\bar{\sigma} = \sqrt{\frac{3}{2}} f_{\theta} \sigma_{\theta}$$

$$\bar{e}^p = \sqrt{\frac{2}{3}} \frac{1}{f_{\theta}} e_{\theta}^p$$

$$f_{\theta} = \sqrt{r_{11} \cos^4 \theta + \sin^4 \theta + 2r_{66} \sin^2 \theta \cos^2 \theta + 2r_{12} \sin^2 \theta \cos^2 \theta}$$

For a material with a given anisotropy (e.g. particular r 's), the workhardening is specified by the function $h(\bar{e}^p)$. This function is usually expressed in the form of a power law. An example of such a hardening law is a three parameter model used by Kenaga [12] to represent a Boron-Aluminum metal-matrix composite. It appears as

$$\bar{e}^p = \left[\frac{\bar{\sigma} - \bar{\sigma}_y}{\alpha} \right]^{\beta} \quad (2.23)$$

where $\bar{\sigma}_y$, α , and β are curve fitting parameters.

In the work to follow, the r 's are constants; so the function $h(\bar{e}^p)$ is the only means by which the work hardening can be changed.

It is interesting to note in Figs. 2.3-2.6 that all parametric cases utilize an identical work-hardening function, yet the individual uniaxial elastic-plastic slopes are different.

YIELD CRITERION UNDER MULTIAXIAL LOADING

For the case of an ideally isotropic material under a uniaxial stress state, a single value of yield will suffice. But a multiaxial stress complicates the definition of the yield point, and it actually becomes a yield surface. A further complication is the introduction of anisotropy into the material. It is apparent that the locus of yield points under various combinations of stress forms a surface in stress space.

A possible interpretation of effective stress ($\bar{\sigma}$) is a single surface in space for a single point on the work-hardening curve. Therefore, one can say that yield will occur at a value of effective stress, say $\bar{\sigma}_y$, and is a function of the plastic strain. That is, the general yield criterion can be written as

$$\bar{\sigma}_y(\bar{e}^p) = \frac{3}{2} (r_{11}\sigma_{11}^2 + \sigma_{22}^2 + 2r_{12}\sigma_{11}\sigma_{22} + 2r_{66}\sigma_{12}^2) \quad (2.24)$$

In general, this expression defines the yield surface for an orthotropic material under a multiaxial state of stress.

Parametric Study of the Plasticity Coefficients

In order to provide a graphical representation of the orthotropic ellipsoid, the yield surface is plotted in σ_{11} , σ_{22} , σ_{12} space. A

parametric study of r_{11} , r_{12} , and r_{66} is illustrated in Fig. 2.7.

The study of r_{11} indicates a definite distortion of the ellipsoid in the direction of increasing σ_{11} for decreasing r_{11} . It is clear that r_{12} (which multiplies the stress cross term $\sigma_{11}\sigma_{22}$) affects the symmetric elongation along the plane $\sigma_{11} = \sigma_{22}$. This result implies that yield in a uniaxial stress state oriented along a principle material axis will not be affected by r_{12} . But yield in a multiaxial stress will be.

The plasticity coefficient r_{66} can be studied by observing the influence of σ_{12} . It is seen that a decreasing r_{66} elongates the ellipsoid in the direction of the shear stress component. This has the effect of decreasing the contribution of σ_{12} towards yielding.

Isotropic Behavior

It is of interest to consider the requirements necessary for isotropic yield behavior. A material is isotropic if the yield criterion is invariant under a rotation of axes. That is

$$\begin{aligned}\bar{\sigma}_y^2 &= \text{const} = \frac{3}{2} (r_{11}\sigma_{11}^2 + \sigma_{22}^2 + 2r_{12}\sigma_{11}\sigma_{22} + 2r_{66}\sigma_{12}^2) \\ &= \frac{3}{2} (r_{11}\sigma_{11}'^2 + \sigma_{22}'^2 + 2r_{12}\sigma_{11}'\sigma_{22}' + 2r_{66}\sigma_{12}'^2)\end{aligned}$$

where σ_{11}' , σ_{22}' , σ_{12}' are in the rotated system. In order for this to be true for any transformed stresses, then it is necessary that

$$\begin{aligned}r_{11} &= 1.0 \\ r_{12} + r_{66} &= 1.0\end{aligned}\tag{2.25}$$

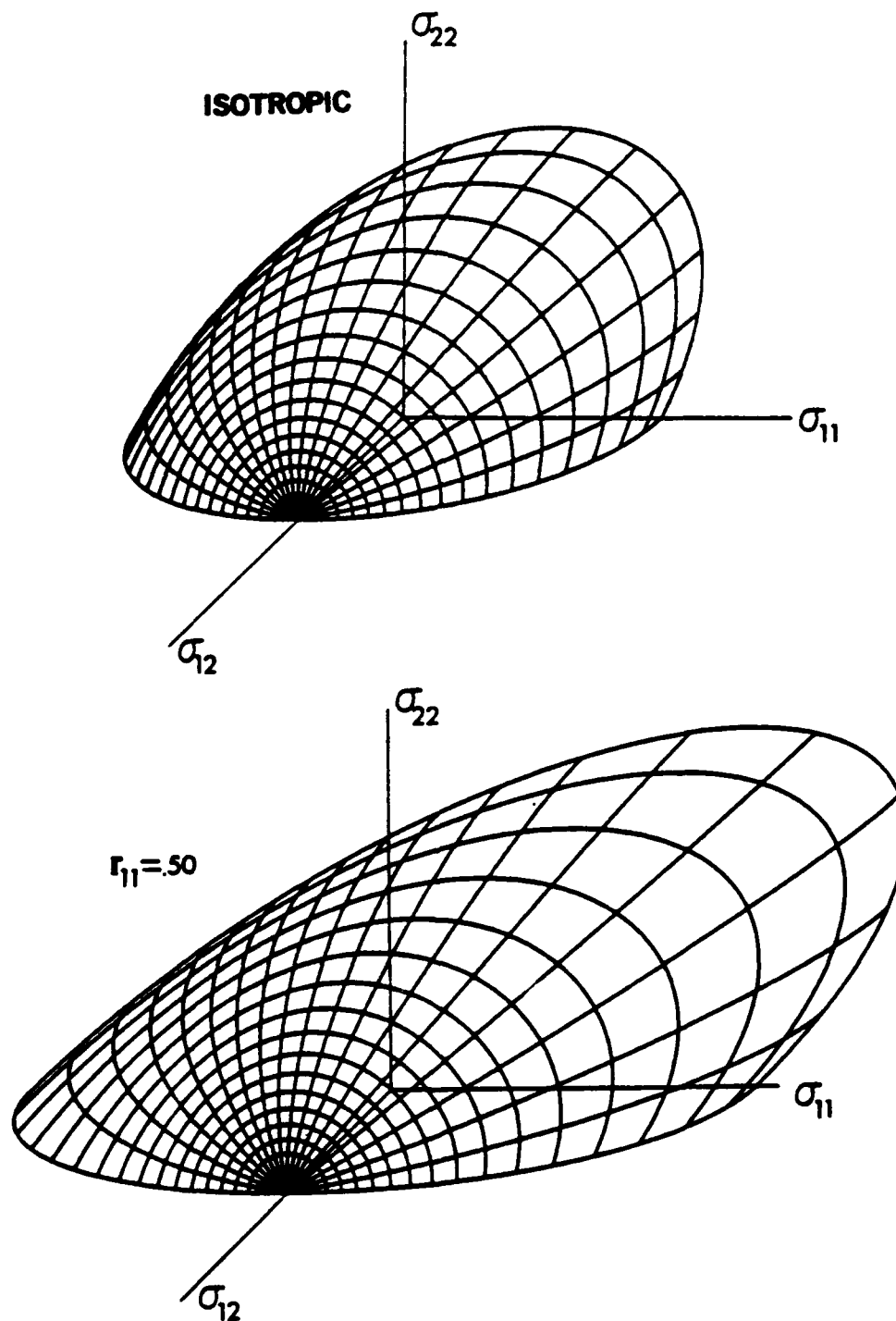


Figure 2.7 Illustration of the yield surface in σ_{11} , σ_{22} , σ_{12} stress space for different values of the plasticity coefficients.

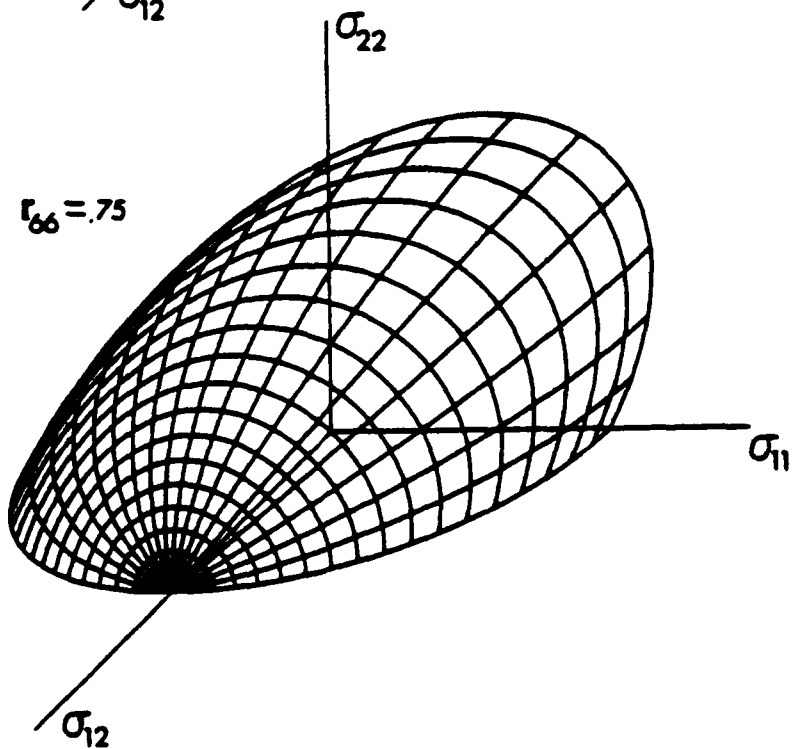
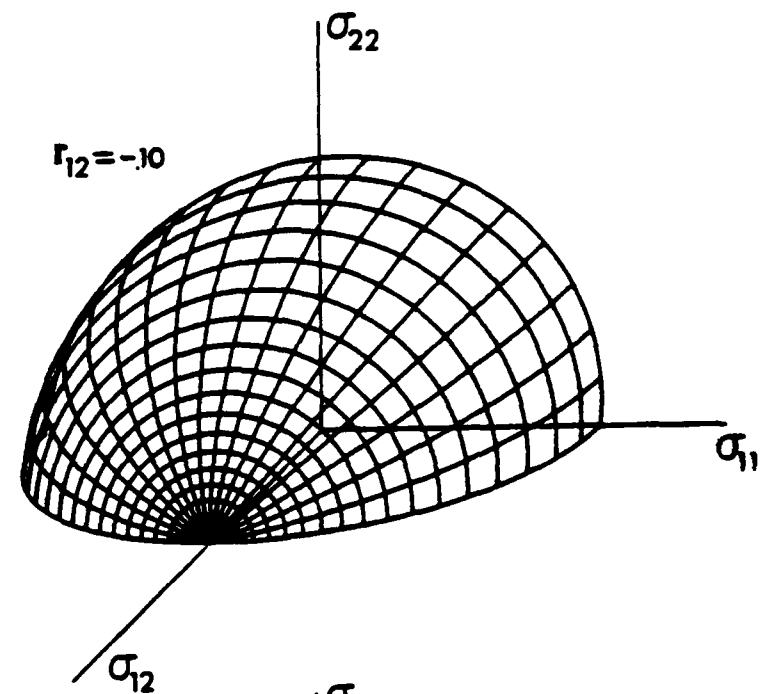


Figure 2.7 continued

It is interesting to note that this is more general than the usual isotropic restrictions of

$$r_{11} = 1.0 \quad r_{12} = -.50 \quad r_{66} = 1.50$$

This point is demonstrated in Fig. 2.8 where the values

$$r_{11} = 1.0 \quad r_{12} = -.25 \quad r_{66} = 1.25$$

are used. These curves are identical to those of Fig. 2.3.

Effect of Work-hardening on the Yield Surface

The anisotropic yield locus was shown to be

$$\bar{\sigma}_y(\bar{\epsilon}^p) = \frac{3}{2} (r_{11}\sigma_{11}^2 + \sigma_{22}^2 + r_{12}\sigma_{11}\sigma_{22} + 2r_{66}\sigma_{12}^2)$$

After the onset of initial yielding, plastic deformation will occur. If isotropic hardening is assumed, the yield surface in stress space will expand to each new stress as work-hardening continues as illustrated in Fig. 2.9. Isotropic hardening results in equal tension and compression for a uniaxial specimen. Note that the yield criterion is anisotropic even though the hardening is isotropic. This is often a common point of misunderstanding.

Anisotropic work-hardening theory accounts for changes in the shape of the yield locus during plastic deformation. Anisotropic hardening can be introduced by letting the plasticity coefficients vary as a function of some state variable. This can be expressed as

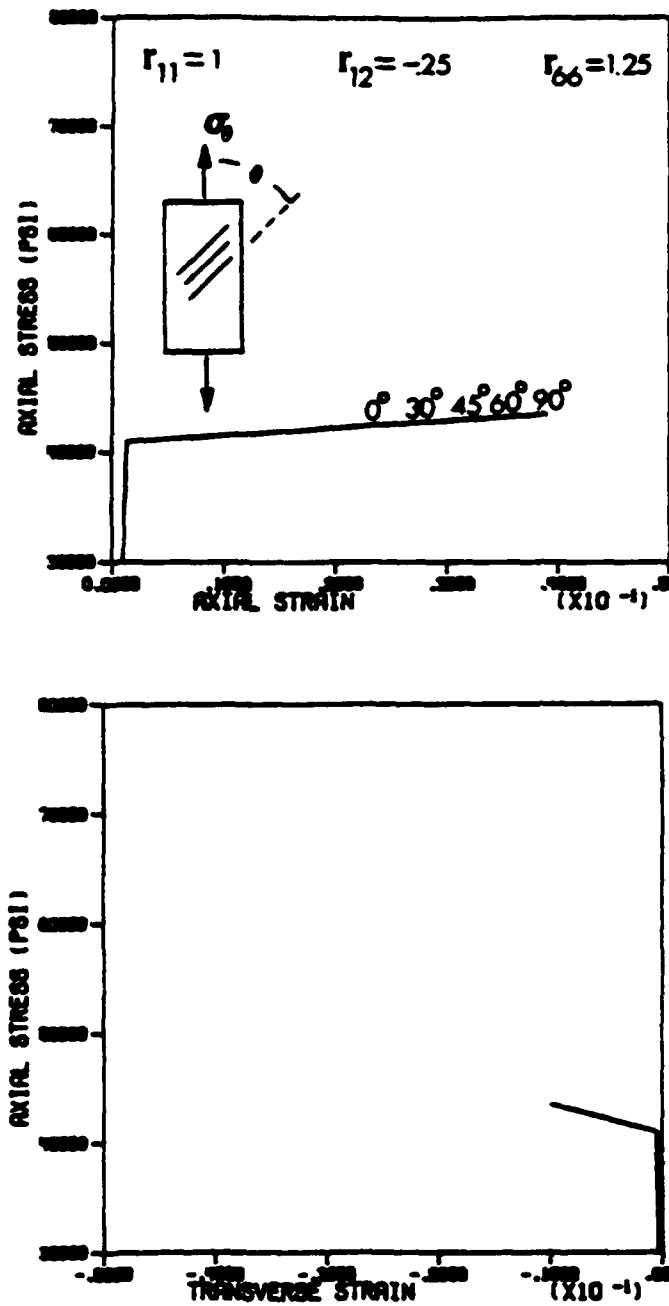


Figure 2.8 Uniaxial elastoplastic response of a material in which the plasticity coefficients are constrained to non-typical isotropic values.

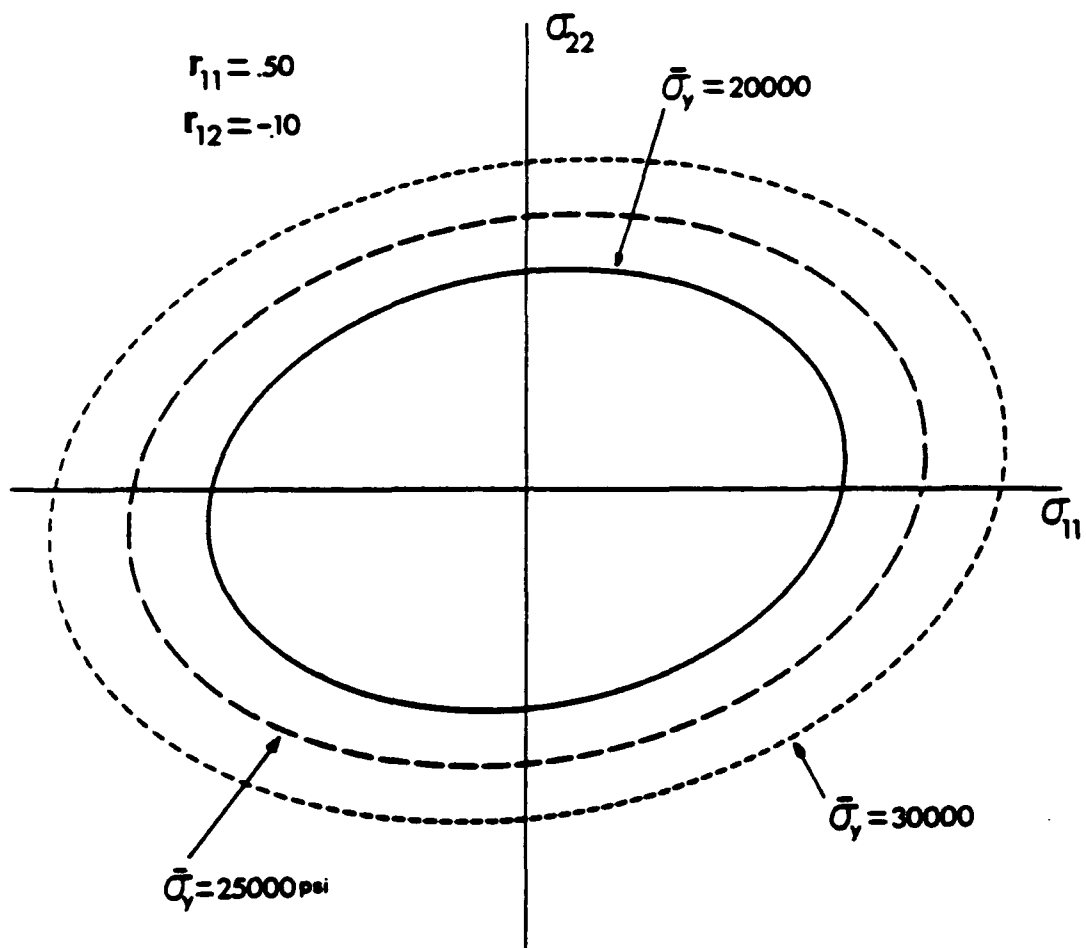


Figure 2.9 Illustration of isotropic hardening of an anisotropic yield surface.

$$\bar{\sigma}_y(\bar{e}^P) = F(\bar{\sigma}, r_{ij}(\bar{\phi}))$$

where $\bar{\phi}$ is some function of the plasticity, say \bar{e}^P . A graphic depiction of this hardening behavior is presented in Fig. 2.10, where not only is $\bar{\sigma}_y$ changing, but so are r_{11} and r_{12} .

LOAD PATH DEPENDENCE OF ACCUMULATED STRAIN

The plasticity theory formulated is incremental. The advantage of this approach is that it allows modelling of complex loading paths (including unloading). Hence, a discussion of path dependence is pertinent.

Deformation Theory

The deformation theory of plasticity developed in 1924 by Hencky assumes a unique stress-strain relationship. As presented by Kachanov [8]

$$\sigma_{ij} = \frac{\epsilon}{3k} \delta_{ij} + \frac{2\tau_s}{\Gamma} e_{ij}^P \quad (2.26)$$

where

$$\begin{aligned} \epsilon &= \text{unit volume change due to mean pressure} \\ \tau_s &= \text{effective yield stress} \end{aligned}$$

and Γ is related to work-hardening. For example, Γ can be written as a function of the effective stress or effective plastic strain as

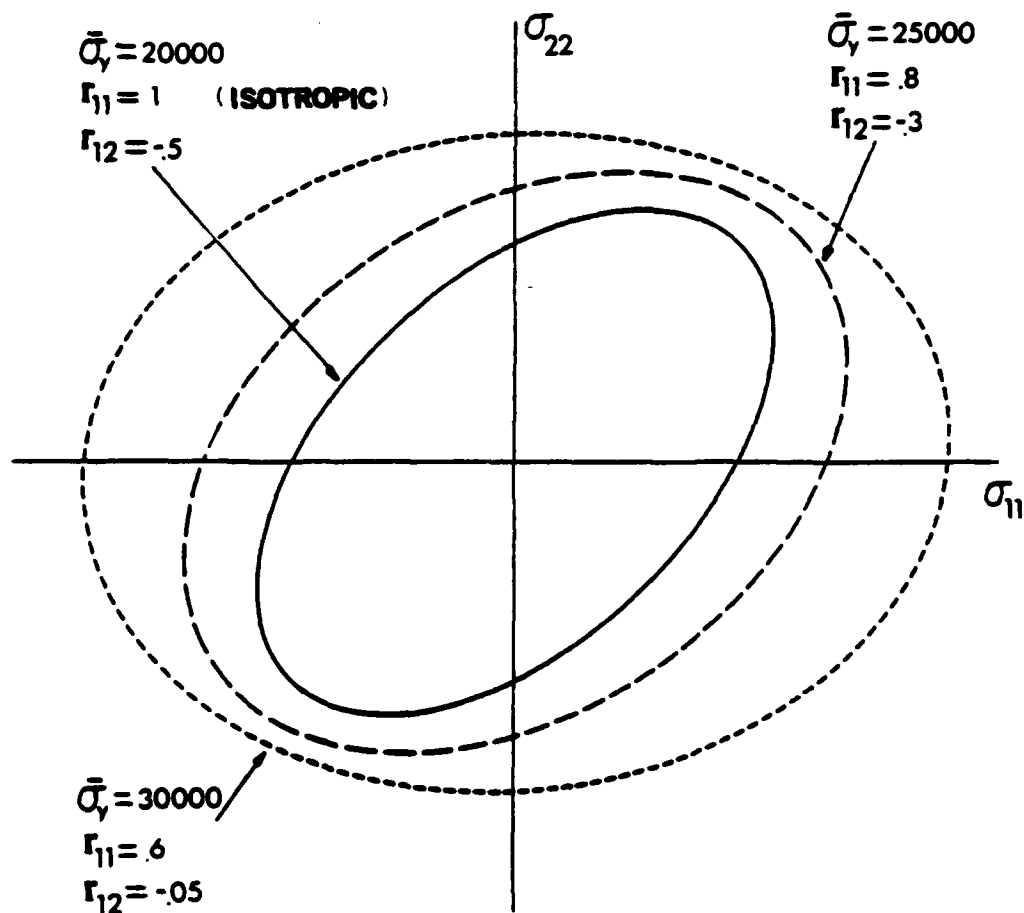


Figure 2.10 Illustration of anisotropic hardening of an initially isotropic yield surface.

$$\Gamma = f(\bar{\sigma}, \bar{\epsilon}^p)$$

It was also shown by Kachanov that the governing equations of deformation theory correspond to a non-linear elastic constitutive representation. Having the load-deformation path uniquely defined results in significant advantages during numerical analyses, in that a Newton-Raphson solution algorithm is easily implemented. Unfortunately, there are limitations to the use of a deformation theory.

Kachanov demonstrated that the governing equations of deformation theory coincide with incremental theory only during simple loading. The two theories agree only when the stress components maintain the same proportion to each other. A simple unloading path such as uniaxial unloading would violate the requirements for deformation theory.

Unloading and Cyclic Loading

A monotonic uniaxial loading and corresponding unloading are depicted in Fig. 2.11. One can imagine that the loading processes can be viewed as a non-linear elastic material response. But upon unloading, it becomes quite evident that the elastoplastic response is not well represented by a single valued stress-strain relationship. Since the study of problems with elastic unloading and residual stresses is of primary interest in this research, then only incremental theory will be used.

The uniaxial stress-strain behavior of a cyclic loading path is pictured in Fig. 2.12. This illustration further reinforces the idea of a non-unique stress-strain response and the limitations of the deformation theory. Parenthetically, this figure also highlights

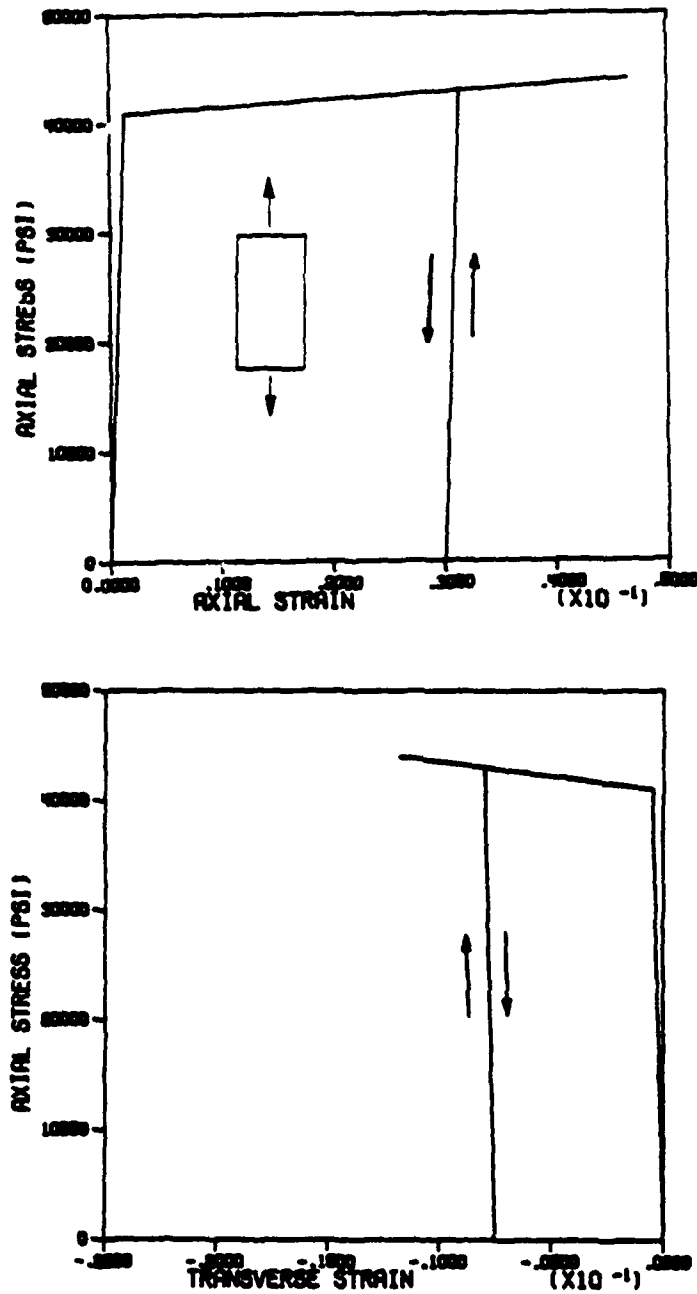


Figure 2.11 Uniaxial elastoplastic response of an isotropic material which is loaded, unloaded, then reloaded.

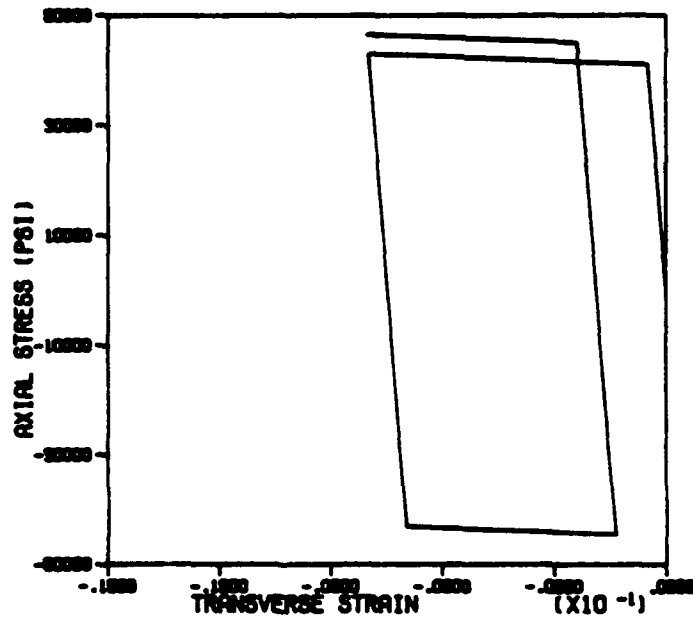
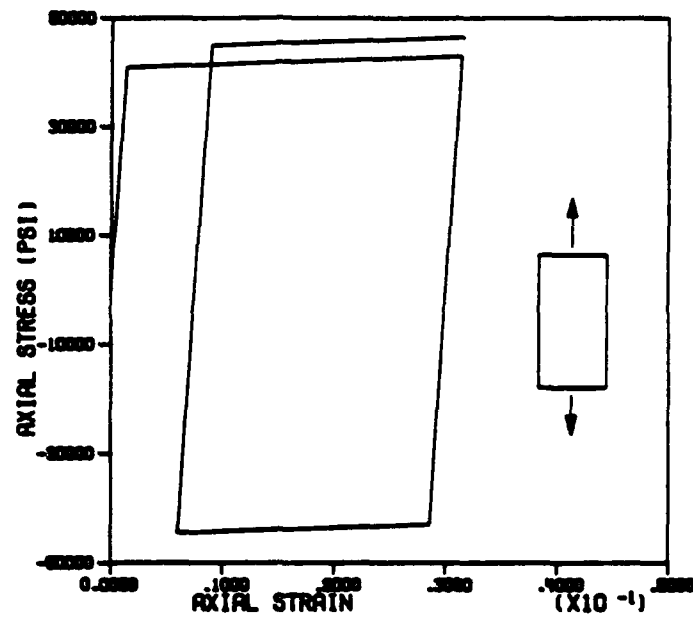


Figure 2.12 Uniaxial elastoplastic response of an isotropic material under cyclic loading.

the effects of isotropic hardening, that is, the self-similar expansion of the yield surface.

This parametric study highlights the complexity of the yield criterion in a multiaxial stress state. If anisotropy were introduced along with a complex geometry, one could see the difficulty in predicting yield, as well as subsequent work-hardening. Because of this behavior, Section 3 will deal with the implementation of the theory into a finite element program.

Some Particular Complex Loading Paths

Complex loading paths can be induced by the application of multiaxial loads in sequence; for example, a uniaxial load followed by a transverse load. Figure 2.13 compares three different load paths involving the normal stress components. Figure 2.14 on the other hand, illustrates the effect of shear along with a normal stress component. In both figures, the case of simultaneous load application (which would be the deformation case) is included. These results clearly indicate the strong path dependence of accumulated strain. The final stress-strain response is obviously not unique when different loading paths are taken. This rules out deformation theory for this class of problems.

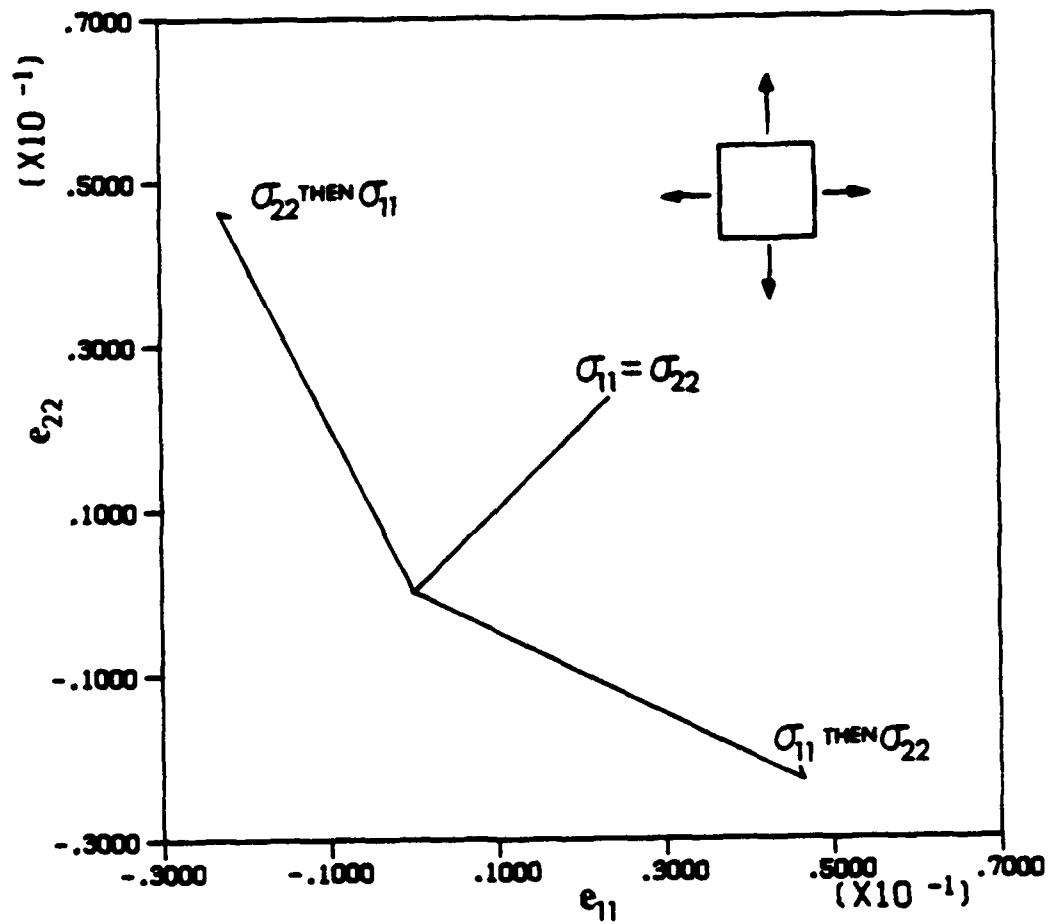


Figure 2.13 Elastoplastic deformation of an isotropic material for three complex loading paths involving both normal stress components.

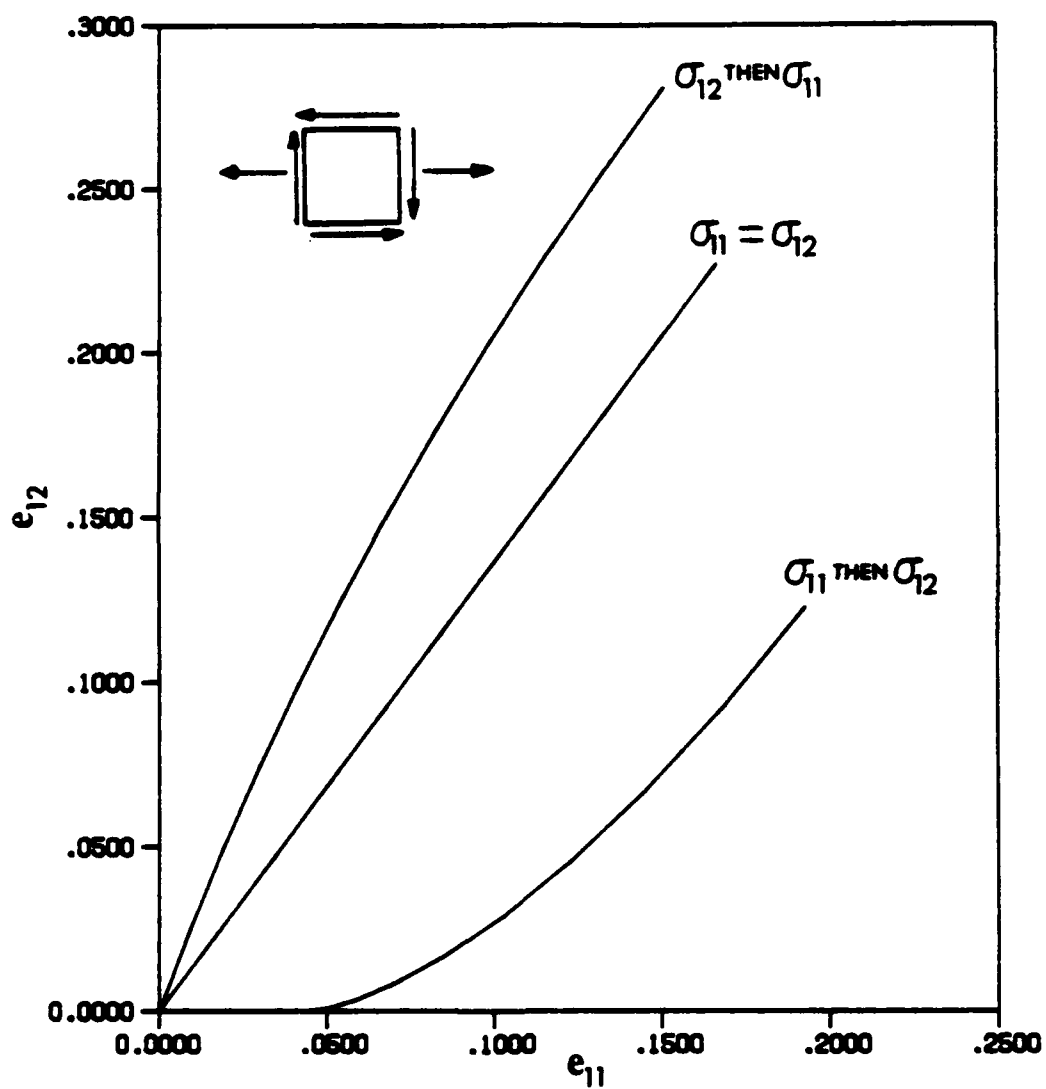


Figure 2.14 Elastoplastic deformation response of an isotropic material for three complex loading paths involving a normal and a shear stress component.

SECTION 3 FORMULATION OF COMPUTATIONAL TOOLS

INTRODUCTION

The study and application of orthotropic plasticity under multi-axial loading requires the development of computational tools. Without these tools, it is very difficult and expensive to gain insight into these intricate non-linear problems. The incremental formulation of plasticity makes the digital computer an ideal vehicle to investigate load-deformation behavior under complex loading conditions.

This section discusses the development of a finite element program designed to analyze orthotropic elastic-plastic problems. The associated pre-processing and post-processing software are also developed. The lamination theory discussed in Section 2 is extended and included in a computer program which predicts load deformation behavior of laminated orthotropic elastic-plastic materials.

OVERALL VIEW OF PROGRAM ANPLAST

A self-contained finite element program and peripheral software written in Fortran 77 is presented.

Program Structure and Philosophy

The ANPLAST finite element program is designed for plane stress anisotropic elastic-plastic analysis. It solves the non-linear problem by dividing the total applied load into small load increments and then summing up all pertinent quantities such as stress, strain,

displacement, and nodal loads [14]. The global stiffness matrix is updated at the beginning of every loading increment to account for the inherent material non-linearity associated with plasticity. The analysis continues until the maximum load specified is reached, or as an alternative, the number of yielded elements has exceeded a maximum specified by the user. The element and nodal quantities can be output in a number of optional formats.

A descriptive FORTRAN flow diagram of the ANPLAST program is shown in Fig. 3.1. This program is designed so that the main program provides the control and accounting of the analysis while the subroutines carry out the main functions. The list of subroutines and a brief description of each follows:

INPUT:	Read in model, geometry, boundary conditions and initialize the program control parameters.
MESG:	Provide warning and error messages.
AMAT:	Form the element strain-nodal displacement matrices.
LOAD:	Read in the incremental nodal loads.
FORMK:	Form the global stiffness matrix.
ESMAT:	Form the element stiffness matrix.
SSE:	Form the incremental elastic stress-strain relations.
SSP:	Form the incremental elastic-plastic stress-strain relations.
ROT4:	Angular transformation of 4th order tensor.
ROT2:	Angular transformation of 2nd order tensor.
INVERT:	Inversion of 3x3 matrix
DCMPBD:	Decomposition of global stiffness [15] matrix.
SLVBD:	Solution of global system of equations [15].

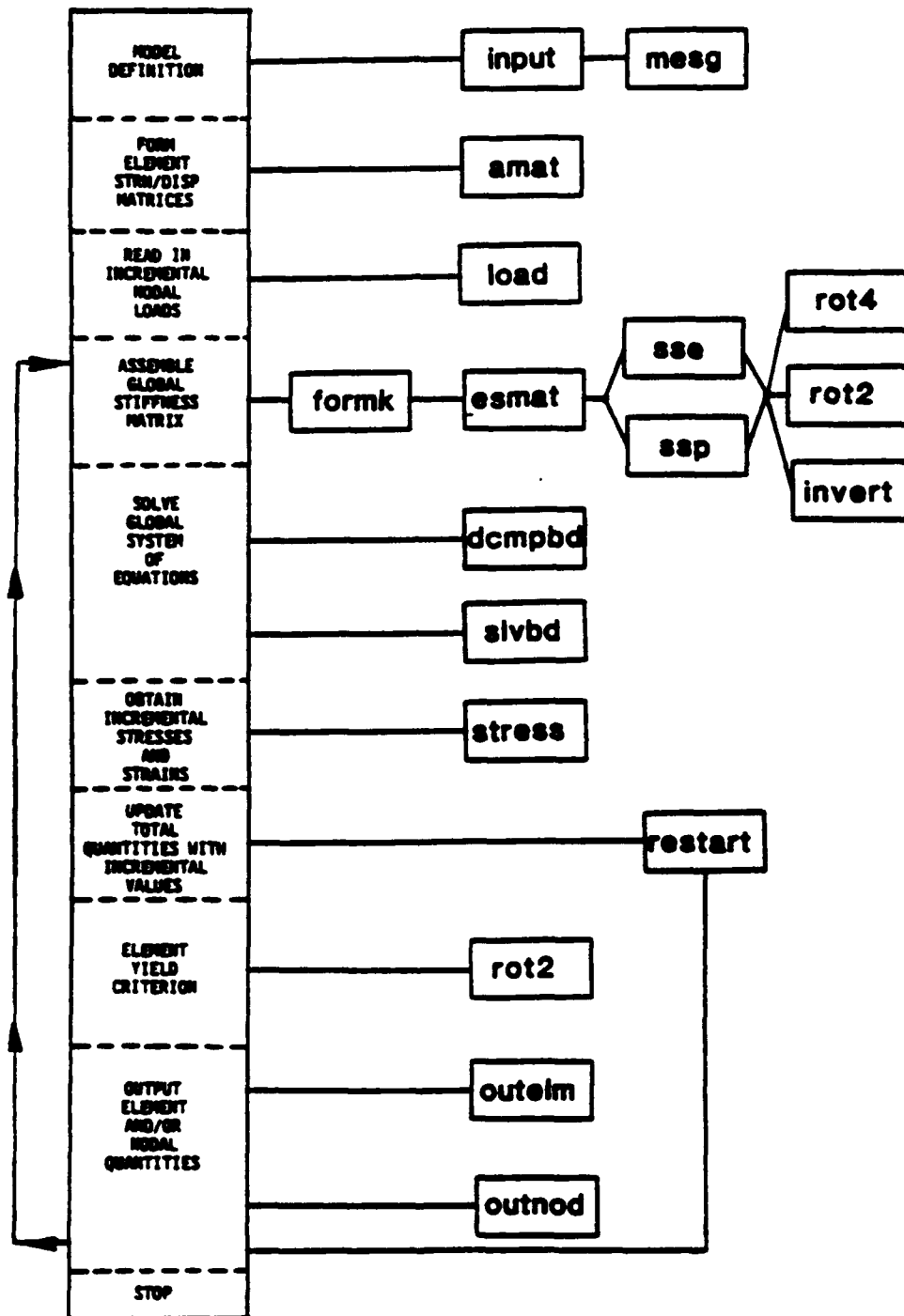


Figure 3.1 Flow Diagram of the ANPLAST finite element program.

STRESS: Calculate incremental element stresses and strains.
OUTELM: Output element stresses and strains.
OUTNOD: Output nodal stresses and strains.
RESTRT: Read and write element/nodal quantities for restart.

Comparison of Solution Algorithms

Using the finite element technique to analyze solids results in the formation of a large number of simultaneous equations. There is a choice to include the solution algorithm directly into the FORTRAN code, or utilize scientific library utility routines (such as IMSL). It was decided to incorporate the equation solver directly into the ANPLAST structure. The ANPLAST program consequently is self contained and therefore does not require any peripheral software other than the usual FORTRAN 77 libraries.

A parallel version of ANPLAST which utilizes the IMSL routines was also developed to verify the efficiency of the solution algorithm taken from Segerlind [15]. The computation time on identical analyses demonstrated that the IMSL version was actually less efficient than the hardwired solution routines. Of course to be fair, it must be realized that the IMSL routines are more general in nature, and easy to access. In summary, the ANPLAST solution algorithms are efficient and accurate and are more than adequate for the purposes of this research.

Program Re-start Capabilities

The majority of analyses conducted with ANPLAST involve an incremental approach to the non-linear problem. This approach usually requires at least 10 to 15 increments and results in considerable

computation time. In addition, the size of each loading increment must be estimated prior to the analysis and may turn out to be inappropriate. Further, the amount of data which can be printed out for each increment is significant and usually not known prior to the analysis.

Because of these difficulties, a "restart" option was built into ANPLAST. This "restart" capability permits the analysis to be stopped and started again at a later time. The analysis can be restarted at whatever increment has been previously written to the restart file. Two blocks of information are stored: the element quantities and the nodal values. The analysis is re-started by reading these quantities in and re-initializing the appropriate arrays. New incremental loading is supplied and the analysis continued.

An additional benefit of the restart capability is the post processing of the output. Only a minimal amount of information needs to be printed out after each increment, since the analysis can be restarted at any previous increment and all of the desired information recovered.

Numerical Form of the Incremental Constitutive Relations

The incremental plastic strains represented in Eq. 2.14 have to be written in a more explicit form so that they are compatible with the finite element method. Starting with the equation for the effective stress

$$\bar{\sigma} = \sqrt{\frac{3}{2} (r_{11}\sigma_{11}^2 + \sigma_{22}^2 + 2r_{12}\sigma_{11}\sigma_{22} + 2r_{66}\sigma_{12}^2)}$$

gives the effective stress increment as

$$d\bar{\sigma} = \frac{3}{2} \frac{1}{\bar{\sigma}} [(r_{11}\sigma_{11} + r_{12}\sigma_{22}) d\sigma_{11} + (r_{12}\sigma_{11} + \sigma_{22}) d\sigma_{22} + 2r_{66}\sigma_{12}d\sigma_{12}] \quad (3.1)$$

When this is substituted back into the incremental flow rule of Eq. 2.14, the expression becomes [16]

$$\begin{Bmatrix} de_{11}^p \\ de_{22}^p \\ de_{12}^p \end{Bmatrix} = \begin{bmatrix} a_{11}a_{11} & a_{11}a_{22} & a_{11}a_{33} \\ a_{22}a_{11} & a_{22}a_{22} & a_{22}a_{33} \\ a_{33}a_{11} & a_{33}a_{22} & a_{33}a_{33} \end{bmatrix} \begin{Bmatrix} d\sigma_{11} \\ d\sigma_{22} \\ d\sigma_{12} \end{Bmatrix} \frac{9}{4} \frac{1}{\bar{\sigma}^2} \left(\frac{d\bar{\epsilon}^p}{d\bar{\sigma}} \right) \quad (3.2)$$

where

$$a_{11} = r_{11}\sigma_{11} + r_{12}\sigma_{22}$$

$$a_{22} = r_{12}\sigma_{11} + \sigma_{22}$$

$$a_{33} = 2r_{66}\sigma_{12}$$

In symbolic matrix notation this is written as

$$\{de^p\} = [C]^p \{d\sigma\} \quad (3.3)$$

It is clear that the incremental plastic flow is a function of the current stress state, effective stress, degree of work-hardening, and the current increment of stresses ($d\sigma_{11}$, $d\sigma_{22}$, $d\sigma_{12}$). It is interesting to note that the incremental plastic strains are not always

orthotropic with respect to the incremental stresses. For example, when σ_{12} is non-zero, it is possible that the products $a_{11}a_{33}$ and $a_{22}a_{33}$ are non-zero, and the normal incremental strain components are then coupled to the incremental shear stress. This is an indication that the intuition developed from elastic analyses may not always aid in understanding orthotropic plasticity.

The expression for the total incremental stress-strain relationship is obtained by summing the elastic and plastic strain increments

$$\{de\} = [c] \{d\sigma\} \quad (3.4)$$

where

$$[c] = [c]^e + [c]^p$$

The $[c]$ matrix relating incremental stresses and strains will be utilized directly when establishing the element stiffness matrix.

Numerical Implementation of Loading and Unloading

The ANPLAST program is designed for cyclic loading and unloading. Therefore, each element is permitted to yield, work-harden, unload back into the elastic region, and then re-load back to the new yield surface. This transition from elastic to elastic-plastic is calculated on the element level and is not constrained by the direction of loading at the remote location. There is no limit to the number of times an element may pass through the elastic-plastic transition. This capability will make possible a cycle by cycle analysis when

investigating cyclic fatigue. At the present, only isotropic hardening is available, but other hardening theories could be added with little difficulty.

FORMULATION OF THE CONSTANT STRAIN TRIANGLE

The linear displacement constant strain triangle (CST) [15,17] was chosen as the primary finite element in ANPLAST. The simplicity of the formulation and implementation into a large FORTRAN program provides considerable justification for choosing this element.

The Strain-Nodal Displacement Relations

A typical triangular element is represented in Fig. 3.2, along with its displaced shape [17]. Because of the linear displacement assumptions, the displacements at any global point (x,y) can be expressed as the following linear functions

$$\begin{aligned} u(x,y) &= u_i + c_1x + c_2y \\ v(x,y) &= v_i + c_3x + c_4y \end{aligned} \tag{3.5}$$

The constants c_1 , c_2 , c_3 , and c_4 can be obtained in terms of the corner displacements and the geometry of the element.

$$c_1, c_2, c_3, c_4 = F(u_i, v_i, u_j, v_j, u_k, v_k)$$

The three global strain components within the element can be obtained from the assumed displacement field as follows

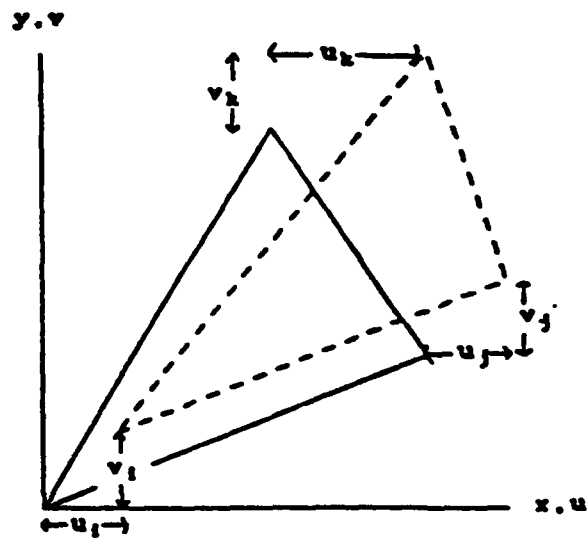
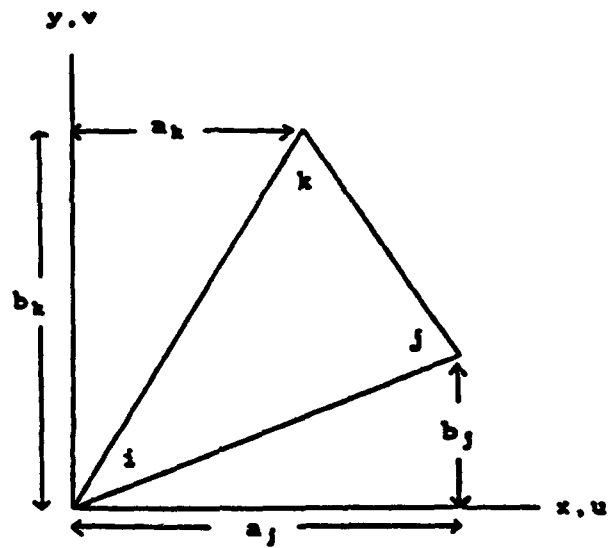


Figure 3.2 Dimensions and assumed displacements of a constant strain triangle finite element.

$$\begin{aligned}
 e_{xx} &= \frac{\partial u}{\partial x} = c_1 \\
 e_{yy} &= \frac{\partial v}{\partial y} = c_4 \\
 e_{xy} &= \frac{\partial u}{\partial y} + \frac{\partial v}{\partial x} = c_2 + c_3
 \end{aligned}
 \tag{3.6}$$

The strains may be represented entirely in terms of nodal displacements as defined in Fig. 3.2.

$$\begin{Bmatrix} e_{xx} \\ e_{yy} \\ e_{xy} \end{Bmatrix} = \frac{1}{2A} \begin{bmatrix} b_j - b_k & 0 & b_k & 0 & -b_j & 0 \\ 0 & a_k - a_j & 0 & -a_k & 0 & a_j \\ a_k - a_j & b_j - b_k & -a_k & b_k & a_j & -b_j \end{bmatrix} \begin{Bmatrix} u_i \\ v_i \\ u_j \\ v_j \\ u_k \\ v_k \end{Bmatrix}$$

where

A = element area

or in symbolic form

$$\{e\} = [A] \{q\}
 \tag{3.7}$$

where $\{q\}$ are the nodal displacements.

Element Stiffness Matrix Formulation

The incremental element stiffness matrix $[K]$ can now be obtained by use of Castigliano's Theorem, or other similar energy principles [18] as

$$[K] = \iint [A]^T [C] [A] \, dx dy \quad (3.8)$$

Since the strains and stresses are constant throughout the element, all three of the matrices may be brought outside the integrals, and the area integration carried out explicitly. Since the element is triangular and has straight edges the area integration is direct and exact. Note, that when an element becomes elastic-plastic, $[C]$ becomes stress dependent and consequently so does $[K]$. This is why the global stiffness matrix needs to be updated at the beginning of every increment when plasticity has occurred.

FORMULATION OF THE ISOPARAMETRIC ELEMENT

It is generally thought that the isoparametric element offers some advantage in efficiency and accuracy compared to the CST. For this reason, a quadratic 8-node isoparametric element is implemented into ANPLAST. The descriptive flow diagram and subroutine descriptions are found in Figs. 3.3-3.4.

The Strain-Nodal Displacement Relations

Isoparametric elements are those for which the functional representation of deformational behavior is employed in representation of the element geometry [18].

$$\begin{aligned} x &= \sum N_i u_i & y &= \sum N_i v_i \\ u &= \sum N_i x_i & v &= \sum N_i y_i \end{aligned} \quad (3.9)$$

where

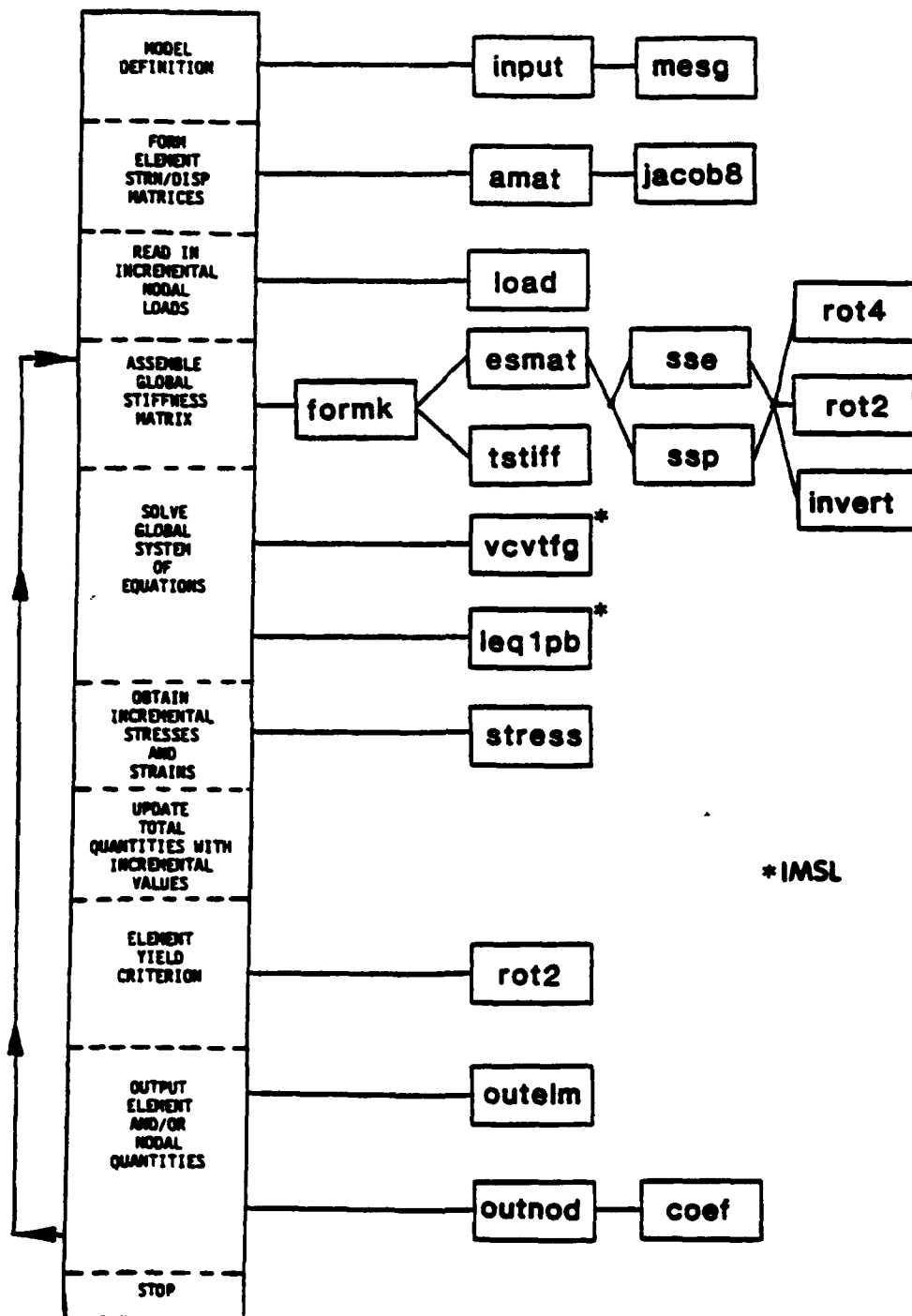


Figure 3.3 Flow Diagram of an alternate version of ANPLAST which utilizes an isoparametric quadrilateral element.

INPUT:	Read in model geometry, boundary conditions and initialize the program control parameters.
MESG:	Provide warning and error messages.
AMAT:	Form the element strain-nodal displacement matrices.
JACOB8:	Form Jacobian matrix and determinant.
LOAD:	Read in the incremental nodal loads.
FORMK:	Form the global stiffness matrix.
ESMAT:	Form the element stiffness matrix.
TSTIFF:	Form full global stiffness matrix.
SSE:	Form the incremental elastic stress-strain relations.
SSP:	Form the incremental elastic-plastic stress-strain relations.
ROT4:	Angular transformation of 4th order tensor.
ROT2	Angular transformation of 2nd order tensor.
INVERT:	Inversion of 3x3 matrix.
VCVTFG:	Transform stiffness matrix to band-symmetric form.
LEQ1PB:	Solution of global system of equations.
STRESS:	Calculate incremental element stresses and strains.
OUTELM:	Output element stresses and strains.
OUTNOD:	Output nodal stresses and strains.
COEF:	Supply coefficients for nodal extrapolation.

Figure 3.4 Subroutine description for the isoparametric element version of ANPLAST.

x, y = geometry of element

u, v = displacement field

N_i = shape functions

The shape functions for the general 8-noded isoparametric element illustrated in Fig. 3.5 are

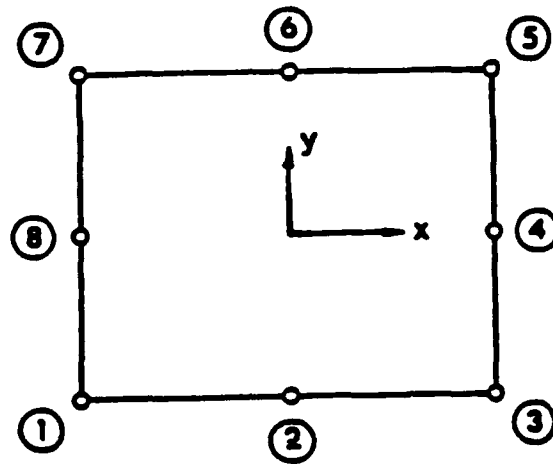
$$\begin{aligned}
 N_1 &= -\frac{1}{4} (1-\xi)(1-\eta)(\xi+\eta+1) & N_2 &= \frac{1}{2} (1-\xi^2)(1-\eta) \\
 N_3 &= \frac{1}{4} (1+\xi)(1-\eta)(\xi-\eta-1) & N_4 &= \frac{1}{2} (1-\eta^2)(1+\xi) \\
 N_5 &= \frac{1}{4} (1+\xi)(1+\eta)(\xi+\eta-1) & N_6 &= \frac{1}{2} (1-\xi^2)(1+\eta) \\
 N_7 &= -\frac{1}{4} (1-\xi)(1+\eta)(\xi-\eta+1) & N_8 &= \frac{1}{2} (1-\eta^2)(1-\xi)
 \end{aligned} \tag{3.10}$$

The strain-nodal displacement matrix can be found by application of the basic differential definitions of strain [18]

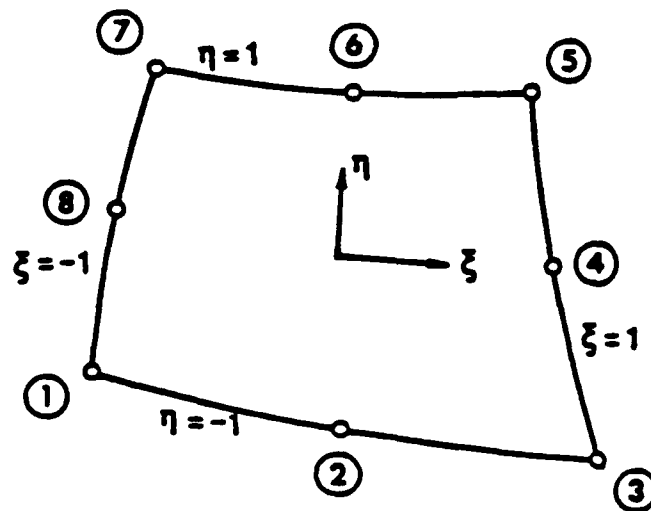
$$\begin{Bmatrix} e_{xx} \\ e_{yy} \\ e_{xy} \end{Bmatrix} = \left[F \left(\frac{\partial N_i}{\partial x}, \frac{\partial N_i}{\partial y} \right) \right] \begin{Bmatrix} u_i \\ v_i \end{Bmatrix}$$

or in symbolic notation

$$\{e\} = [A] \{q\} \tag{3.11}$$



Parent Element



Isoparametric Element

Figure 3.5 Local coordinate system for the 8-node isoparametric quadrilateral element.

and the derivatives are calculated by

$$\begin{Bmatrix} \frac{\partial N_i}{\partial x} \\ \frac{\partial N_i}{\partial y} \end{Bmatrix} = [J]^{-1} \begin{Bmatrix} \frac{\partial N_i}{\partial \xi} \\ \frac{\partial N_i}{\partial \eta} \end{Bmatrix}$$

where $[J]^{-1}$ is the inverse Jacobian transformation matrix which can be calculated by

$$[J] = \begin{bmatrix} \sum_{i=1}^8 \frac{\partial N_i}{\partial \xi} & \sum_{i=1}^8 \frac{\partial N_i}{\partial \eta} \end{bmatrix} \begin{bmatrix} x_1 & y_1 \\ x_2 & y_2 \\ \vdots & \vdots \\ x_8 & y_8 \end{bmatrix}$$

Element Stiffness Matrix Formulation

As was demonstrated for the constant strain triangle in Eq. 3.8 the incremental element stiffness matrix $[K]$ can be obtained by use of Castigliano's Theorem

$$[K] = \iint [A]^T [C] [A] \, dx dy \quad (3.12)$$

Inspection of Eq. 3.11 reveals the strains and stresses are not constant throughout the element. Therefore, the matrix product $[A]^T [C] [A]$ cannot be taken outside the integral. Consequently, a numerical integration scheme must be implemented in the program.

Numerical Integration of Element Matrices

Using the following transformation,

$$dx dy = \det [J] d\xi d\eta$$

the element stiffness matrix now becomes

$$[K] = \int_{-1}^1 \int_{-1}^1 [A]^T [C] [A] |J| d\xi d\eta \quad (3.13)$$

Now, by using the Gaussian quadrature technique, the element stiffness matrix can be calculated by summing the matrix quantity $[A]^T [C] [A]$ at the four selected Gauss points ($\xi = \pm 0.577350$, $\eta = \pm 0.577350$) and multiplying each by the appropriate weighting factor (which in this case is unity). In summary, the stiffness matrix can be represented in symbolic form as

$$[K] = \sum_{i=1}^4 [A]^T [C] [A] |J| w_i \quad (3.14)$$

$$w_i = 1.0 \text{ (weighting function)}$$

It should be noted that for non-linear plasticity analyses, partial yielding may occur in a given element. One particular Gauss point may be yielded while the others are still elastic. This will not present a problem when formulating the element stiffness matrix since the elastic-plastic constitutive relations $[C]^p$ can be utilized when yielding occurs at a particular Gauss point, and then the element

stiffness matrix summed in the usual way.

PRE-PROCESSING AND POST-PROCESSING FEATURES

To make the utilization of ANPLAST more efficient and convenient a number of pre- and post-processing software have been developed.

Mesh Generation and Plotting Features

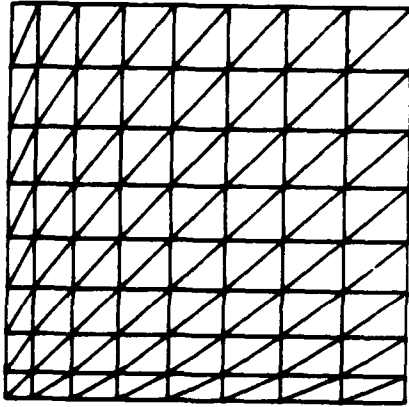
The creation of a geometrical mesh is the first step in a finite element analysis and can often be the most time consuming. Therefore, four generic mesh generators have been developed for rectangular, tapered quadrilateral, radial fan, and circular hole geometries. An example of each type of mesh is illustrated in Fig. 3.6.

All of the programs operate on an interactive basis, prompting the user for appropriate input parameters such as maximum and minimum dimensions as well as mesh density. The mesh generators create two files, one containing the nodal coordinates and the other the element connectivity. The starting node and element numbers are required so that successive files can be combined for constructing a more complex geometry.

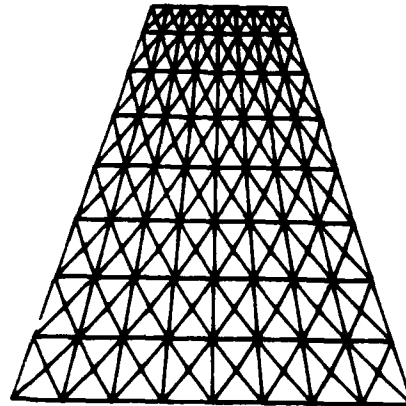
Bandwidth Optimization by Nodal Sweeping

A nodal sweeping technique was developed to join together the various composite meshes into one integral mesh. The interactive nodal sweeping program works by passing a plane or sphere through the composite mesh and fusing it into one by removing any duplicate nodes. This sweeping process also renumbers the nodal connectivity list and alters the stiffness matrix bandwidth. A judicious choice of sweeping orientation can lead to a significant reduction in bandwidth.

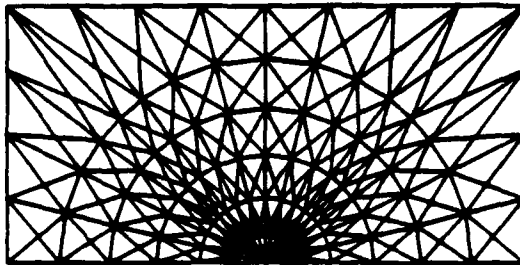
BIASED QUADRILATERAL



TAPERED QUADRILATERAL



RADIAL FAN
(CRACK TIP)



CIRCULAR HOLE

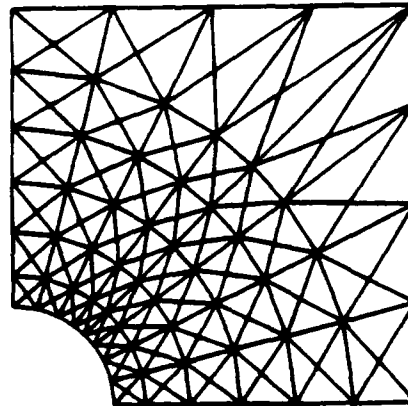


Figure 3.6 A collage of finite element meshes created by the ANPLAST pre-processors. Each mesh design demonstrates biasing of element density.

Considerable gains in analysis efficiency have been evident since developing the nodal sweeping program.

Nodal Averaging of Stresses and Strains

Solution of the finite element equations provides element stresses and strains. For the case of the isoparametric element, the stresses are provided at the Gaussian integration points. The constant strain triangle assumes the stress to be constant across the area of the element. Unfortunately, the element or Gauss point locations usually have no special geometrical significance, while nodes often fall on convenient lines through the mesh. Therefore, nodal averaging techniques were developed.

For both the triangular and quadrilateral elements, the nodal values of stresses are found by averaging the contribution of stress from each connecting element [18]. For the case of the isoparametric element, individual element nodal stresses are calculated by extrapolation of Gauss point stresses using a modified form of the element shape functions [19]. The nodal stresses can be provided directly by ANPLAST in either Cartesian or polar coordinate systems.

Presentation of Results by Contour Plotting

The vast magnitude of results generated by a finite element analysis makes necessary innovative techniques for post processing. One such technique is the contouring of stresses, strains, displacements, or any combination of these quantities. In this particular case, the contouring is based on interpolation of nodal quantities, and plotted using the NCAR package available on the Purdue University Computing Center system.

Sections 4, 5, and 6 will provide examples of the use of the post-processing programs developed for this research.

NUMERICAL EXTENSION OF LAMINATION THEORY

LAMINATE Computer Program

The macroscopic laminate behavior described in Section 2 is adapted for use in an interactive FORTRAN 77 computer program called LAMINATE. The purpose of the LAMINATE program is to study the multi-axial response of elastic-plastic laminates. The incremental laminate load deformation equations can be written as

$$\begin{Bmatrix} dN_x \\ dN_y \\ dN_{xy} \end{Bmatrix} = [A_{ij}] \begin{Bmatrix} de_x^o \\ de_y^o \\ d\gamma_{xy}^o \end{Bmatrix} \quad (3.15)$$

where

$$A_{ij} = \sum_{K=1}^N [\bar{Q}_{ij}] t_K$$

LAMINATE logic has been designed to parallel that of ANPLAST so that loading increments (dN_x, dN_y, dN_{xy}) are applied and the resulting mid-plane strains calculated. This is accomplished by inverting $[A_{ij}]$ after it is numerically evaluated.

As the incremental analysis progresses, the individual layers can become elastic-plastic, and their contribution enters through the formulation of $[\bar{Q}_{ij}]_K$.

The LAMINATE program can analyze a laminate consisting up to 10 orthotropic elastic-plastic layers. Each layer is characterized individually, and obeys its own yield and work-hardening law. The program output consists of individual layer stresses and overall strains.

Modifications to ANPLAST

The ANPLAST finite element program was modified to allow for orthotropic elastic-plastic laminated material response. Basically, the lamination theory developed for the LAMINATE program is applied to ANPLAST. The primary modifications occur in the MAIN program and in subroutine ESMAT where it is necessary to store each of the individual layer stresses and check for yielding in each layer of each element. When formulating the element stiffness matrix it is necessary to sum over each layer through the thickness of the laminate. Only minor modifications are made to the standard ANPLAST input structure. It is interesting to note that analyzing a single layer is a special sub-set of lamination theory, and therefore this version of ANPLAST can be used for all analyses.

COMPUTER PROGRAM PORTABILITY

All of the computational programs developed in this section have been designed to be portable. None of the programs utilize specialized utility routines, such as those from IMSL. ANPLAST and LAMINATE can be easily executed on interactive as well as batch processors. At Purdue, both of these programs have been successfully run on the VAX 11/780, CDC6600, and CYBER 205. The majority of pre-processing and

post-processing programs are best run on an interactive system as this provides the greatest convenience for the user.

Since all of the programs utilize only standard FORTRAN 77 library routines, they are completely portable to other systems. The only limitation will be the amount of memory made available to the programs. As the problems become larger, computers with a virtual memory system appear to offer the only alternative unless out of core solution algorithms are developed.

SECTION 4 ELASTOPLASTIC STUDY OF A SHEET WITH A CIRCULAR HOLE

INTRODUCTION

A thin sheet with a circular hole is analyzed, because it is one of the standard benchmark problems. It is expected that many of the trends discovered for the hole will apply to more severe discontinuities, such as cracked panels. Additionally, there is a body of literature available containing some theoretical and experimental elastoplastic solutions.

The ANPLAST program will be used to investigate the isotropic elastoplastic response of a sheet with a circular hole and comparisons made with some of the solutions in the literature. This study will then be extended to orthotropic plastic flow, by conducting a parametric study of the plasticity coefficients. The numerical results are compared to an elastoplastic experimental study of a metal matrix fiber reinforced sheet. A problem with a remote complex loading path is also considered.

SHEET WITH ISOTROPIC MATERIAL PROPERTIES

Elastic Loading: Comparison with Theoretical Solution

A thin sheet with isotropic elastic material properties was modeled by ANPLAST and analyzed for the case of a uniaxially applied remote load. The finite element mesh used is shown in Fig. 4.1. The fixed grip end condition simulated by inputting very stiff material

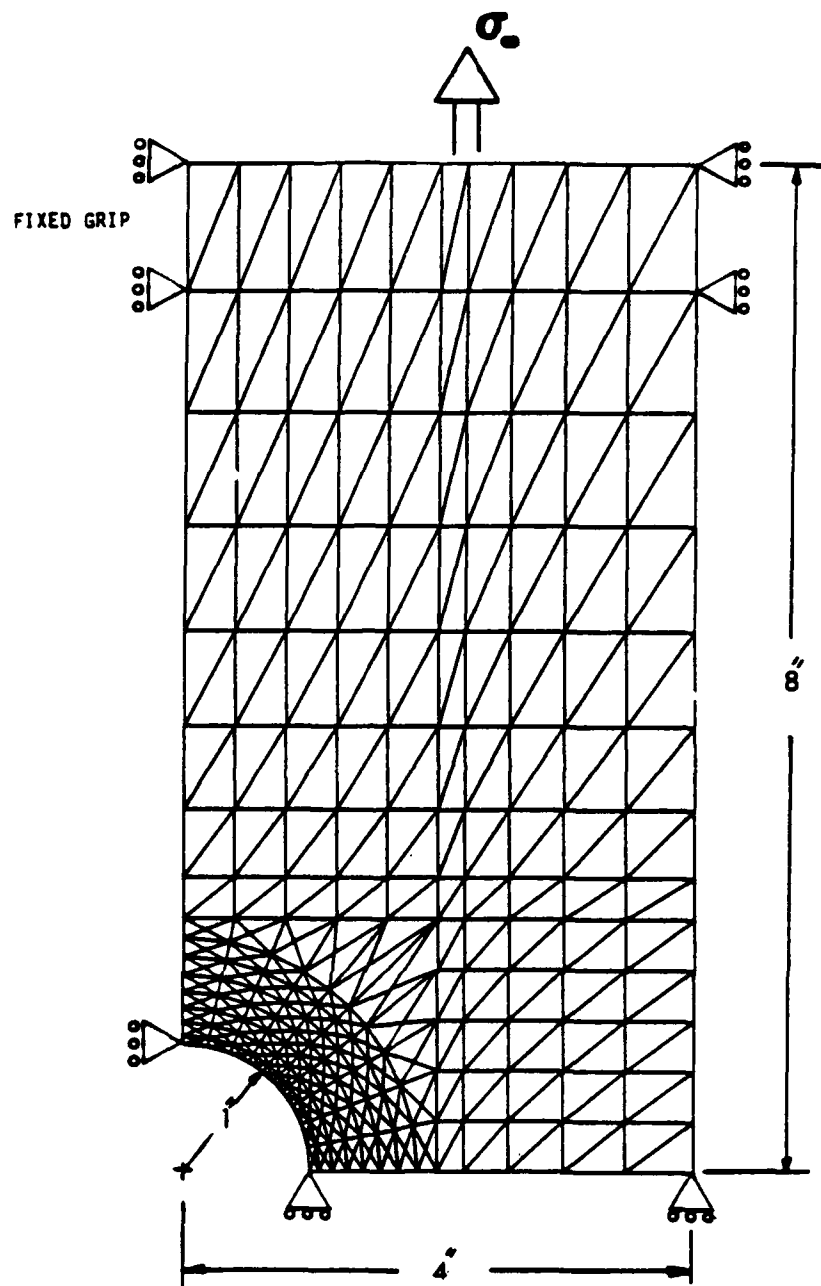


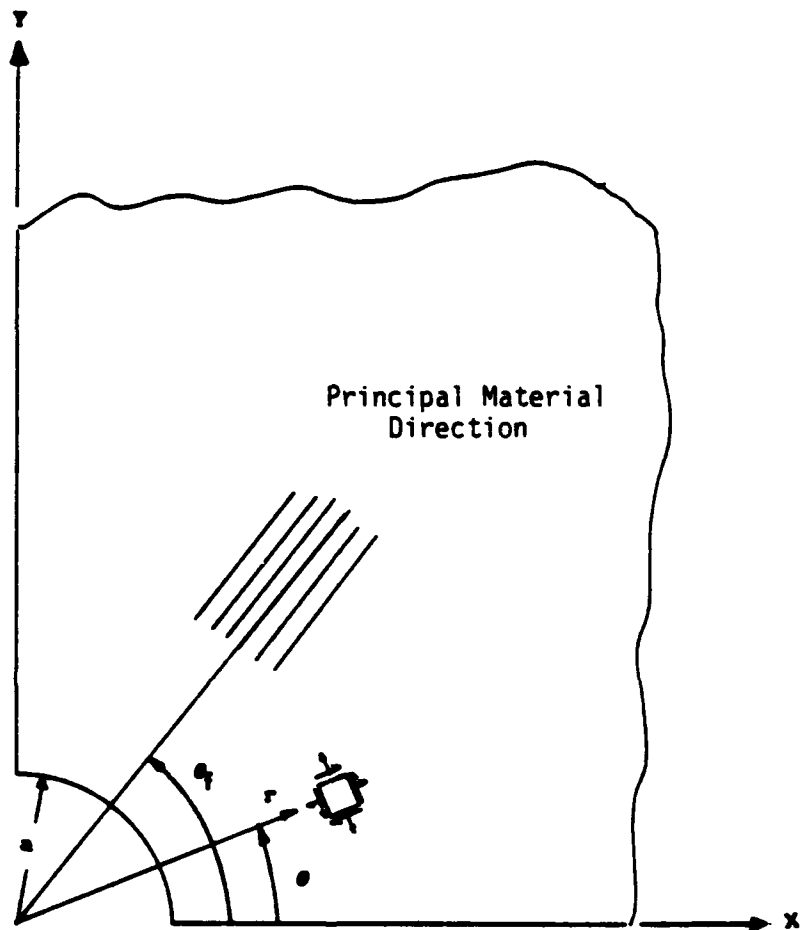
Figure 4.1 Finite element mesh of a sheet with a circular hole subjected to a uniaxial remote load with fixed grip end conditions.

properties to the top row of elements, and restraining rotation by applying two additional boundary restrains.

In the following discussions notational definitions are as shown in Fig. 4.2. A comparison of the nodal stresses and theoretical solution along a horizontal radial line ($\theta = 0^\circ$) is presented in Fig. 4.3. The theoretical solution obtained from the computer program ELLPLAS [12] was also used for the orthotropic analysis. It is clear that the numerical model agrees quite well with theory. The small discrepancies are attributed to the theoretical solution failing to account for the finite dimensions of the sheet.

Figure 4.4 illustrates the elastic effective stress ($\bar{\sigma}$) distribution along three radial lines ($\theta = 0^\circ, 45^\circ, 90^\circ$), and again is in close agreement with theory. The effective stress is of special interest since it indicates the onset of plasticity. Figure 4.4 clearly suggests a strong tendency of yielding to begin along the horizontal symmetry line ($\theta = 0^\circ$) at the edge of the hole. However, at about 1.5 radii from the hole, $\bar{\sigma}$ along the 45° orientation begins to dominate. This suggests that growth of any potential plasticity may begin horizontally, but will eventually produce a lobe in the 45° direction. Of course, the results presented are for a purely elastic analysis and do not account for redistribution of stresses during plastic flow.

An iso-stress contour of the effective stress is presented in Fig. 4.5. This unique contour pictorially represents the elastic prediction of the plastic zone shape at the onset of yielding. Since the contours are labeled with the appropriate values of $\bar{\sigma}$, this figure also provides the location of initial yield, and the direction of



θ_f = ll Material Direction

θ = Angular Orientation of Element

r = Radial Distance

Figure 4.2 Local and global coordinate systems for a sheet with a circular hole.

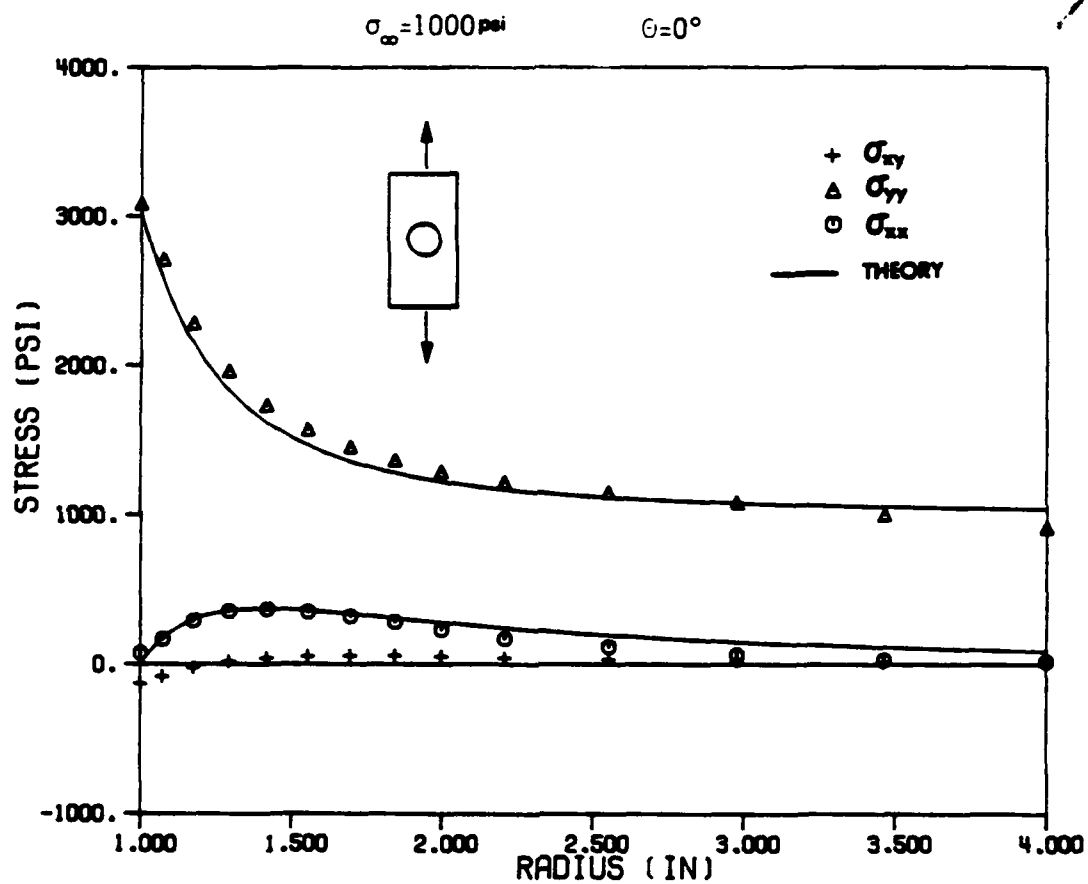


Figure 4.3 Comparison of ANPLAST nodal stresses with the ELLPLAS theoretical solution for a sheet with a circular hole and isotropic material properties.

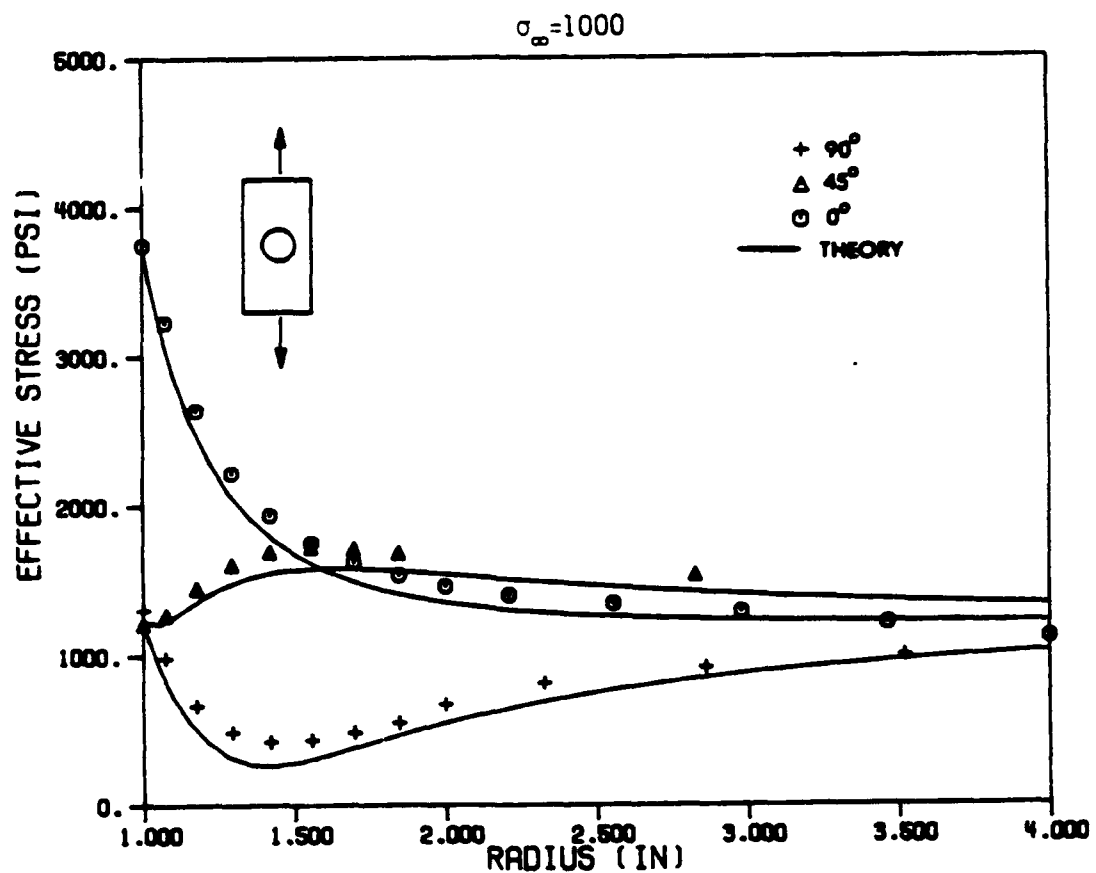


Figure 4.4 Comparison of ANPLAST effective stress distribution with the ELLPLAS theoretical solution for an isotropic sheet with a circular hole.

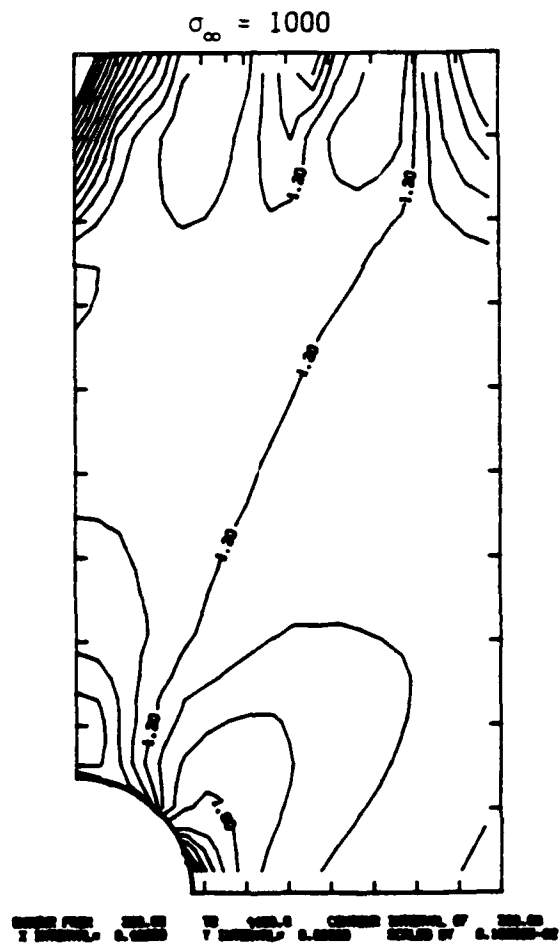


Figure 4.5 Effective stress contour for the sheet with isotropic material properties subjected to elastic loading.

subsequent plastic flow. The contour plot is consistent with the previous discussion involving the effective stress distribution.

ANPLAST Replication of Ramberg-Osgood Stress-Strain Behavior

The isotropic elastic-plastic constitutive model chosen was that of a Ramberg-Osgood work-hardening type material, whose uniaxial behavior is represented as [20]

$$e = \frac{\sigma}{E} \left[1 + \frac{3}{7} \left(\frac{\sigma}{\sigma_y} \right)^{n-1} \right] \quad (4.1)$$

where

- E = elastic modulus
- σ_y = uniaxial yield stress
- n = work-hardening power
- σ = uniaxial stress

The elastic and plastic strain components can be separated, and can be written.

$$\begin{aligned} e^e &= \frac{\sigma}{E} \\ e^p &= \frac{3}{7} \frac{\sigma}{E} \left(\frac{\sigma}{\sigma_y} \right)^{n-1} \end{aligned} \quad (4.2)$$

For a multiaxial stress state, the uniaxial stress quantities are replaced by the effective values, as defined in Section 2. The effective plastic strain can now be written as a function of the

effective stress

$$\bar{\epsilon}^p = \frac{3}{7} \frac{\bar{\sigma}}{E} \left(\frac{\bar{\sigma}}{\bar{\sigma}_y} \right)^{n-1} \quad (4.3)$$

The ANPLAST program is designed so that any general work-hardening law can be utilized. Therefore, according to Eq. 2.14, the slope of the work-hardening relationship must be explicitly defined. For the Ramberg-Osgood work-hardening formulation, this is easily accomplished by differentiating Eq. 4.3 and inverting, to give

$$\frac{d\bar{\sigma}}{d\bar{\epsilon}^p} = \frac{E}{Bn} \left(\frac{\bar{\sigma}}{\bar{\sigma}_y} \right)^{(1-n)} \quad (4.4)$$

where

B = curve fitting parameter

$\bar{\sigma}$ = effective stress

$\bar{\sigma}_y$ = effective yield stress

In addition, the plasticity coefficients are assumed to have the following values for an isotropic material

$$r_{11} = 1.0$$

$$r_{12} = -0.50$$

$$r_{66} = 1.50$$

ANPLAST results for a uniaxially loaded isotropic elastic-plastic specimen are plotted in Fig. 4.6 and compared to the ideal Ramberg-Osgood material response represented by Eq. 4.1. The small deviations in the comparison are due to the nature of the elastic-plastic finite element analysis. While Eq. 4.1 represents a smooth continuous behavior, ANPLAST assumes elastic, then elastic-plastic response characterized by a distinct yield point. These results show that the Ramberg-Osgood form of the stress-strain behavior is adequately replicated. This is important for the later comparisons.

Elastoplastic Response

Isotropic elastic-plastic response of the circular hole problem is of interest for two important reasons. First, it is one of the few non-trivial problems where adequate theoretical and experimental solutions exist. Second, it provides a benchmark from which orthotropic elastoplastic behavior can be gauged. The isotropic elastic-plastic constitutive model chosen is that of a Ramberg-Osgood work-hardening type material, as discussed in the previous section.

An incremental elastic-plastic finite element analysis of the circular hole was conducted. The analysis was conducted by first loading the model elastically until the first element yielded, then taking 10 equal remote load steps of 3000 psi. As predicted by the elastic analysis, yielding occurred at the hole along the horizontal symmetry line. Yield of the first few elements took place at a remote load of 17000 psi. This is reasonable since the elastic stress concentration factor is approximately 3 and the uniaxial yield stress is 50000 psi.

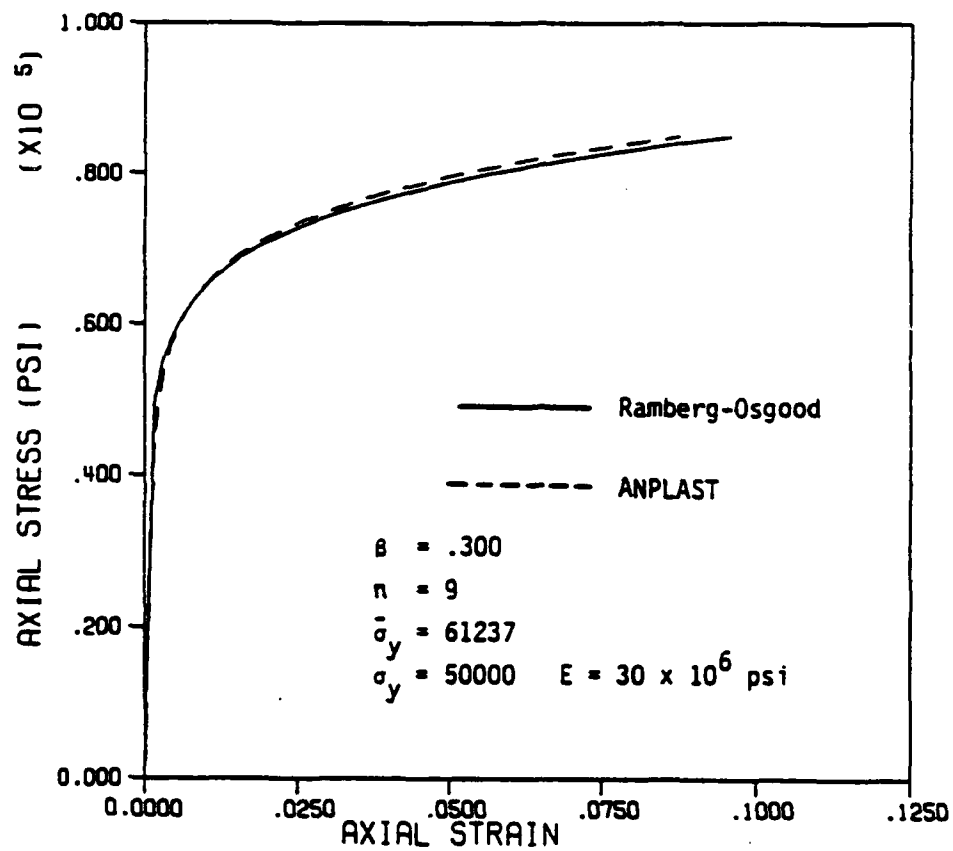


Figure 4.6 Comparison of uniaxial Ramberg-Osgood stress-strain response with the ANPLAST replication of this behavior.

A visualization of plastic zone growth is illustrated in Fig. 4.7. This depiction of plastic zone growth is accomplished by placing an asterisk (*) at the centroid of each element which is currently yielded. The plastic zone initially progresses horizontally then forms a lobe at around $\theta = 45^\circ$ at the higher loads. It is interesting to note that net section yielding does not occur at the horizontal symmetry line, but rather the lobe at $\theta = 45^\circ$ extends across the specimen.

An experimental analysis of the plastic zone growth in an isotropic elastic-plastic material was conducted by P.S. Theocaris and E. Marietos in 1964 [21]. Utilizing the methods of birefringent coatings and electrical analogy, they determined the elastoplastic response of an aluminum alloy (57S) under remote uniaxial loading. The plastic zone boundaries which they found during subsequent load increments (I-VIII), are shown in Fig. 4.8. The growth of these plastic zones progress in the same fashion as that calculated by ANPLAST in the preceding analysis. Though a direct quantitative comparison cannot be offered due to the different material properties, geometry, and loading, the character of the results are the same.

Budiansky and Vidensek [20] arrived at an approximate theoretical solution for the problem of a circular hole in an infinite plate for an isotropic elastoplastic material. They also assumed the elastic-plastic work-hardening was of the Ramberg-Osgood type. Using this solution, the stresses and strains can be calculated at any point in the body.

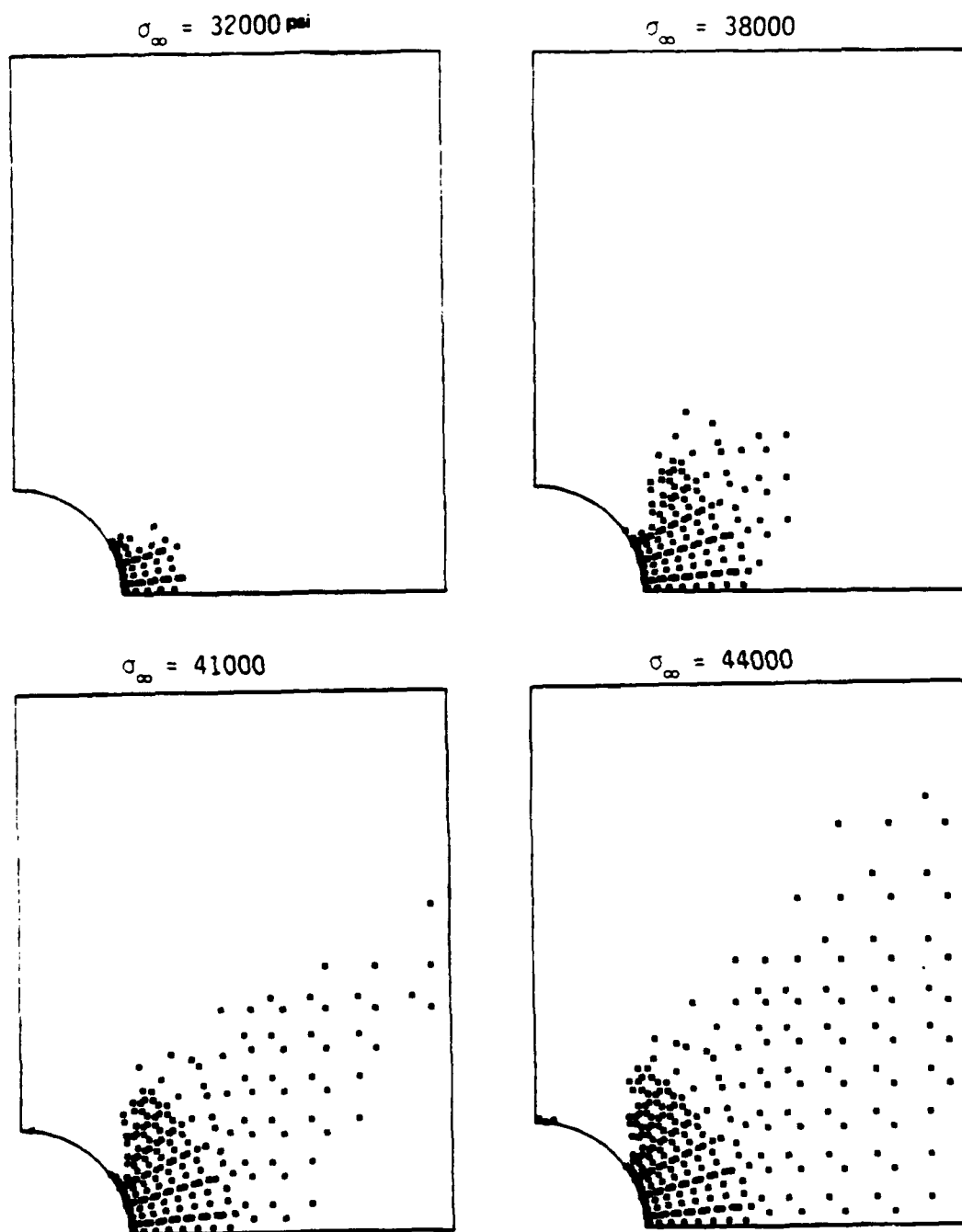


Figure 4.7 Plastic zone growth for an isotropic sheet subjected to elastic-plastic loading.

The ANPLAST nodal stresses were plotted along three radial lines ($\theta = 0^\circ, 45^\circ, 90^\circ$) and compared to the Budiansky-Vidensek solution in Fig. 4.9 for two different remote loads. The effective stress distribution for the same two load levels are shown in Fig. 4.10. The finite element results are in good agreement with the approximate theoretical solution, with the greatest deviation occurring at the higher remote load. Part of the discrepancy can be related to the theoretical solution failing to account for the finiteness of the specimen modeled by ANPLAST.

In 1958, Frocht and Thomson [22] studied the isotropic elastoplastic response of a sheet with a circular hole using the method of photoplasticity. The results for a Ramberg-Osgood type work-hardening material are presented in Fig. 4.11 alongside the ANPLAST and Budiansky-Vidensek solutions. In general, the photoplasticity results fall onto the same distribution as the other two solutions. They also fall above the Budiansky-Vidensek solution at a radius of about 1.5 - 2.0 inches, as did the finite element results. It should be noted that the actual dimensions of Thompson's test specimen were slightly different than that modeled by ANPLAST. The results consequently were normalized with respect to the hole radius and remote load.

The isotropic elastoplastic analysis capability of the ANPLAST program has been verified.

Comparison of the Isoparametric Quadrilateral and Constant Strain Triangle Elements

It has been suggested by a number of authors [19,23] that the higher order isoparametric elements may provide superior performance

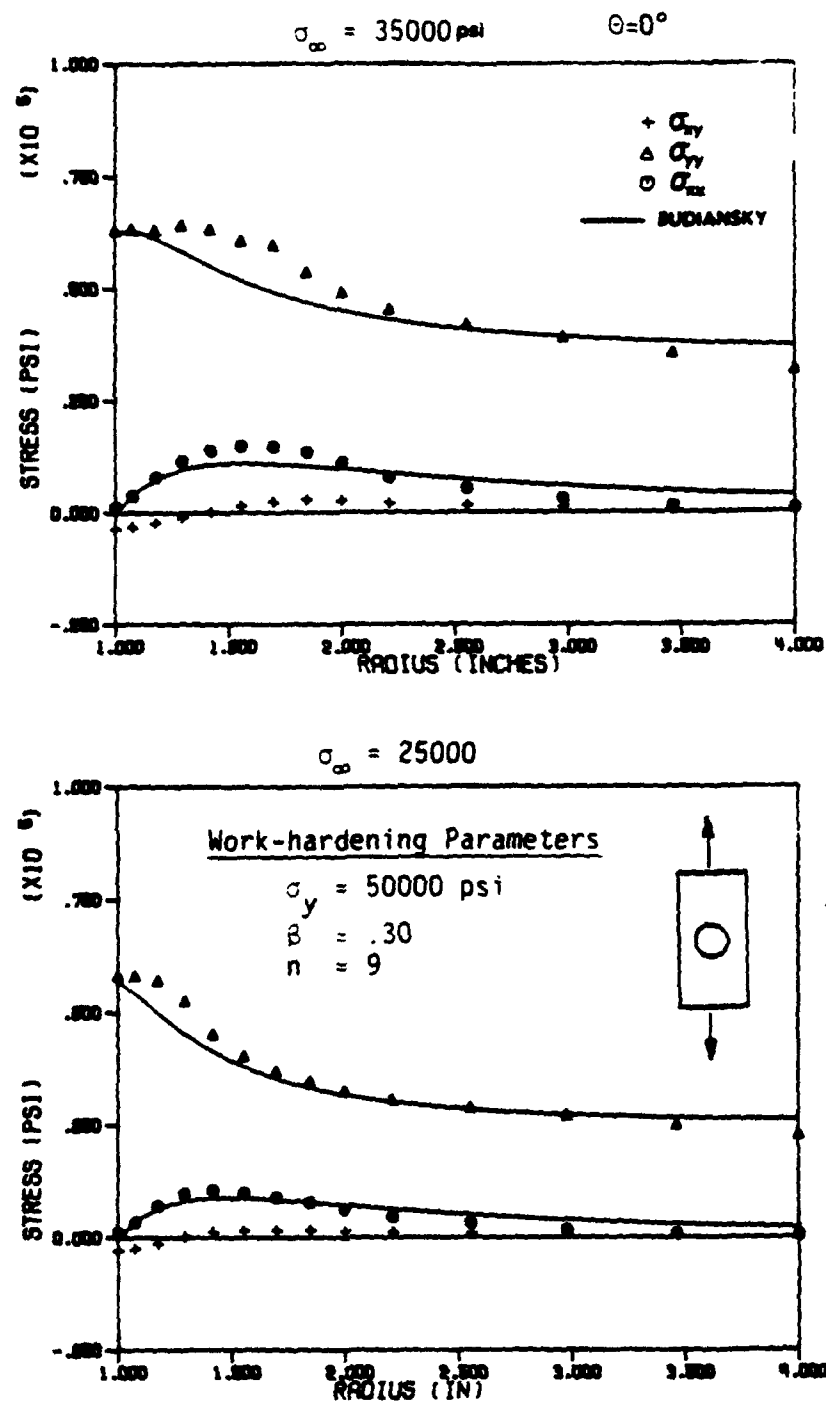


Figure 4.9 Comparison of ANPLAST nodal stresses with the Budiansky-Vidensek [20] theoretical solution for an isotropic sheet with a circular hole subjected to elastic-plastic loading.

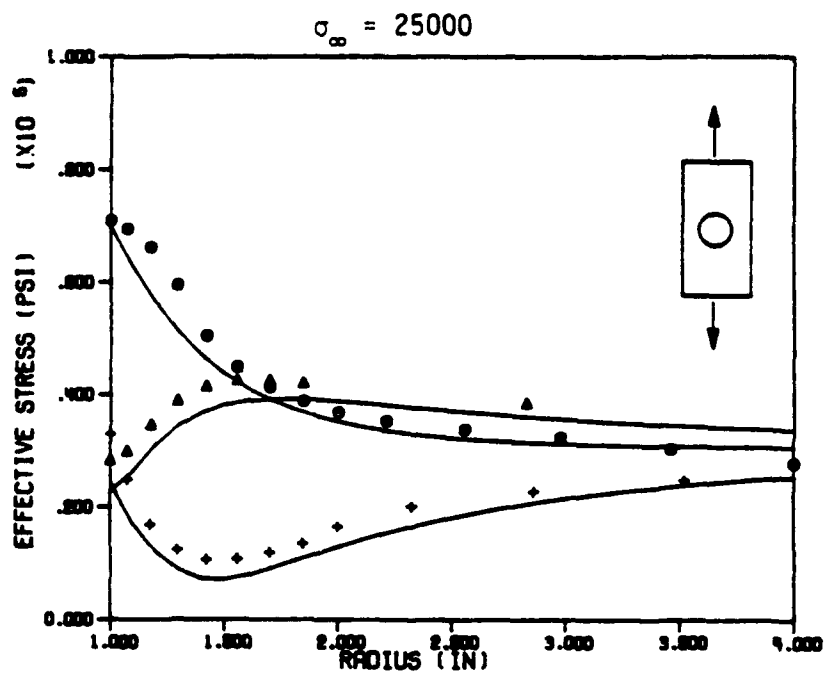
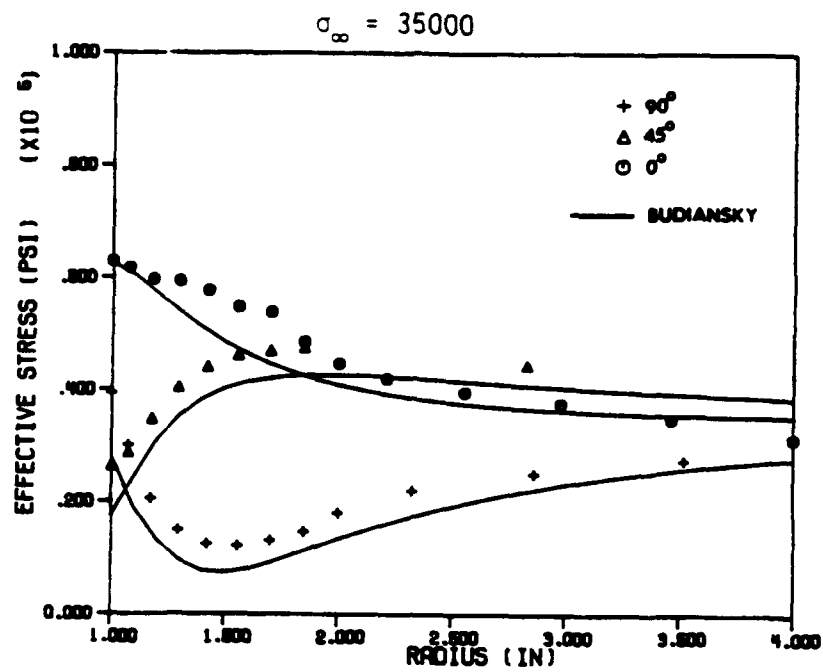


Figure 4.10 Comparison of ANPLAST effective stresses with the Budiansky-Vidensek [20] solution for an isotropic sheet with a circular hole subjected to elastic-plastic loading.

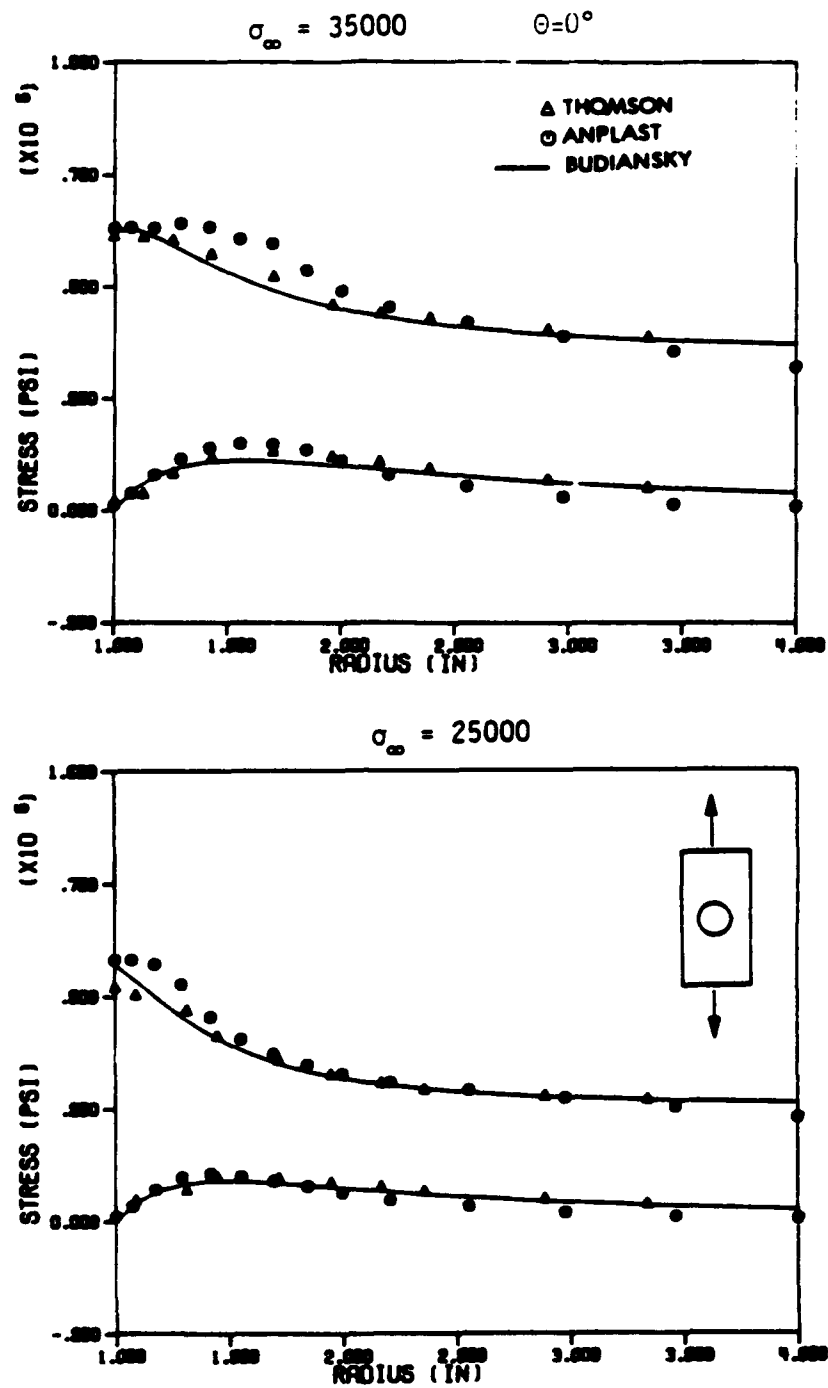


Figure 4.11 Comparison of ANPLAST stresses with an experimental photoplasticity solution by Frocht and Thomson [22] for the isotropic sheet with a circular hole subjected to elastic-plastic loading.

for certain plasticity analyses. The 8-noded quadrilateral with a 4-point Gaussian integration scheme developed in Section 3 was used to analyze the elastoplastic response of the isotropic sheet with a circular hole. The plastic zone visualization for this particular element is handled by placing an asterisk (*) at any Gauss point which has exceeded the yield stress.

The mesh used in this analysis, shown in Fig. 4.12, is of the same geometry as in the previous analysis conducted with the CST. In addition, the material properties are also identical. The elastic stresses are plotted in Fig. 4.13 along the horizontal symmetry line ($\theta = 0^\circ$). Though there are more degrees of freedom for this mesh than the corresponding CST mesh, the results are no better. In fact, the nodal stress (σ_{yy}) on the hole boundary displays considerably more deviation. This is probably due to the particular extrapolation technique [19] used to derive nodal stresses from the Gauss points.

The plastic zone progression is illustrated in Fig. 4.14 for the same remote stress levels as was presented for the CST. The results for the quadrilateral element demonstrate excellent correlation with the CST to the point where any discrepancies are almost indistinguishable. These findings suggest that there is no practical advantage for selecting the isoparametric element over the CST, at least as far as isotropic elastoplastic analyses are concerned. Therefore, due to the simplicity and efficiency of the CST, this element will be the primary analysis tool for this research.

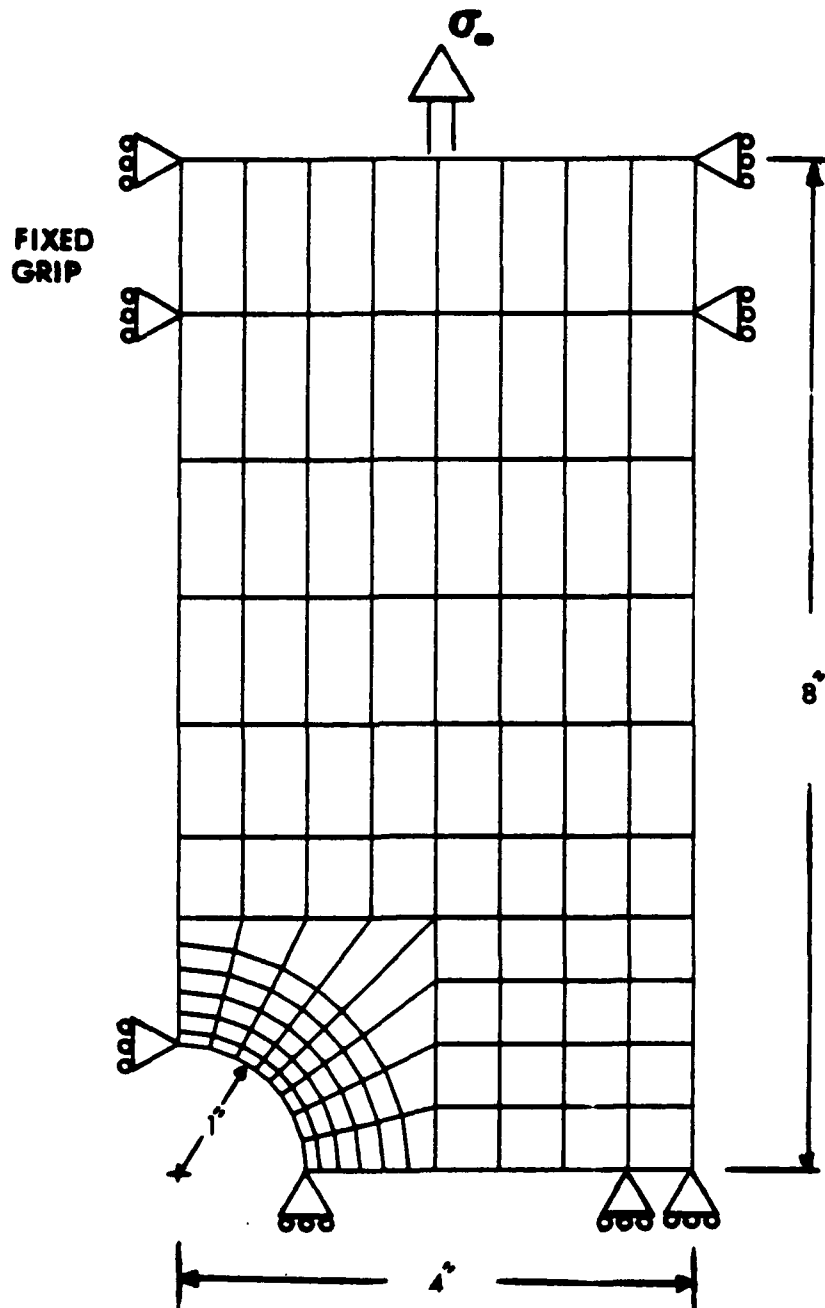


Figure 4.12 Finite element mesh of the sheet with a circular hole utilizing the 8-noded isoparametric quadrilateral element.

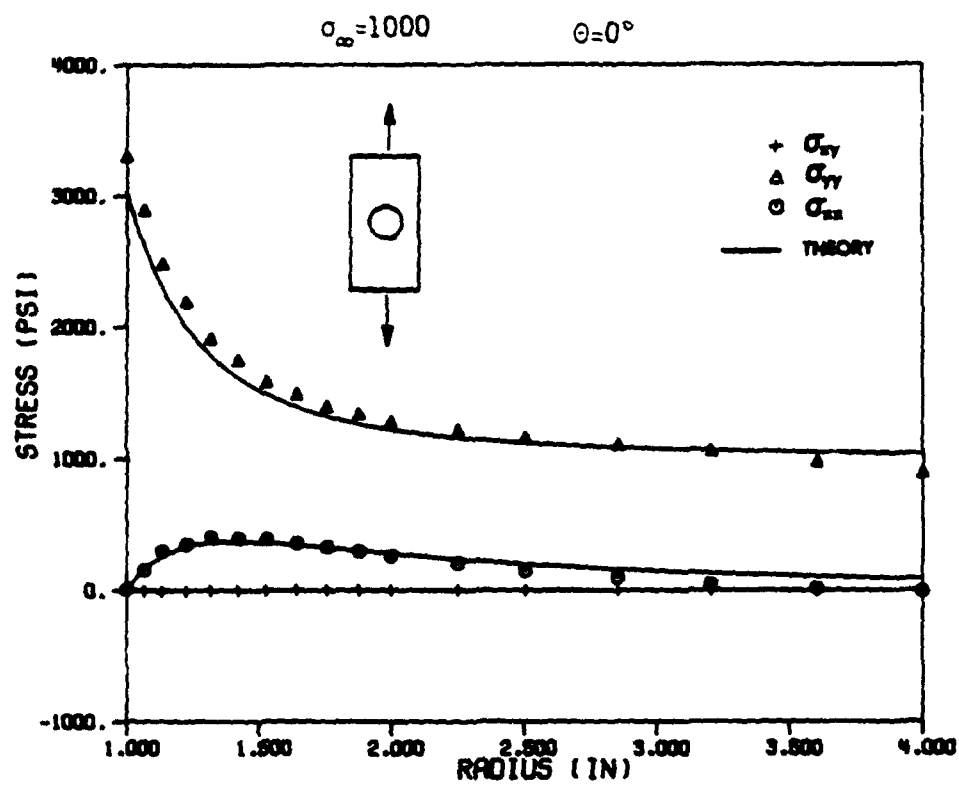


Figure 4.13 Isoparametric quadrilateral stress distribution for an isotropic sheet with a circular hole subjected to elastic loading.

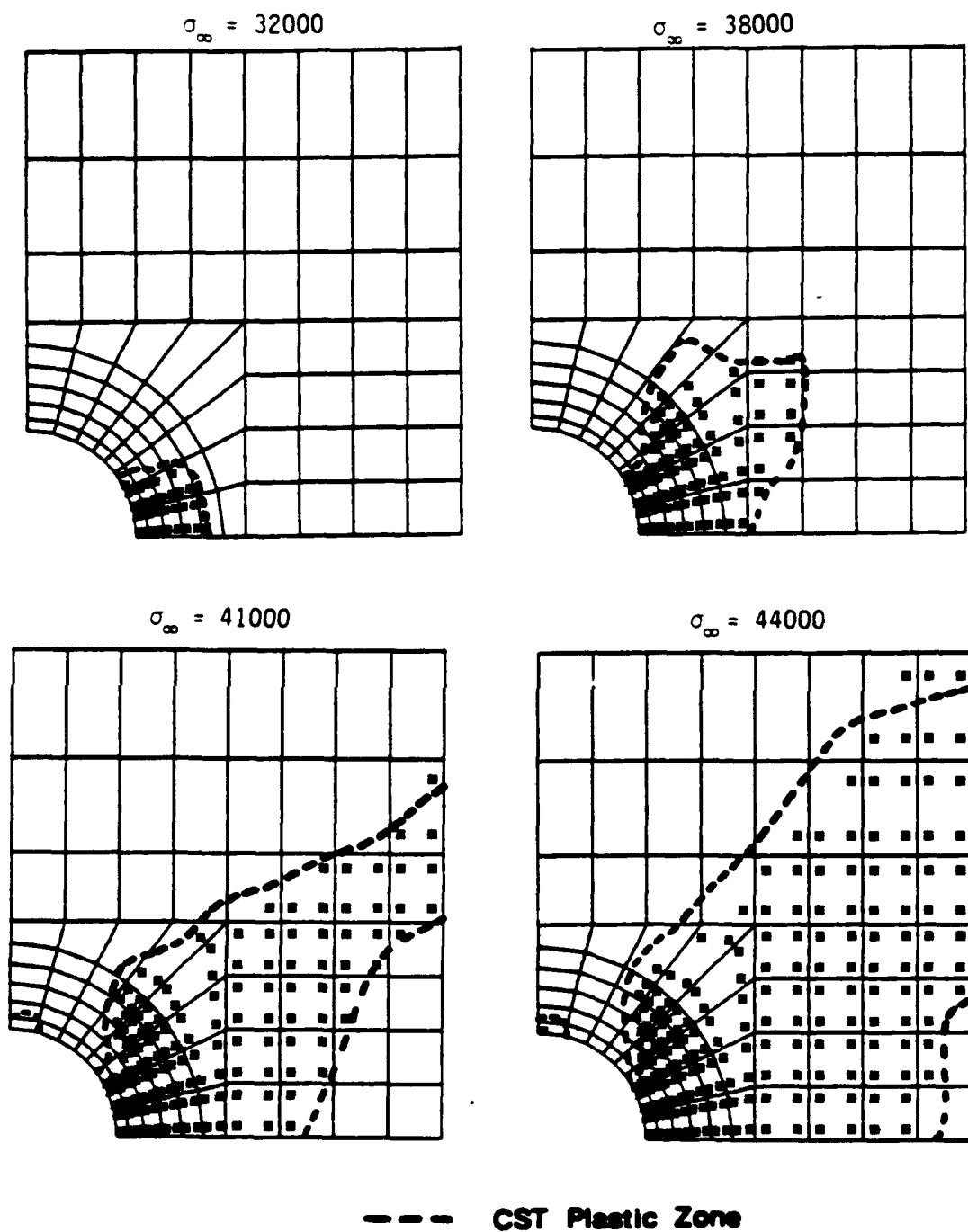


Figure 4.14 Comparison of plastic zone growth for the isoparametric quadrilateral and CST elements for an isotropic sheet subjected to elastic-plastic loading.

SHEET WITH ORTHOTROPIC MATERIAL PROPERTIES

Elastic Loading: Comparison with Theoretical Solution

An elastic analysis of the sheet with a circular hole was conducted for two orthotropic materials. The first, Boron-Aluminum, demonstrates mild orthotropy, while the latter, Graphite-Epoxy, exhibits rather strong anisotropy. Two analyses were conducted for each material, one with the stiff material direction being oriented horizontally ($\theta_f = 0^\circ$), the other with it rotated 90° ($\theta_f = 90^\circ$).

The nodal stresses along the horizontal symmetry line are plotted against the infinite sheet theoretical solution generated by the program ELLPLAS in Figs. 4.15-4.16. The B-Al results are similar to the isotropic material which is what one would expect since this material is only weakly orthotropic. The G-Ep findings highlight the effect of strong anisotropy on the stress distributions. When the anisotropy is strong and the stiff material direction is vertical, the gradient of σ_{yy} in the vicinity of the hole becomes quite steep. Also, this orientation appears to significantly increase the elastic stress concentration factor, while the opposite trend is true for $\theta_f = 0^\circ$.

The finite element results are in good agreement with the theoretical solution in most locations. For the G-Ep($\theta_f = 0^\circ$) specimen, a considerable deviation is apparent for σ_{xx} away from the vicinity of the hole. This can be accounted for by recalling that the theoretical solution is for the infinite sheet. While the finite size effect did not manifest itself noticeably for the isotropic material, it appears that strong anisotropy can increase the finiteness of a particular specimen. It is clear from these results that the

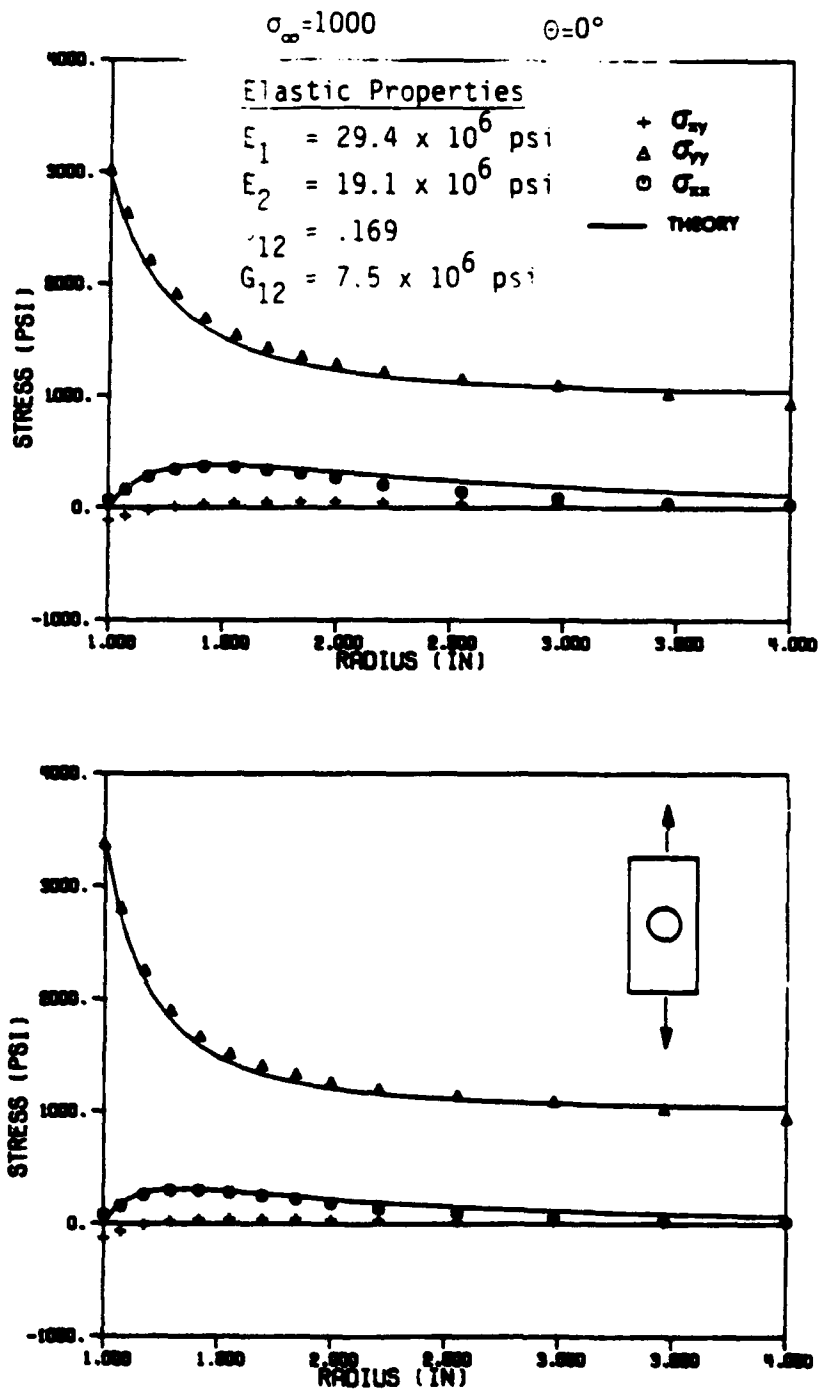


Figure 4.15 Comparison of the ANPLAST stress distribution with the ELLPLAS theoretical solution for a mildly orthotropic (B-A1) sheet with a circular hole subjected to elastic loading.

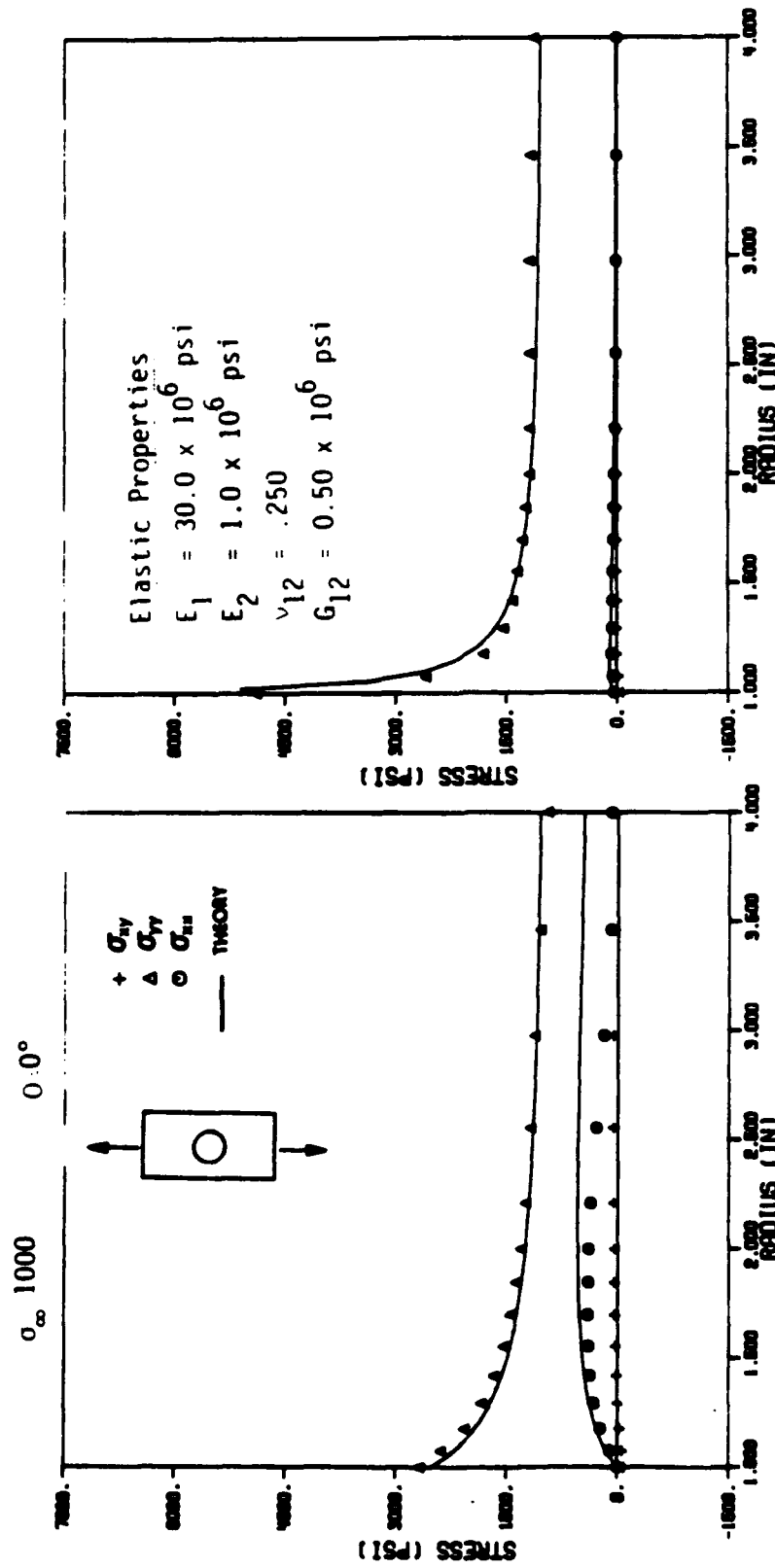


Figure 4.16 Comparison of the ANPLAST stress distribution with the ELLPLAS theoretical solution for a strongly orthotropic (G-Ep) sheet with a circular hole subjected to elastic loading.

orthotropic elastic capabilities of ANPLAST have been verified.

A Study of the Plasticity Coefficients Effect on Plastic Zone Growth

It is the intention of this study to investigate the effect of introducing anisotropy into the plastic flow relations for the sheet with a circular hole. Anisotropy is brought into the problem through the plasticity coefficients, r_{11} , r_{12} , r_{66} . The previous elastoplastic analysis assumed isotropic values of the plasticity coefficients. In this investigation, the plasticity coefficients r_{11} , and r_{66} are varied to determine how they affect yielding and subsequent plastic zone progression. Since the anisotropy of the plasticity is of primary interest, the examples in this section assume elastic isotropy.

The first analysis involves the variation of the plasticity coefficient r_{11} from its isotropic value of unity. The assumed value of r_{11} is chosen to be 0.20. The uniaxial yield stress in the strong direction for this material is 2.23 times greater than in the weak direction. At the same time, it is necessary to reduce the magnitude of r_{12} from -0.50 (isotropic) to -0.20, to prevent the anisotropic effective stress from becoming negative. This finding suggests that there are additional restrictions on the plasticity coefficients than were mentioned in Reference [12], since a negative $\bar{\sigma}$ would indicate negative incremental work, which is physically unreasonable.

When r_{11} is not unity, planar anisotropy is introduced in the sheet, resulting in directional sensitivity of the plastic flow. Two analyses were conducted, one with the strong direction oriented horizontally ($\theta_f = 0^\circ$) and the other with the weak direction horizontally ($\theta_f = 90^\circ$). The Ramberg-Osgood work-hardening law and all the

associated coefficients are as for the isotropic elastoplastic analysis.

The plastic zone visualization for both analyses is pictured in Figs. 4.17-4.18. In comparison to the isotropic case, it is clear that the coefficient r_{11} plays a dominant role in plastic zone progression. While the plots for $\theta_f = 0^\circ$ are somewhat similar to those for the isotropic material, this is clearly not the case for $\theta_f = 90^\circ$. When the strong direction is oriented parallel to the load, it is evident that the plastic zone progresses in the vertical direction, and does not demonstrate the tendency to produce net section yielding. This behavior is understandable, since the major stress component (σ_{yy}) is parallel to the strong principal material direction, and is not as likely to cause yielding.

Yielding at $\theta = 90^\circ$ is apparent for $\theta_f = 90^\circ$, yet is absent for $\theta_f = 0^\circ$. Even the isotropic example eventually exhibited yielding at this location. The explanation for this behavior is directly related to the plastic anisotropy.

An iso-stress contour of effective stress at the onset of yield is presented for both analyses in Fig. 4.19. These plots show that the initial progression of the plastic zone in the vicinity of the hole is strongly correlated with the stress distribution for the elastic solution. These contours also highlight the strong gradient of $\bar{\sigma}$ at the horizontal hole perimeter ($\theta = 0^\circ$).

Effective stress contours for $\theta_f = 0^\circ$, and $\theta_f = 90^\circ$ at remote loads of 34000 psi and 76000 psi, respectively are shown in Fig. 4.20. Both of these load levels represent a state where considerable

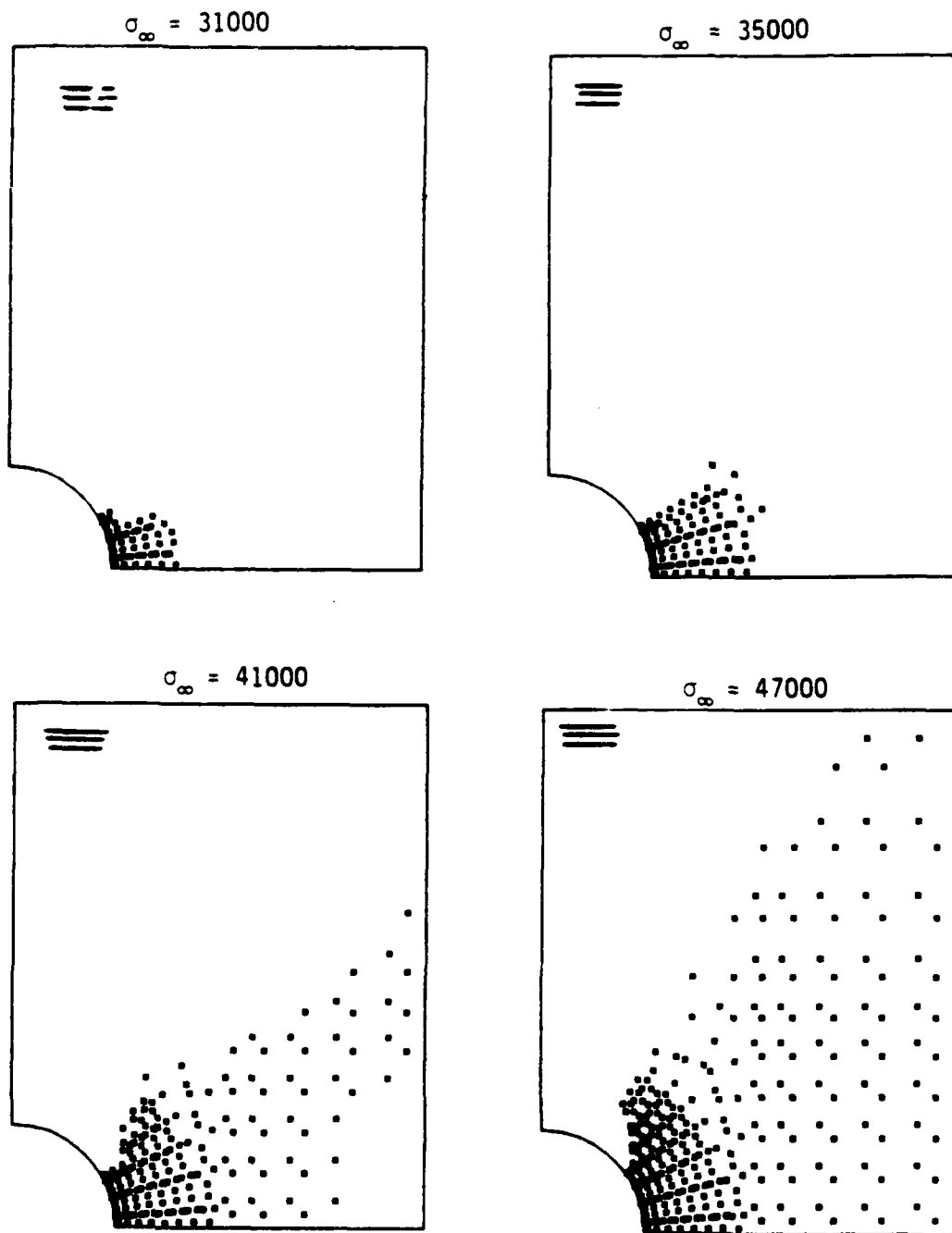


Figure 4.17 Plastic zone growth for an orthotropic sheet subjected to elastic-plastic loading. The strong material direction is oriented perpendicular to the remote load.

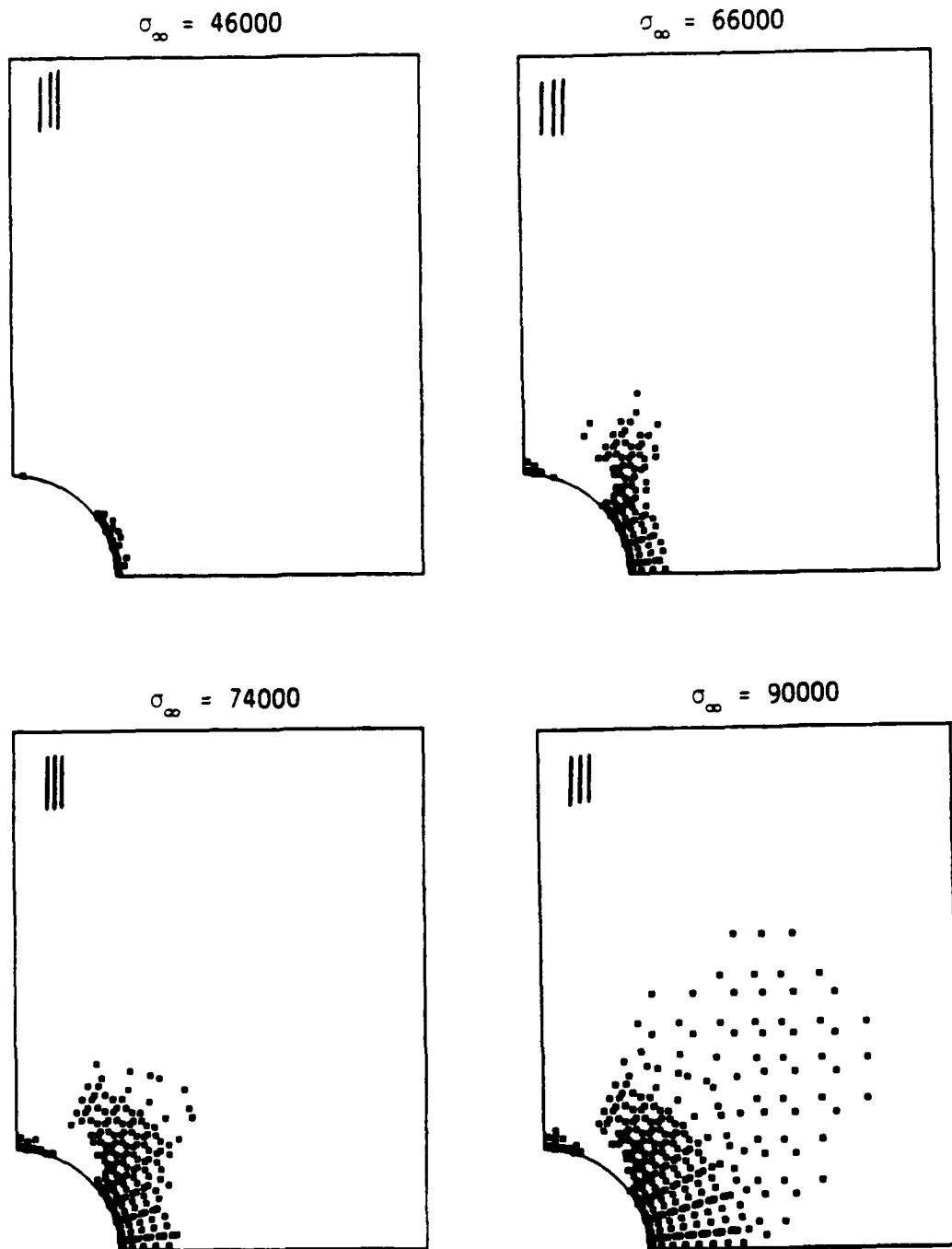


Figure 4.18 Plastic zone growth for an orthotropic sheet subjected to elastic-plastic loading. The strong material direction is oriented parallel to the remote load.

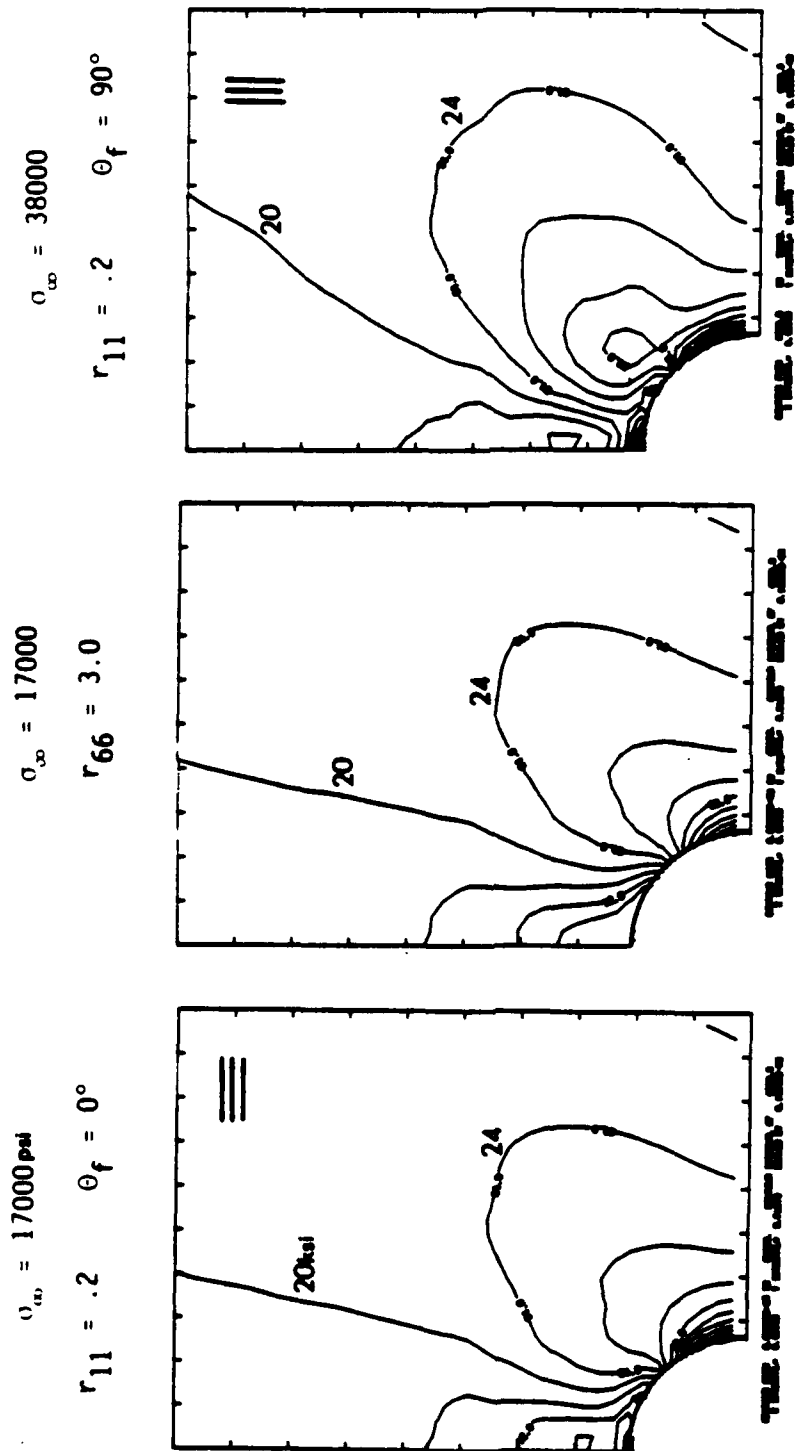


Figure 4.19 Effective stress contours for three orthotropic sheets at the onset of yielding.

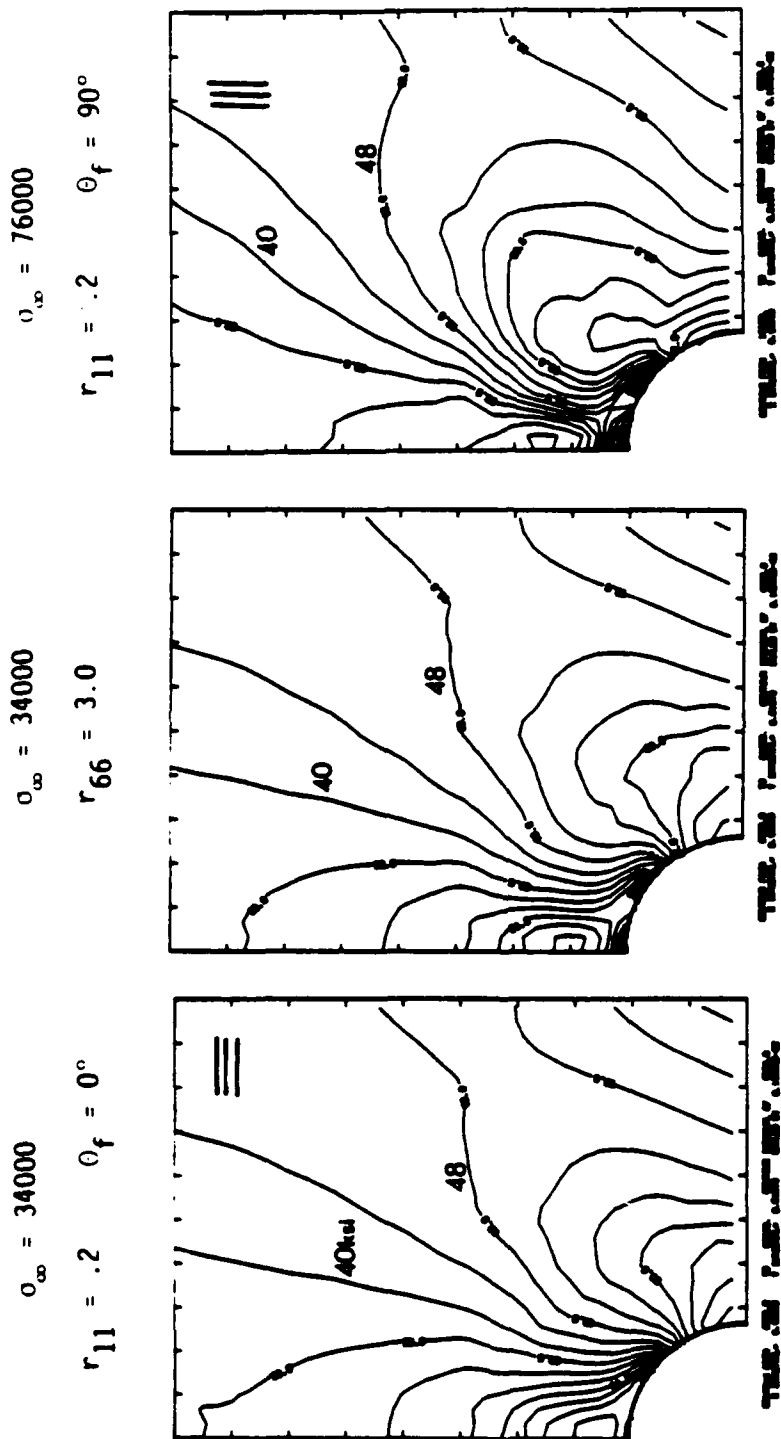


Figure 4.20 Effective stress contours for three orthotropic sheets after considerable plastic flow has occurred.

plasticity has occurred. These contours again accurately portray the outline of the elastic elastic-plastic boundary, and are strikingly similar to the elastic contours. One could hypothesize that the shape of these contours will not deviate to any great extent, until the plasticity has grown to such a scale that it interacts with the finite boundaries.

That plastic work-hardening has occurred behind the initial yield boundary can be detected by noticing an increase of some contours above the initial yield ($\bar{\sigma}_y$). Although this study has not approached the subject of work-hardening and its effect on plastic zone growth, it can be assumed that this parameter will control the rate at which the growth occurs. It is likely that the degree of work-hardening will not affect the shape of the plastic zone, rather that role is reserved for the plasticity coefficients.

A similar investigation of the plasticity shear coefficient r_{66} was conducted by setting r_{11} back to its isotropic value (1.0) and letting r_{12} stay at -.20. The coefficient r_{66} was doubled from its previous value and assumed to be 3.0. Both $\theta_f = 0^\circ$ and $\theta_f = 90^\circ$ were studied, but the analyses indicated that these two cases produce nearly identical results. This finding makes sense if one considers that r_{66} multiplies only the shear term, and the transformation of the stresses to either material coordinate system orientation will produce a shear of the same absolute magnitude. Therefore, only one analysis will be discussed.

The plastic zone visualization for this analysis is presented in Fig. 4.21 and the results are almost identical to those of Fig. 4.17.

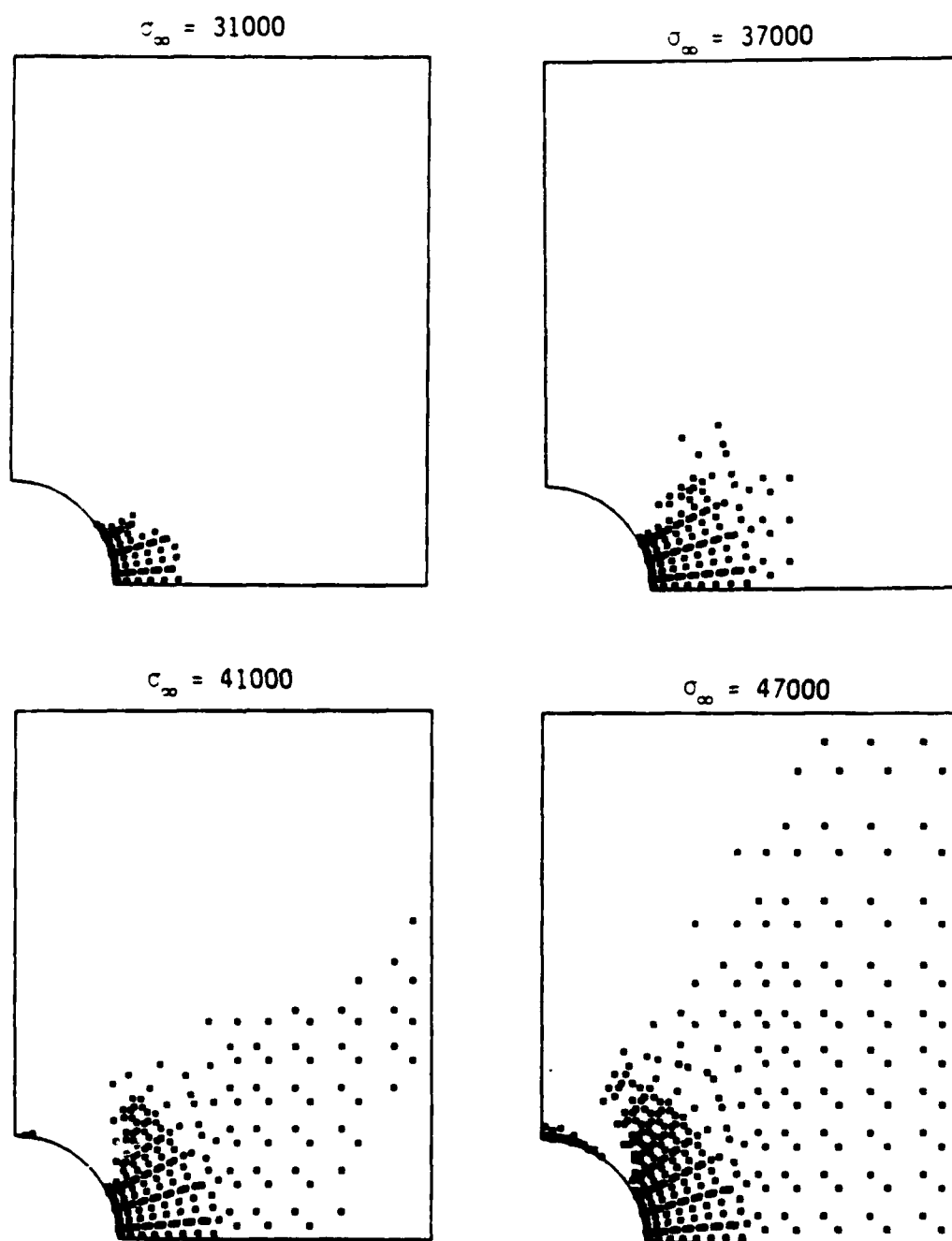


Figure 4.21 Plastic zone growth for an orthotropic sheet ($r_{66} = 3.0$) under elastic-plastic loading. The orientation of the principal material directions does not affect this illustration.

One of the subtle differences is a slight tendency for the plastic zone to drift a bit more in the $+\theta$ direction at the lower remote loads. This can be associated with the accentuation of the shear stress which is a maximum at approximately $\theta = 45^\circ$.

The effective stress contour at the inception of yield is presented in Fig. 4.19. This contour is nearly identical to the previous study of r_{11} for $\theta_f = 0^\circ$. In summary, it appears that the effect of r_{66} on plastic zone growth for this particular geometry, loading, and principal material orientation is negligible.

A Study of Unloading and the Resulting Residual Stresses

A most interesting aspect of studying plasticity problems is the effect of load reversal or unloading and the resulting residual stresses which are created. When a sheet with a circular hole is loaded beyond its elastic limit a plastic zone results. The material inside this zone is permanently deformed, and upon load reversal the elastic material surrounding it tends to clamp down and produce significant compressive stresses. It is the purpose of this section to determine if the presence of plastic anisotropy will have a prominent effect on the residual stress distributions.

The first unloading case involves the isotropic elastoplastic material analyzed earlier in this section, and will serve as the basis for comparison. In all cases, the maximum remote load was chosen to be two times the load required to initiate yielding. The result of this was a maximum remote load of 34000 psi for all examples except for the anisotropic material where $r_{11} = 0.20$ and $\theta_f = 90^\circ$.

The unloading was carried out by first taking a small unloading step which resulted in all elements becoming elastic (falling inside their yield surfaces). With this accomplished, and the global stiffness matrix reassembled, one large unloading step to zero was taken. In no case did any elements yield again. If yielding had occurred, incremental unloading would have been required.

The residual stress distribution for each analysis is presented in Figs. 4.22. Since the maximum load and plastic zone size are not the same for each case, a direct comparison of the stress levels is not appropriate. But it is clear that the character of the results are the same. The vertical stress component, σ_{yy} , demonstrates a significant negative residual stress component in the vicinity of the hole perimeter while the other stresses are negligible. In each case a compressive residual stress (σ_{yy}) is present out to approximately $\frac{1}{2}$ " to 1" away from the hole. In general, this brief study suggests that planar anisotropy does not have a significant effect on the residual stresses due to unloading.

A COMPLEX LOADING PATH

All of the previous analyses of the circular hole have involved monotonic uniaxial remote loading. The purpose of this section is to study the effect of non-proportional remote loading on plastic zone growth and compare the final state of elastoplastic deformation for each loading path.

The finite element mesh for this analysis is shown in Fig. 4.23. The mesh used in the previous analyses was modified so that the external dimensions are equal, and the fixed grip end condition

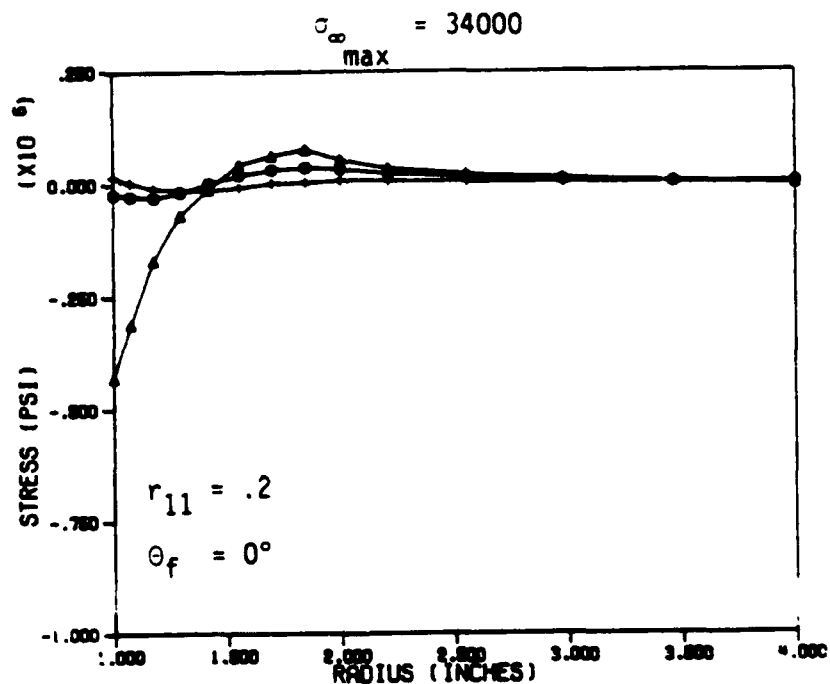
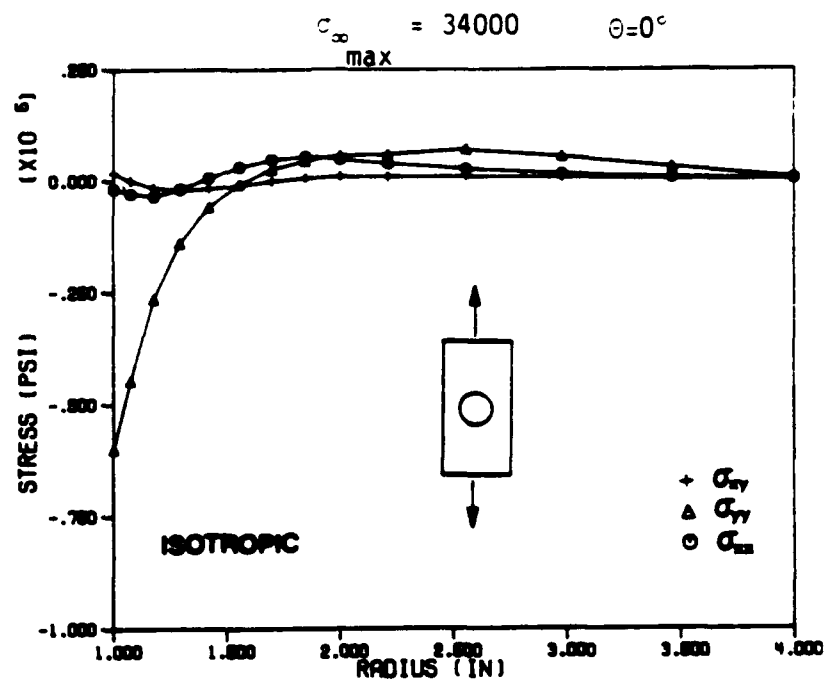


Figure 4.22 ANPLAST residual stress distribution after unloading from a remote stress which was twice that necessary to initiate yielding.

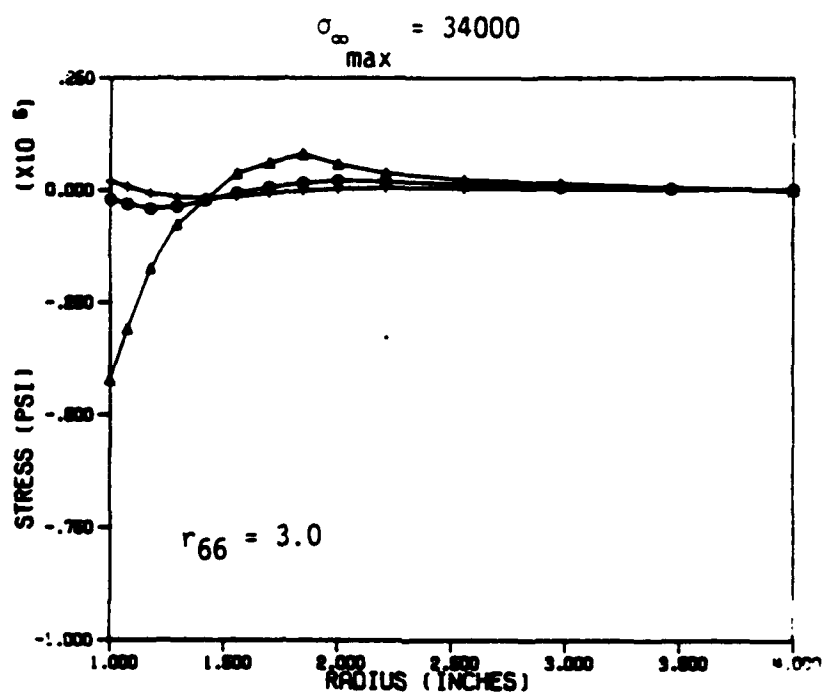
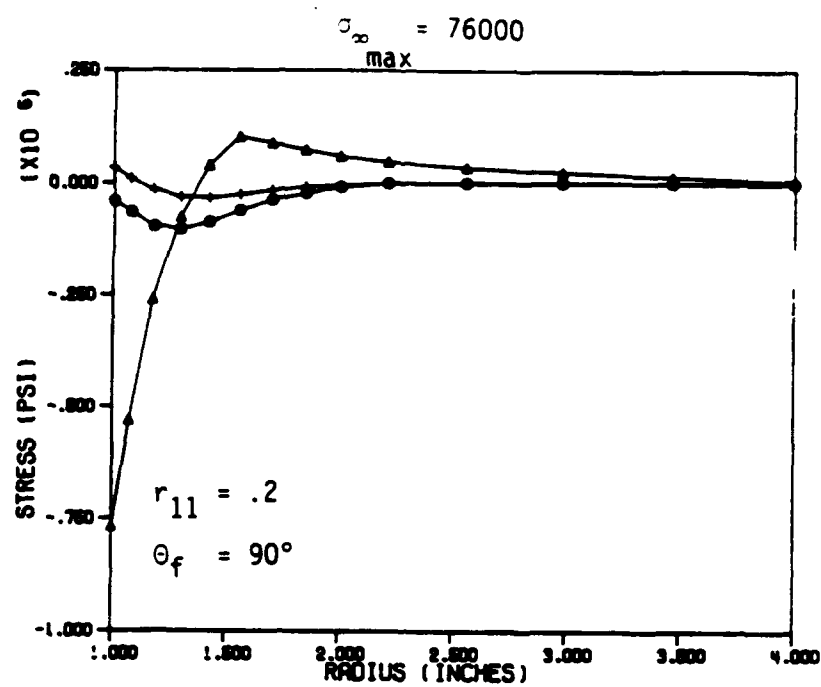


Figure 4.22 continued

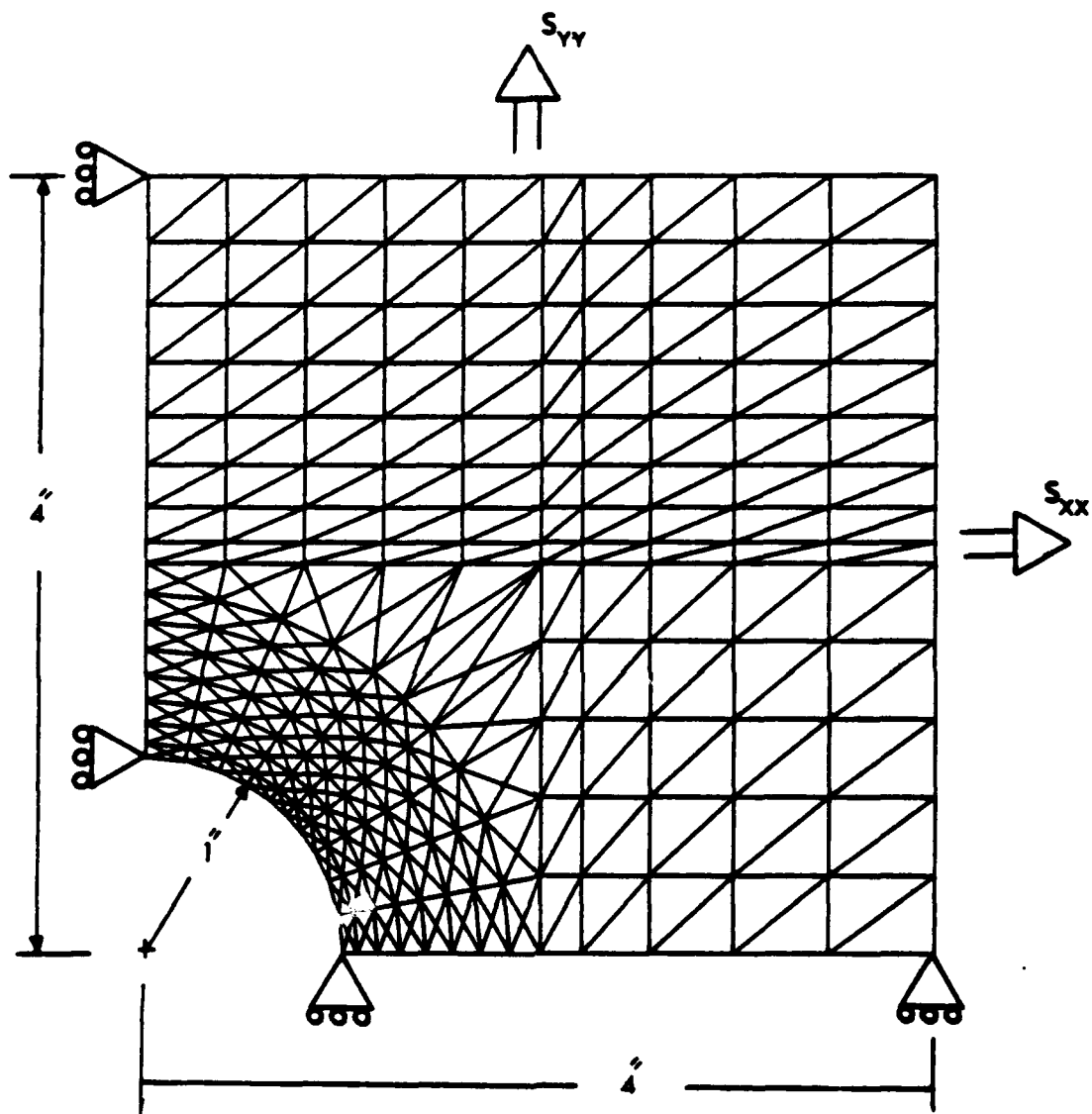


Figure 4.23 Finite element mesh of a sheet with a circular hole for analysis of complex loading paths.

removed. Three separate loading cases analyzed are as follows

- I) Vertical Remote Stress (s_{yy}) to 41000 psi followed by a Horizontal Remote Stress (s_{xx}) to 41000 psi
- II) Horizontal Remote Stress (s_{xx}) to 41000 psi followed by a Vertical Remote Stress (s_{yy}) to 41000 psi
- III) A simultaneous application of both remote stresses s_{xx} and s_{yy} to 41000 psi.

The isotropic elastoplastic material properties from the earlier analyses are used in all three cases.

Discussion of Plastic Zone Growth

The plastic zone growth for Cases I and II illustrated in Figs. 4.24-4.25 are identical except that they are oriented oppositely about the respective symmetry axes. In both of these cases, the plastic zone progression during the uniaxial portion of the loading is of the same character that was observed in Fig. 4.7 for the fixed grip analyses. After achieving a uniaxial remote load of 41000 psi, the opposing transverse remote load is applied incrementally with interesting results. All but six elements unload into the elastic regime, until the transverse load reaches 33000 psi at which time additional yielding occurs at the hole perimeter and remote locations.

The resulting re-yielding of material near the hole does not take on the shape one would expect for a monotonically increasing uniaxial load. The stress state is more complex due to the biaxial nature of the remote loads, and the previous work-hardening has altered the respective effective yield stress for all of the previously yielded material. Further complications result from the assumed non-linear

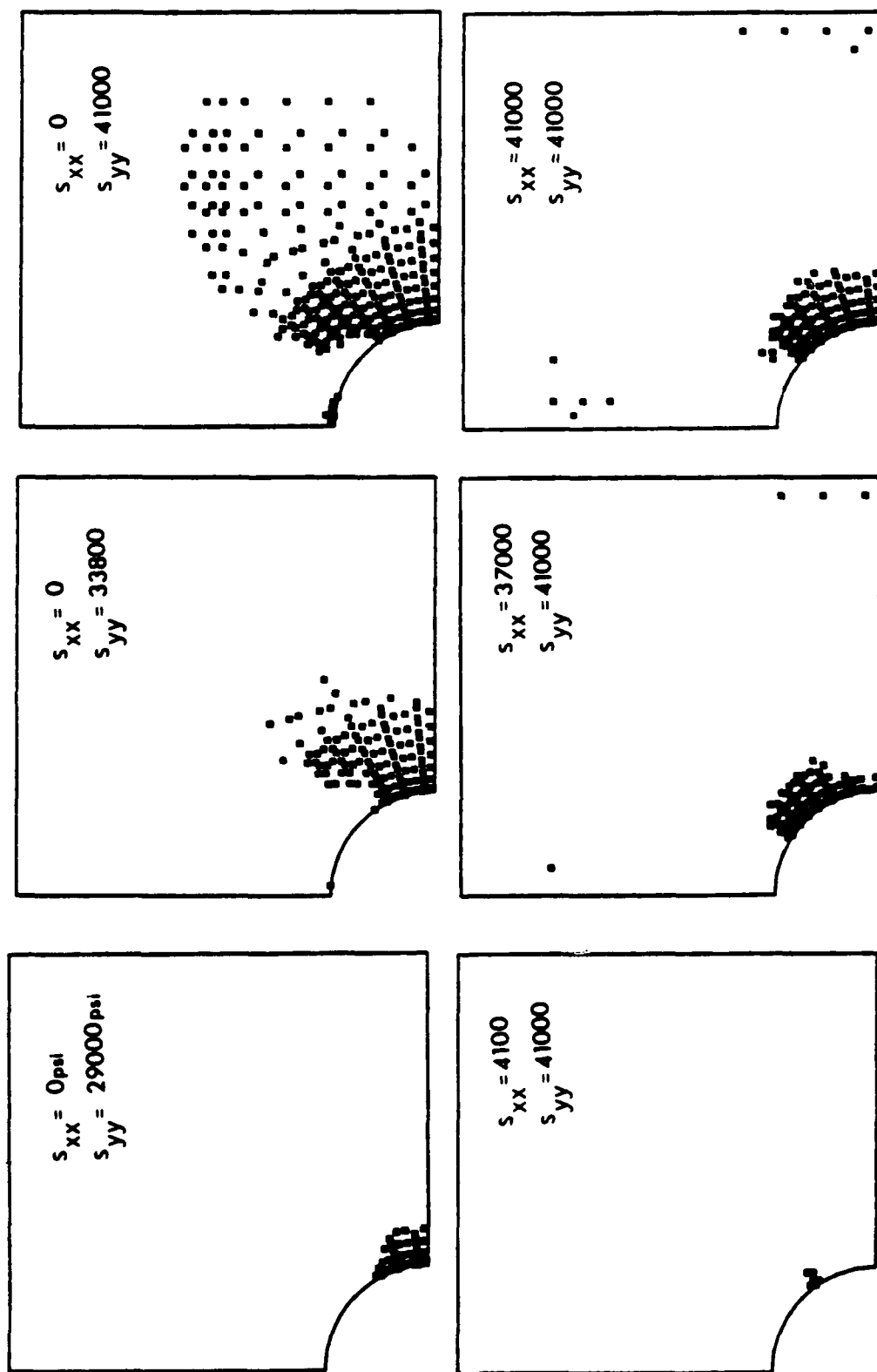


Figure 4.24 Plastic zone growth for an isotropic sheet subjected to non-proportional remote loading (Case I).

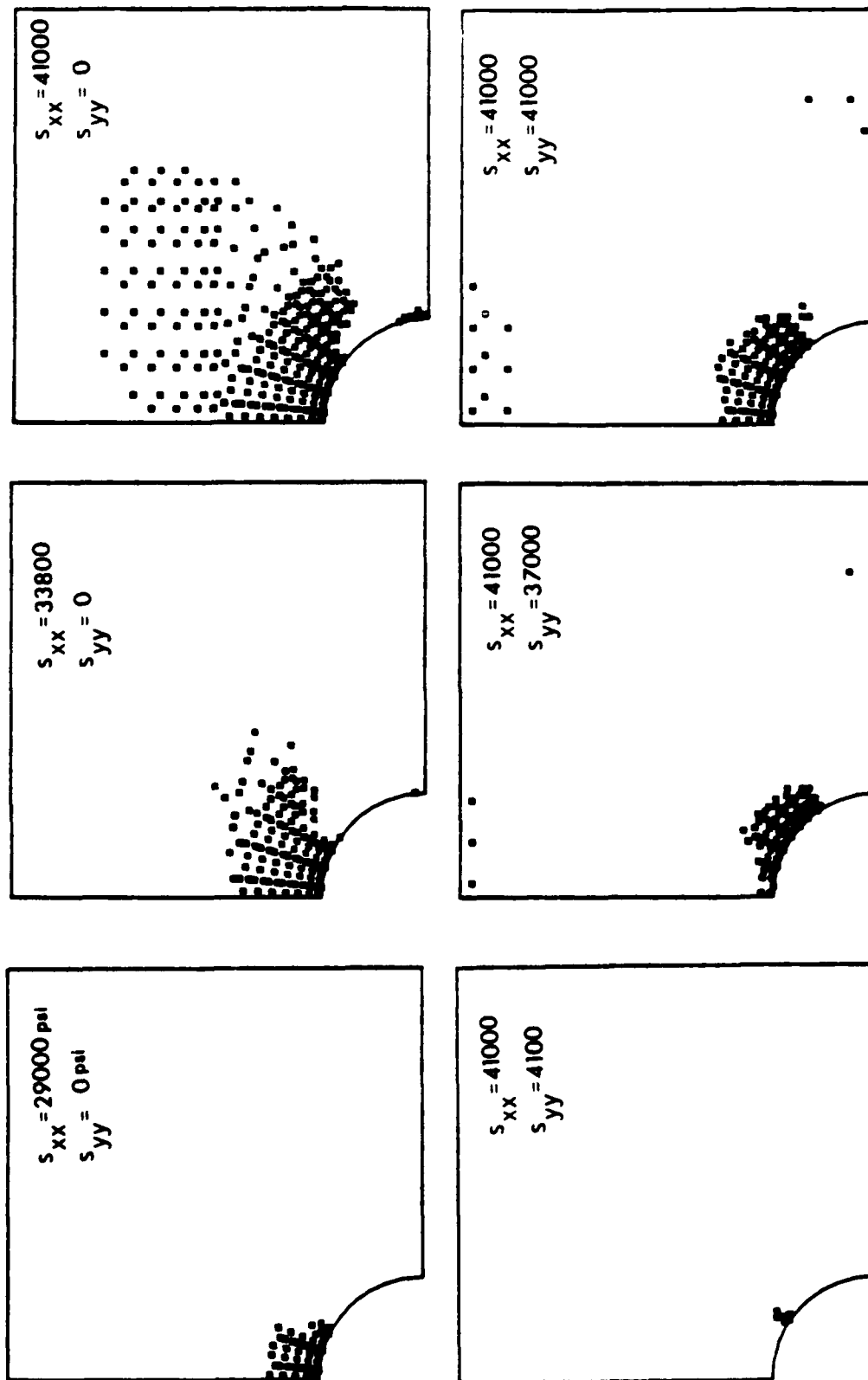


Figure .25 Plastic zone growth for an isotropic sheet subjected to non-proportional remote loading (Case II).

work-hardening law. Each element which has been plastically deformed can be at a different location on the effective stress-effective plastic strain relation.

The plastic zone visualization for Case III shown in Fig.4.26 represents a simultaneous application of the remote loads. Although the loading is biaxial, the remote components are stressed at identical rates which results in proportional loading. Both the geometry and loading are symmetric at all times as is the plastic zone progression. With most of the shear stresses removed due to the equibiaxial loading, the plastic zone progresses in rings. It is interesting to note that unlike the previous two cases, plastic deformation never reaches any of the remote loading boundaries.

Comparison of Permanent Deformation at the Final Loading Level

The previous study of plastic zone progression clearly demonstrates that the distribution of currently yielded material is different for each loading path even though the final remote stress state is the same. This finding suggests that plastic deformation in each case is likely to be different. A shortcoming of this particular plastic zone visualization technique is its inability to relay quantitative information regarding the level of plastic straining. Whether an element has experienced extensive plastic deformation or has just yielded, the same asterisk (*) is placed at the centroid.

An iso-value contour of the plastic deformation would provide the necessary quantitative information. A suitable measure of plastic deformation for this purpose is the effective plastic strain ($\bar{\epsilon}^P$). Contours of $\bar{\epsilon}^P$ for Cases I, II and III are presented in Figs. 4.27.

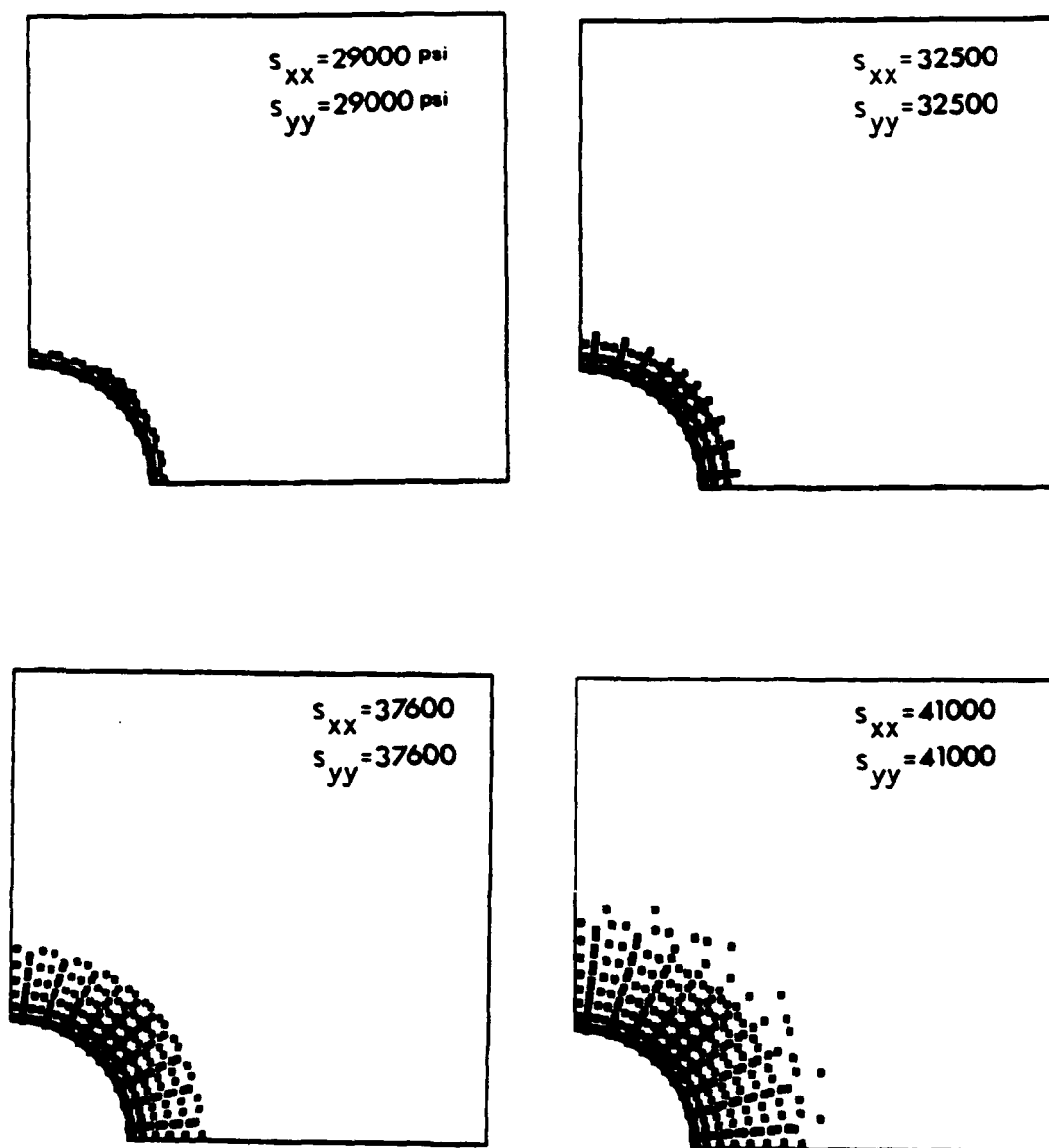


Figure 4.26 Plastic zone growth for an isotropic sheet subjected to a simultaneous biaxial remote loading (Case III).

$$s_{xx} = 41000 \text{ psi}$$

$$s_{yy} = 41000 \text{ psi}$$

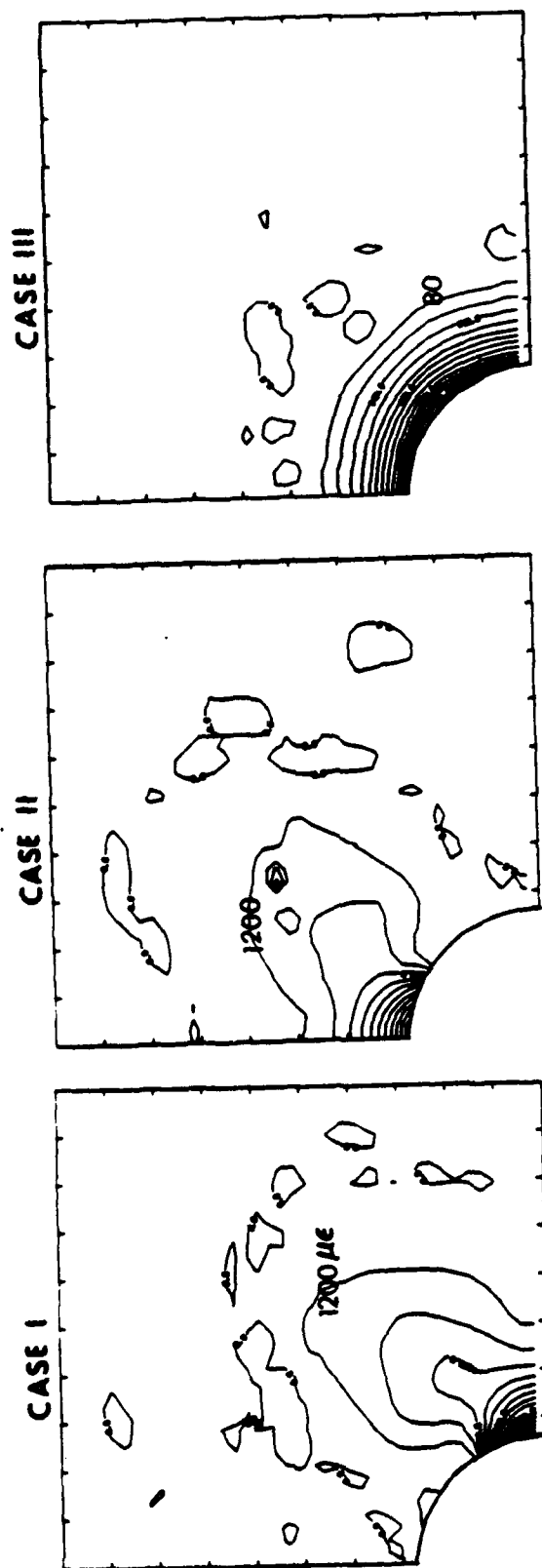


Figure 4.27 Effective plastic strain contour for the isotropic sheet at the final deformation state.

It is obvious from these contours that the final distribution and magnitudes of permanent deformation are quite different for each loading path, even though the final remote stress states are identical. These findings substantiate the premise of load path dependency and highlight the necessity of an incremental plasticity approach.

COMPARISON TO EXPERIMENTAL RESULTS FOR A CONTINUOUS FIBER REINFORCED METAL MATRIX COMPOSITE

An experimental study of the elastoplastic response of a unidirectional Boron-Aluminum metal matrix composite strip with a circular hole was conducted by S. Rizzi [24]. This particular experiment involved loading a B-Al specimen as shown in Fig. 4.28. Multiple strain gage recordings were taken in the vicinity of the hole. The finite element mesh used to analyze the test specimen is the same as for the other fixed grip analyses except the dimensions were scaled to those of Fig. 4.28.

The test was run by increasing the load until certain present breakpoints were reached at which time the specimen was unloaded to zero. Since most of the strains were recorded continuously, a strain distribution at any load can be easily obtained.

An elastic analysis was conducted to reconfirm ANPLAST's predictive capability for an orthotropic material. The elastic properties used are those described for B-Al in Reference [12]. The test specimen did not appear to demonstrate any permanent deformation until arriving at a remote stress of approximately 4000 psi. Therefore, to ensure a purely elastic response the comparison is made at a much lower load. The experimental results shown in Fig. 4.29 are plotted against the

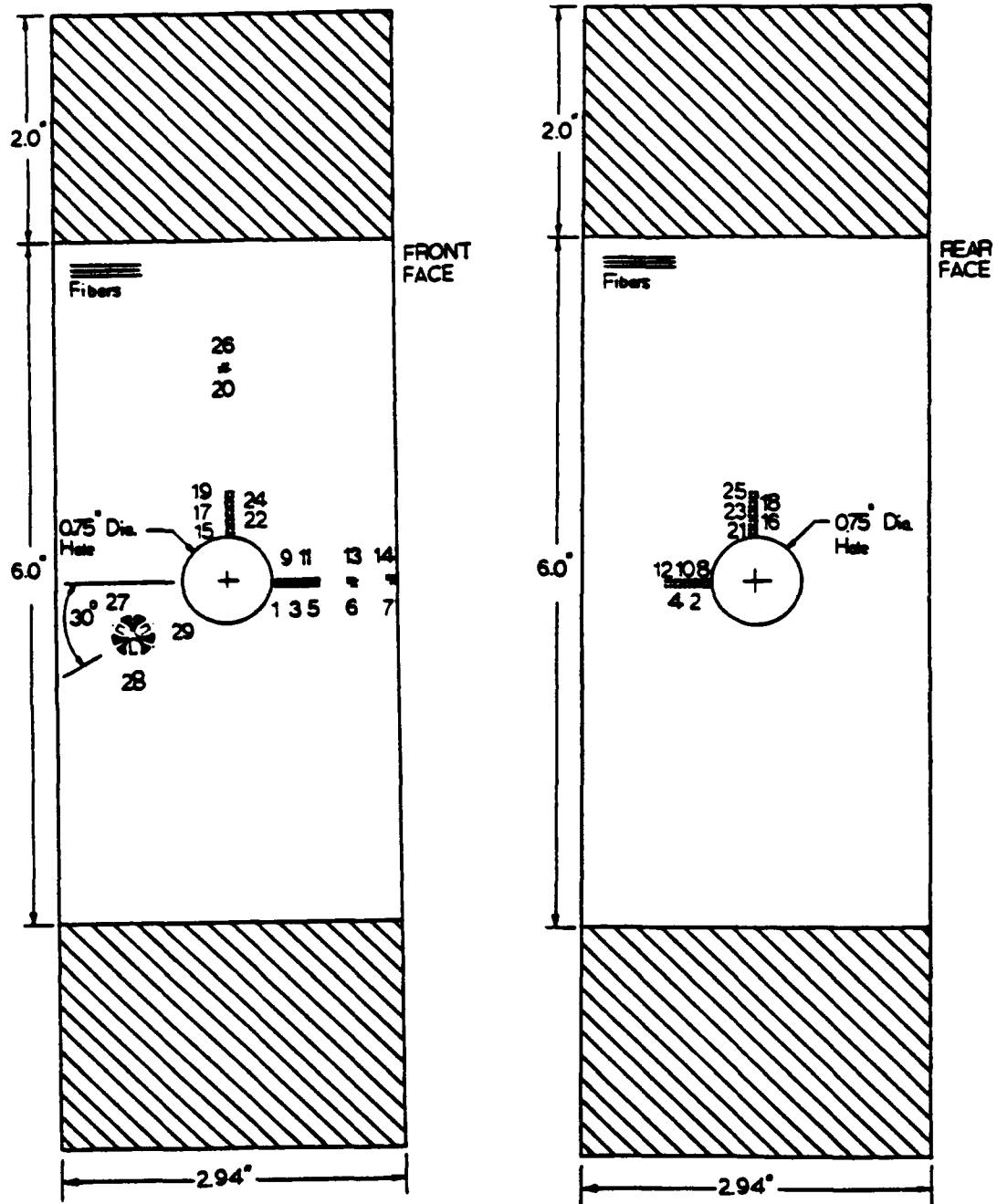


Figure 4.28 Geometry of test specimen used by Rizzi [24] for experimental determination of the stress-strain behavior of a Boron-Aluminum metal matrix composite.

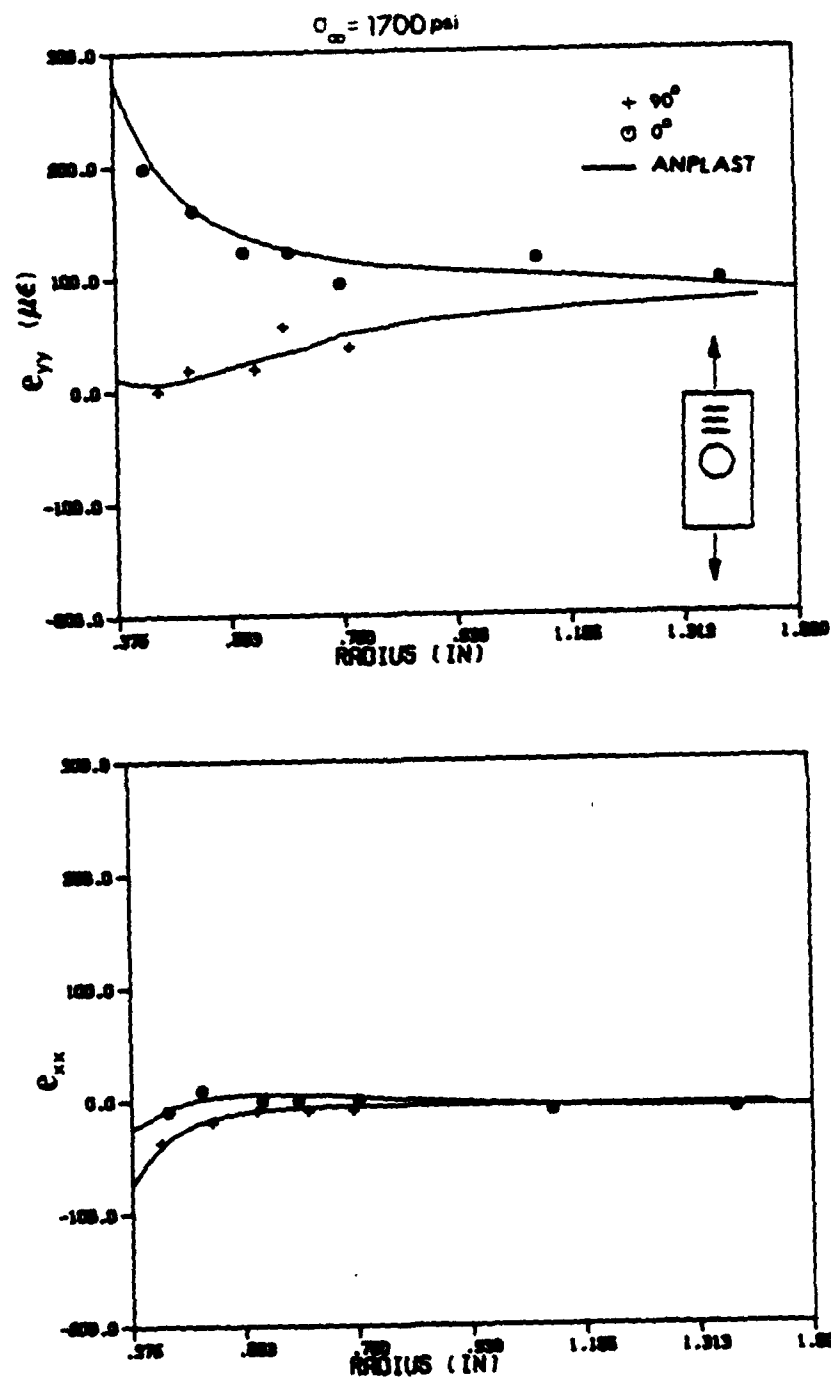


Figure 4.29 Comparison of ANPLAST strains with the experimental results of Rizzi [24] for a B-Al sheet with a circular hole subjected to uniaxial elastic loading.

finite element solution at a remote stress of 1700 psi. The correlation between the two solutions is acceptable, the differences attributable mainly to the inherent inaccuracies of measuring low strain levels.

The elastoplastic material properties were also chosen from Reference [24]. The elastic-plastic loading path was chosen so that it follows the test procedure as close as possible. The elastic analysis revealed that initial yielding would occur at the horizontal hole perimeter ($\theta = 0^\circ$) at a remote stress of 4000 psi. Therefore, the first loading step, which must be elastic, goes straight to 4000 psi, and then the remainder of the elastic plastic loading steps vary in magnitude but are never larger than 500 psi. The ANPLAST loading path is explicitly defined in Fig. 4.30. Notice that increments 2, 6, 14 and 17 coincide with the test unload points. The desired residual stresses and strains are obtained by re-starting the analyses at these unload points for elastic unloading. Re-yielding of elements during unloading was never observed.

The plastic zone visualization in Fig. 4.31 follows the expected pattern developed throughout this section. At the maximum remote stress of 10700 psi, the plastic zone has progressed completely across the specimen. Along the horizontal symmetry line, plasticity has also spread across the net section, but only during the last couple loading increments. Therefore, it is reasonable to assume that little or no permanent strain will be found at the outer strain gage locations. To evaluate the analysis more critically, a direct study of the elastic-plastic strains is in order.

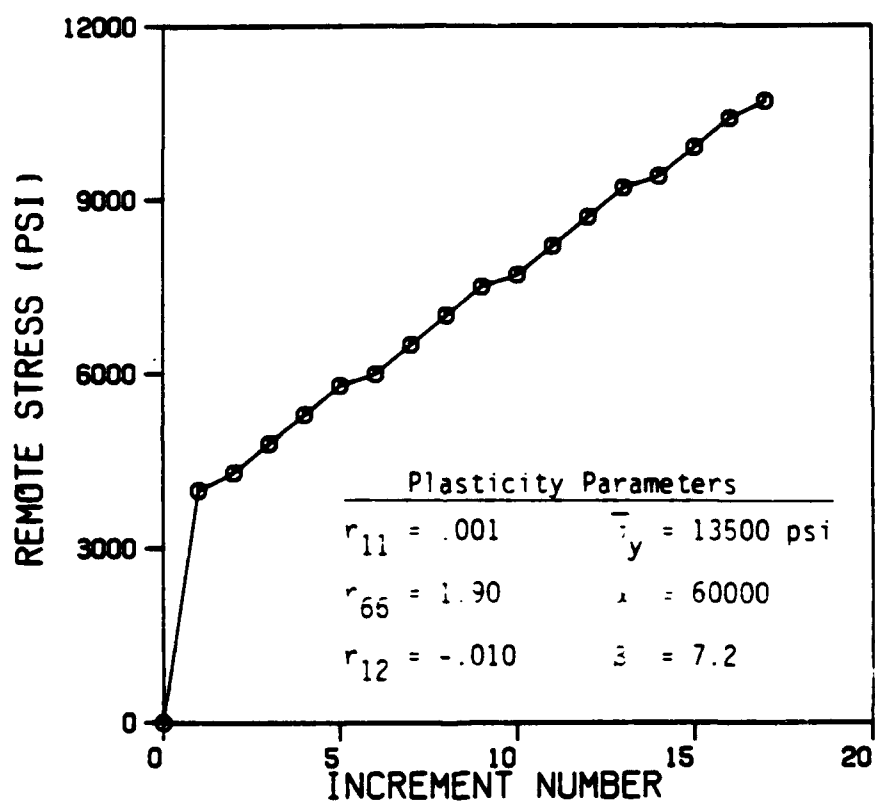


Figure 4.30 ANPLAST incremental loading path for analysis of the B-A1 strip with a circular hole.

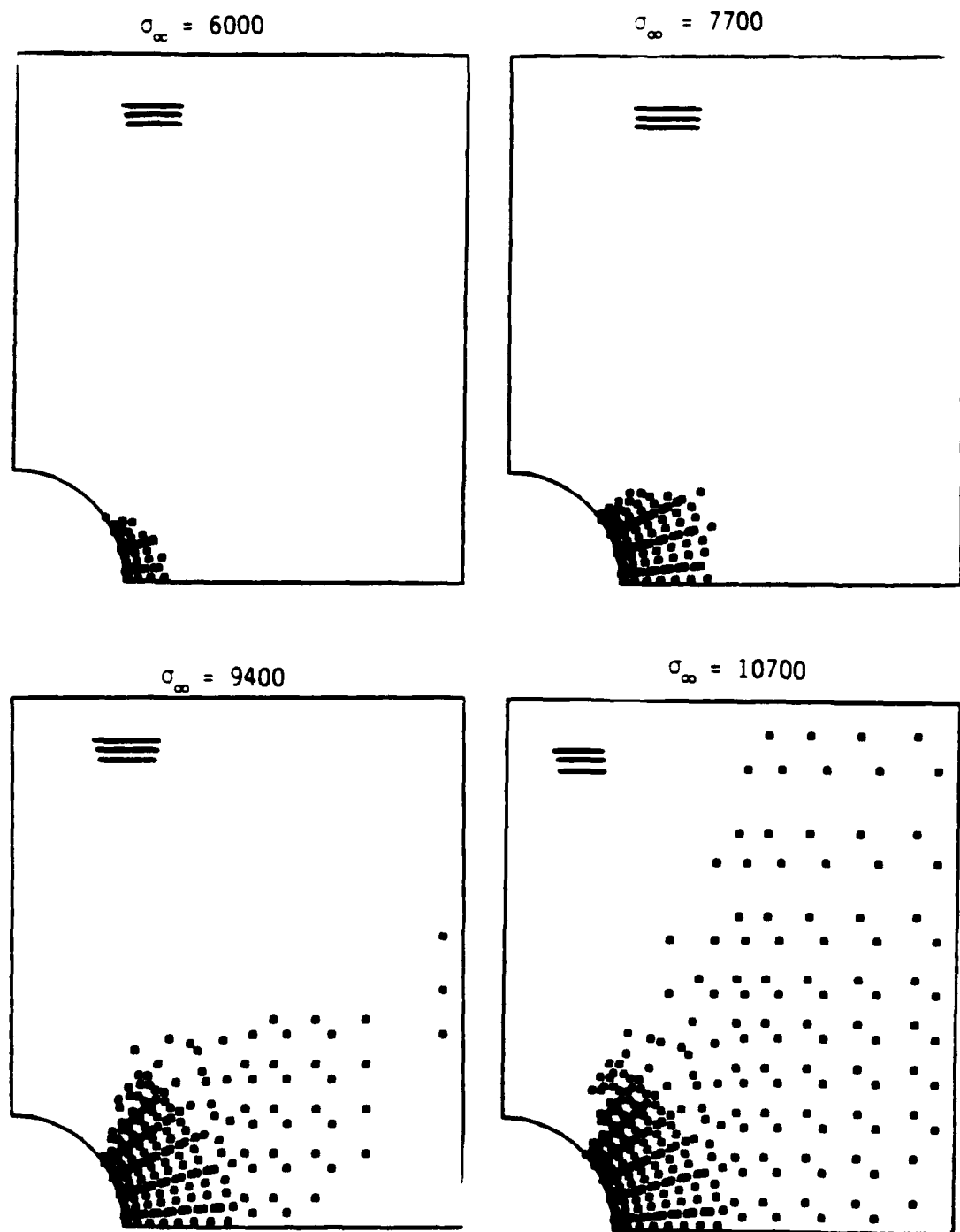


Figure 4.31 Plastic zone growth for the B-A1 strip subjected to elastic-plastic loading.

The longitudinal and lateral strain distributions for three elastic-plastic remote stresses (6000 psi, 7700 psi, 10700 psi) are plotted against the experimental results in Figures 4.32-4.33. The residual strains produced after unloading are included within each plot. The agreement between the numerical solution and the experimental results are quite good.

Due to the very stiff nature of the reinforcing fibers, the lateral strains (e_{xx}) are small in magnitude and both the analysis and experiment demonstrate this. The longitudinal (e_{yy}) residual strains demonstrate that ANPLAST does a good job of predicting the plastic deformation. The lack of any substantial residual strains at the remote gage locations is in agreement with the plastic zone visualization. It is interesting to note that even though net section yielding occurs, the elastic strains still dominate, even at the hole.

Figure 4.34 highlights the stress-strain response at the innermost strain gage during the complete load-time history of the test. These results substantiate the premise that ANPLAST more than adequately predicts the response of structures which exhibit anisotropic elastoplastic behavior.

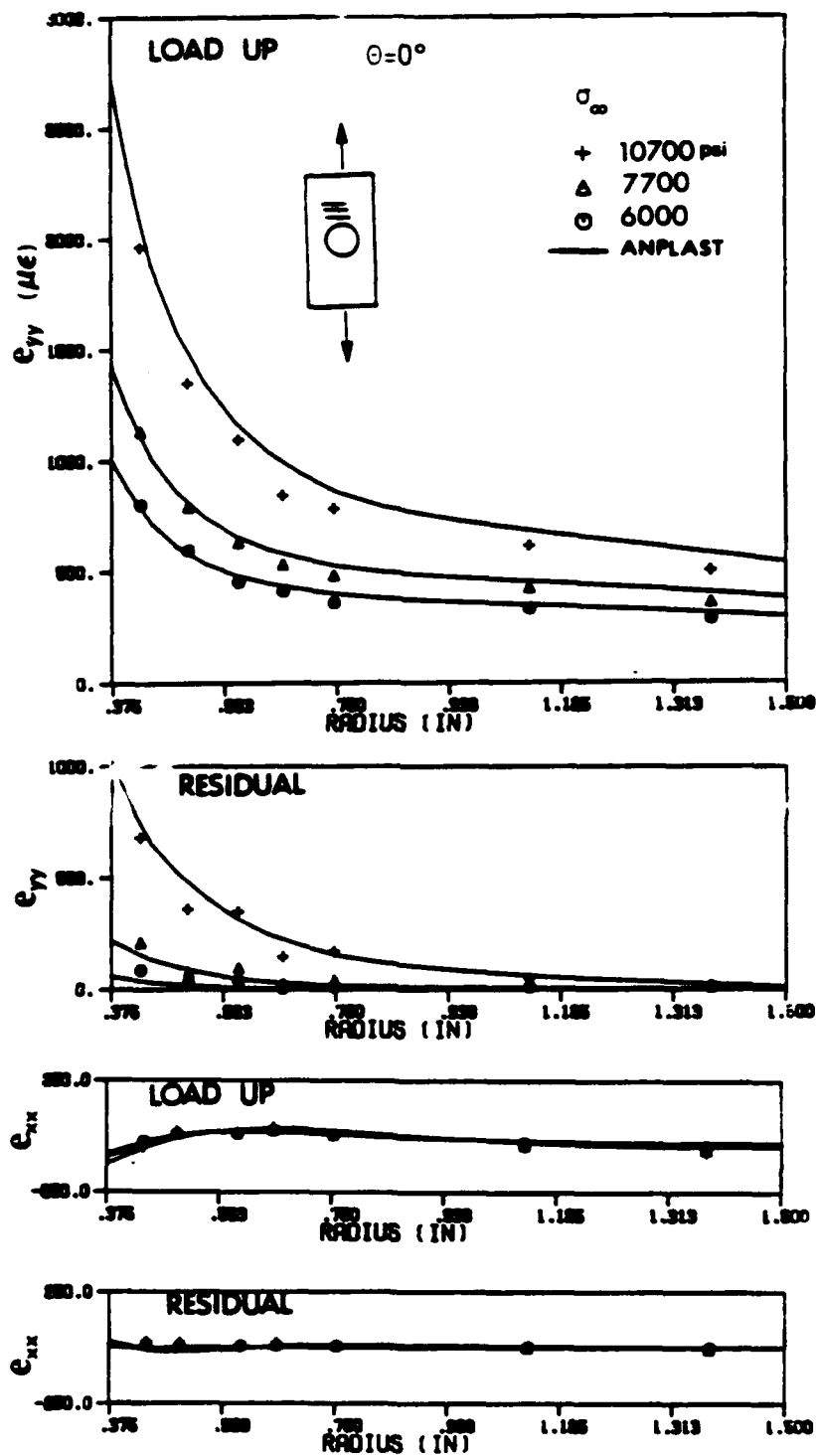


Figure 4.32 Comparison of ANPLAST strains with experimental results of Rizzi [24] for the B-Al strip with a circular hole subjected to elastic-plastic loading.

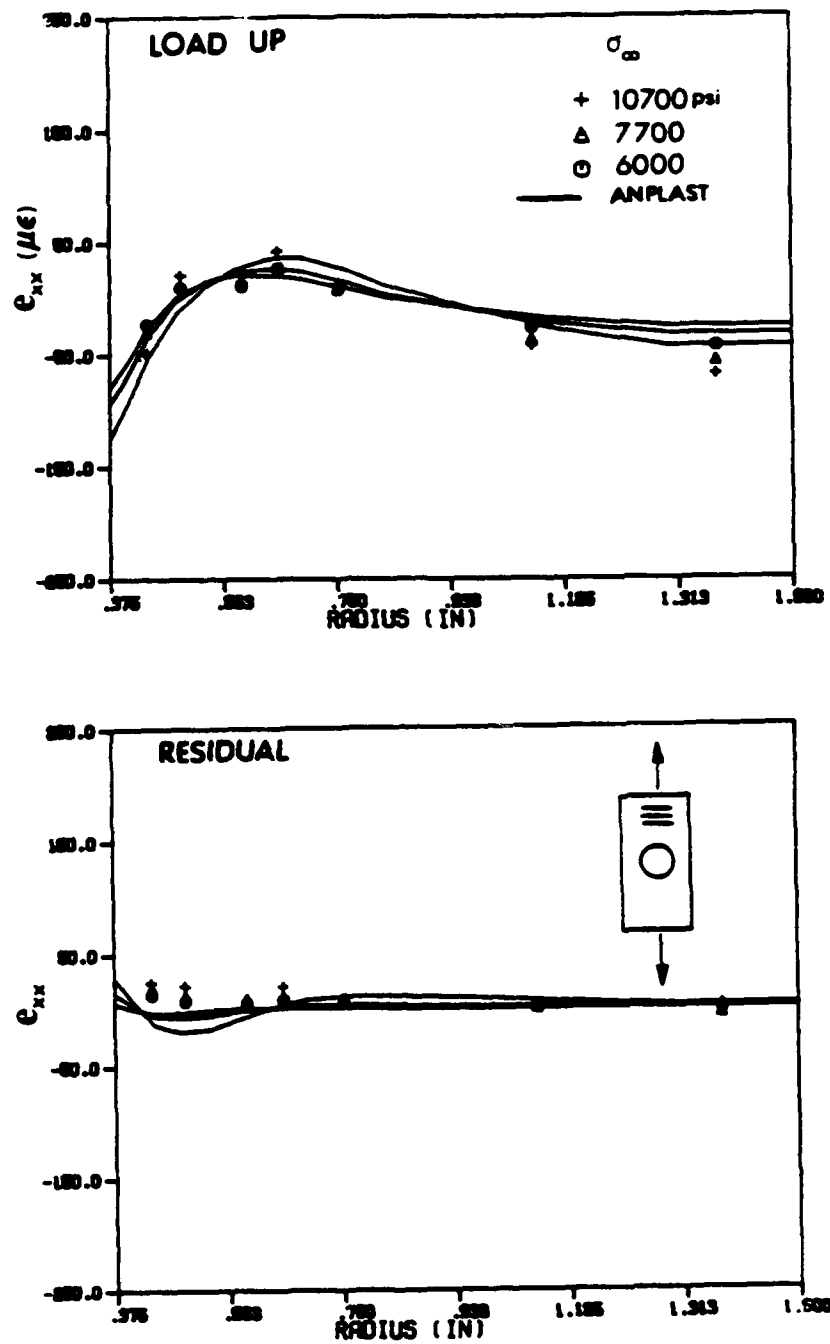


Figure 4.33 Comparison of ANPLAST lateral strains with the experimental results of Rizzi [24] presented on expanded scale.

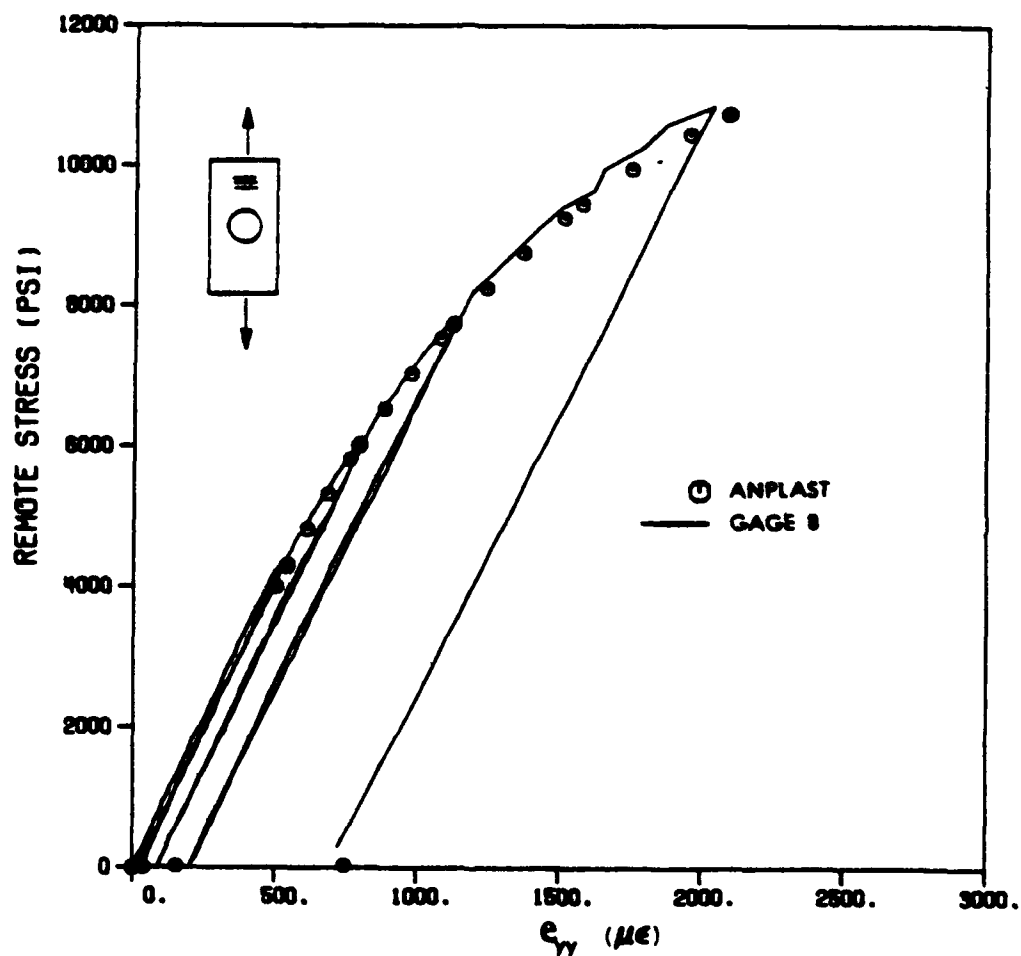


Figure 4.34 Comparison of ANPLAST longitudinal strain with the experimental results of Rizzi [24] for the complete load-history of the test. The strain gage is located at the innermost position along the horizontal symmetry line.

SECTION 5 ELASTOPLASTIC STUDY OF CRACKED PANELS

INTRODUCTION

The study of fracture and fatigue crack propagation often requires an understanding of the deformation state in the vicinity of the crack tip. The purpose of this section is to investigate some of the material and loading parameters which effect crack tip plasticity. Special attention will be given to the relative effect of anisotropy on plastic zone growth.

This section will first deal with the elastic study of center-cracked and edge-cracked panels using ANPLAST. Two numerical techniques for extracting the Mode I stress intensity factor, will be presented. An elastoplastic analysis of large scale yielding in isotropic and orthotropic edge cracked panels will also be conducted using ANPLAST.

ELASTIC ANALYSIS OF CENTER CRACKED PANELS

The center cracked panel provides a benchmark problem to further verify the performance of ANPLAST. This geometry also furnishes the opportunity to study the affect of anisotropy on the stress distributions.

Comparison of Stress Distribution with Theory

The center cracked panel provides the simplest geometry for consideration of the elastic stress distribution in the vicinity of the

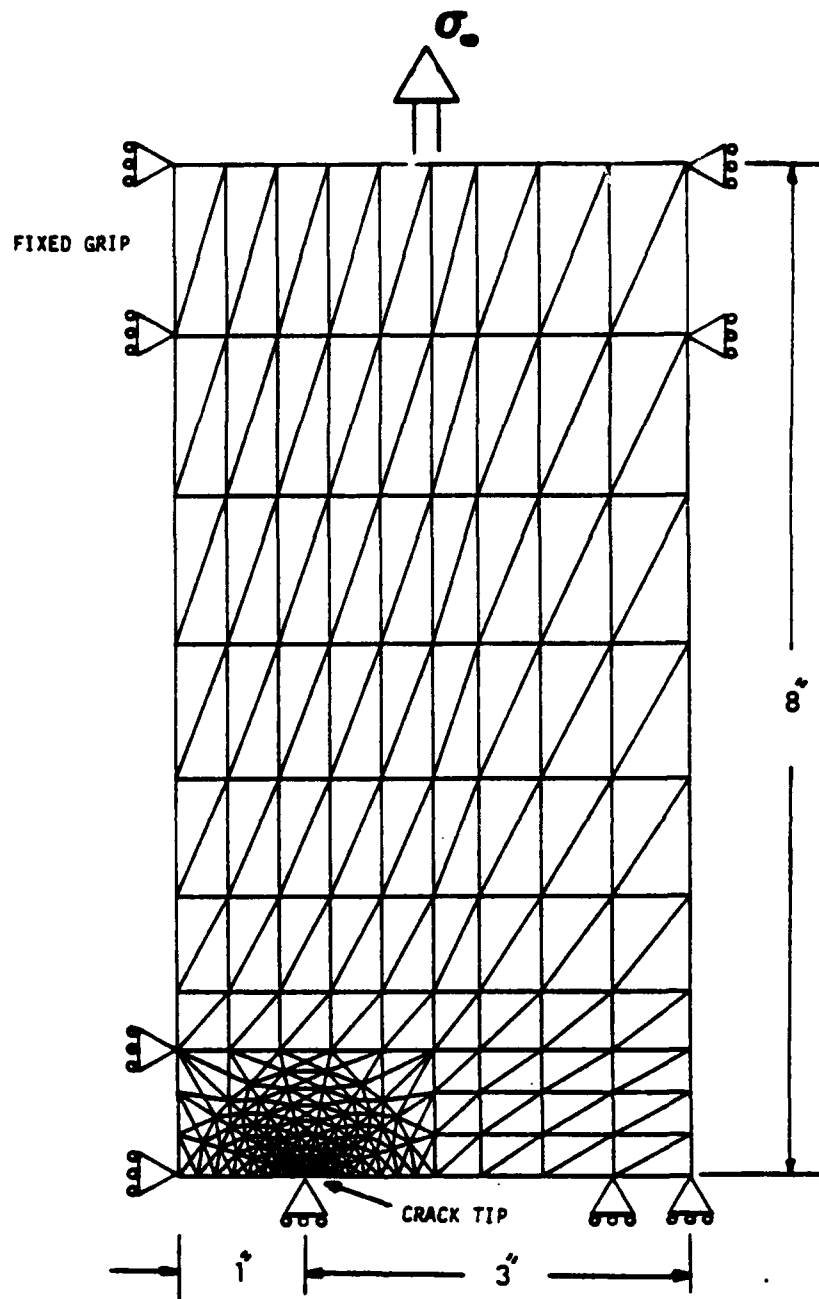
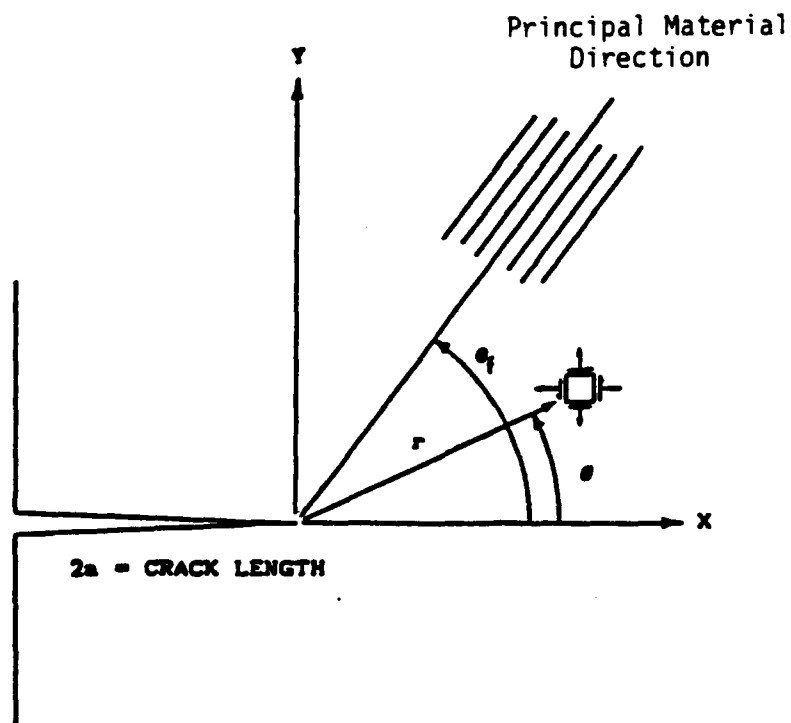


Figure 5.1 Finite element mesh of a center cracked panel with a uniaxial remote load and fixed grip end conditions.



θ_f = θ Material Direction

θ = Angular Orientation of Element

r = Radius of Element

Figure 5.2 Illustration of the local and global coordinate systems for a cracked panel.

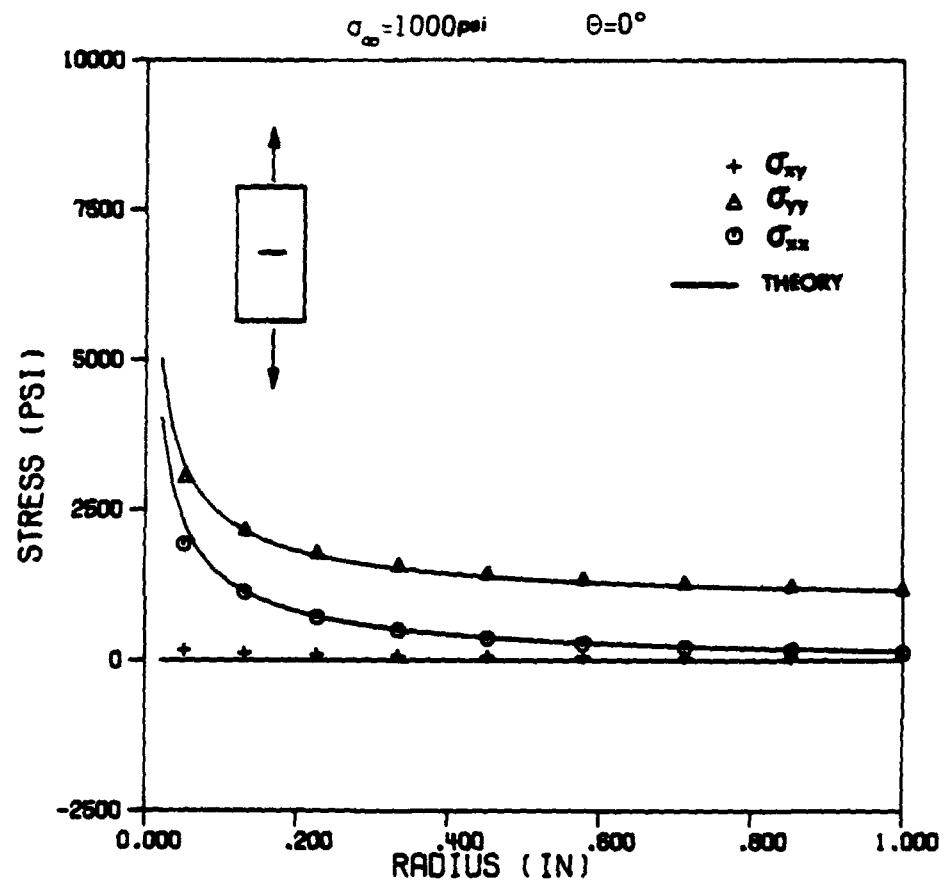


Figure 5.3 Comparison of the ANPLAST stress distribution with the ELLPLAS theoretical solution for an isotropic panel with a center crack subjected to elastic loading.

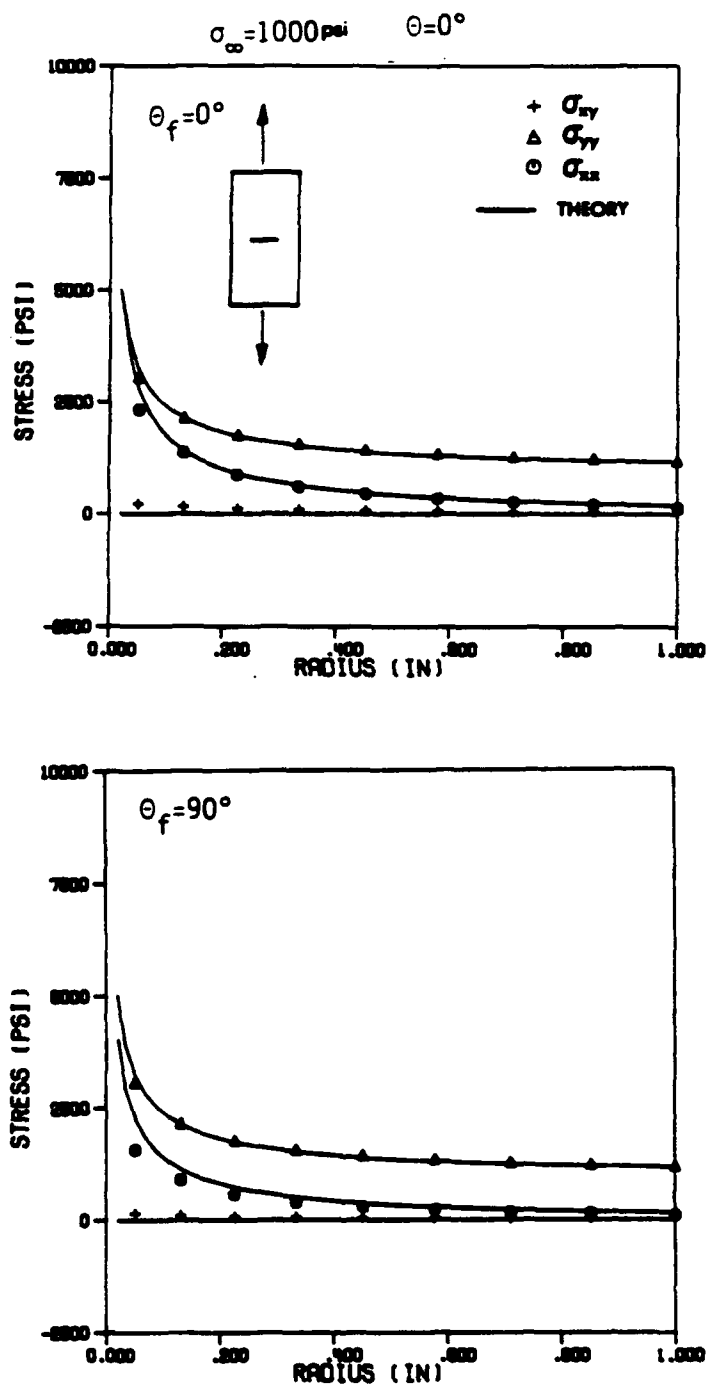


Figure 5.4 Comparison of the ANPLAST stress distribution with the ELLPLAS theoretical solution for a weakly orthotropic (B-A1) panel with a center crack subjected to elastic loading.

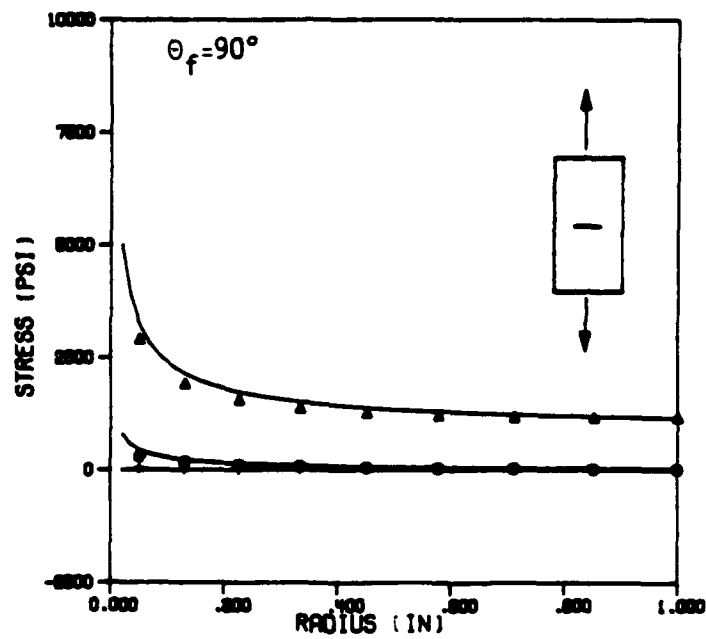
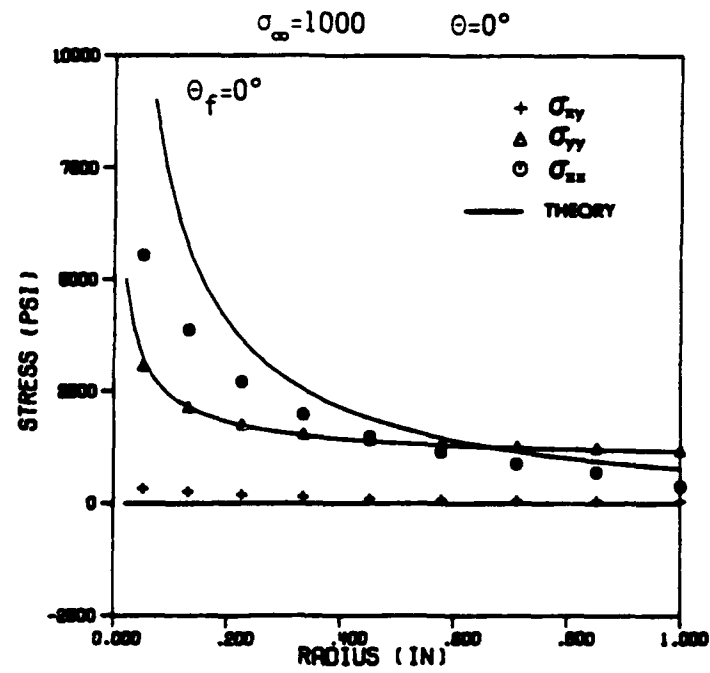


Figure 5.5 Comparison of the ANPLAST stress distribution with the ELLPLAS theoretical solution for a strongly orthotropic (G-Ep) panel with a center crack subjected to elastic loading.

crack. A finite panel with a center crack as illustrated in Fig. 5.1, was analyzed with ANPLAST and the results compared to the theoretical solution provided by ELLPLAS. Isotropic and anisotropic materials are investigated.

In the following discussions notational definitions are as shown in Fig. 5.2. The stress distributions along a horizontal radial line ($\theta = 0^\circ$) are presented in Figs. 5.3-5.5. The ANPLAST distribution of stresses for the isotropic panel and both B-A1 orientations are in close agreement with the theoretical solution. The more strongly anisotropic graphite-epoxy panel exhibits different behavior, especially when the fibers are parallel to the crack ($\theta_f = 0^\circ$). In this case, σ_{xx} dominates in the general vicinity of the crack tip.

The numerical model of the center cracked panel represents a finite width and length sheet. The ELLPLAS solution is that for an infinite sheet. Though the finite effect is minimal for the isotropic material and weakly anisotropic B-A1, it appears that strong anisotropy can amplify the finiteness of the specimen. This is evident from the behavior of σ_{xx} in the graphite epoxy center cracked sheet. When the fibers are parallel to the crack, σ_{xx} decays dramatically over the width of the specimen, while for $\theta_f = 90^\circ$, this stress component has dropped to almost zero a very small distance from the crack tip. These results indicate that if an accurate elastic analysis is desired in the vicinity of the crack tip, mesh density should be a factor of anisotropy as well as geometry.

Philosophy of Finite Element Mesh Design

The analysis of the center cracked panel from the previous section used a radially designed finite element mesh. A symmetric radial fan is centered about the crack tip and the mesh density is biased toward the crack tip. An alternative to this mesh design would be a rectangular mesh as illustrated in Fig. 5.6. One possible advantage for selecting the rectangular design would be the ease of mesh generation. A concern, is the relative accuracy in representing the stress distribution in the vicinity of the crack.

An elastic analysis was conducted utilizing the rectangular mesh; the results are presented in Fig. 5.7. The numerical results are again plotted against the theoretical solution and compared to the respective plot for the radially designed mesh. While the stress distributions for the rectangular mesh are reasonable, it is apparent for $\theta = 90^\circ$, that the radial design is superior. It is interesting to note that the rectangular mesh contains 104 more d.o.f. than does the radial mesh.

An elastic analysis was used to compare the two mesh designs, yet it is the study of plasticity which is given primary emphasis in this research. When considering the initiation of yield and subsequent plastic flow, one must recall that these processes are calculated on the element level. It is obvious that the radial mesh design provides many more elements in the θ direction, thus allowing a better description of the gradients associated with plasticity. Therefore, all elastoplastic analyses of cracked panels will utilize a radially designed mesh.

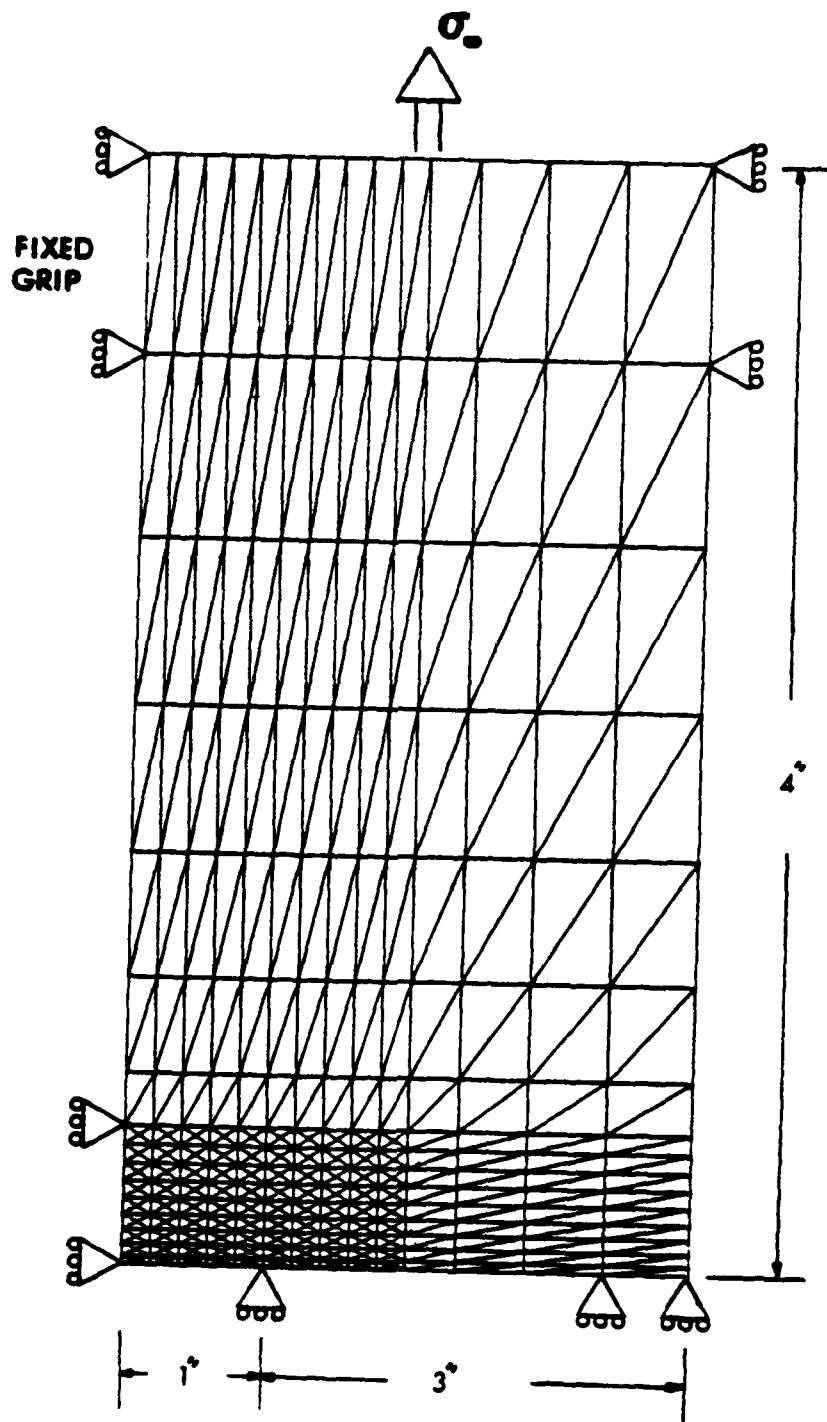


Figure 5.6 Finite element mesh of a center cracked panel which utilizes a rectangular grid design in the vicinity of the crack tip.

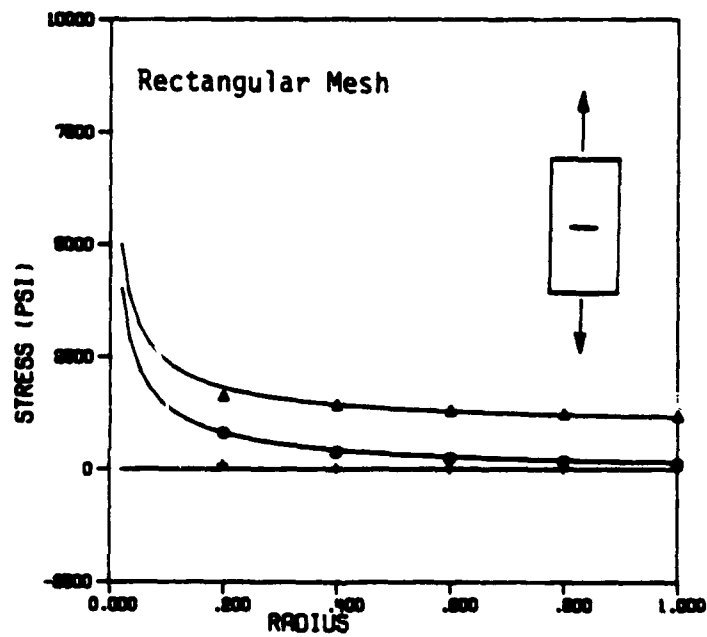
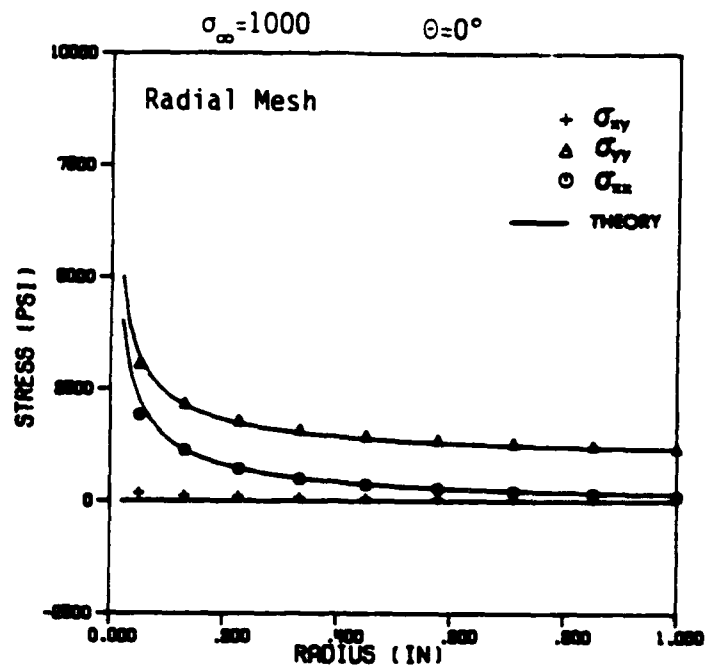


Figure 5.7 Comparison of ANPLAST stress distribution for the radial and rectangular mesh designs of an isotropic center cracked panel subjected to elastic loading.

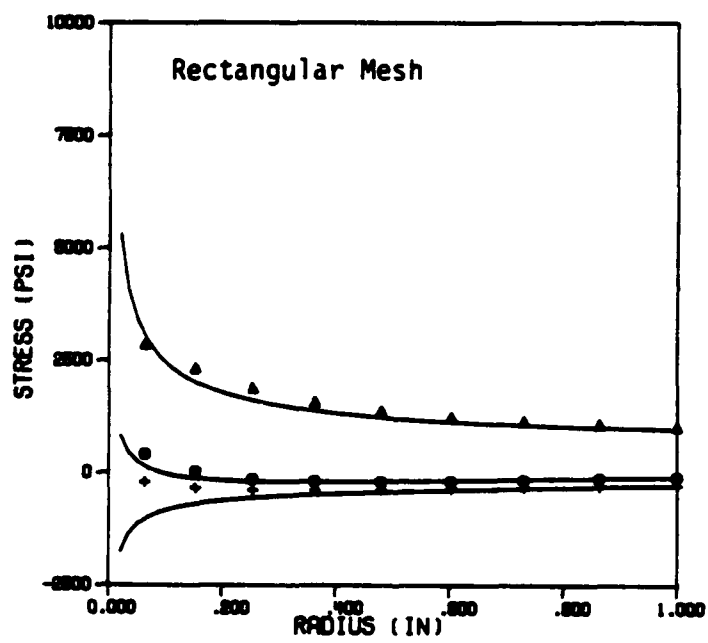
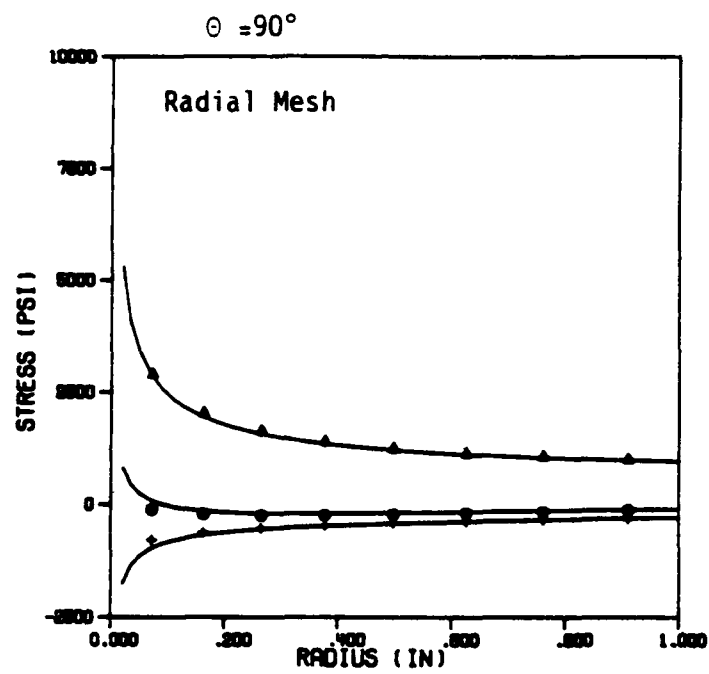


Figure 5.7 continued

Comparison of Constant Strain Triangle and Isoparametric Quadrilateral Elements

The primary finite element used in the ANPLAST program is the constant strain triangle (CST). It has been suggested by a number of authors [23, 25] that the higher order isoparametric element with a reduced integration scheme may provide superior results for analyses involving strong anisotropy. Therefore, the 8 node isoparametric element developed in Section 3 was used to analyze the center cracked panel and the results compared to the CST. The mesh used for this analysis is illustrated in Fig. 5.8.

The results from the comparative study are presented in Fig. 5.9. The results are presented for an isotropic, B-Al ($\theta_f = 0^\circ$), and G-Ep ($\theta_f = 90^\circ$) material. Note the erratic behavior of the two nodal stresses closest to the crack tip. This is due to the nodal extrapolation technique failing to account for the 8 node quadrilateral being degenerated to a 6-node triangle.

Of interest is the σ_{xx} distribution for the graphite epoxy specimen since this resulted in the greatest deviation for the CST. It appears that the quadrilateral element does provide a better representation of this stress gradient. But rather than the 8 noded quadrilateral possessing any inherent advantage, the improved performance is likely due to the available degrees of freedom. The quadrilateral mesh has almost twice the degrees of freedom than does the CST mesh. Therefore, a more refined CST mesh should produce results similar to the 8 node quadrilateral, for approximately the same cost (running time). The use of either element in a appropriately refined mesh

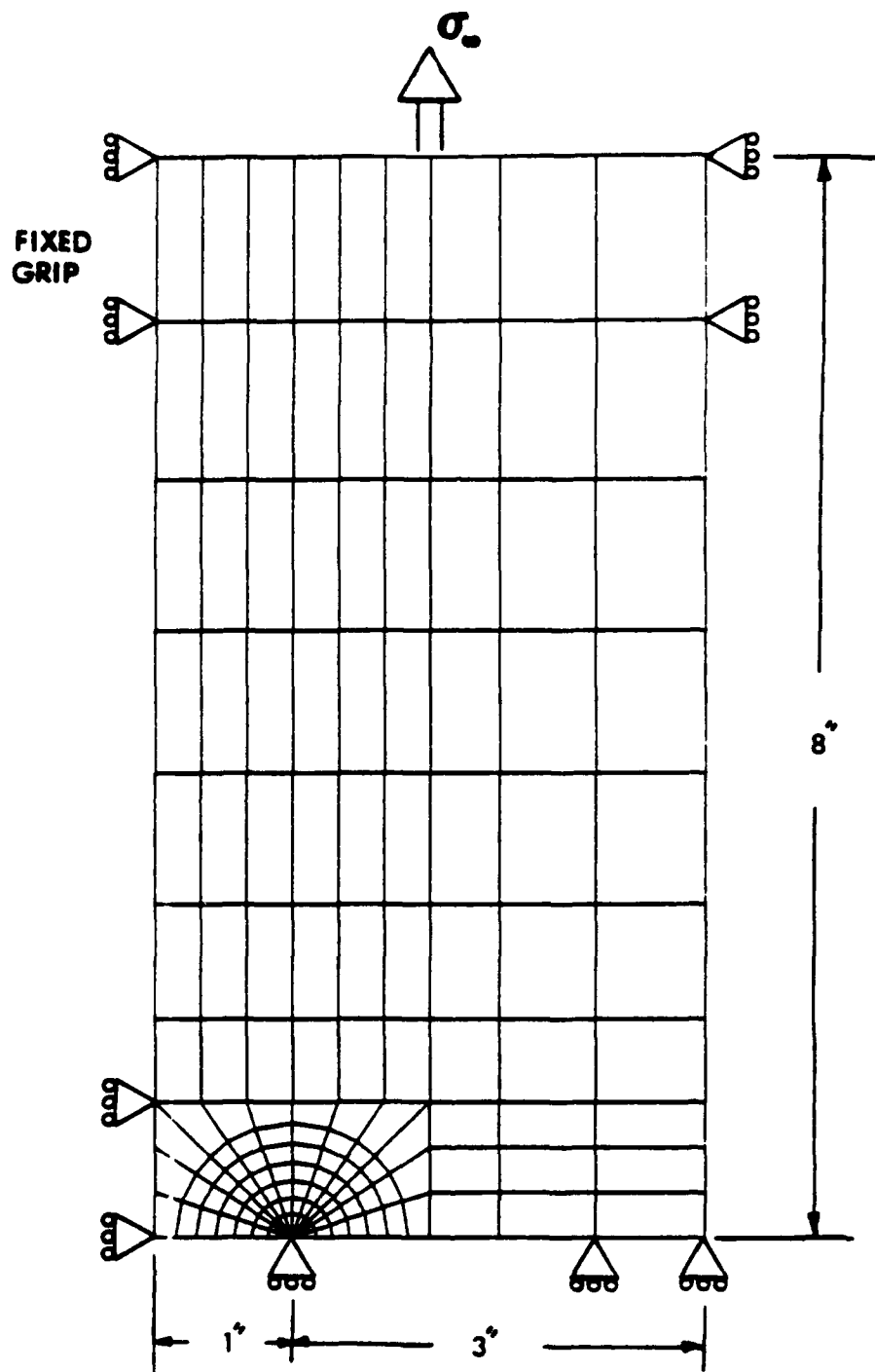


Figure 5.8 Finite element mesh of the center cracked panel utilizing 8-nodes isoparametric elements.

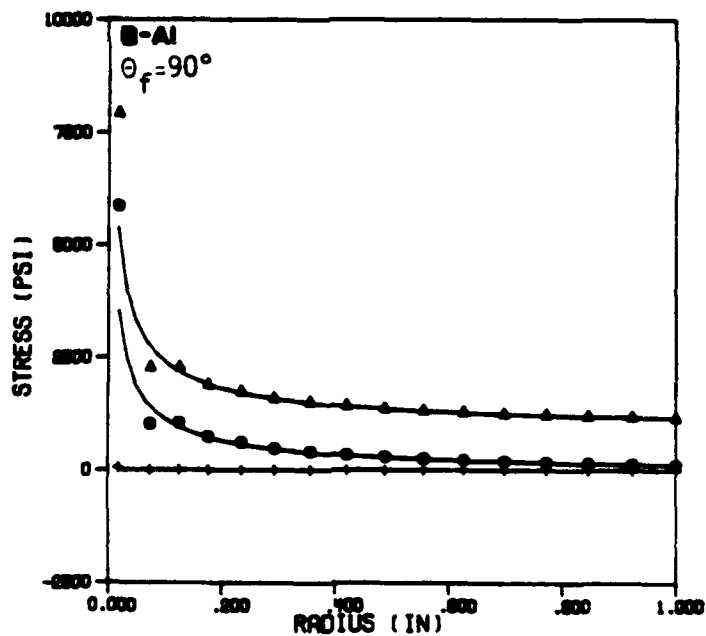
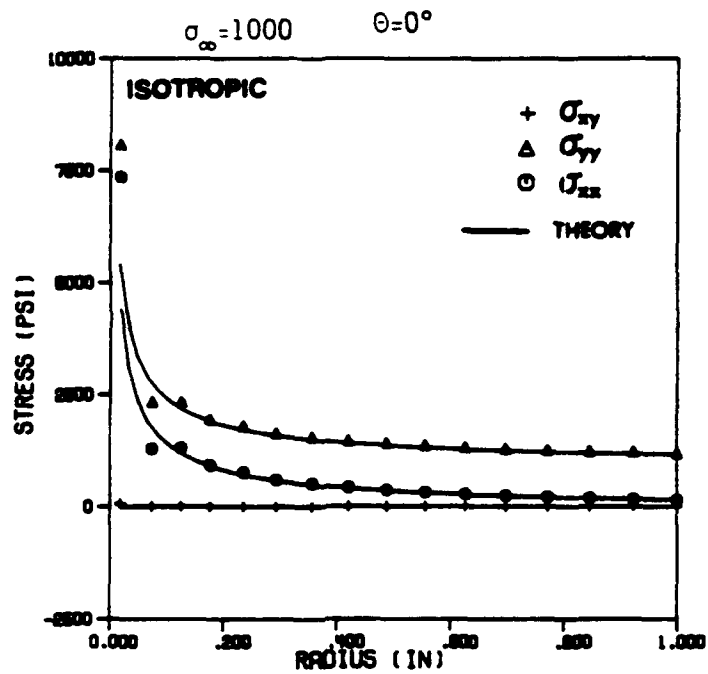


Figure 5.9 Comparison of the isoparametric element results with the ELLPLAS solution for the center cracked panel subjected to elastic loading.

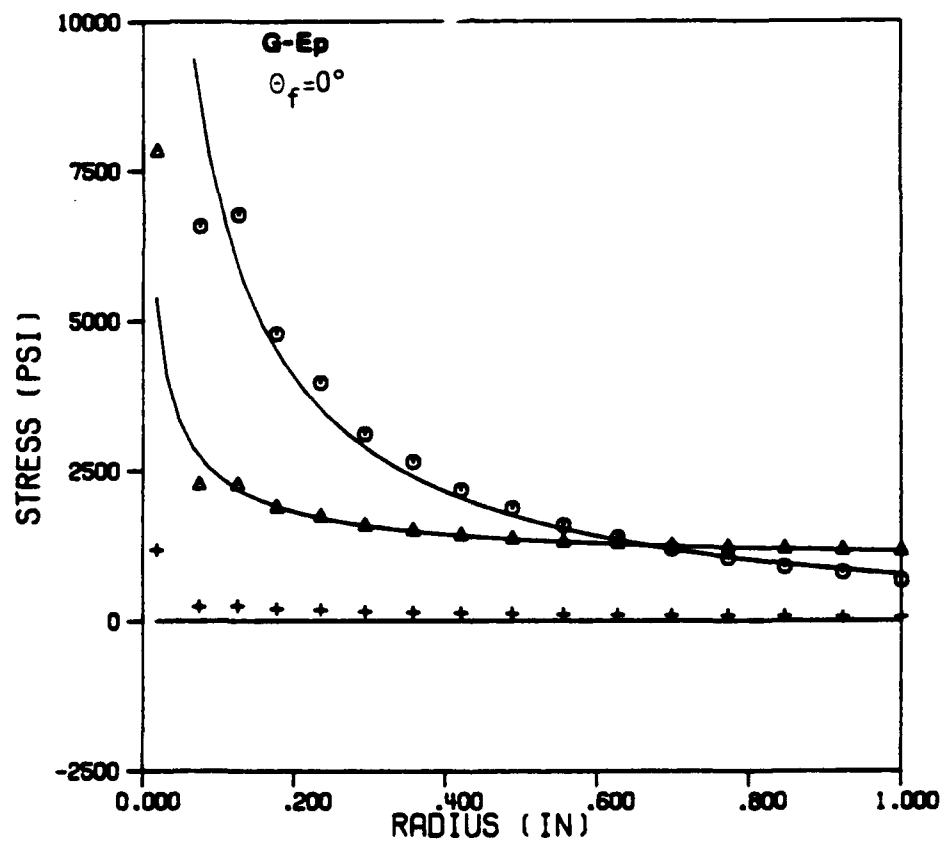


Figure 5.9 continued

should result in adequate performance.

ELASTIC ANALYSIS OF AN EDGE CRACKED PANEL

All of the material behavior investigated in this research has exhibited an elastic response before the onset of plasticity, and it is clear that the elastic stress distribution plays a significant role in subsequent plasticity. In addition, the elastic behavior of cracks is analyzed because of the necessity for understanding some basic fracture mechanics parameters and how they are influenced by anisotropy.

Effect of Anisotropy on Stress Distribution

It is reasonable to expect that the elastic stress distribution in the vicinity of the crack tip for the edge cracked panel retains the same character as was discussed for the center crack. For cases of isotropic or weakly anisotropic material behavior, σ_{yy} will dominate along the horizontal cross section. The introduction of strong anisotropy will exaggerate the finiteness of the panel and redistribute the stress gradients. Therefore, similar modeling techniques were utilized for analyses of the edge cracked panel as was used for the center crack.

A detailed understanding of the individual stress components does not provide any direct information concerning the onset of yield. But an equivalent quantity such as the Von-Mises [2] effective stress parameter provides useful insight into isotropic elastoplasticity. A parametric study on the effect of elastic anisotropy via the Von-Mises stress can be conducted in a meaningful way only if one assumes all plasticity behavior is isotropic.

Five elastic analyses of an edge cracked panel as shown in Fig. 5.10 were conducted for an isotropic, B-Al ($\theta_f = 0^\circ, 90^\circ$), and G-Ep ($\theta_f = 0^\circ, 90^\circ$) material. The results are in the form of iso-stress contours of the Von-Mises quantity as illustrated in Figs. 5.11-5.13. Since all of the materials were assumed to behave in an isotropic plastic manner, the Von-Mises contours leads us to the conclusion that plastic zone shape is strongly linked to the strength and orientation of the elastic anisotropy. This is clearly illustrated for the G-Ep specimen response, which demonstrates the significant distortion of the contours in the stiff material direction. By noting the maximum contour level, one can conclude that the remote load which initiates yield is also a function of the strength and orientation of the elastic anisotropy.

It is clear that elastic anisotropy can have a substantial effect on the elastoplastic response. Earlier sections have documented the consequences of introducing anisotropy into the plastic flow relationships. For orthotropic-elastic orthotropic-plastic materials, these two effects will superimpose and result in an extremely complex structural response. This highlights the convenience of using a numerical tool, like ANPLAST, to analyze these types of problems.

Stress Intensity Determination by an Energy Technique

The advantage of using an energy technique to calculate fracture parameters lies in the fact that no extrapolation or curve-fitting is needed. In particular, the strain energy release rate, g_I , of a cracked panel can be derived by investigating the change in compliance of the system as the crack extends. It can be shown [26] that the

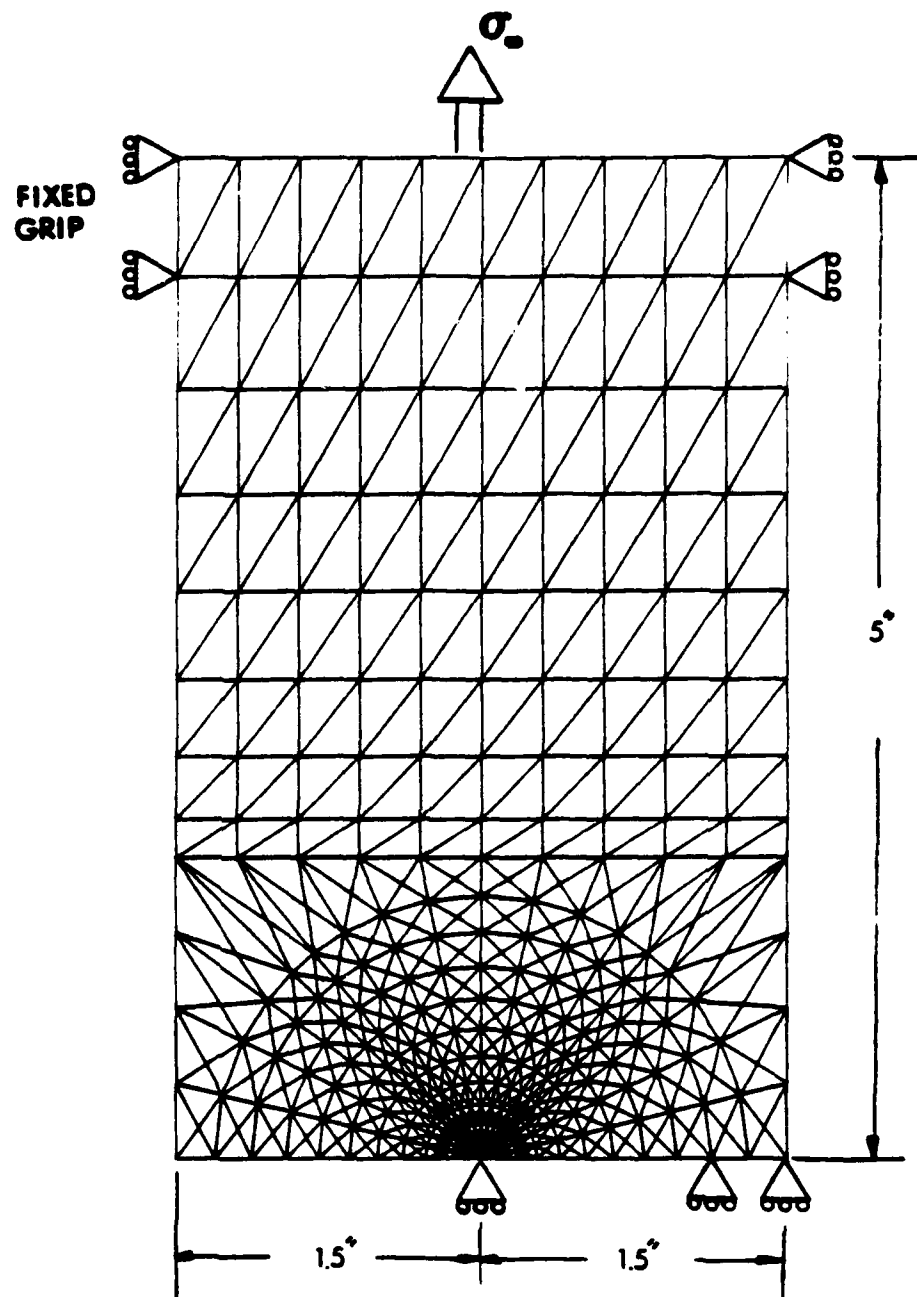


Figure 5.10 Finite element mesh of a transverse edge cracked panel with a uniaxial remote load and fixed grip end conditions.

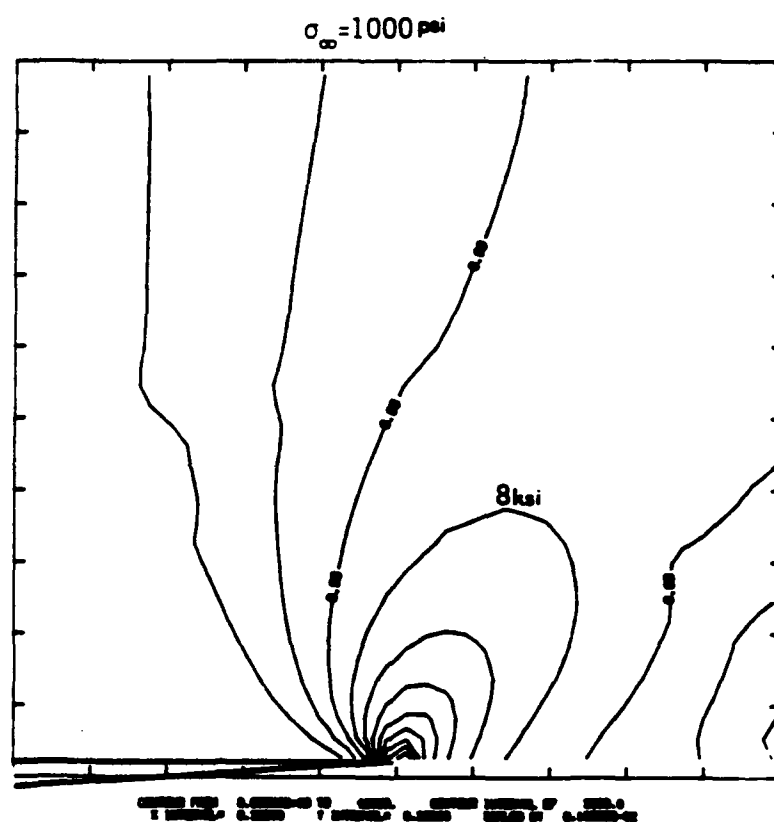


Figure 5.11 Mises stress contour of a isotropic edge cracked panel subjected to elastic loading.

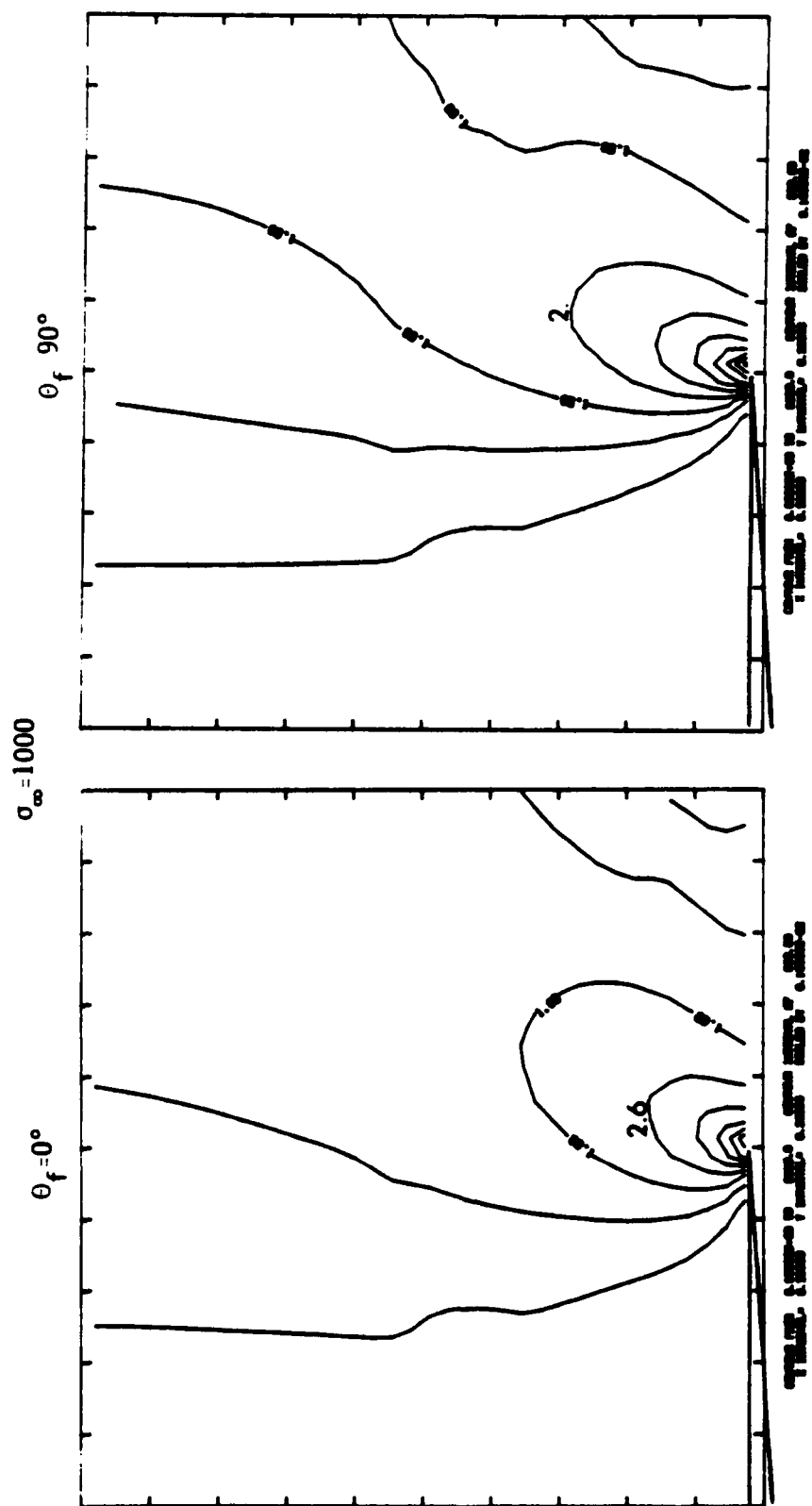


Figure 5.12 Mises stress contour of a weakly orthotropic (B-A1) edge cracked panel subjected to elastic loading.

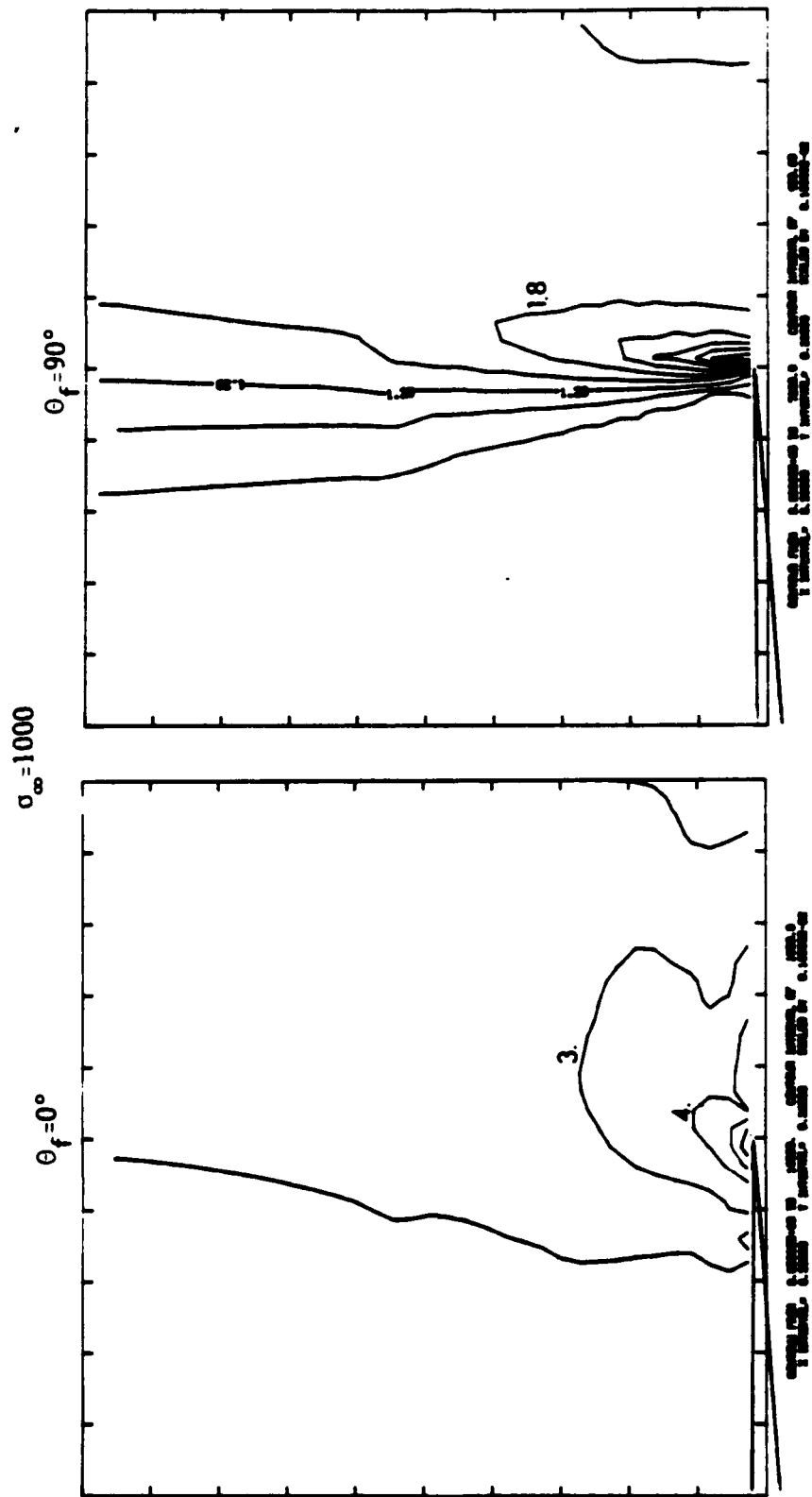


Figure 5.13 Mises stress contour of a strongly orthotropic (G-Ep) edge cracked panel subjected to elastic loading.

change in elastic strain energy during crack extension is equal to the change in potential energy (ΔV) and can be expressed as

$$\Delta V = -\left[\int_0^{u_2} P d\delta - \int_0^{u_1} P d\delta \right] = -\frac{1}{2} P(u_2 - u_1) \quad (5.1)$$

where $(u_2 - u_1)$ is the deflection of the system in the direction (δ) of the applied force (P), at the point where the force is applied. The change in strain energy (ΔU) can now be equated to the compliance of the system

$$\Delta U = \Delta V = \frac{1}{2} P(\Delta u) \quad (5.2)$$

and the strain energy release rate defined as the change in strain energy due to a small increment of crack extension (Δa) becomes

$$g_I = \frac{\partial U}{\partial a} = \lim_{\Delta a \rightarrow 0} \frac{\Delta U}{\Delta a} = \frac{1}{2} \frac{P \Delta u}{\Delta a} = \frac{1}{2} \frac{(\text{work})}{\Delta a} \quad (5.3)$$

It is now clear that g_I can be estimated by measuring the deflections of the system at the point of load application.

The compliance method is ideally suited for use with the finite element method. Since the finite element technique directly solves for displacements, no interpolation of stresses or strains is required. The work done by external forces is easily calculated by multiplying the applied nodal loads by the respective change in displacements due to a small crack extension. It is interesting to note that deriving g_I

by the compliance method does not require any special technique or program when investigating orthotropic materials.

Although g_I can be used directly in many fracture and fatigue crack propagation applications, it is still quite common to utilize the stress intensity factor (K_I). The relation between g_I and K_I for an isotropic material under a plane stress condition is [26]

$$g_I = \frac{K_I^2}{E} \quad (5.4)$$

where E is the modulus of elasticity. After calculating g_I , it is easy to find K_I . For an orthotropic material, the relation is not readily available, but is in the form

$$g_I = \frac{K_I^2}{\beta}$$

where

$$\beta = f(E_1, E_2, \nu_{12}, G_{12}) \quad (5.5)$$

To determine β analytically is cumbersome, but taking advantage of the properties of the center-cracked panel, β can be found numerically.

For a center-cracked panel, where the finite width effects are negligible, K_I is identical for both the isotropic and orthotropic material cases [27]. Therefore, K_I can be found from the simple expression

$$K_I = \sigma_{\infty} \sqrt{\pi a}$$

Using the compliance method previously explained, and the center-cracked finite element model, g_I is calculated for a B-A1 specimen with the fibers oriented parallel to the crack. Since β was calculated and found to have a value of 9.11×10^6 psi, it is possible to find K_I for any B-A1 edge-cracked geometry.

A stress intensity calibration chart prepared for an edge-cracked panel is illustrated in Fig. 5.14. The solid line represents the solution for an isotropic material, with bending restrained. The four finite element meshes used for these analyses are similar to the mesh in Fig. 5.10 except for the length of the crack. The triangular data points represent K_I derived by extrapolation of the stresses as discussed in the next section.

Stress Intensity Determination by Extrapolation of the Stresses

The determination of the Mode I stress intensity factor K_I by direct extrapolation of the stresses is of interest in this section. For anisotropic materials, the near field stresses can be represented in terms of K_I , r , and θ as [27]

$$\begin{aligned}\sigma_{xx} &= \frac{K_I}{\sqrt{2\pi r}} f_{xx}(\theta) \\ \sigma_{yy} &= \frac{K_I}{\sqrt{2\pi r}} f_{yy}(\theta) \\ \sigma_{xy} &= \frac{K_I}{\sqrt{2\pi r}} f_{xy}(\theta)\end{aligned}\tag{5.6}$$

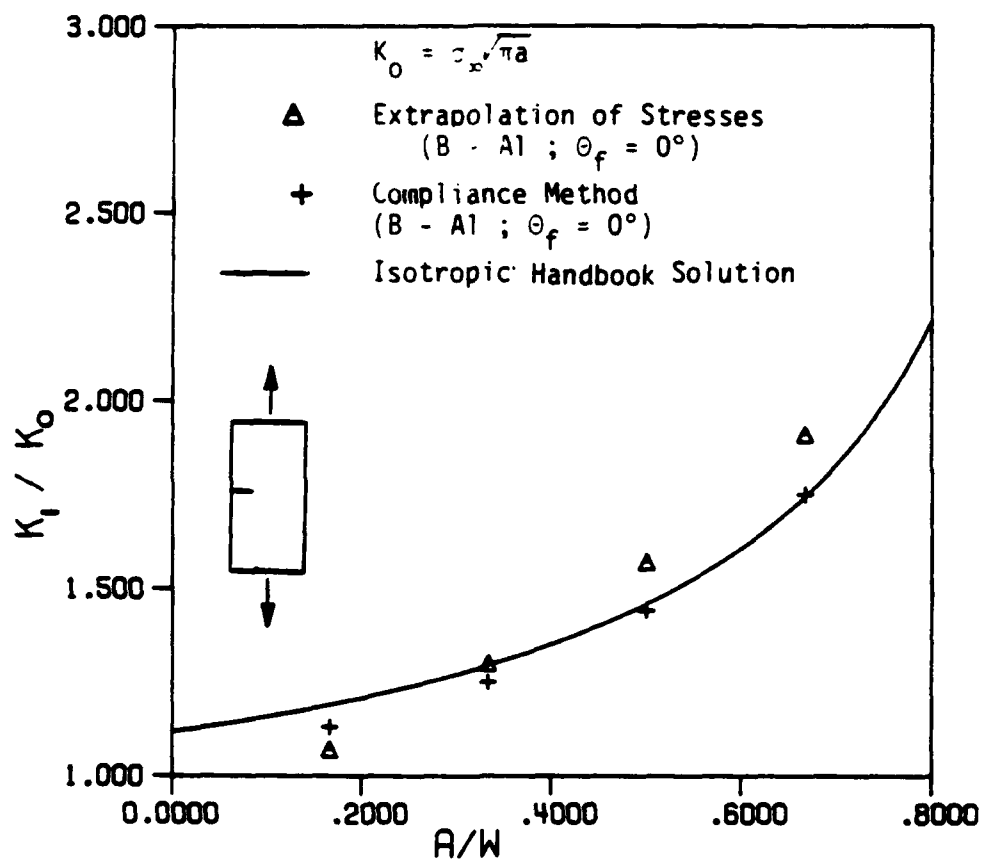


Figure 5.14 Stress Intensity Factor (K_I) chart for the edge cracked panel containing the isotropic handbook solution and that obtained by ANPLAST for B-A1.

where $f_{ij}(\theta)$ = appropriate functional form of θ . This equation can be easily re-arranged so that K_I appears on the left handside of each expression as

$$K_I = \frac{\sigma_{ij} \sqrt{r} \sqrt{2\pi}}{f_{ij}(\theta)} \quad (5.7)$$

Assuming that $f_{ij}(\theta)$ is known, it is apparent that K_I can be obtained from a finite element analysis since the stresses σ_{ij} at each location (r, θ) are known. Ideally, any selection of stress points would result in the same value of K_I . Unfortunately, if stresses are sampled from the FEM results at various angular and radial locations, differing values of K_I are obtained. Because of this variation, an extrapolation technique along with a least squares curve fitting procedure must be used.

The first step is to design a finite element mesh which centers a radial fan on the crack tip. This mesh orientation provides many lines of constant θ on which the extrapolation technique can be used. After the finite element analysis is completed, the nodal stresses are post-processed and plotted along radial lines, as shown in Fig. 5.15. Note that in this figure the ordinate is $(\sigma_{xx} + \sigma_{yy}) \sqrt{r}$ and the abscissa is simply \sqrt{r} . It was found in Reference [16] that the sum of the normal stress components behave in a more predictable manner, so this technique was utilized here. The reason for plotting the stresses in this manner can be demonstrated by again rearranging Eq. 5.6 written as

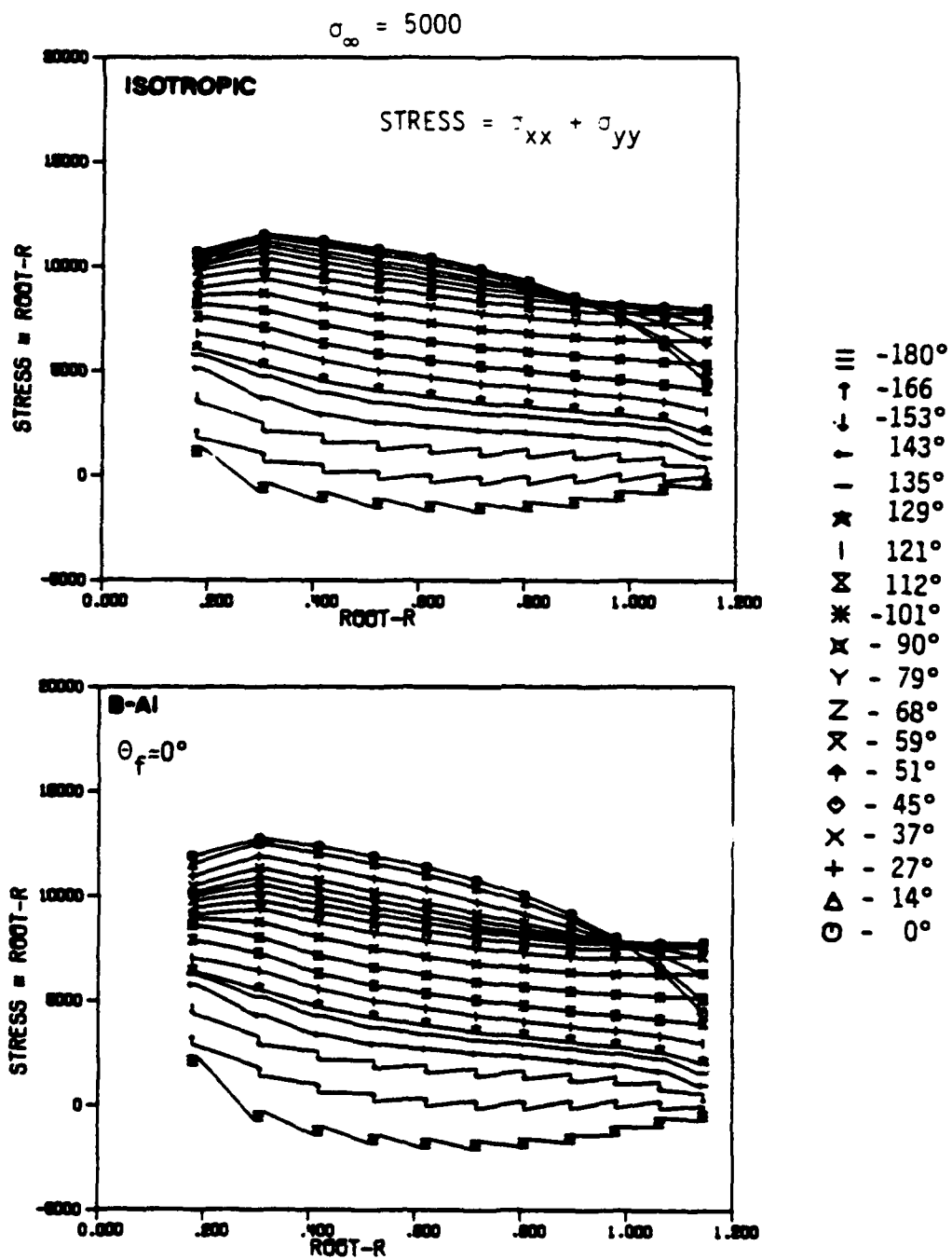


Figure 5.15 Stress distribution along 19 radial lines emanating from the crack tip of the transverse edge cracked panel.

$$\frac{K_I[f_{xx}(\theta) + f_{yy}(\theta)]}{\sqrt{2\pi}} = (\sigma_{xx} + \sigma_{yy}) \sqrt{r} \quad (5.8)$$

Since K_I is defined in the limit as the radial distance approaches zero, one can extrapolate the results in Fig. 5.15 for each radial line. In essence, each line is being extended to find its intercept with the y-axis. This is done in a least squares sense by curve fitting a straight line through each set of data points. Usually, the nodal stress closest to the crack-tip is excluded since it appears to be distorted. Now, for each of the nineteen (19) radial orientations, $(\sigma_{xx} + \sigma_{yy}) \sqrt{r}$ is obtained.

The next step is to use ELLPLAS to provide $f_{ij}(\theta)$. The advantage of utilizing ELLPLAS is that it can furnish $f_{ij}(\theta)$ for an orthotropic material as well as an isotropic material. Entering some value of K_I and multiplying by $f_{ij}(\theta)$, the left hand side of Eq. 5.8 can be calculated. K_I is now determined by using a least squares fit of the data provided in the previous exercise. The results for an isotropic and B-A1 edge-crack are illustrated in Fig. 5.16. It is interesting to note that the stress intensity factor K_I extrapolated for both cases was the same (17000 psi $\sqrt{\text{in}}$) and is probably due to the weak elastic anisotropy exhibited by B-A1.

It is apparent from the results presented that the energy method is the most accurate and simplest for finding K_I . Although it requires two analyses to be run, the post-processing of data is minimal and the results are very good. The stress component extrapolation technique was investigated as a means of determining the quality of the field

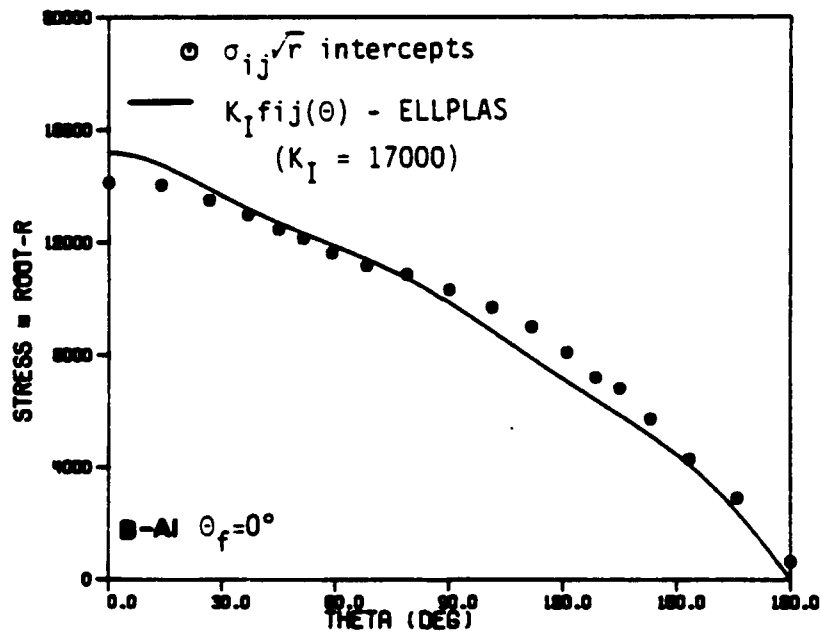
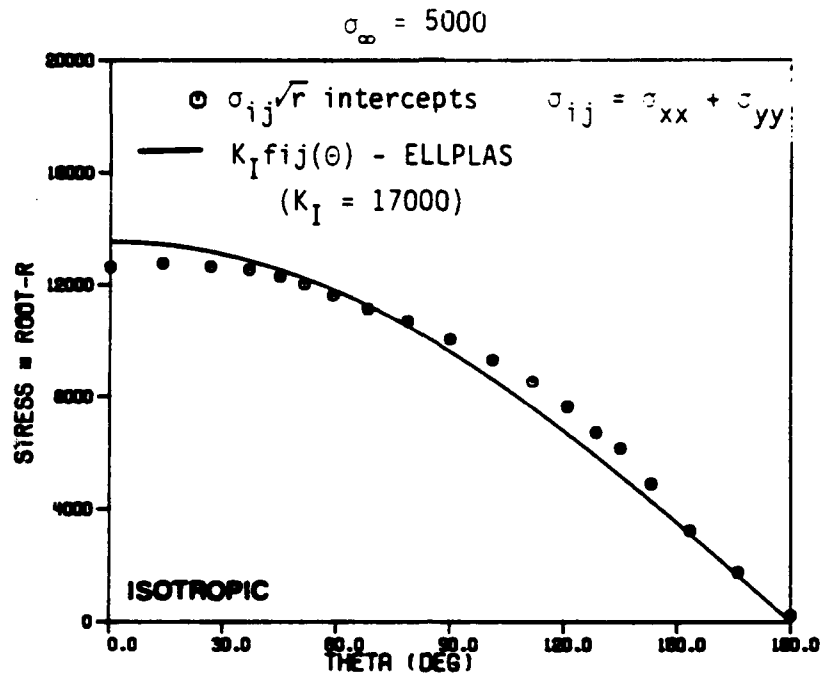


Figure 5.16 Stress Intensity Factor calibration plot. A least squares curve fit of $K_I F_{ij}(\theta)$ vs the 19 radial intercept values ($\sigma_{ij}\sqrt{r}$).

quantities for subsequent plasticity analysis. In general, the quality of these results is good.

ISOTROPIC ELASTIC-PLASTIC ANALYSIS OF AN EDGE CRACK

The isotropic elastoplastic behavior of an edge cracked panel was investigated to provide a benchmark solution from which orthotropic elastoplastic response can be compared.

A Study of Plastic Zone Growth

An isotropic elastic-plastic analysis of the transverse edge-crack was conducted. Work-hardening was expressed by the Ramberg-Osgood relationship discussed in the previous sections. The progression of the plastic zone is illustrated in Fig. 5.17. Note the distinctive lobe at about 60° , where the Von-Mises yield criterion [2] predicts the maximum extent of the plastic zone. Fig. 5.18 provides additional insight into the effective stress distribution and how it ultimately controls the plastic zone development. At a remote stress of 24,500 psi, the plastic zone has progressed more than halfway across the width of the specimen, indicating that large scale yielding is being considered.

The consequences of mixed mode loading on plastic zone growth investigated by the analysis of an oblique crack illustrated in Fig. 5.19. The remote loading is uniaxial, but shear stresses are now introduced along the plane of the crack. The plastic zone progression illustrated in Fig. 5.20 demonstrates a significant departure from the transverse crack behavior. The effective stress contours in Fig. 5.21 substantiate the qualitative plastic zone representation. Considering the previously discussed analogy which relates plastically deformed

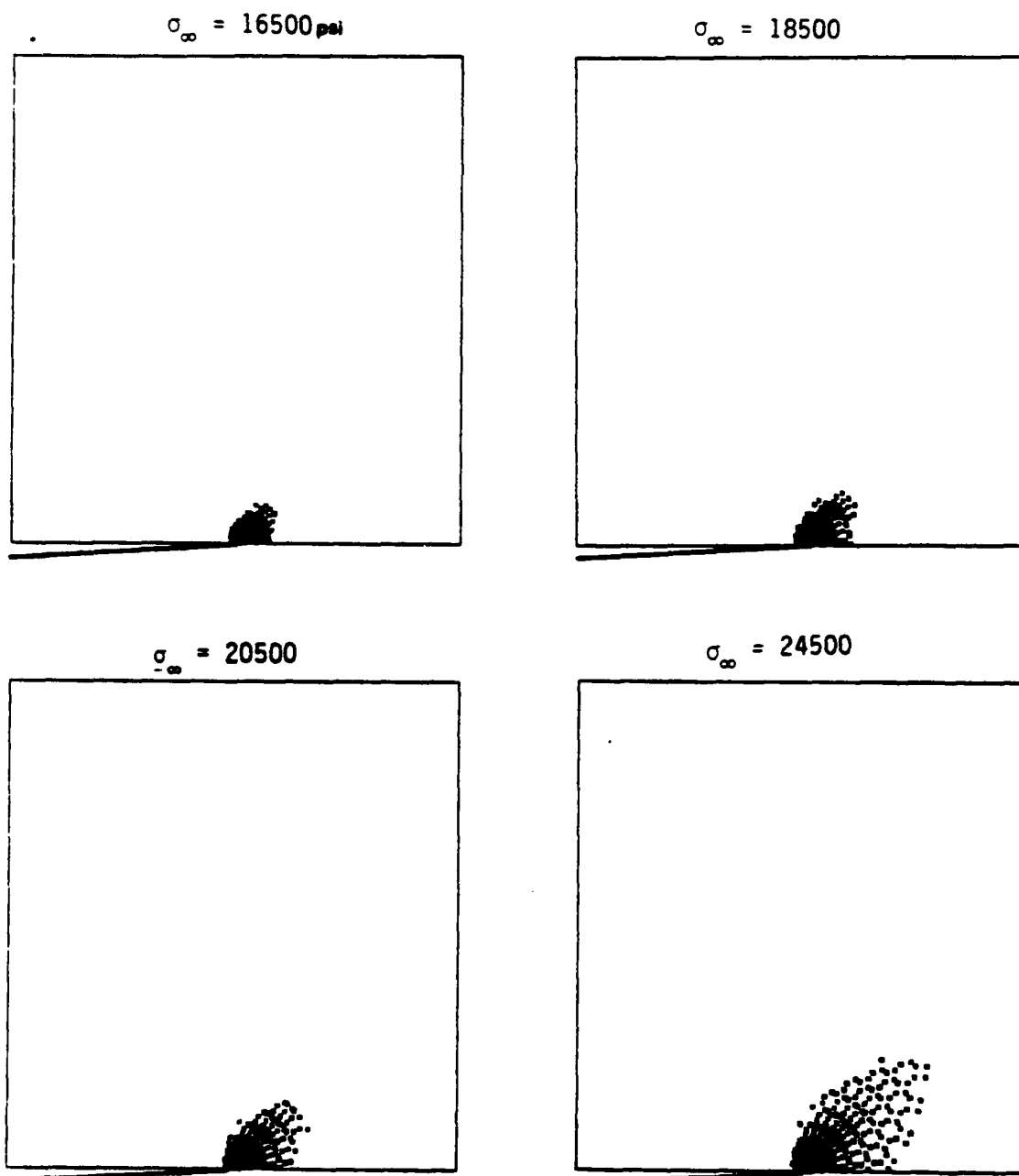


Figure 5.17 Plastic zone growth for an isotropic edge-cracked panel subjected to elastic-plastic loading.

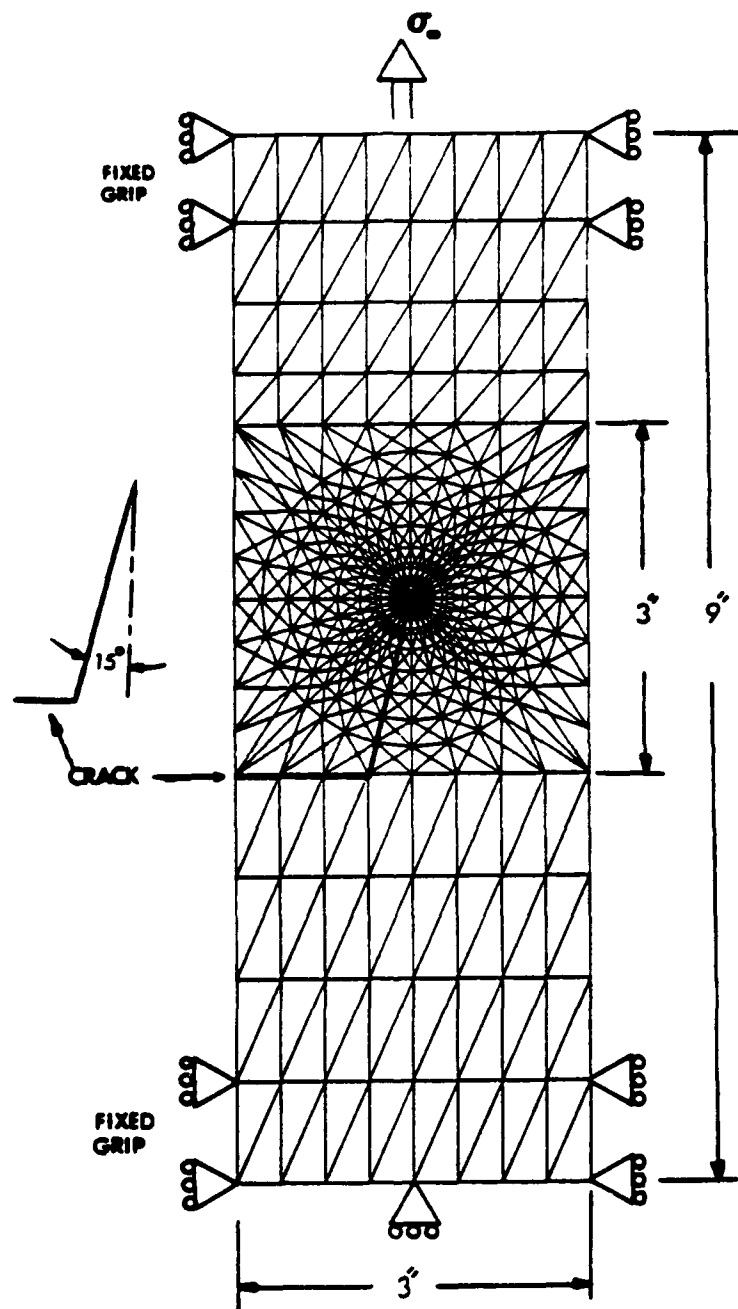


Figure 5.19 A finite element mesh of an oblique edge-cracked panel subjected to uniaxial loading and fixed grip end conditions.

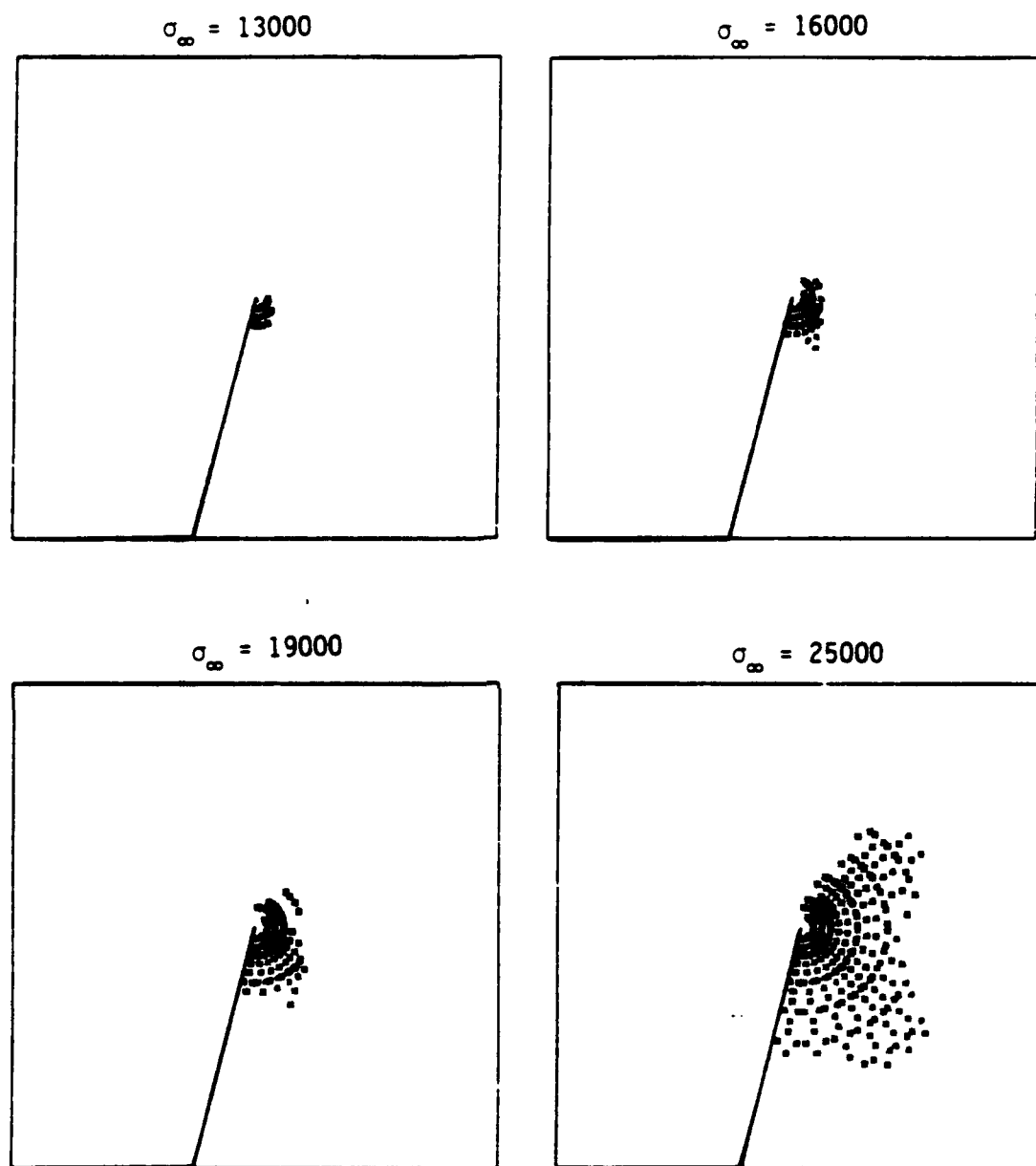


Figure 5.20 Plastic zone growth for an isotropic oblique edge-cracked panel subjected to elastic-plastic loading.

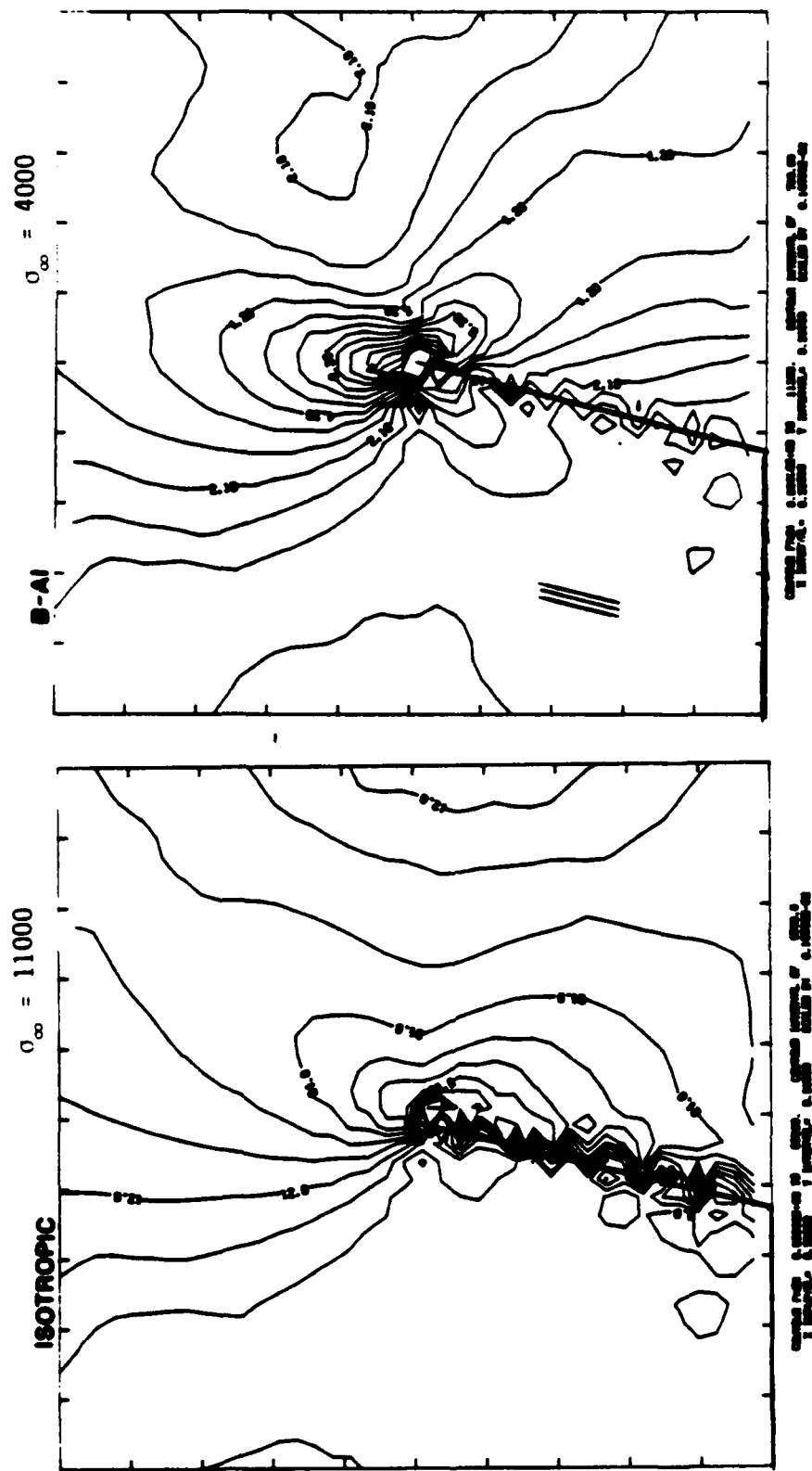


Figure 5.21 Effective stress contours for the oblique edge-cracked panel at the onset of yielding.

material to damage initiation, it is clear that under cyclic loading the oblique crack will tend to turn and propagate horizontally, which has been observed in the laboratory [28].

The Effect of a Remotely Applied Transverse Stress

In most practical applications the remote loading is rarely uniaxial. For an elastic analysis of a crack perpendicular to a remote uniaxial load, classical LEFM suggests that the addition of a remote load parallel to the crack will not contribute to K_I . In a superficial manner, this suggests that a transverse biaxial loading will have no effect on fracture or fatigue crack propagation. If plasticity is considered, then a transverse remote stress will change the character of the problem.

Three different ratios (χ) of transverse to axial load were applied to the transverse edge cracked model. The axial (s_{yy}) remote stress was used to gauge the load incrementation and the transverse stress (s_{xx}) was added simultaneously in the stated proportion. Three sets of plastic zones progressions are illustrated in Fig. 5.22.

The lowest level of transverse loading ($\chi = 0.5$) results in a change in both size and shape of the plastic zone in comparison to the purely uniaxial remote loading. The effect of the remote biaxial stress appears to be a flattening of the 60° lobe. At a remote load of 7500 psi, the plastic zone for the uniaxial case is more than halfway across the width of the net cross-section, but for the transverse loading cases ($\chi = 0.5$ and $\chi = 1.0$) it is visibly reduced.

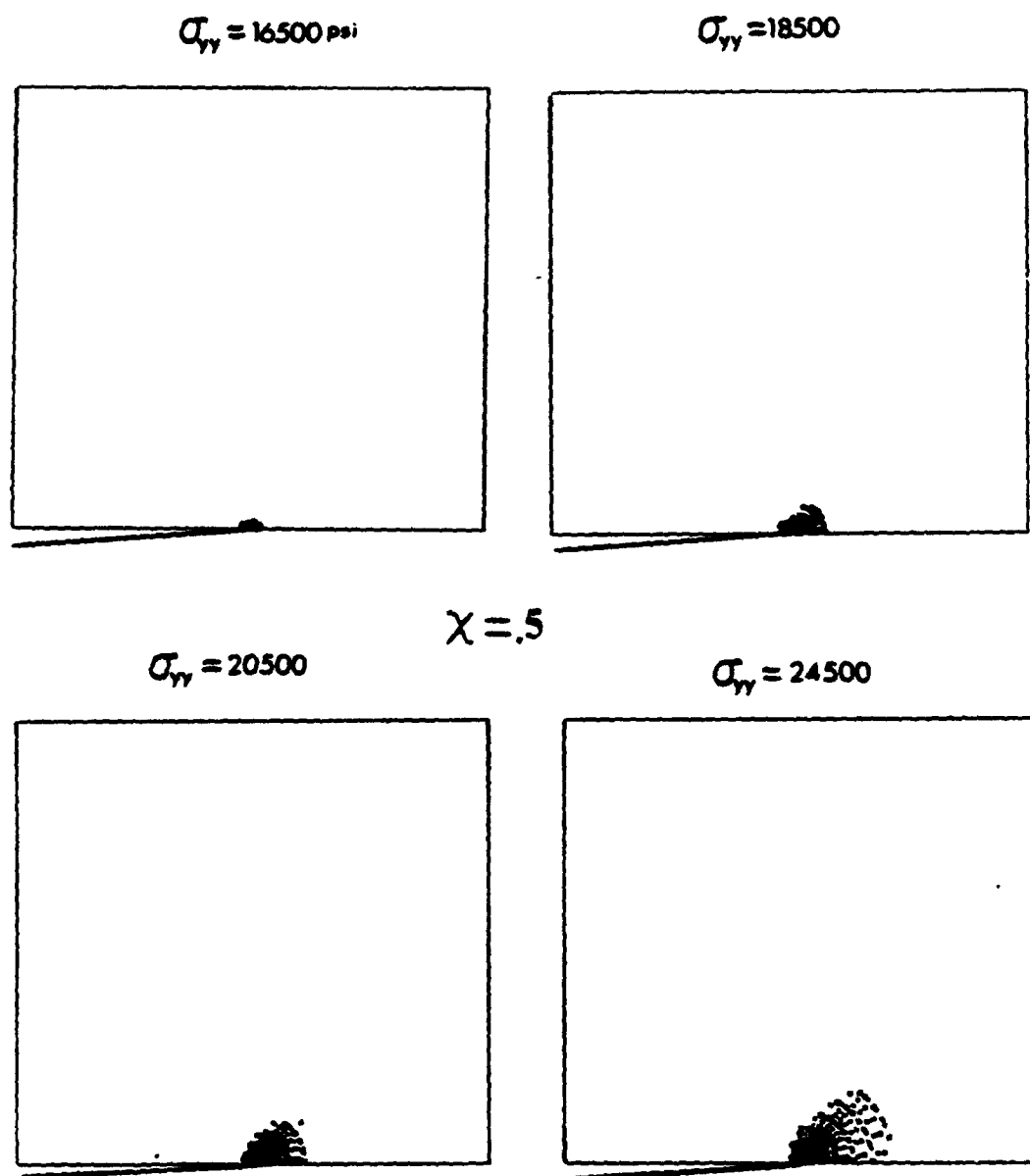


Figure 5.22 Plastic zone progression for an isotropic transverse edge-cracked panel subjected to proportional biaxial remote loading.

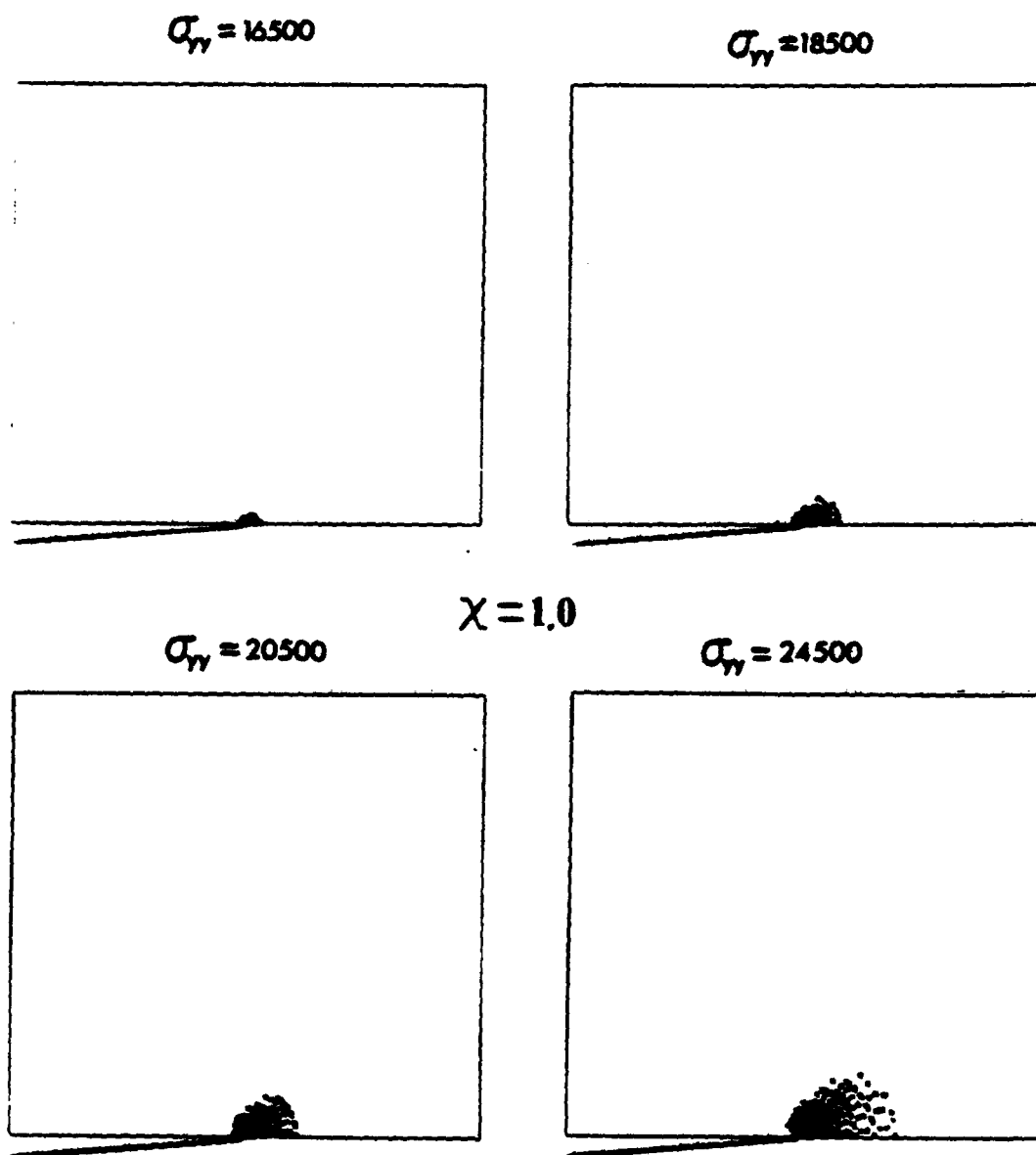


Figure 5.22 continued

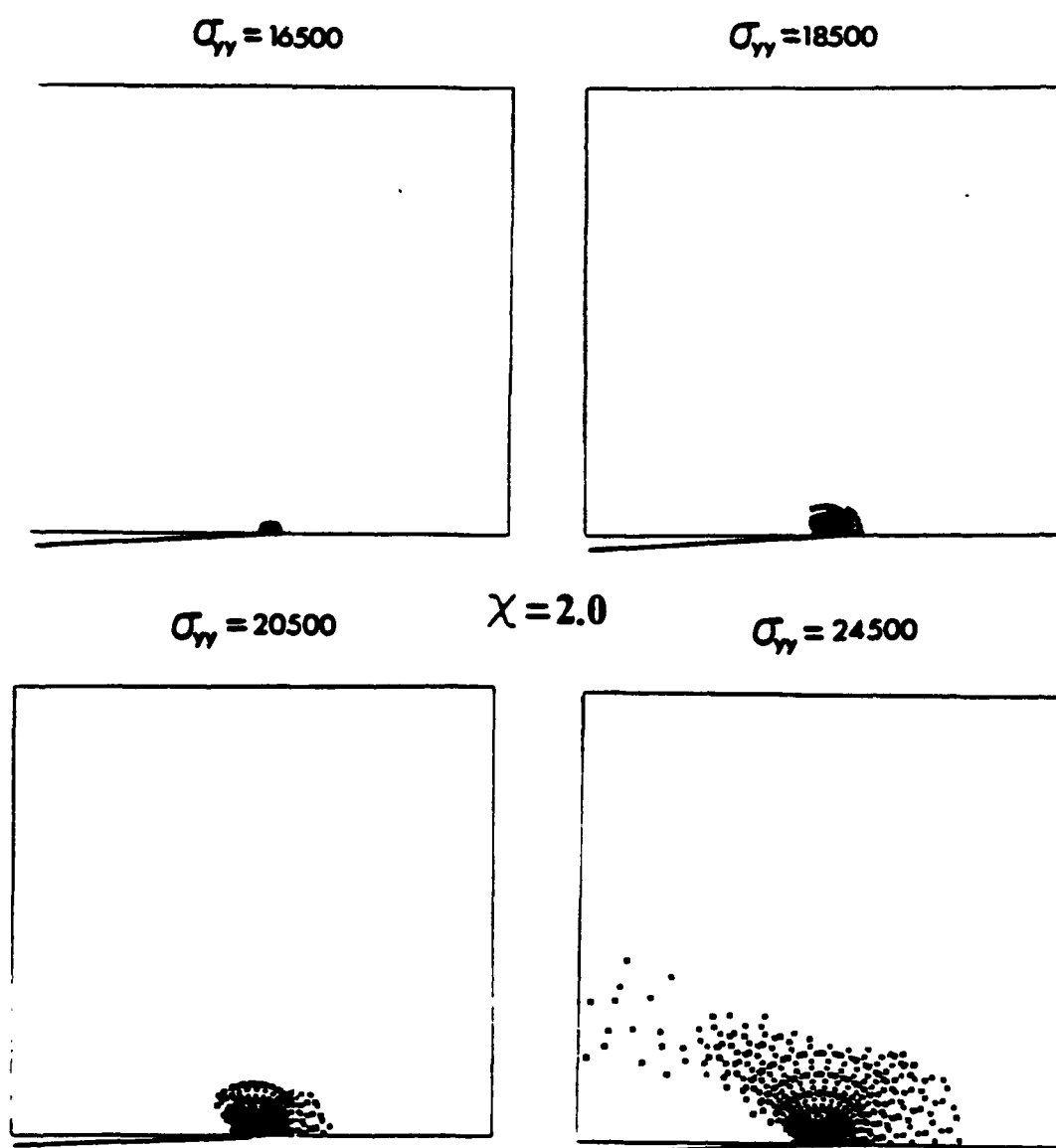


Figure 5.22 continued

This behavior is related to the shape of the isotropic yield locus. If yield has been reached for a purely uniaxial stress, the application of a transverse load results in a translation inside the yield surface, and an unloading to an elastic state. For the edge crack analysis, the biaxial loading is proportional, but a similar reduction in yielding is observed with respect to the uniaxial remote load.

The maximum transverse remote loading ($\lambda = 2.0$) demonstrates significantly different plastic zone progression. The transverse load appears to have completely dominated the Mode I component of the plastic zone. The crack tip acts as a concentration which initiates yielding, but the transverse loading quickly induces net section yielding.

It has been demonstrated that the plastic zone is significantly altered due to a transverse remote load. Therefore, it is reasonable to assume that transverse loading will in turn have an impact on fracture and fatigue behavior.

A Study of Unloading and the Resulting Residual Stresses

The transverse edge cracked specimen was loaded into the elastic-plastic regime to a remote load of 21000 psi and then unloaded. This unloading was conducted in an incremental manner to allow the yielded material to become elastic again. Indeed, after a very small unloading increment, the entire panel (all elements) becomes elastic, until the last unloading increment where a few elements in the vicinity of the crack tip re-yield.

The elastic material which surrounds the plastic zone compresses the permanently deformed material upon unloading. The outcome of this compressing action results in residual stresses, especially near the crack tip where the plastic strains are the greatest. Fig. 5.23 presents the residual stress distribution for the above unloading case and a 1.35 overload followed by unloading. In both cases, the classical compressive stress (σ_{yy}) is present in the near vicinity of the crack tip. It is the compressive residual stress component which is thought of as retarding any subsequent fatigue crack propagation.

ORTHOTROPIC ELASTIC-PLASTIC ANALYSIS OF AN EDGE CRACK

The effect of anisotropy was considered in the analysis of the edge cracked panel to gain a better understanding of the differences from isotropic behavior.

The Effect of Anisotropy on Plastic Zone Growth

The progression of the plastic zone in an orthotropic (B-A1) elastoplastic transverse edge cracked panel was investigated. The plastic zone visualization is presented in Fig. 5.24 for the case where the fibers are parallel and perpendicular to the crack. The elastic effective stress contours are plotted in Fig. 5.25. As was the case for the isotropic edge crack, large scale yielding was considered.

The results for the transverse crack parallels the elastoplastic analysis of a sheet with a circular hole. The plastic zone shape for the isotropic material and B-A1 ($\theta_f = 0^\circ$) are similar, while for $\theta_f = 90^\circ$ a significant departure is observed. With the fibers perpendicular to the crack the majority of plastic deformation occurs in a vertical band directly above the crack tip. Unlike the circular hole, a small

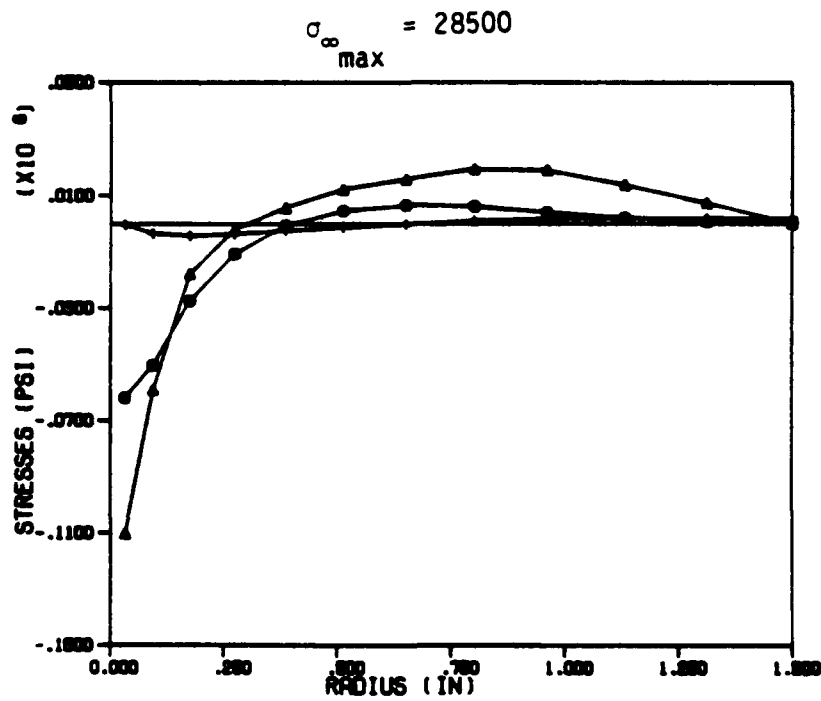
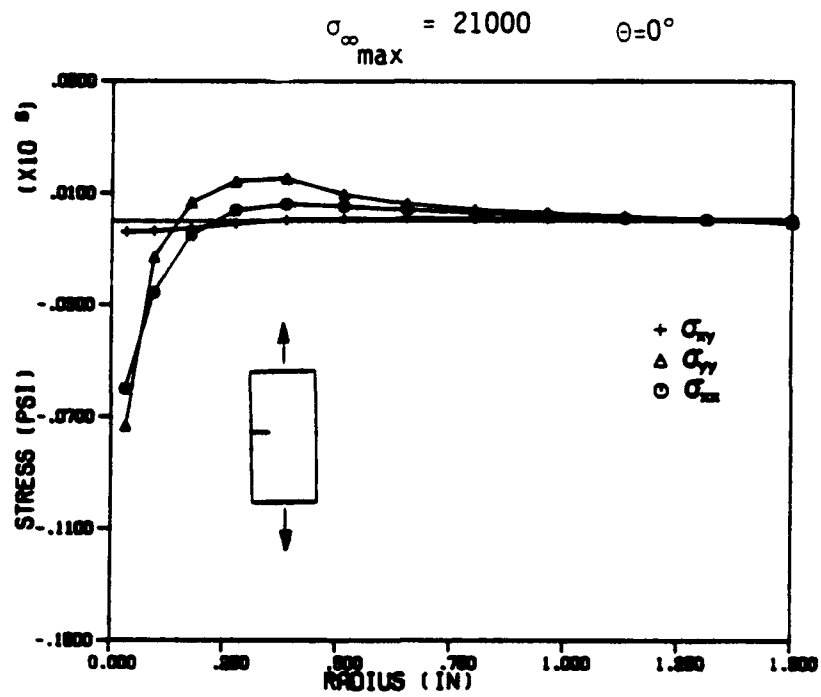


Figure 5.23 ANPLAST residual stress distribution following unloading for an isotropic transverse edge cracked panel.

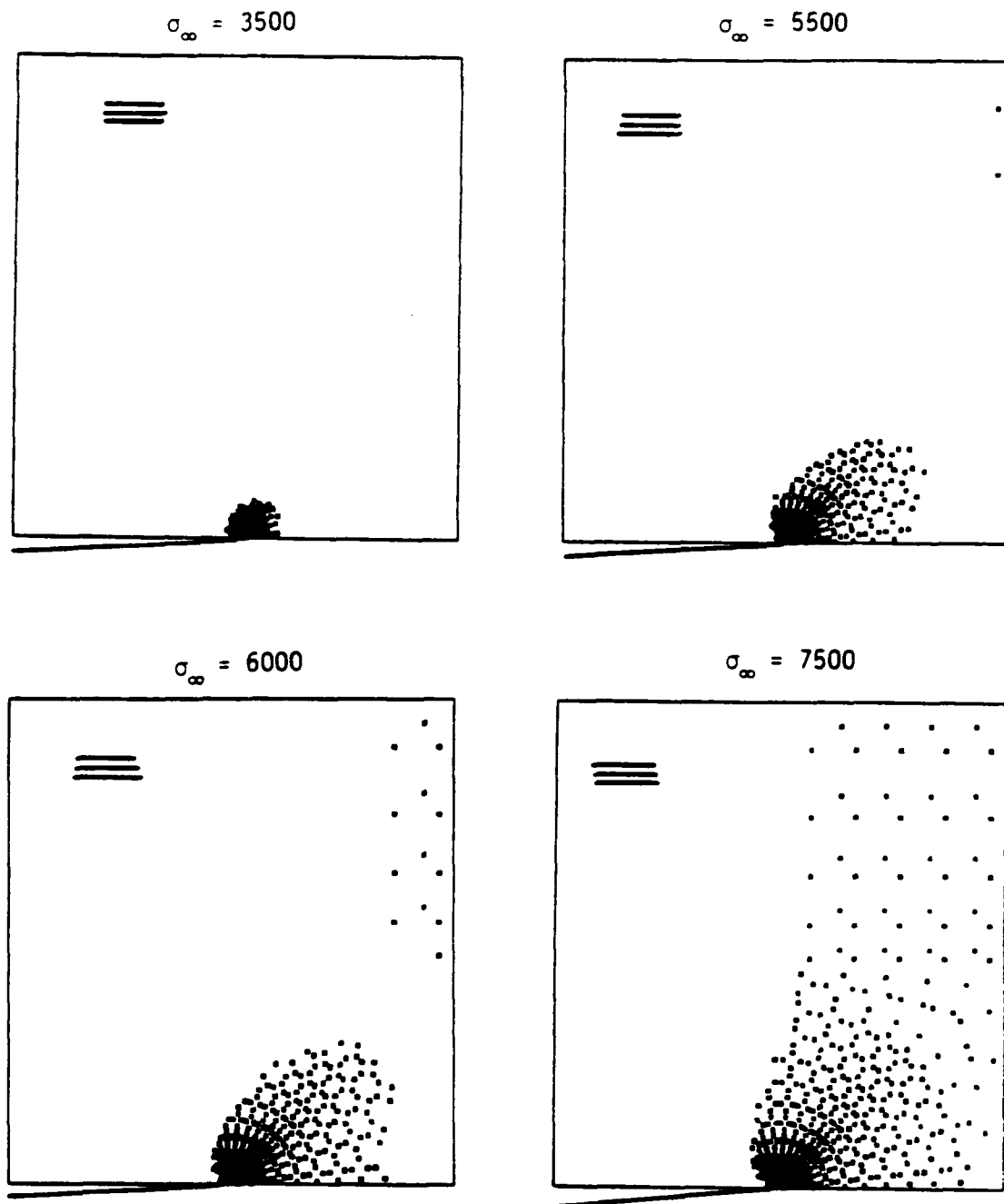


Figure 5.24 Plastic zone growth for an orthotropic B-Al transverse edge-cracked panel subjected to elastic-plastic loading.

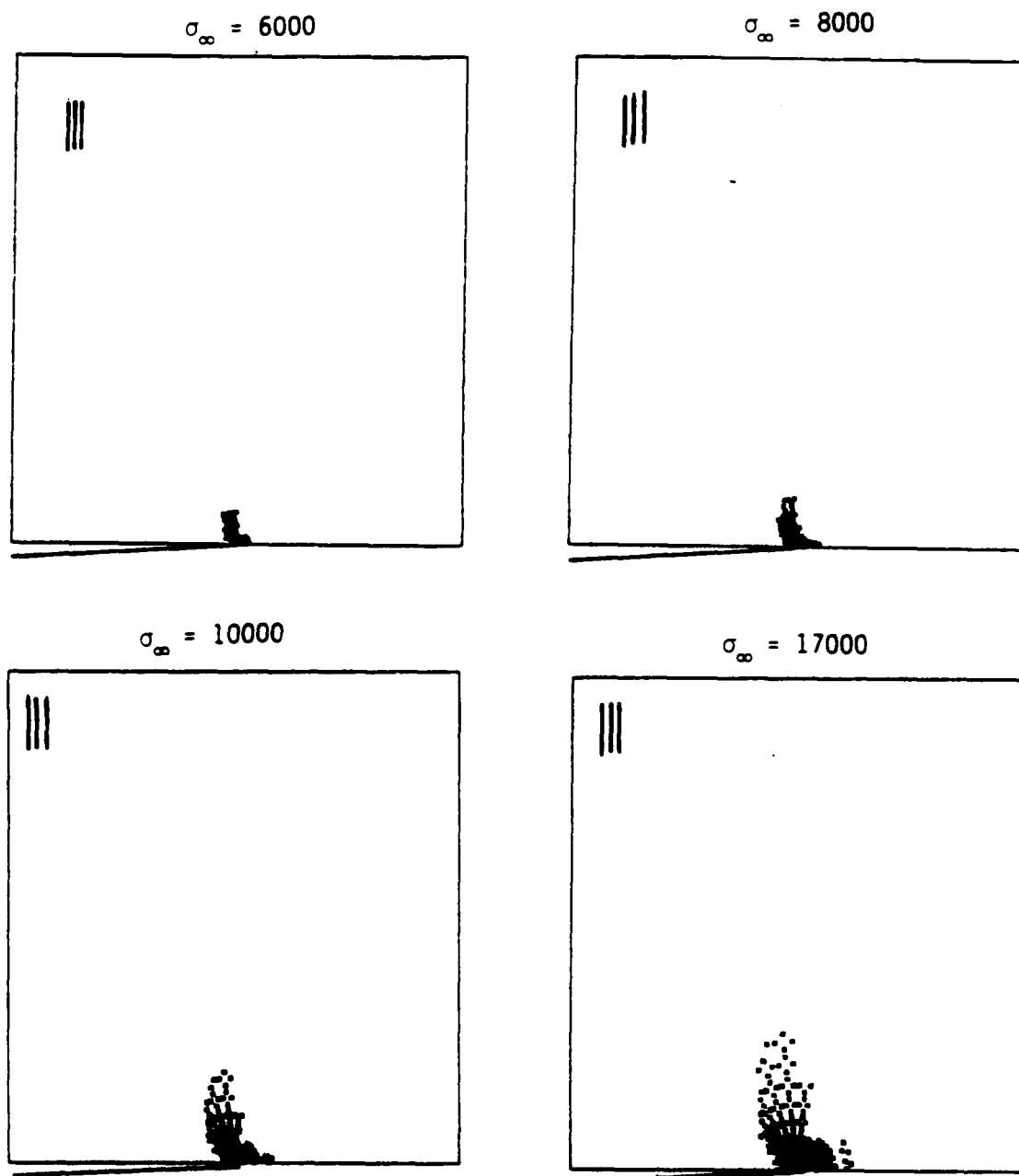


Figure 5.24 continued

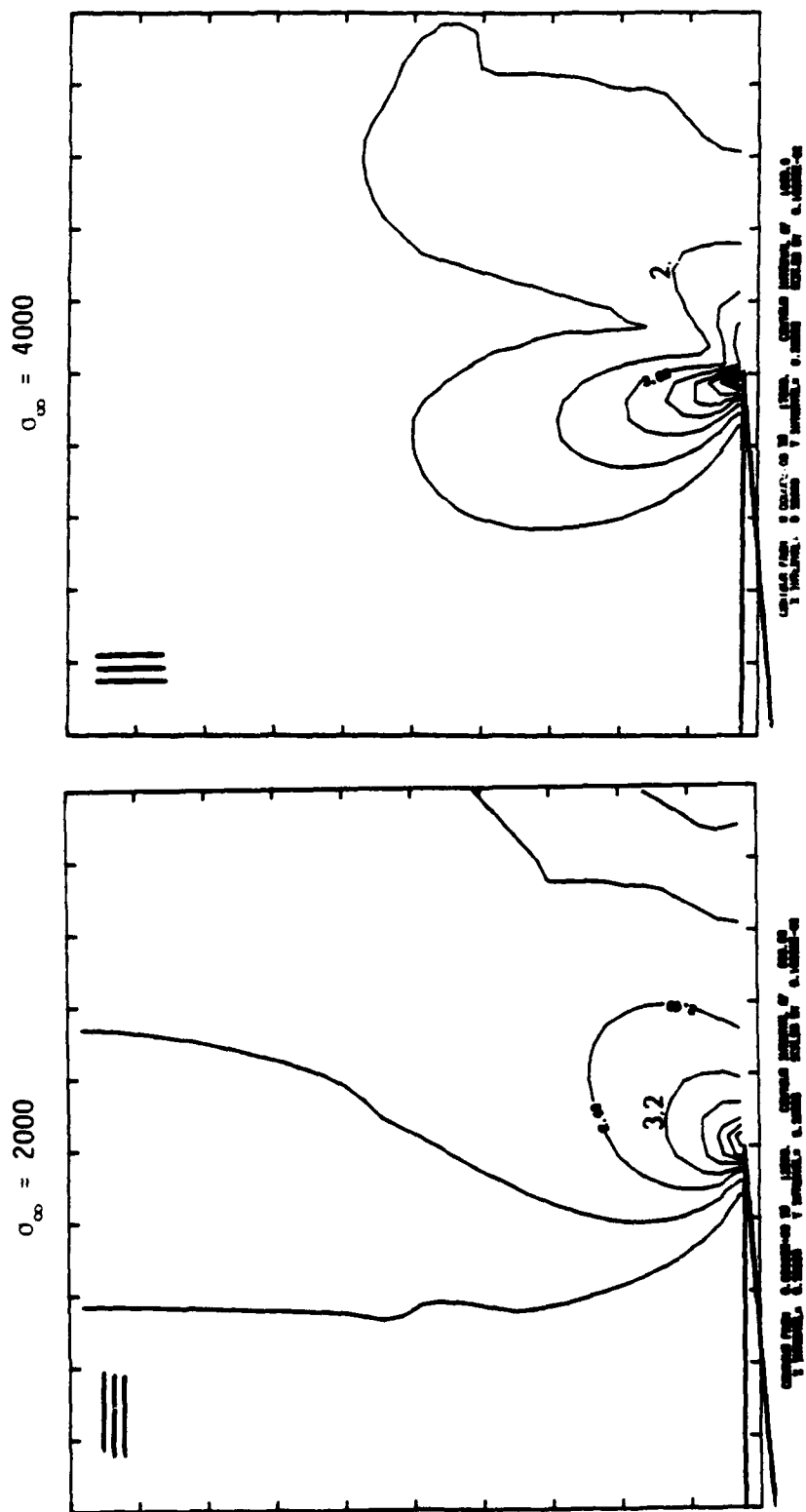


Figure 5.25 Effective stress contours of an orthotropic B-Al transverse edge-cracked panel at the onset of yielding.

area of permanent deformation is present in front of the crack tip.

The oblique crack model was also analyzed to investigate plasticity effects in B-Al under a mixed mode loading. Fig. 5.26 illustrates the growth of the plastic zone for the case where the fibers are running parallel to the crack. The results are significantly different from those observed for the isotropic case. The B-Al plastic zone tends to produce two lobes: one directly in line with the crack tip (parallel to the fibers) and another at 120° in a clockwise orientation.

These results again support the assumption that under cyclic loading, plastically deformed material represents a likely sight for further crack initiation. It has been observed in the laboratory [12] for B-Al edge cracked specimens that fatigue crack propagation proceeds parallel to the fibers, which is consistent with Fig. 5.26.

The Effect of a Remotely Applied Transverse Stress

The consequences of a remotely applied transverse stress on a B-Al edge cracked panel was studied. The analysis parallels the study for the isotropic panel, except the transverse to axial load ratios (χ) were 1.0, 2.0, and 4.0 respectively. The plastic zone visualizations are presented in Fig. 5.27. Only the case of the fibers parallel to the crack ($\theta_f = 0^\circ$) is analyzed.

The plastic zone progression for all load ratios demonstrates that the transverse loading has almost no effect on plastic deformation. Both the shape and relative magnitude of these plastic zones are unaltered. This behavior can be explained if one considers the anisotropy induced by the fiber orientation. The predominant stress

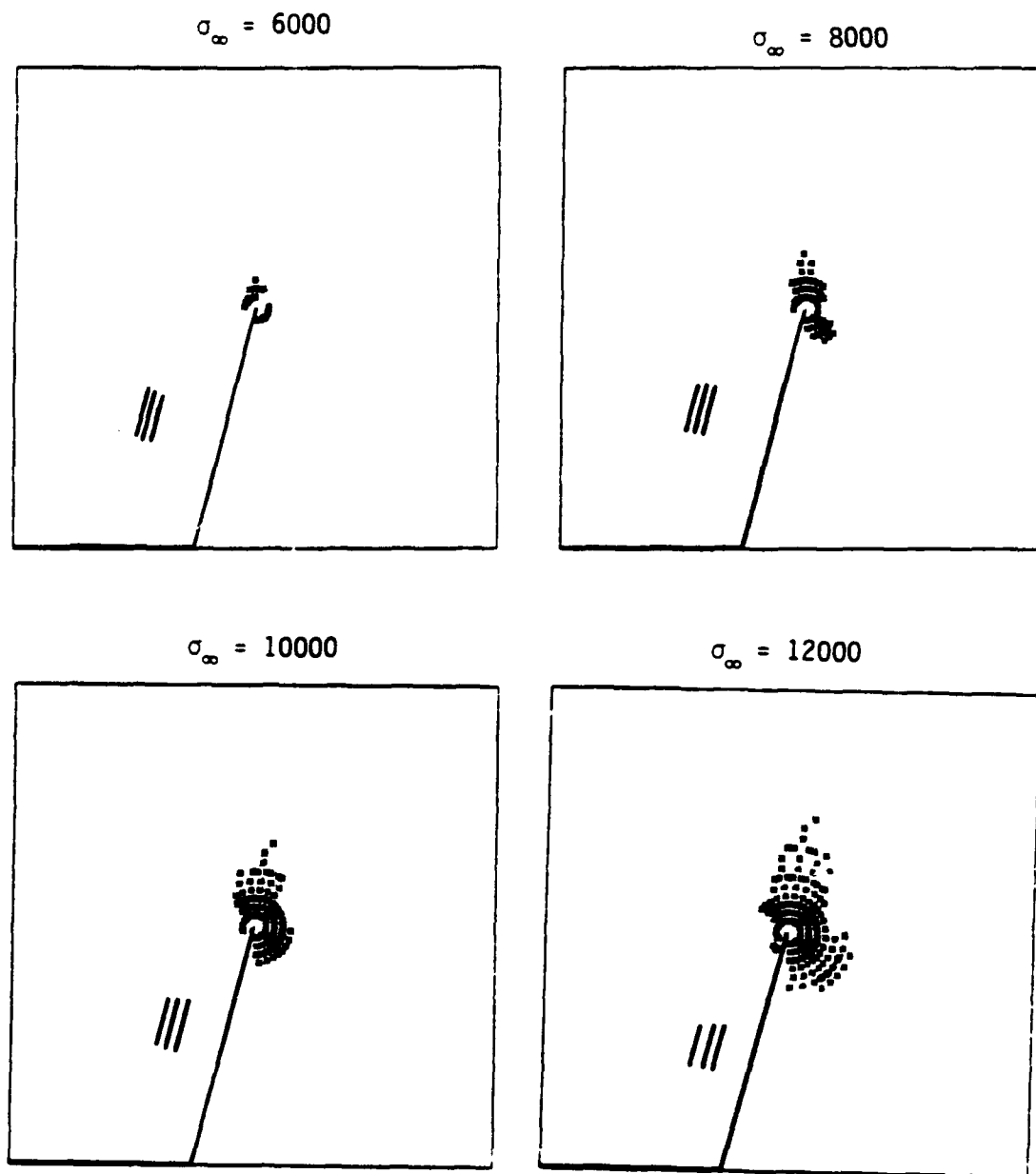


Figure 5.26 Plastic zone growth for an orthotropic B-Al oblique edge-cracked panel subjected to elastic-plastic loading.

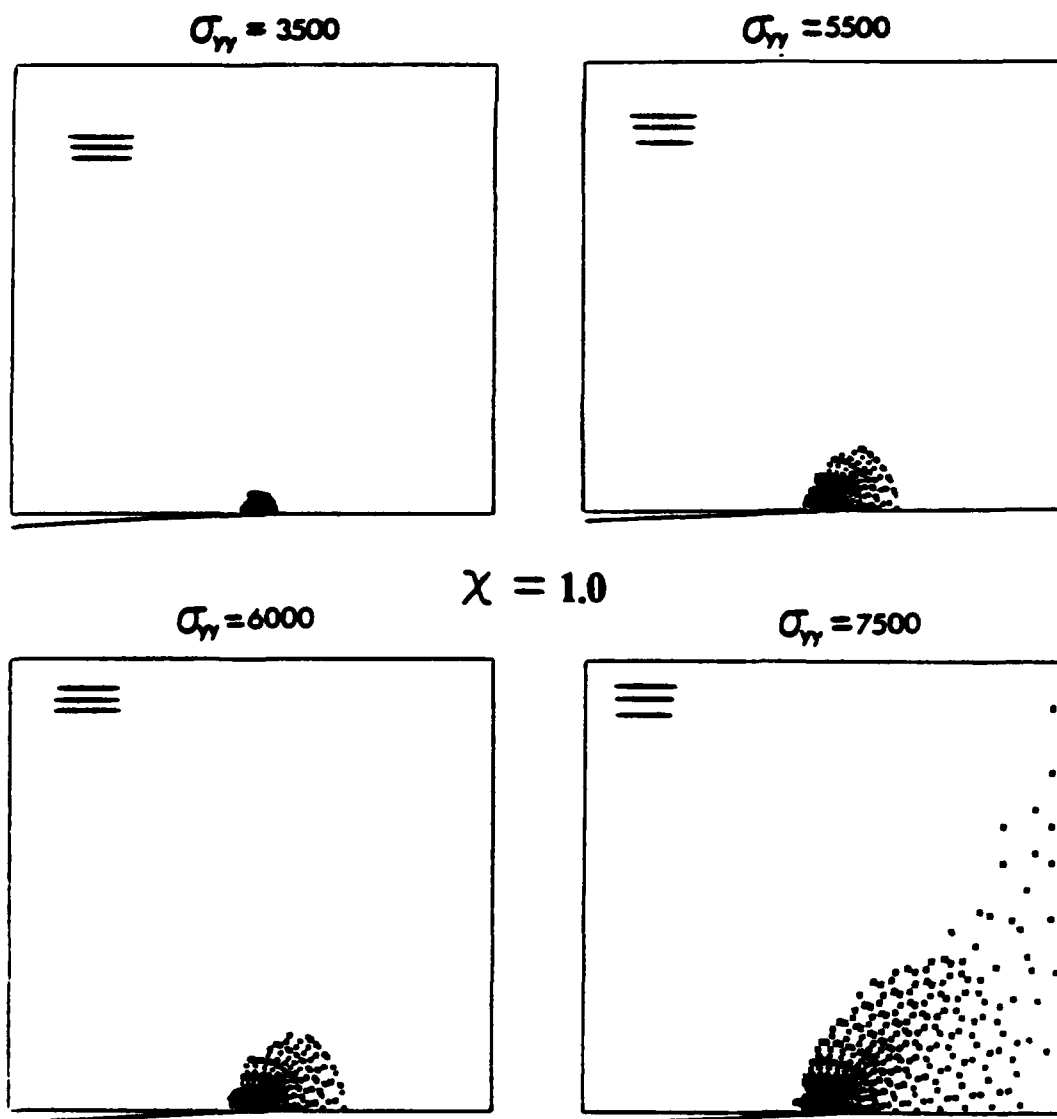


Figure 5.27 Plastic zone growth for an orthotropic B-Al transverse edge-cracked panel subjected to proportional biaxial remote loading.

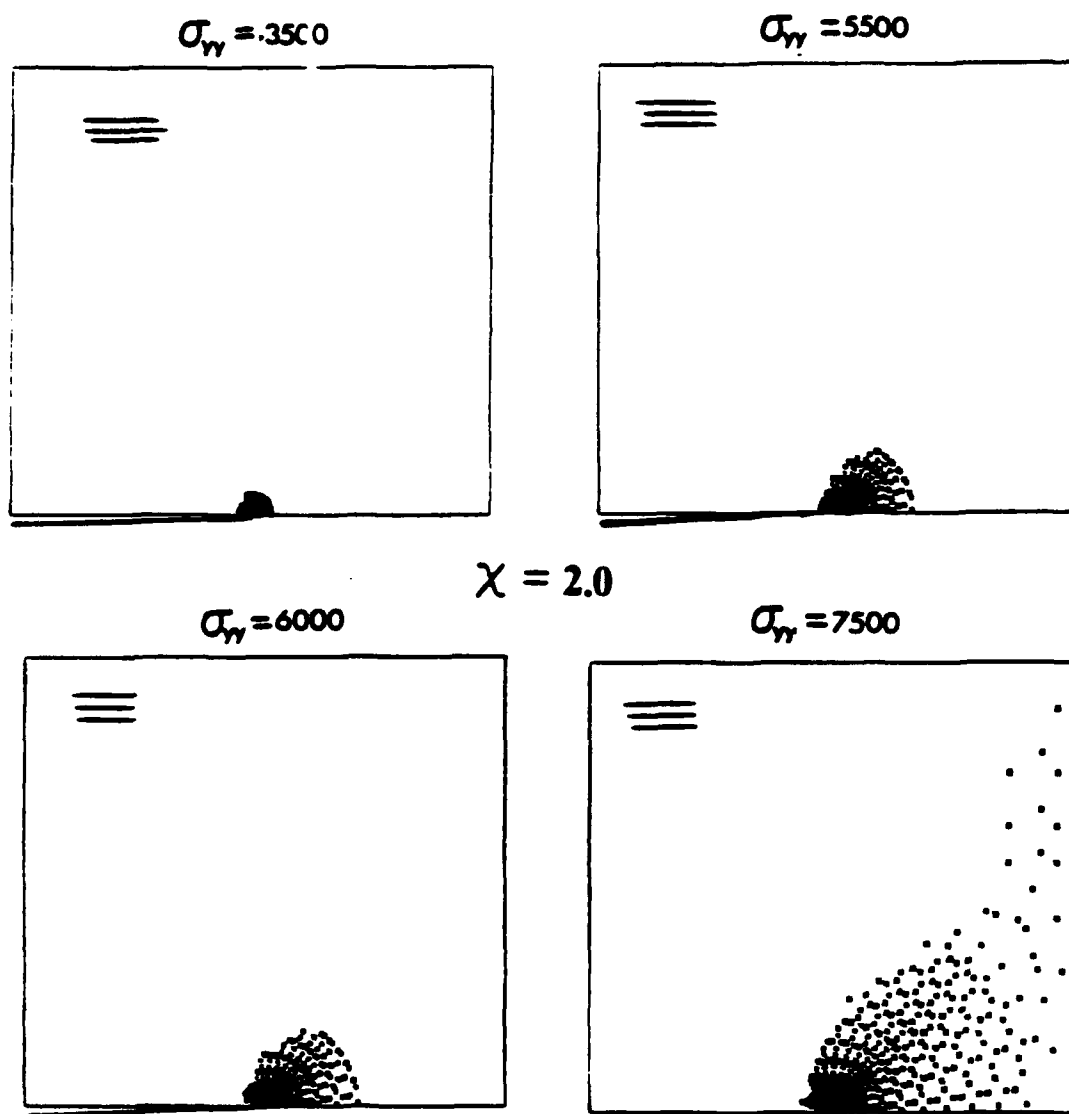


Figure 5.27 continued

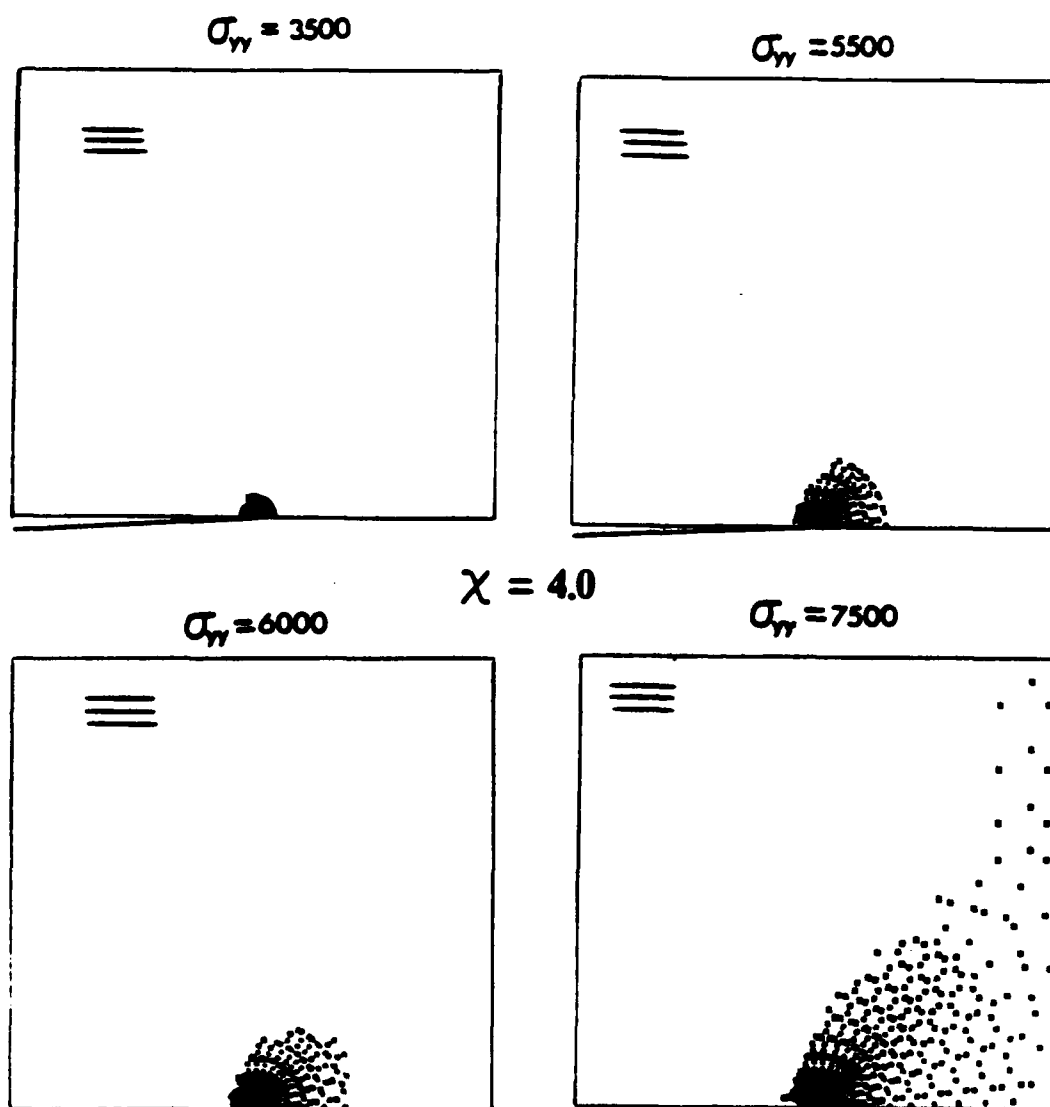


Figure .27 continued

induced by the transverse load, $s_{xx}(\sigma_{11})$, is multiplied by the plasticity coefficient r_{11} in the effective stress calculation. Since r_{11} is only 0.001 for B-Al, the transverse stress has almost no effect on yield.

One location where the plastic zone does appear to be affected is towards the fixed grip location. Here, the transverse stress has the effect of unloading a few elements due to the tilt of the yield locus as was discussed for the isotropic material. In any case, one can state with some authority that transverse loading will not strongly influence fracture or fatigue of a B-Al edge cracked specimen with this particular material orientation.

A Study of Unloading and the Resulting Residual Stresses

The B-Al edge cracked panel was subjected to two separate load excursions. The residual stress distributions are plotted in Fig. 5.28. The results exhibited are almost identical to the isotropic examples. Rather large compressive stresses can be found in the vicinity of the crack tip, with σ_{yy} dominating in both cases.

Again, the classical line of thinking is that residual compressive stresses tend to inhibit further fatigue crack propagation. Therefore, one can conclude that any deviation from classical retardation for orthotropic plastic materials is not a stress related phenomenon.

A Look at the Crack Opening Profile

It has been suggested [26] that the crack opening displacement (COD) can be used as a nonlinear fracture mechanics parameter for elastic-plastic materials. It is assumed that the displacement profile of the crack is related to the state of deformation in the

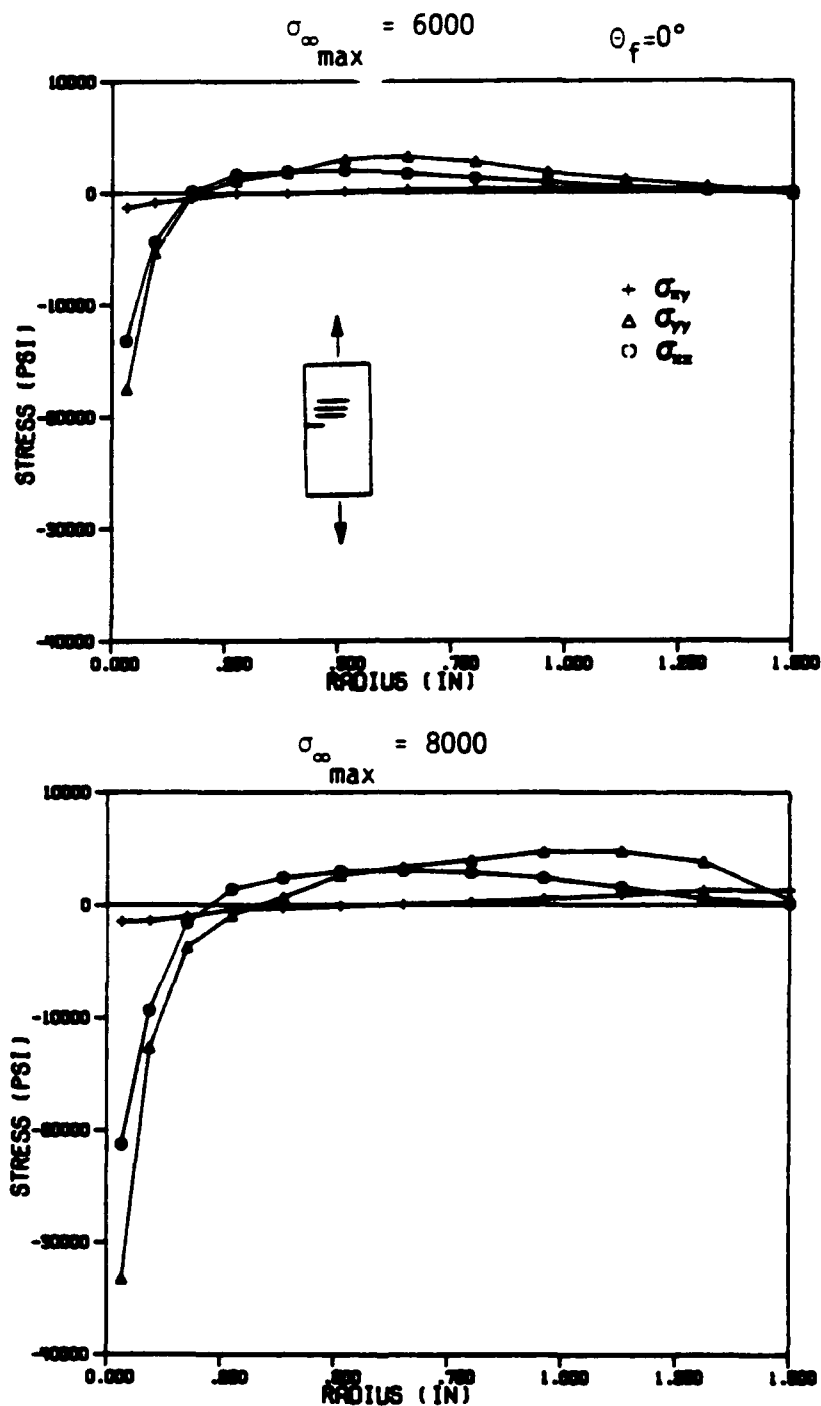


Figure 5.28 ANPLAST residual stress distribution following unloading for an orthotropic B-A1 transverse edge-cracked panel.

vicinity of the crack tip, yet independent of the particular specimen geometry. The advantage of this technique is obvious to the experimentalist. The crack opening displacement is relatively easy to measure and does not require the sophisticated instrumentation necessary when trying to obtain near field stresses and strains.

The crack opening profiles for the isotropic and B-Al ($\theta_f = 0^\circ$, 90°) edge cracked analyses are presented in Fig.5.29. Three sets of profiles are plotted; elastic loading, elastic plastic loading, and complete unloading. For the elastic and elastic-plastic loading cases, all of the profiles have approximately the same shape, with only small deviations occurring a small distance from the tip. The unloading profiles demonstrate a much stronger contrast in shape. The peak value of displacement is different with respect to the crack opening. This indicates that while the near tip displacement is approximately proportional to crack opening during monotonic loading, the amount of elastic-plastic near tip recovery is not.

It should be noted that the triangular fan which is centered about the crack tip is experiencing a large amount of deformation due to the discontinuity in geometry. It is likely that a single linear displacement element is not adequate to represent this large gradient. Therefore, the resulting displacement spike is not realistic, and any errors in displacements near the tip will have an additive effect.

The consequences of these findings have not been fully developed. It may turn out that these particular profiles can be related to a crack closure phenomenon [29], as illustrated by the contrast of the isotropic and B-Al ($\theta = 0^\circ$) profiles after unloading. It has been

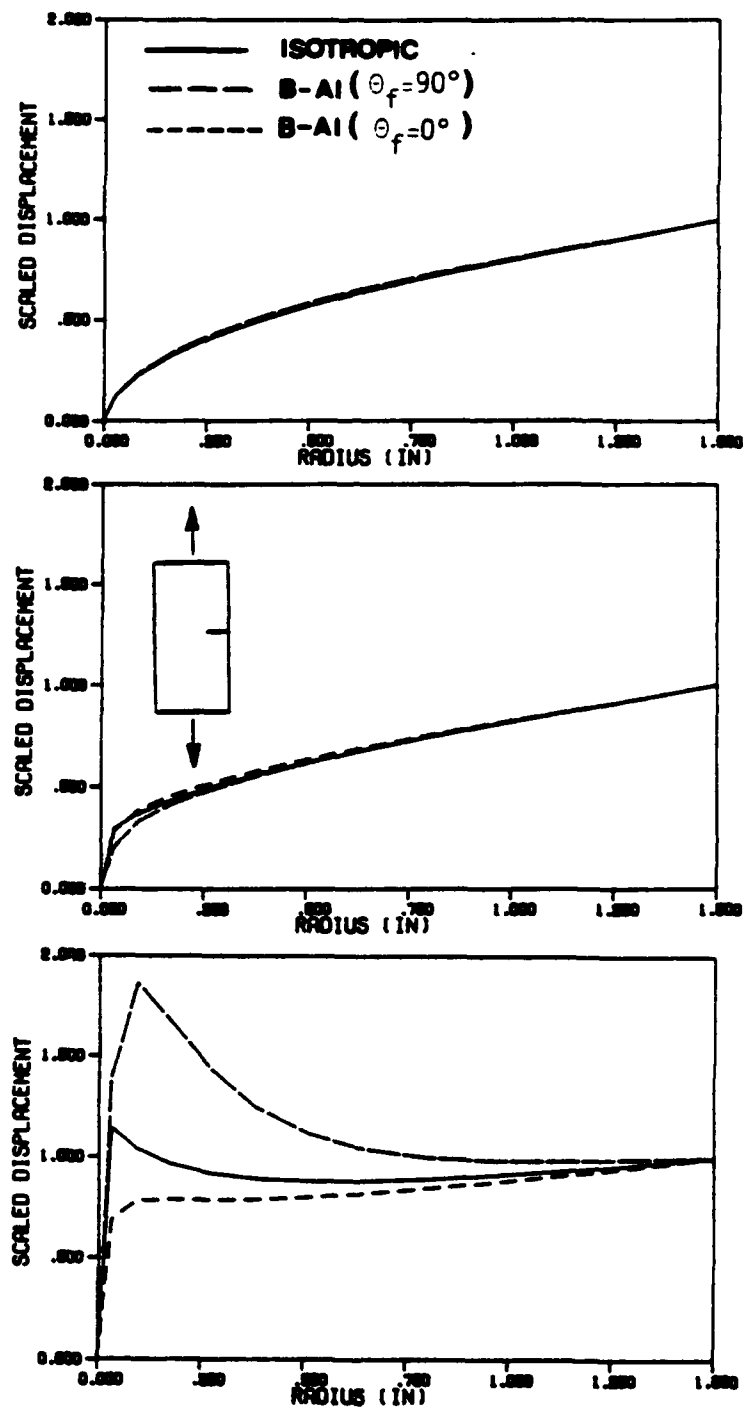


Figure 5.29 Crack opening profiles for a transverse edge-cracked panel under uniaxial remote loading. Note that the displacements are normalized by the outer edge displacement.

observed in the laboratory [12], that retardation effects in B-Al ($\theta = 0^\circ$) edge cracked panels are minimal in comparison to isotropic specimens of the same geometry. It could be proposed that the lack of a "dipping" of the B-Al profile negates any contact with the opposite face upon unloading which could produce the crack closure effect. But, before any firm conclusions could be proposed, additional research would be required.

Comparison to Experimental Results for a Continuous Fiber Reinforced Metal Matrix Composite

An experimental study of the elastoplastic response of a unidirectional Boron-Aluminum metal matrix composite edge cracked panel was conducted by D. Kenaga [12] and S. Rizzi [24]. This particular study involved testing both a transverse and oblique edge cracked specimen, as illustrated in Fig. 5.30. Multiple strain gage recordings were taken in the vicinity of the crack tip. The finite element meshes used to analyze these test specimens are the same as for the other fixed grip analyses, except the dimensions were scaled to those of Fig. 5.30.

The tests were run by first cycling the load to produce a distinct crack, then applying the strain gages. The specimens were cycled again until the crack tip propagated to the vicinity of the first strain gage. The strain gages were then zeroed and a monotonic overload applied. The ANPLAST analyses incorporates monotonic loading to the maximum stress.

The results for the gage nearest the crack tip along the plane of the crack was presented in Fig. 5.31. In both cases the finite

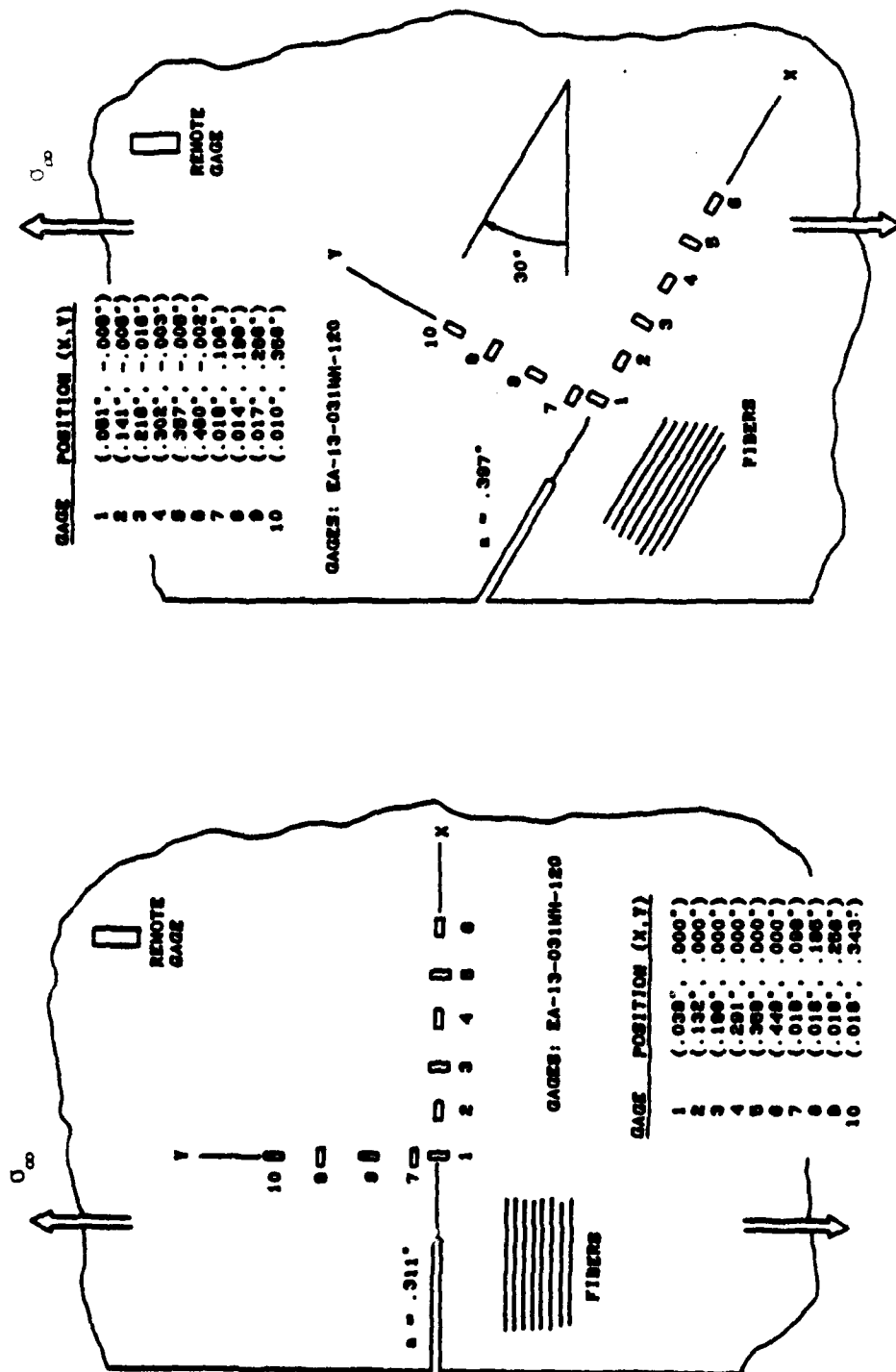


Figure 5.30 Geometry of edge cracked test specimens used by Kenaga [12] for the experimental determination of the stress-strain behavior of a B-A1 metal matrix composite.

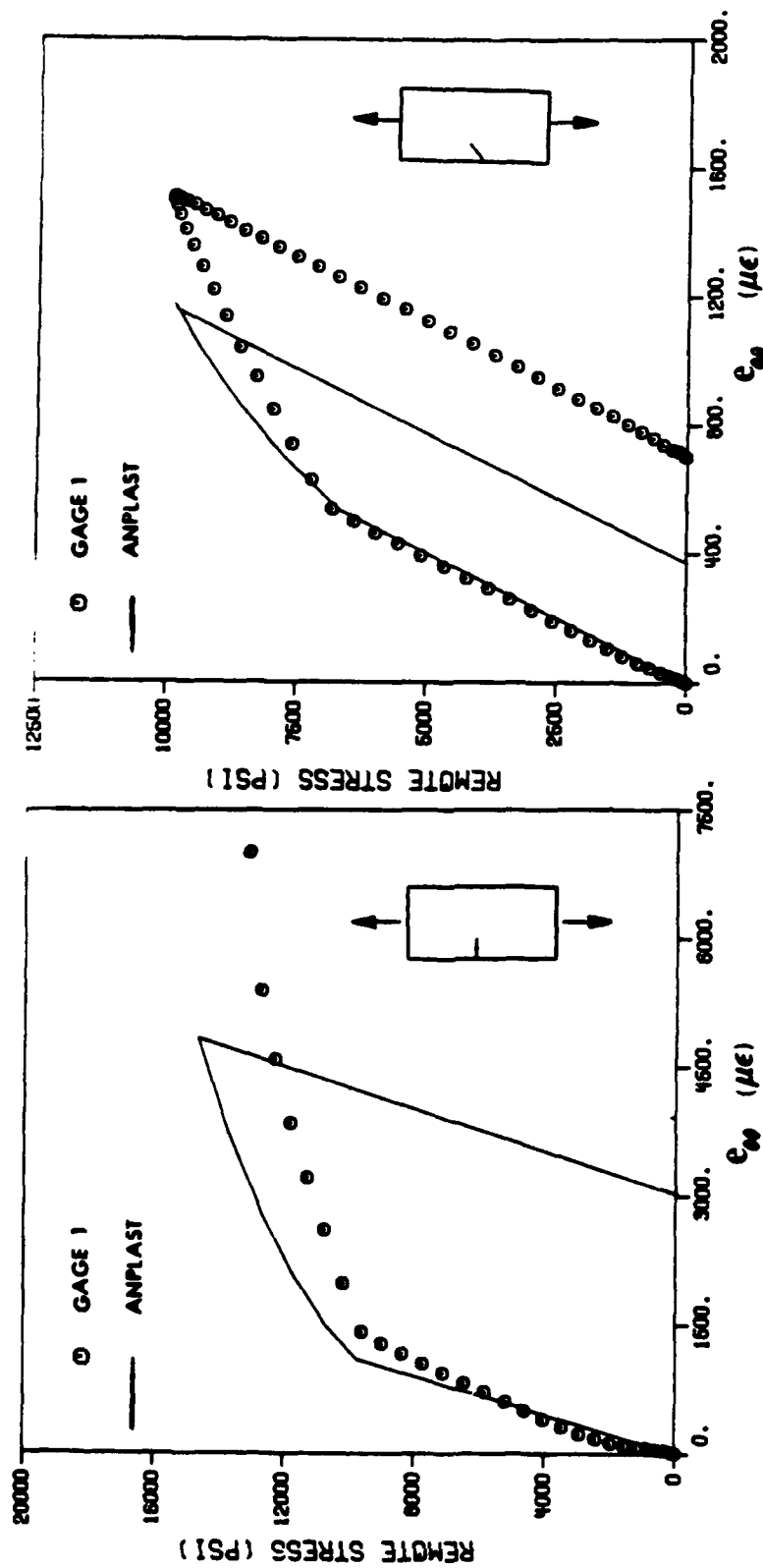


Figure 5.31 Comparison of ANPLAST strains with the experimental results of Kenaga [12] and Rizzi [24] for a B-A1 panel with a transverse and oblique edge crack.

element results overestimate the amount of work-hardening measured. It is apparent that the cyclic loading prior to the overload changed the elastoplastic material properties of the B-Al. Obviously, some type of damage has been induced into the B-Al microstructure by the cycling of the load which softens the resulting plastic work-hardening.

The material properties used in ANPLAST to analyze these problems were derived from monotonically loaded uniaxial specimens with no prior load conditioning. If a more representative analysis were required, then the appropriate elastic and plastic material parameters would have to be obtained from similarly damaged test specimens. Another possibility would be to represent the material properties as a function of damage level and incorporate this in the material characterization. Of course, further research would be necessary before this approach can be judged feasible.

SECTION 6 STUDY OF LAMINATED ELASTOPLASTIC MATERIALS

INTRODUCTION

Thin sheets of material are often layered (or laminated) together to obtain a composite which exhibits superior performance. While elastic analyses of laminated structures have been thoroughly studied, only recently have elastic-plastic materials been considered [30,31]. The purpose of this chapter is to extend the previous research on homogenous anisotropic elastoplastic materials and combine it with the incremental lamination theory. Then, utilizing the previously developed computational tools, the complex behavior of various laminated structures will be explored.

In this section, the global behavior of a laminate consisting of isotropic elastoplastic layers is first investigated utilizing the LAMINATE program. A laminate composed of orthotropic layers is also

analyzed and comparisons drawn to the isotropic example. The ANPLAST finite element program is used to analyze a laminated plate with a circular hole, for both isotropic and orthotropic layer construction.

ELASTIC-PLASTIC LAMINATE BEHAVIOR: ISOTROPIC LAYERS

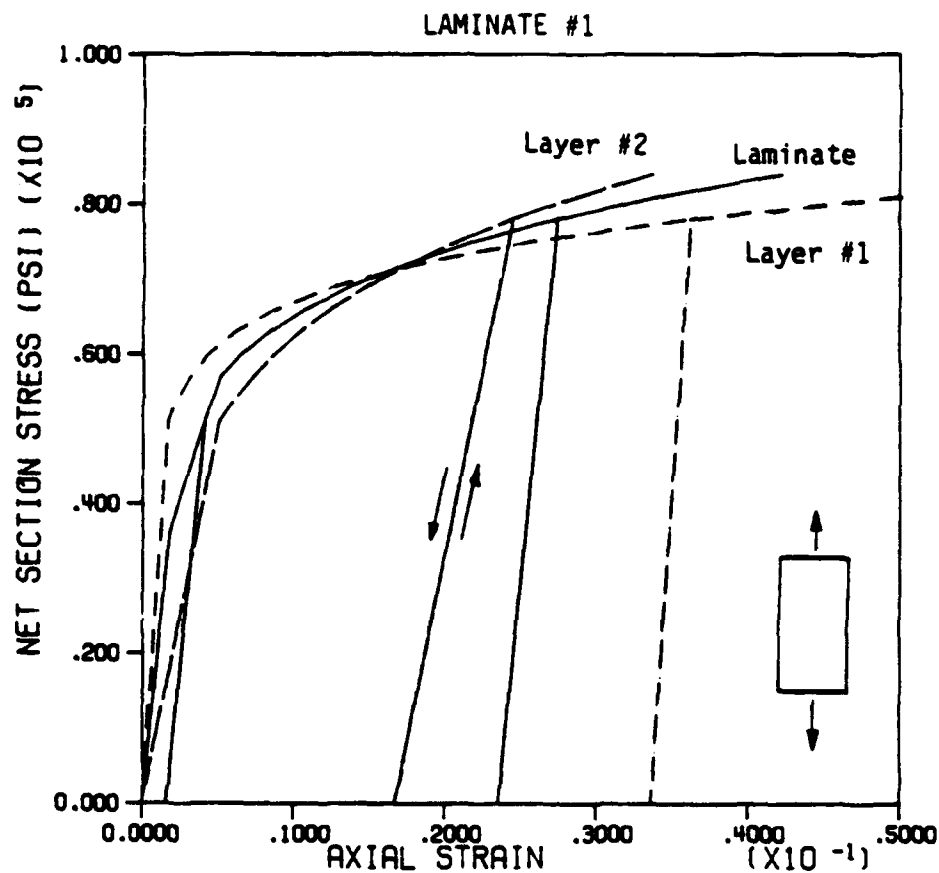
The global response of a laminate consisting of isotropic elastic-plastic layers was studied. Uniaxial and multiaxial behavior was investigated using LAMINATE.

Global Response Due to Uniaxial Loading and Unloading

The uniaxial response of a laminate consisting of two isotropic elastic-plastic materials was analyzed, and the results are illustrated in Fig. 6.1. The elastoplastic material properties chosen resemble what one might find for a typical steel and aluminum alloy. The work-hardening behavior is assumed to be of the Ramberg-Osgood type. Though the analysis requires only two distinct layers, at least 4 laminae would be required for symmetric behavior.

The uniaxial response of the base materials was also included to reinforce the concept that global laminate behavior is a superposition of individual layer response. The first indication of this averaging effect is the two distinct break points for the laminate. The laminate first experiences yield at less than 40,000 psi. This behavior is due to the mismatch in elastic material properties. Layer #1 being three times stiffer than Layer #2, it carries a significantly greater proportion of the remote laminate loading. Therefore, it approaches yield at a much greater rate than does a specimen consisting of a single layer. Unloading is also included to demonstrate that permanent deformation is present after the initial yield. It is interesting to note that after the initial yield, the slope of the stress-strain response is nearly constant. This is due to the dominance of elastic stiffness contribution of Layer #2.

At approximately 57000 psi, Layer #2 yields and the entire laminate becomes elastic-plastic. The global stress-strain response now becomes non-linear due to the contribution of each lamina's non-linear work-hardening law. It is apparent that the laminate response



Layer #1

$E = 30 \times 10^6$ psi
 $\sigma_y = 50000$ psi
 $\epsilon = .30$
 $n = 9$

Layer #2

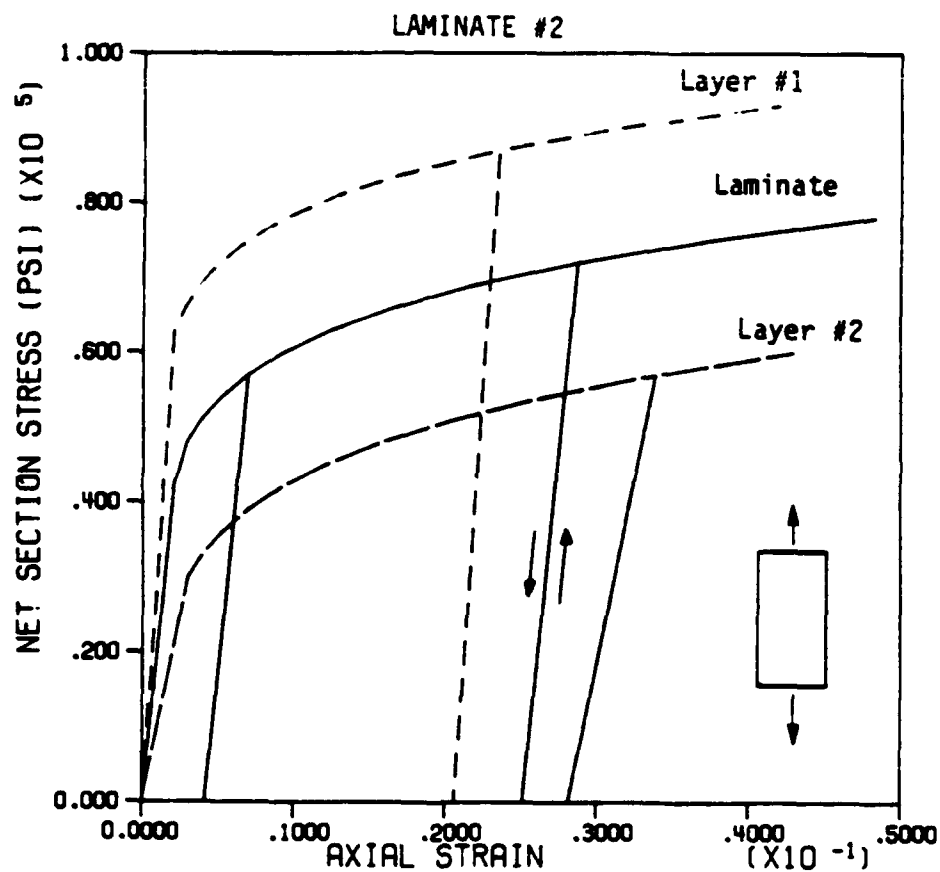
$E = 10 \times 10^6$ psi
 $\sigma_y = 50000$ psi
 $\epsilon = .30$
 $n = 7$

Figure 6.1 Uniaxial load-deformation response of an isotropic laminate (Laminate #1).

tends to average the response of the individual layers. The laminate was unloaded again to demonstrate the resulting permanent deformation.

The effect of changing the layer material properties on global laminate response was studied next. The elastic material properties are unchanged from the previous example, only the uniaxial yield stresses for each material was changed. Layer #1 is now assumed to have a yield stress twice the value of Layer #2. This change in material properties does not alter the general behavior of the laminate, as illustrated in Fig. 6.2. It is apparent that the elastoplastic stress-strain response of the base materials are more disperse, yet the laminate tends to average the responses. The initial yield still occurs in Layer #1 (steel alloy) due to the elastic disparity, but is soon followed by yielding in Layer #2 (aluminum alloy). Note that both laminate yield points occur completely between the base material yields. The laminate yield points for the previous example straddled the individual material yields, i.e., one higher, one lower.

The ratio of axial to transverse stresses within each layer is presented in Fig. 6.3. The presence of a transverse stress in each lamina is due to the mismatch of the contractural strain contribution in each layer. During the elastic loading range, the mismatch is directly associated to the difference of the Poisson ratios. After Layer #1 has yielded, this mismatch becomes even more pronounced due to the contribution of the plastic Poisson ratio, which in this case is $\frac{1}{2}$. When both layers have become elastic-plastic, the tendency is for the transverse stress to become negligible as axial loading is continued.



Layer #1

$E = 30 \times 10^6$ psi
 $\sigma_y = 60000$ psi
 $\beta = .30$
 $n = 9$

Layer #2

$E = 10 \times 10^6$ psi
 $\sigma_y = 30000$ psi
 $\beta = .30$
 $n = 7$

Figure 6.2 Uniaxial load-deformation response of an isotropic laminate (Laminate #2).

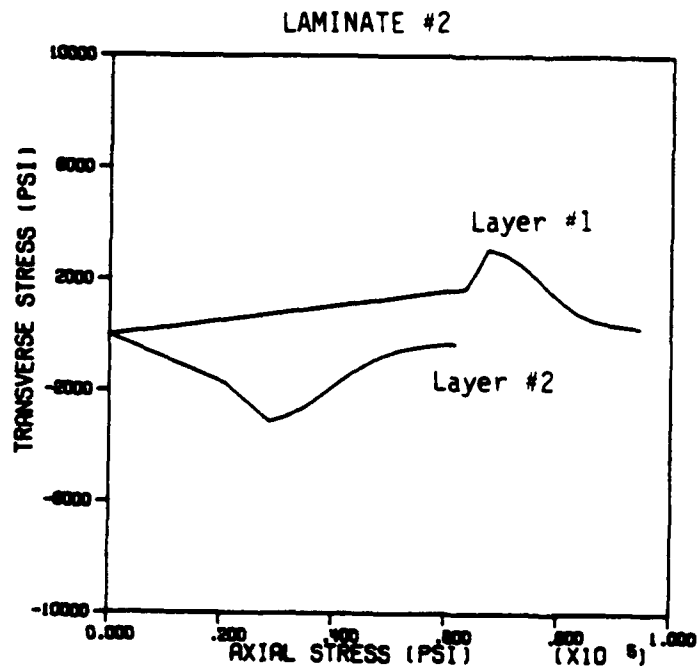
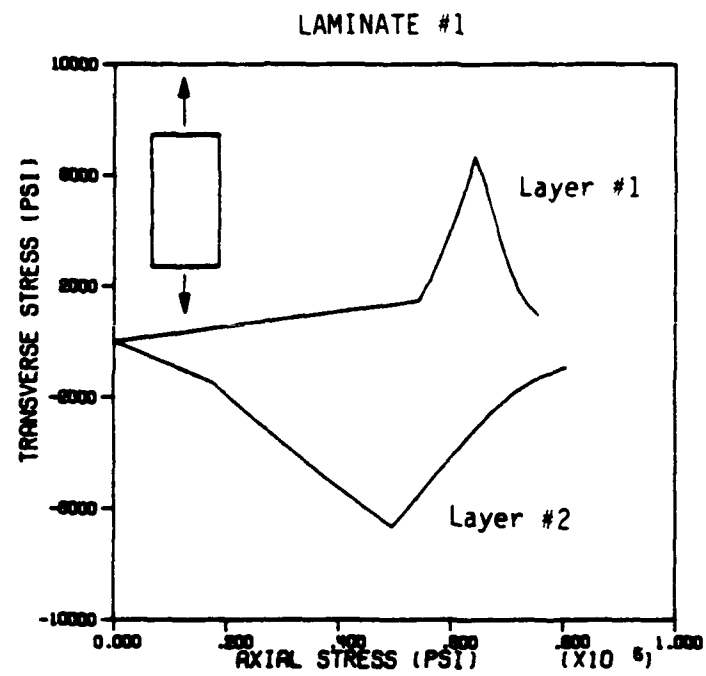


Figure 6.3 Axial and transverse layer stress distribution during uniaxial loading of an isotropic laminate.

It is quite clear that the slope of the plots in Fig. 6.3 are not constant, which indicates non-proportionality of the normal stresses. It is interesting to note that this non-proportional stress state occurs even though the remote laminate loading is monotonic uniaxial. This non-proportionality does not present a problem since the formulation of the plasticity flow rule is entirely incremental. These results suggest that a deformation theory of plasticity would not be adequate for elastic-plastic laminates.

The lamination of isotropic elastic-plastic layers appears to produce a composite with a unique response. The global behavior of the laminate is a function of the elastic and post yield plasticity parameters of the individual laminas. It has been demonstrated that many different laminate behaviors can be characterized with knowledge of the base layer material properties and use of the LAMINATE program. Ideally, one could combine several materials and arrive at a composite behavior which envelopes the best attributes of each base material.

Laminate Response Due to Cyclic Loading

The global response of a laminate under a uniaxial load cycled between fixed load limits was investigated. Laminate #1 elastoplastic properties were selected for the analysis. Fig. 6.4 illustrates the uniaxial laminate response when subjected to cyclic loading. After both layers have yielded (A, B) and considerable work-hardening has occurred, the laminate was unloaded (C) and cycled three times between fixed limits which are equal in tension and compression.

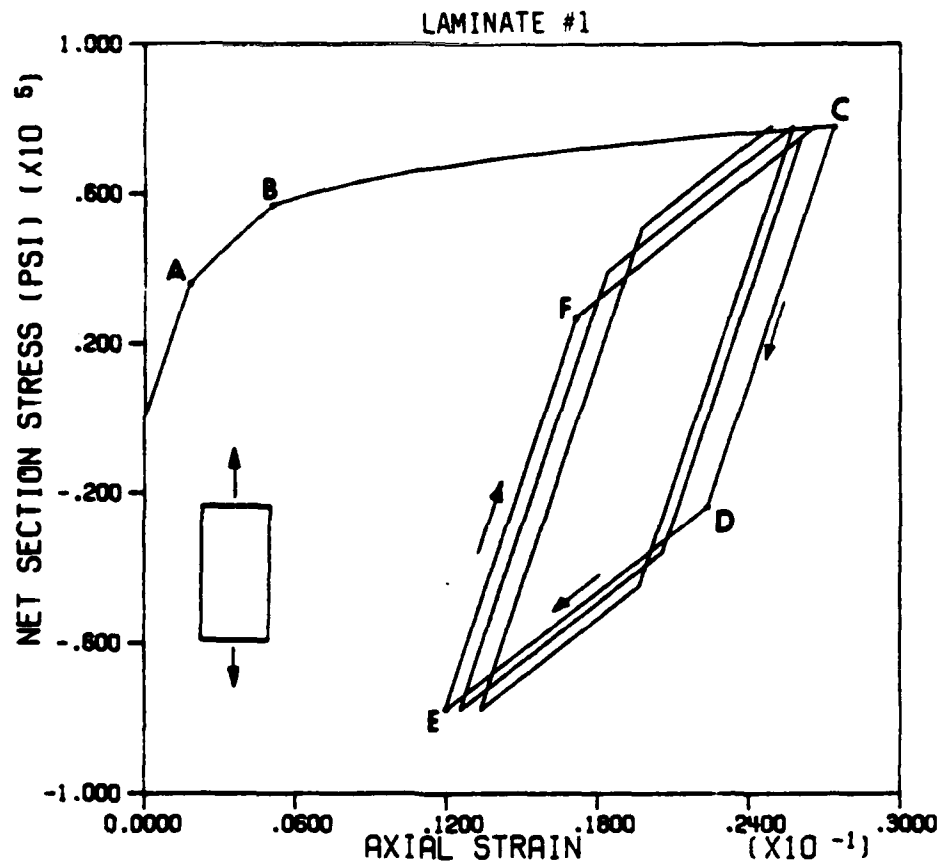


Figure 6.4 Stress-strain response of an isotropic laminate cycled between fixed load limits.

The unloading process from point C to D proceeds in an elastic manner as is consistent with elastoplastic theory but yields at point D, rather than continuing elastically until the lower load limit is reached. This appears to be a contradiction of the isotropic hardening assumption which predicts self-similar expansion of the yield surface. This behavior can be accounted for if one recalls that each lamina is constrained by its own individual elastic-plastic yield criterion and isotropic work-hardening relationships. The interrelation of these different elastoplastic materials through the lamination assumptions results in this complex behavior.

During the second and third cycles, the hysteresis loop appears to become narrower, and the corresponding tension and compression yield points move closer to the fixed limits. If the cyclic loading continues, it has been demonstrated that the hysteresis loop eventually collapses to a straight line bounded by the fixed load limits.

The degree of permanent deformation exhibited by the individual layers cannot be discerned. The layer stresses are plotted against net section strain in Fig. 6.5. It is clear that Layer #1 underwent elastic-plastic work-hardening, while Layer #2, the aluminum alloy, stayed entirely elastic. The explanation of this phenomenon lies in the much greater elastic stiffness of Layer #1. As a result of the first order laminate assumptions, stiff layers tend to stress to a greater extent than more flexible layers. An interesting aspect of this behavior is that the elastic-plastic response is dominated by the relative magnitude of the elastic properties, and not just the plasticity parameters.

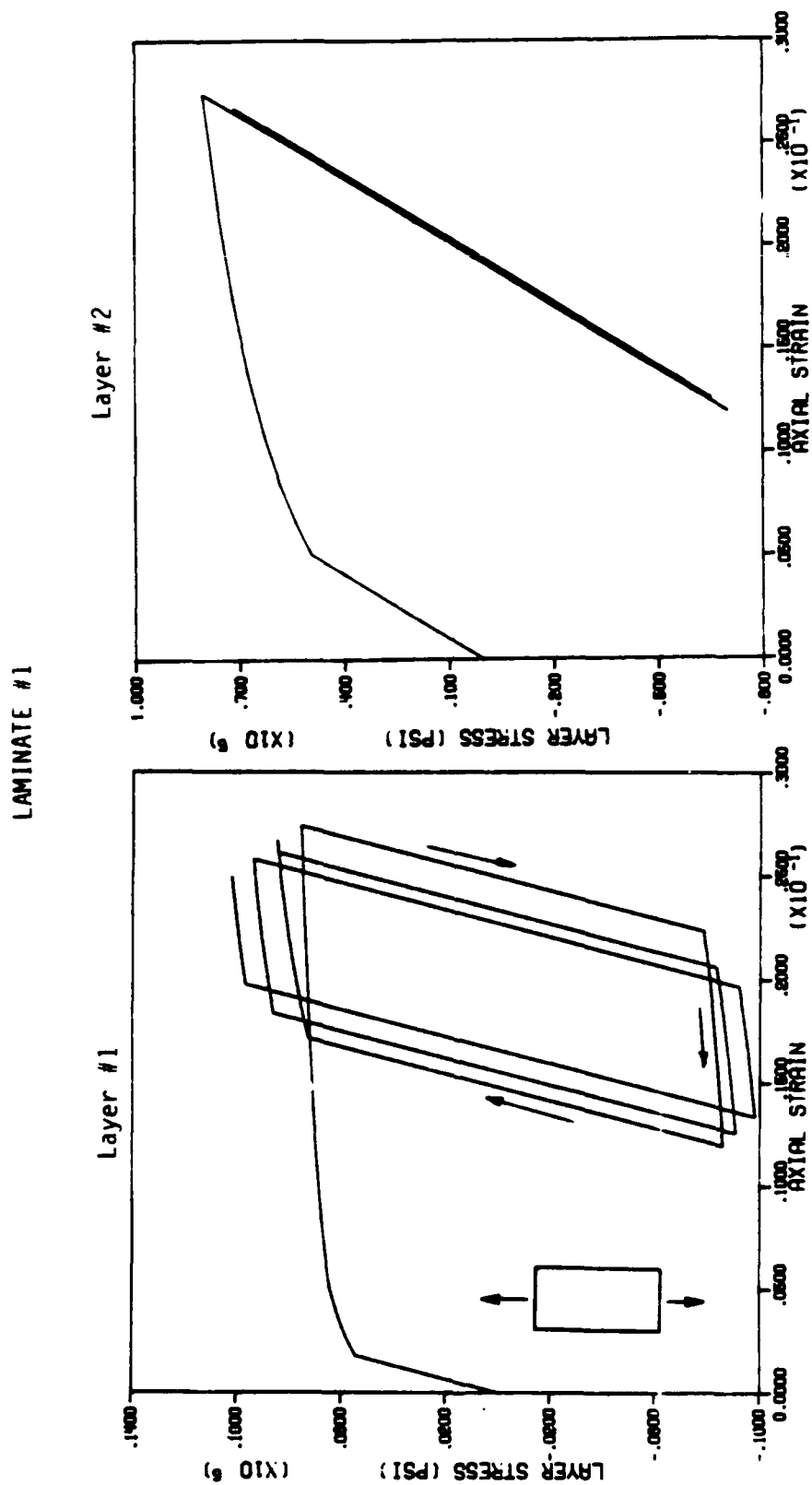


Figure 6.5 Layer stress-strain response of an isotropic laminate cycled between fixed load limits.

A Study of the Laminate Yield Surface

The results from the previous section infer that Laminate #1 does not exhibit isotropic hardening. Rather, a form of kinematic hardening [8] or a combination of isotropic and kinematic hardening behavior seems apparent. Figure 6.6 depicts the translation and expansion of the laminate yield surface during the cyclic loading represented in Fig. 6.4. The yield surface is defined by utilizing the multiaxial capability of the LAMINATE program. The first plot (⊙) is for the initial yield surface (A), which is centered about the origin. The next plot (Δ) is a representation of the laminate yield surface immediately after unloading (C). The translation of the yield locus accounts for the different values of yield in tension and compression (C, D). It is also clear that the yield surface is expanding, signifying a combined isotropic-kinematic work-hardening. The third yield locus (+) is representative of the laminate after re-load (E). The yield surface has translated towards negative σ_{11} , with very little expansion. The last plot depicts the laminate yield surface after many cycles, when the hysteresis loop has collapsed to a line. It is apparent that the anisotropy of yield induced by the initial load cycles eventually dissipates as the laminate continues to work-harden.

A multiaxial loading path and subsequent work-hardening was considered next. A set of yield surfaces at three consecutive levels of load is illustrated in Fig. 6.7. The initial yield surface takes the familiar form of an ellipsoid centered about the origin (⊙). The yield surfaces at points (Δ) and (+) indicate both kinematic and

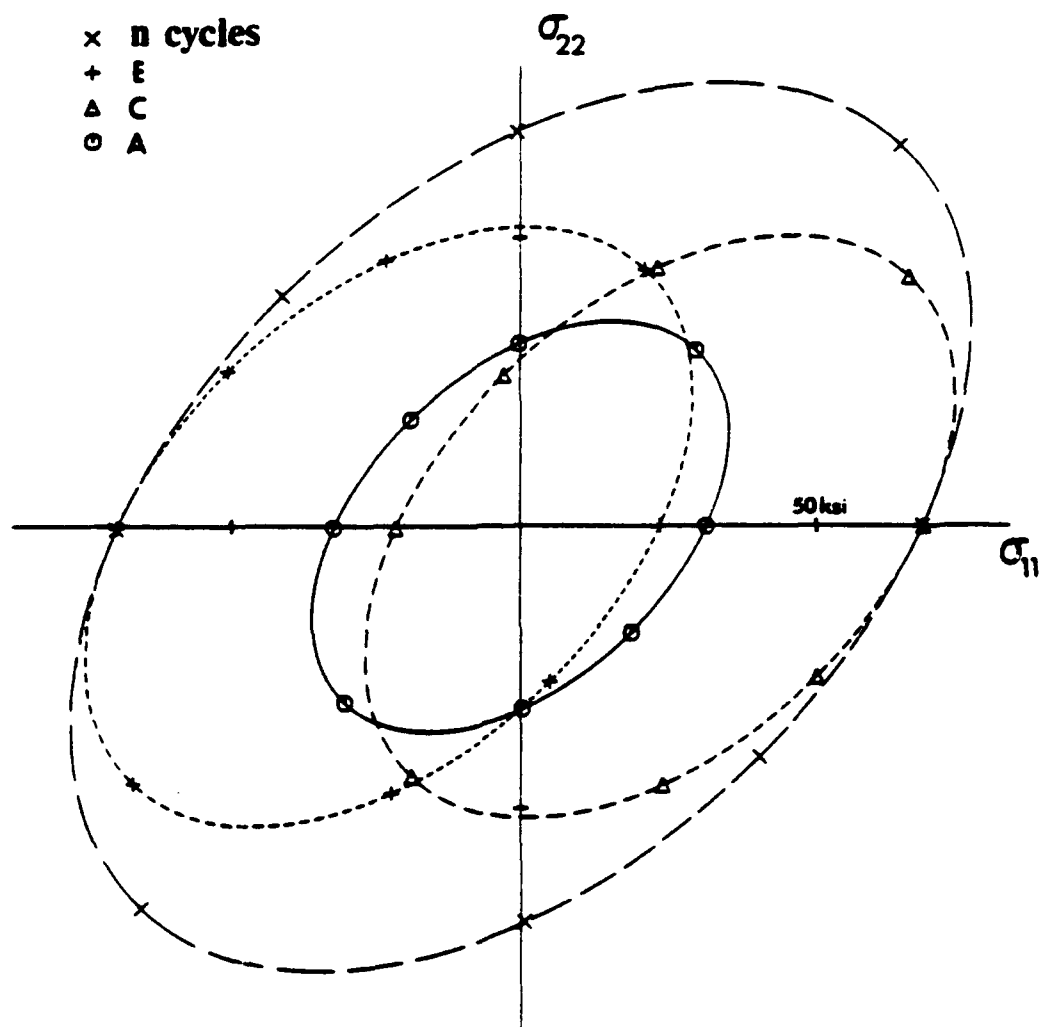


Figure 6.6 Illustration of the yield surface for an isotropic laminate during uniaxial cyclic loading between fixed load limits.

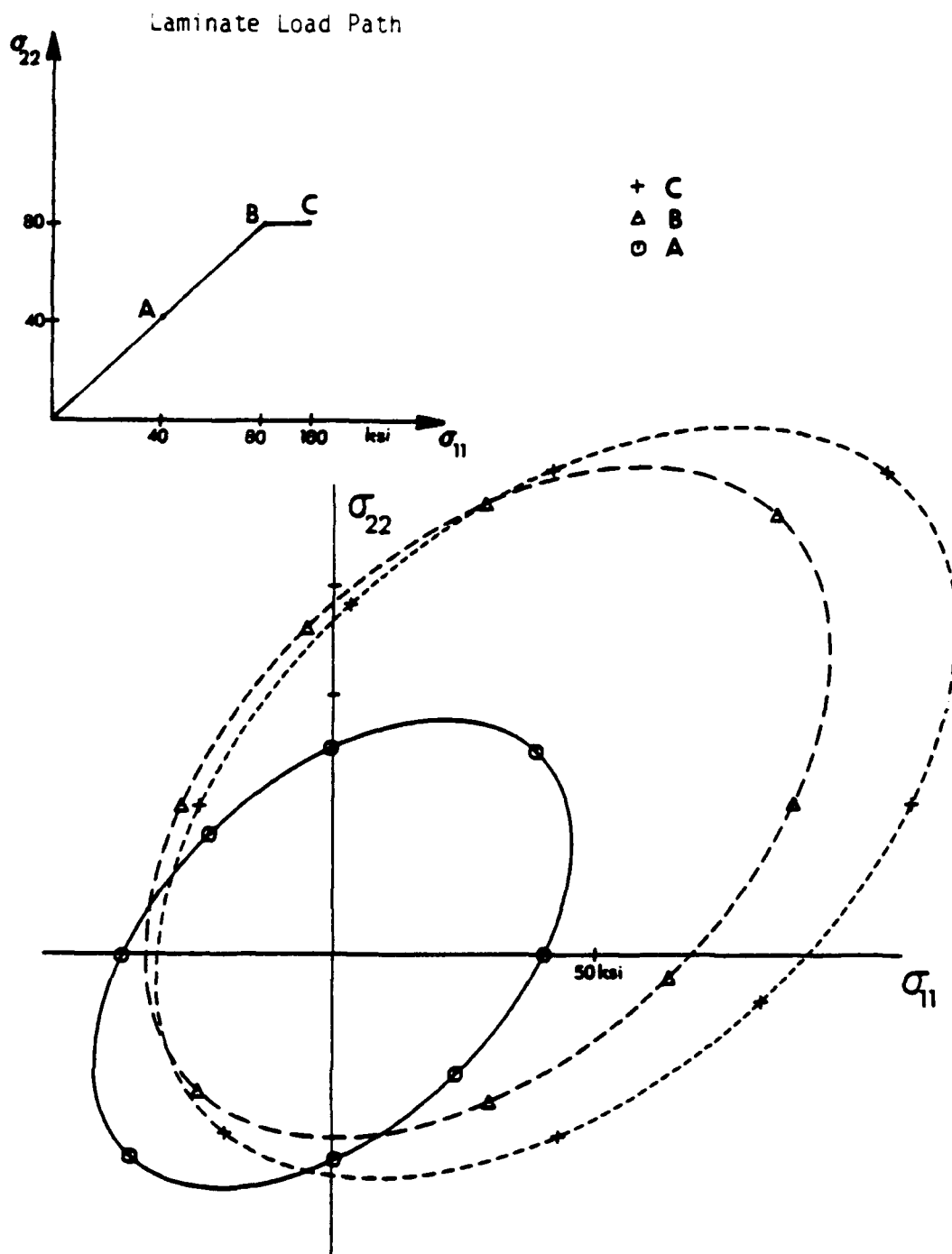


Figure 6.7 Illustration of the yield surface for an isotropic laminate during a multiaxial non-proportional loading path.

isotropic hardening, which is consistent with the cyclic loading results.

Though only isotropic hardening behavior is assumed for each individual layer, the laminate demonstrates a more complex response. In fact, depending on the particular make-up of a laminate, it is likely that global load-deformation response cannot be described by classical elastoplasticity theory. Fortunately, the researcher need not bother with the laborious task of characterizing the laminate as a homogenous material; rather, one need only have a knowledge of the simpler lamina properties, and a properly formulated lamination theory.

Path Dependency Due to Multiaxial Loading

Two sets of complex loading paths involving multiaxial stresses were studied. Figure 6.8 illustrates the normal and shear strain dependence on load path selection. These plots draw a strong similarity to the study conducted in Section 2, which concerned strain dependence on load path for a homogenous elastic-plastic material (Fig. 2.13). The same conclusions can be reached for the laminate as for the homogenous material; stress-strain response is not unique for complex loading paths.

ELASTIC-PLASTIC LAMINATE BEHAVIOR: ORTHOTROPIC LAYERS

Laminates consisting of orthotropic elastoplastic layers were considered and comparisons made with isotropic laminate behavior. This topic is of practical interest since many metal matrix composite applications require lamination.

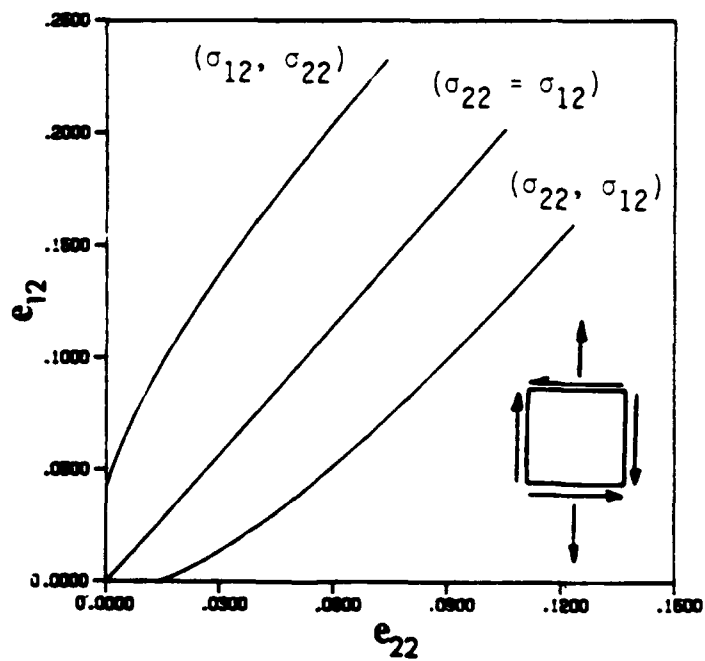
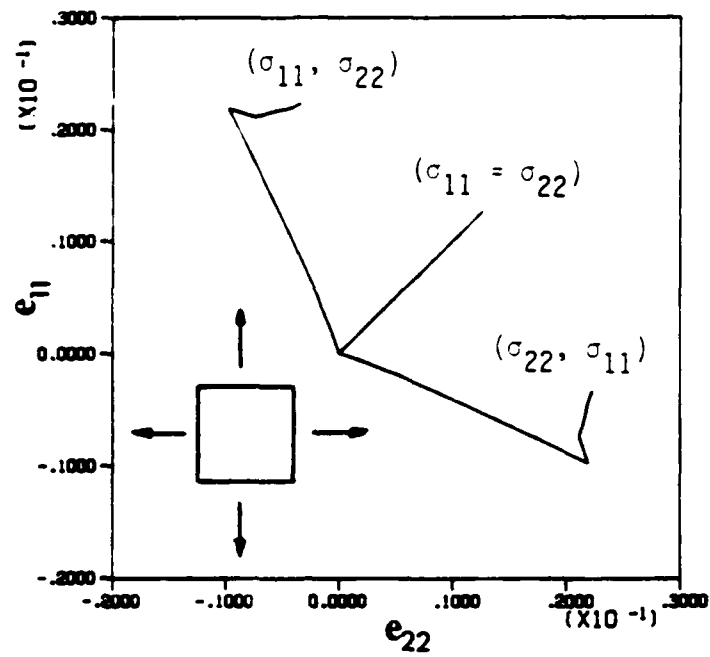


Figure 6.8 Deformation response of an isotropic laminate due to different complex loading paths.

Global Response Due to Uniaxial Loading and Unloading

The uniaxial response of a laminate $[0^\circ/90^\circ]_5$ consisting of two orthotropic elastic-plastic materials (B-A1) is pictured in Fig. 6.9. The laminate exhibits an initial linear behavior, then becomes non-linear after the 90° ply yields. Though the 0° ply eventually yields its stiffness contribution remains essentially elastic due to the fiber-load alignment. Note how the laminate response again falls between the homogenous layer material behavior.

The unloading behavior initially demonstrates the classical elastic response, but at approximately 20,000 psi re-yields. It is clear that the yield surface has been distorted during the tensile work hardening, introducing some degree of additional anisotropy. After the load is completely removed, a permanent net section laminate strain is incurred, substantiating the idea that plastic deformation is occurring in the various layers. This type of behavior has been observed by Dvorak [30] and Sova [32].

The stresses in the laminas during laminate deformation are illustrated in Fig. 6.10. Transverse stresses in the individual layers are apparent as was the case with the isotropic laminate. The contractural mismatch is due to the orthotropic nature of each layer, and the particular lay-up design $[0^\circ/90^\circ]_5$. The ratio of the principal stress components denoted by the slopes of each plot is obviously not constant. This again reinforces the non-proportionality of the stress state.

The induction of transverse stress into the laminas during laminate deformation has an effect on subsequent yield. For example,

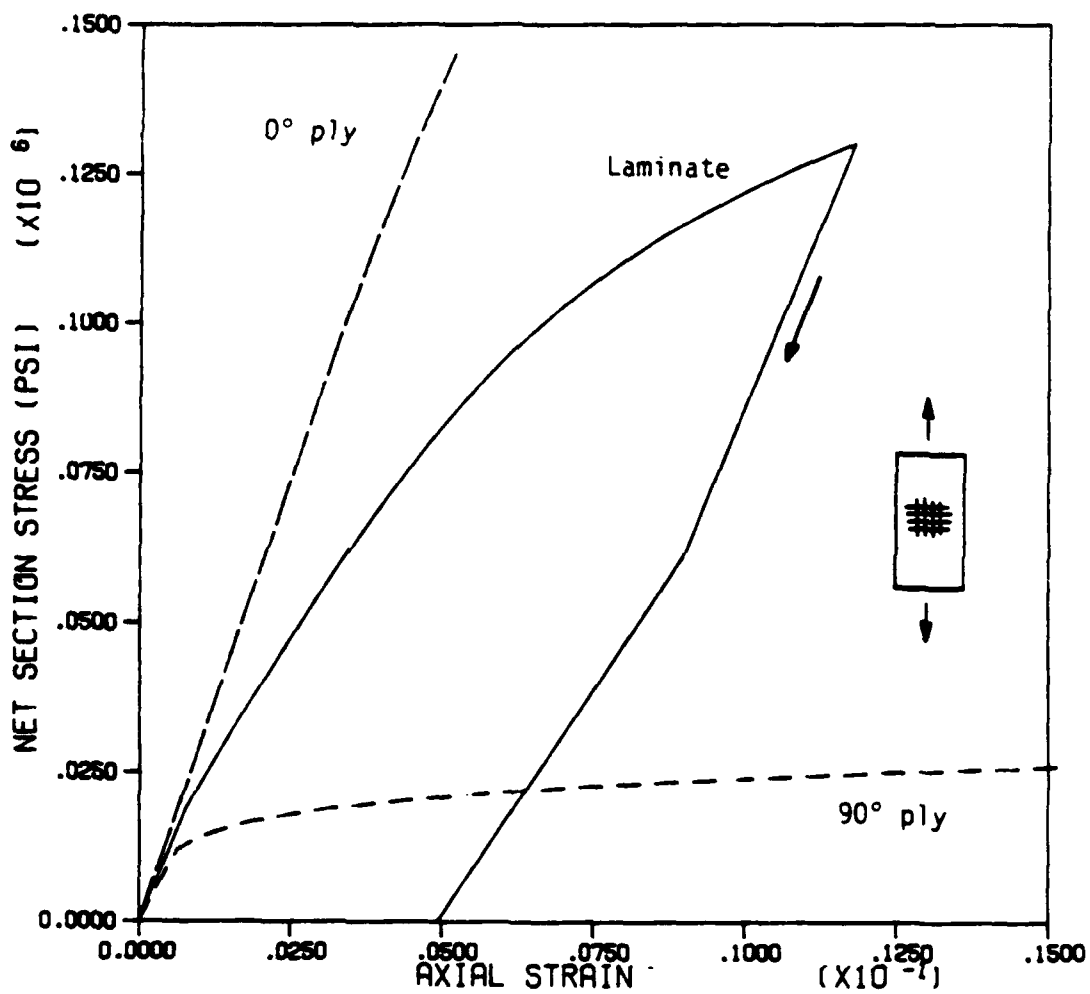


Figure 6.9 Uniaxial load-deformation response of an orthotropic B-Al laminate $[0^\circ/90^\circ]_s$.

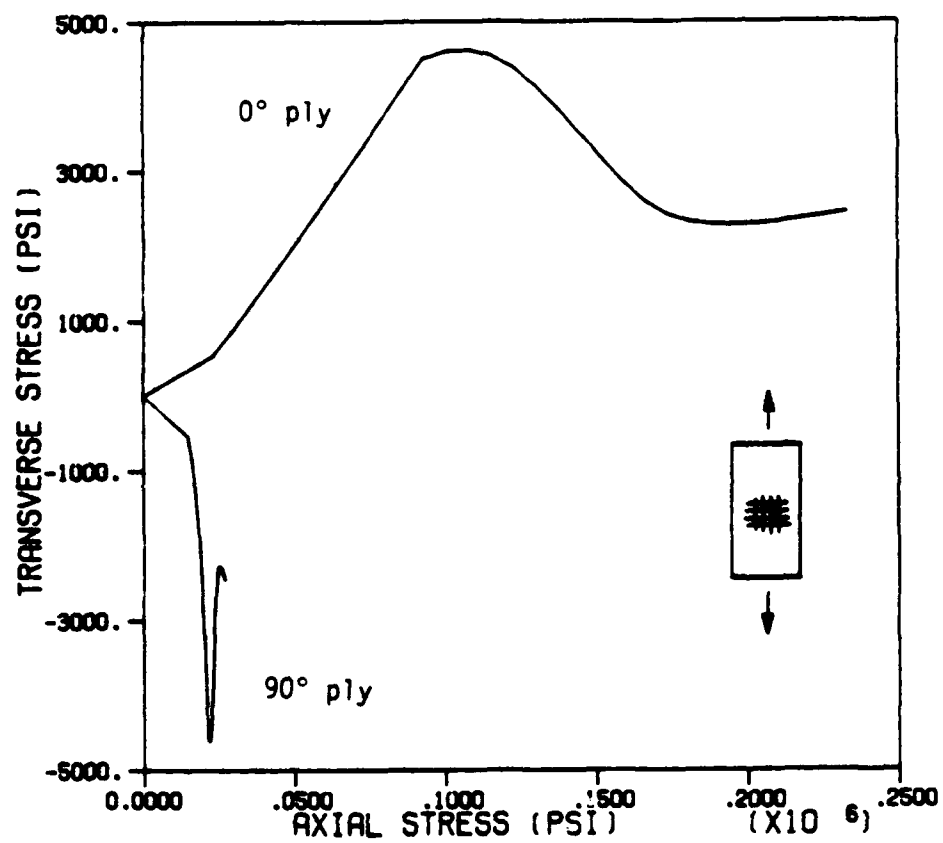


Figure 6.10 Axial and transverse layer stress distribution during monotonic uniaxial loading of the B-A1 laminate.

the 0° ply has the larger axial stress, but, due to the anisotropy of the yield criterion, this stress component does not significantly contribute to yielding. Conversely, the transverse stress present in this ply does contribute.

Laminate Response Due to Cyclic Loading

The global response of this same laminate subjected to a uniaxial load cycled between fixed load limits was studied. The B-Al results are illustrated in Fig. 6.11. After initial yield, the laminate work-hardened until unloading at point B. The load was removed and the laminate underwent an equal amount of compression. The laminate was then reloaded until the upper limit was reached. The process was repeated for another two cycles.

The results are very similar to those for the isotropic laminate. Unloading initially occurs elastically, but reverse yielding occurs before the bottom load limit is reached, again indicating that non-isotropic hardening occurs. The hysteresis loops for the Boron-Aluminum laminate are initially narrower and collapse to a line faster than for the isotropic laminate. This behavior is associated with the greater ductility demonstrated by the isotropic materials. Due to the fiber orientation of the 0° ply, plastic deformation is retarded.

The stress-strain behavior in the individual laminae are plotted in Fig. 6.12. The 90° ply, which yields first, experiences considerable plastic deformation as suggested by the large hysteresis loops. The 0° ply demonstrates almost purely elastic behavior throughout. This behavior is consistent with the view that very little permanent deformation can occur parallel to the stiff fibers.

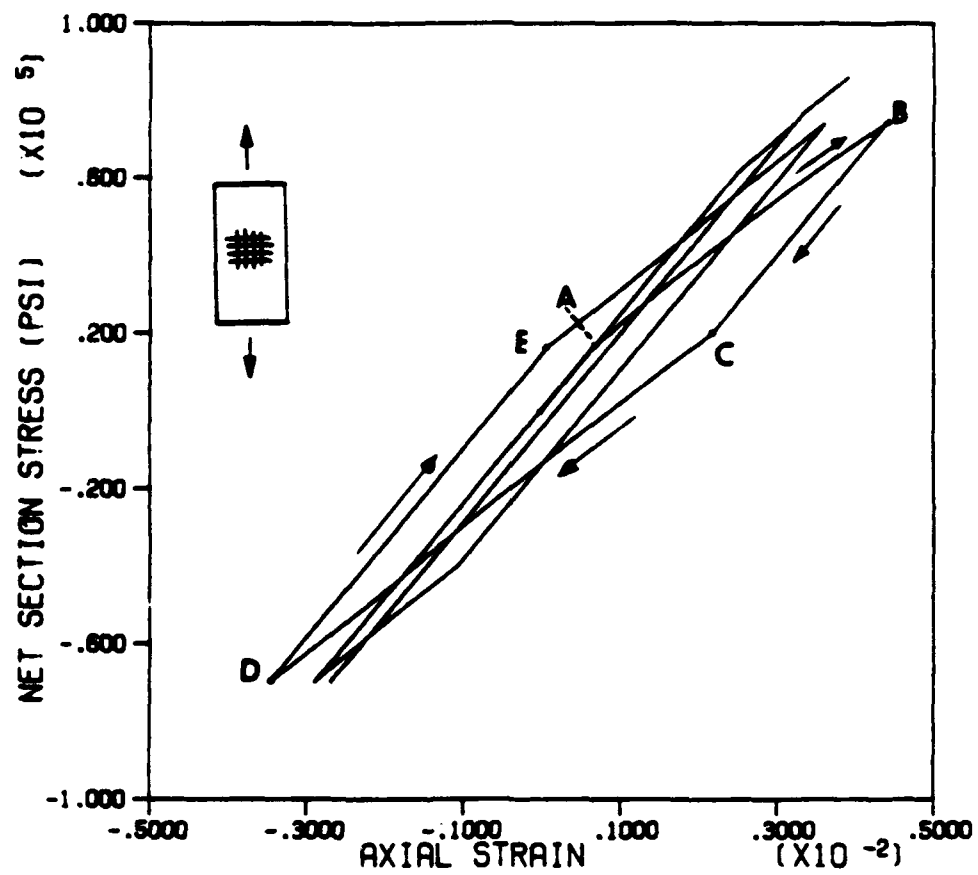


Figure 6.11 Stress-strain response of the B-A1 laminate cycled between fixed load limits.

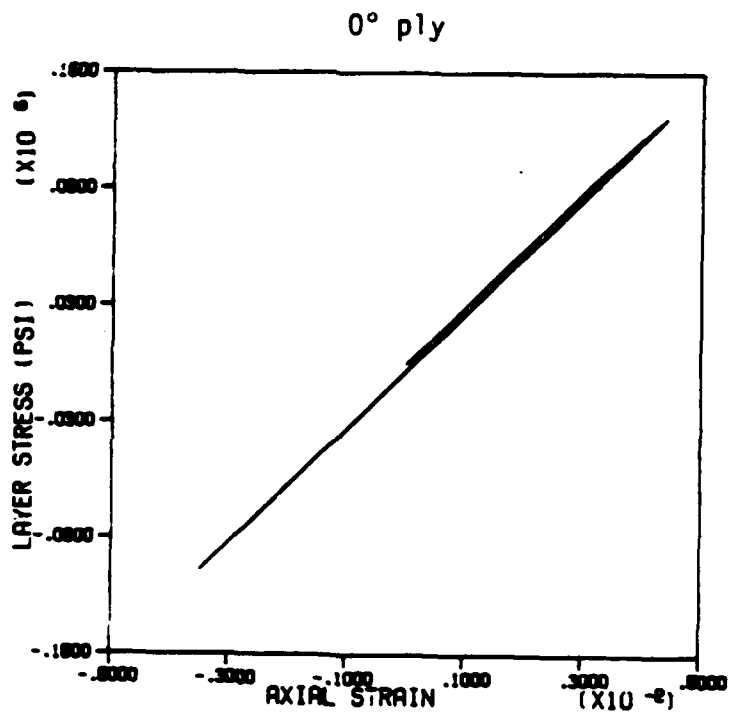
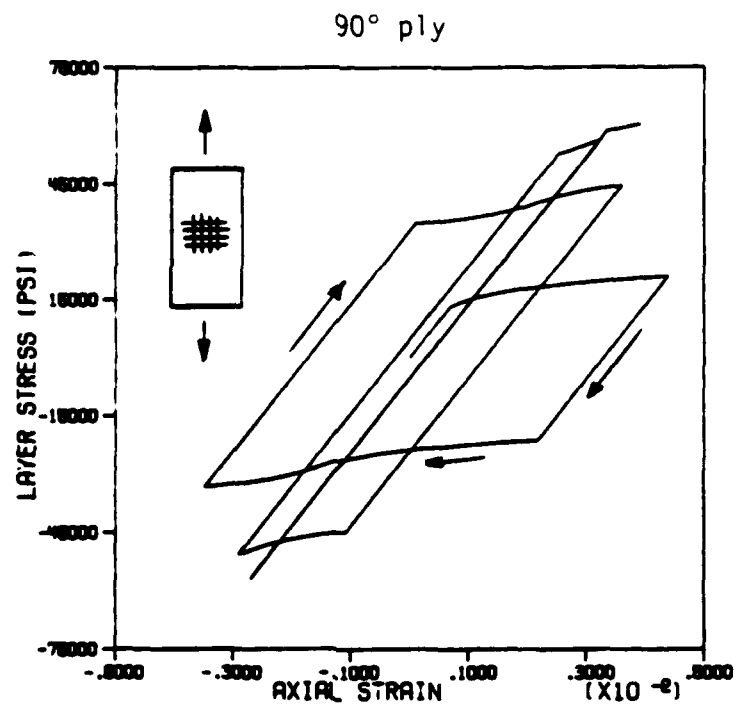


Figure 6.12 Layer stress-strain response of the B-A1 laminate cycled between fixed load limits.

It is interesting to note that while the isotropic laminate behavior was dominated by the ratio of the elastic stiffnesses, the Boron-Aluminum laminate is not strongly dependent on elastic properties. Instead, the Boron-Aluminum is dominated by the anisotropy of yield, and the corresponding orientation of the individual laminae.

A Study of the Laminate Yield Surface

The laminate unloading and cyclic loading behavior demonstrates that the work-hardening is not isotropic. Figure 6.13 depicts four yield surfaces at various load points from the cyclic loading example in Fig. 6.11.

The initial yield locus (\odot) in Fig. 6.13 is almost square in shape. This is quite different than that depicted for the isotropic laminate. This contrasting behavior is due to the fibers being aligned with each principal axis. This results in biaxial stresses having a negligible effect on the laminate yield surface. Only the stress within each layer that is transverse to the fibers contributes to the yield. The yield surface reported by Dvorak [30] takes a similar form.

The second plot (Δ) represents the laminate yield surface after tensile work-hardening to load point B. The yield surface has both translated in an approximate rigid body sense, and experienced distortion. The third locus ($+$) represents the yield surface at the bottom of the first load cycle (D) and has also undergone a translation and further distortion. Finally, at the end of the third loading cycle, the yield locus (\times) extends from the maximum to the minimum load limit.

x n cycles
 + D
 Δ B
 ⊖ A

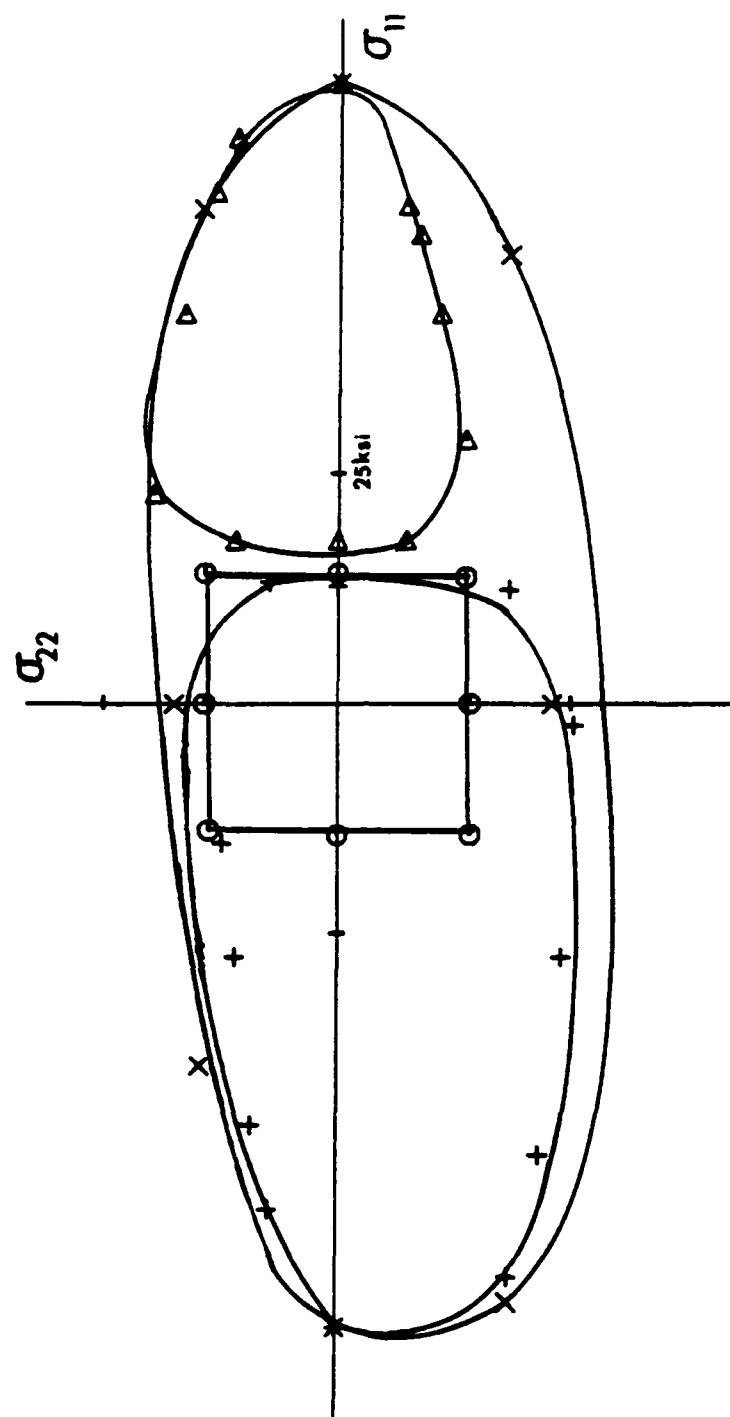


Figure 6.13 Illustration of the yield surface for the B-A1 laminate during uniaxial cyclic loading between fixed load limits.

It is obvious that B-A1 laminate work-hardening is highly anisotropic. The anisotropy of the work-hardening is not only induced by the rigid body translation, but the distortion of the yield locus as well. Note that the yield surface tends to distort in the direction of the applied load, but expands a relatively small amount in the transverse direction. It is likely that this type of deformation is due to the relatively stiff behavior of the fibers in resisting transverse plastic deformation.

The yield and work-hardening behavior studied in this section provides justification for not analyzing the laminate on the macroscopic scale. The theoretical mechanics necessary to describe this unusual yield surface and subsequent work-hardening would be much too cumbersome. Understanding the elastic-plastic behavior at the "mini-level" and superimposing the responses via a lamination theory, appears to offer the straightforward approach.

Path Dependency Due to Multiaxial Loading

Load path dependency of strain was investigated to demonstrate the non-unique stress-strain response. Two complex loading paths involving sequenced multiaxial loads were applied to the B-A1 laminate. Figure 6.14 illustrates the normal and shear strain dependence on the particular load path. These load paths are similar to those for the isotropic laminate, in that there is a wide disparity in the final deformation state.

The similarity of the isotropic homogenous, isotropic laminate, and anisotropic B-A1 laminate response confirms that the non-proportionality of the stresses has a dominant effect on the final

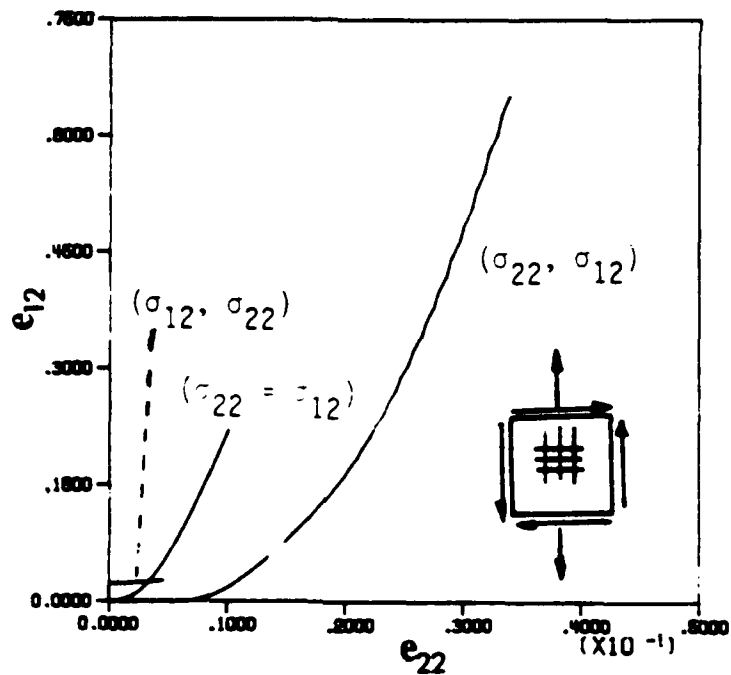
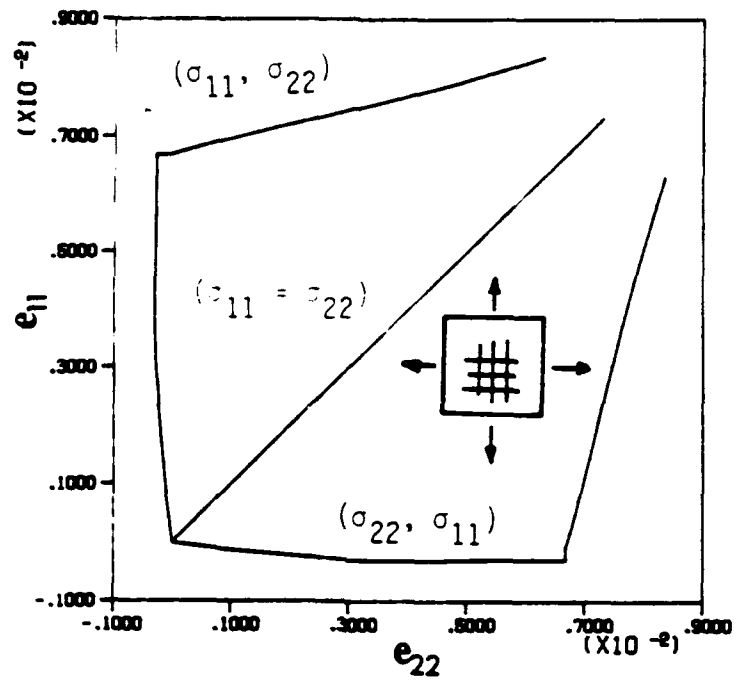


Figure 6.14 Deformation response of the B-A1 laminate due to different complex loading paths.

deformation state, regardless of anisotropy or material construction.

ANALYSIS OF A LAMINATED SHEET WITH A CIRCULAR HOLE: ISOTROPIC LAYERS

The ANPLAST finite element program was used to analyze a laminated sheet with a circular hole. The laminated sheet is constructed of two isotropic layers, as characterized in Fig. 6.1. The geometry and loading of the finite specimen is illustrated in Fig. 4.1.

A Study of Plastic Zone Growth Within Each Layer

Growth of the plastic zone within each layer is illustrated in Fig. 6.15. As expected, yielding is initiated in Layer #1 (Steel Alloy) due to its much greater elastic stiffness. The initial yield is located at the perimeter of the hole, along the symmetry line, where the hoop stress (σ_{yy}) is a maximum. Yield is initiated in Layer #2 (Aluminum Alloy) at a greater remote load.

The shape and growth of the plastic zone within each layer parallels the behavior of a homogenous isotropic material, as was analyzed in Section 4. It is apparent that the two layers interact in such a way that the character of the plasticity is a function of the individual layer properties, but the magnitude of plastic zone growth is a superposition of the two responses. On the element level total strain within each layer is the same, yet different levels of plastic zone growth are found. This indicates that the elastic (e^e) and plastic (e^p) components of strain can be different for each layer, but their sum must be the same.

A more quantitative presentation of plastic zone growth is obtained by plotting contours of effective stress as shown in Fig.

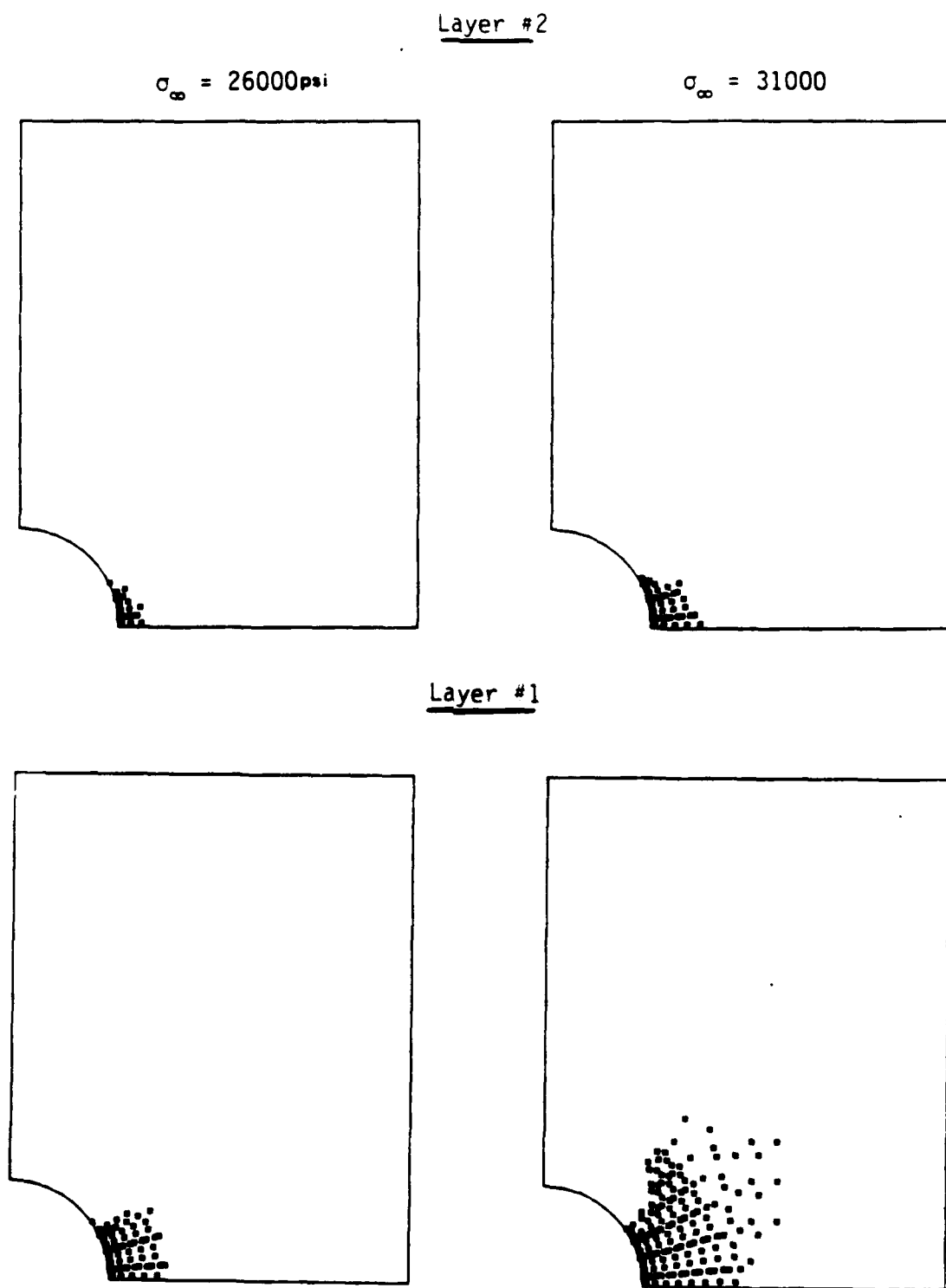


Figure 6.15 Plastic zone growth in each layer of an isotropic laminated sheet subjected to elastic-plastic loading.

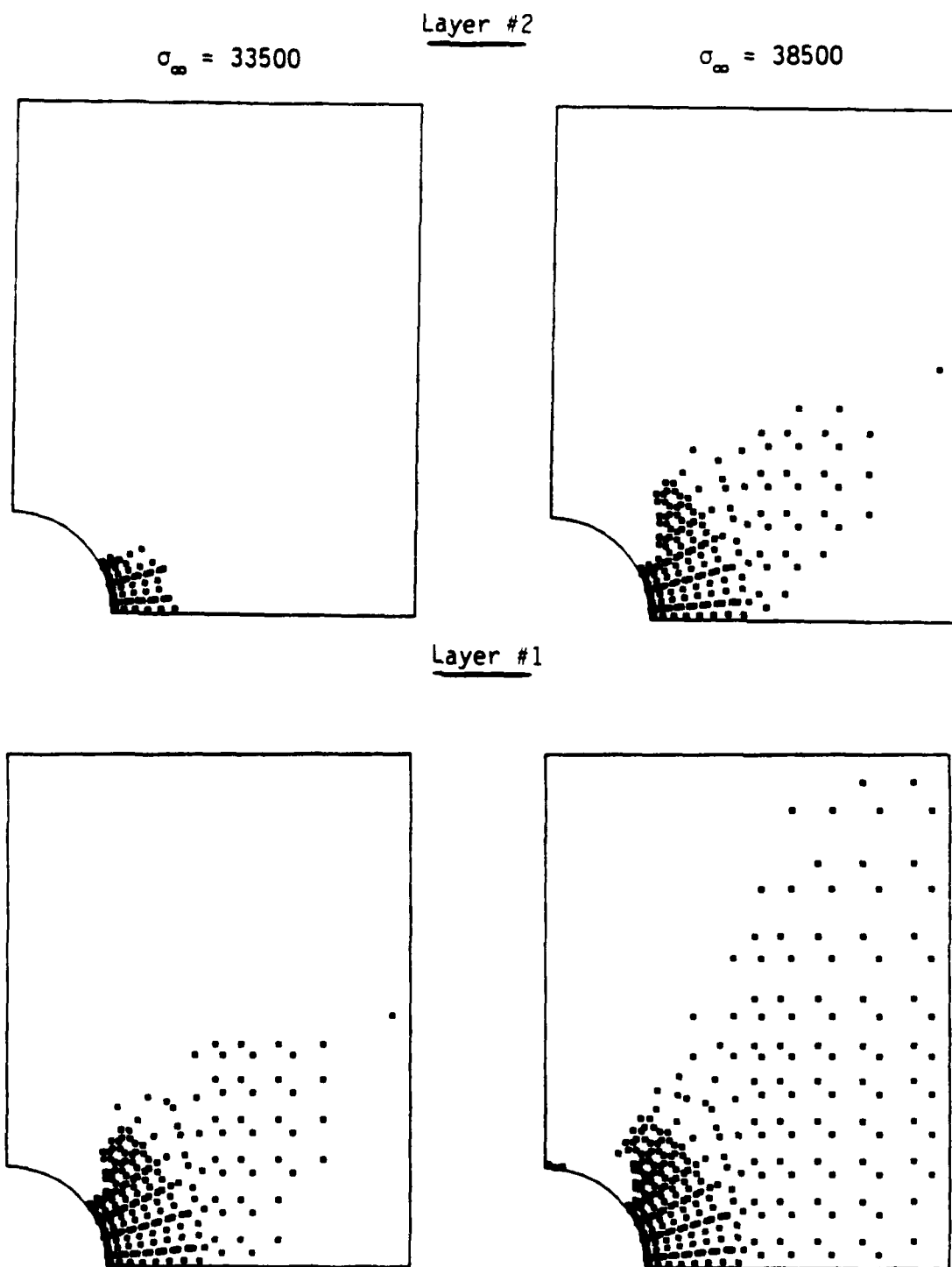


Figure 6.15 continued

6.16. These contours reiterate the different states of plastic deformation in each layer.

A Study of Residual Stresses and Strains Due to Unloading

The specimen was first unloaded by taking a small negative loading step, which allowed the elements to become elastic. The small unloading increment also provided an opportunity for re-assembly of the stiffness matrix. The load was removed in ten equal increments. In this particular case, both layers and all elements became elastic during the unloading, and did not re-yield.

The residual stress (σ_{yy}) distributions are illustrated in Fig. 6.17. Layer #1 exhibits the expected compressive residual stress component, while the magnitude of stress in Layer #2 is considerably less. The reason for this behavior involves the greater degree of permanent deformation experienced by Layer #1. In addition, since Layer #1 is stiffer, it will unload faster for an equal increment of laminate strain. It is interesting to hypothesize that while the compressive residual stress in Layer #1 may be sufficient to retard crack initiation due to an overload this may not be the case for Layer #2.

ANALYSIS OF A LAMINATED SHEET WITH A CIRCULAR HOLE: ORTHOTROPIC LAYERS

An analysis of the laminated sheet with a circular hole subjected to uniaxial remote loading was conducted with ANPLAST. The laminated sheet consisted of two layers of B-A1 $[0^\circ/90^\circ]_S$.

A Study of Plastic Zone Growth Within Each Layer

Growth of the plastic zone within each layer is illustrated in Fig. 6.18. The initiation of permanent deformation occurs in the 90°

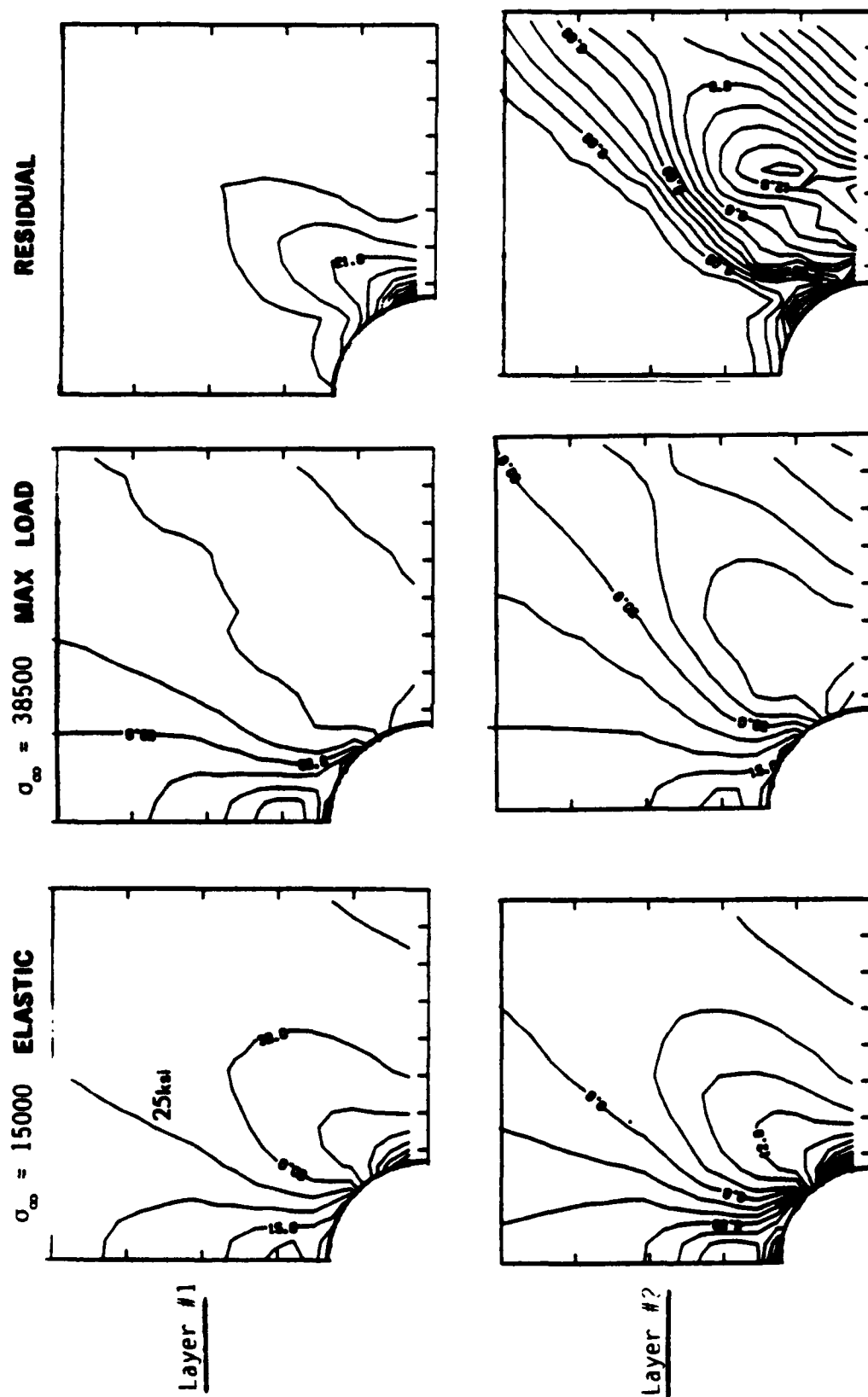


Figure 6.16 Effective stress contours in each layer for the isotropic laminated sheet subjected to elastic-plastic loading.

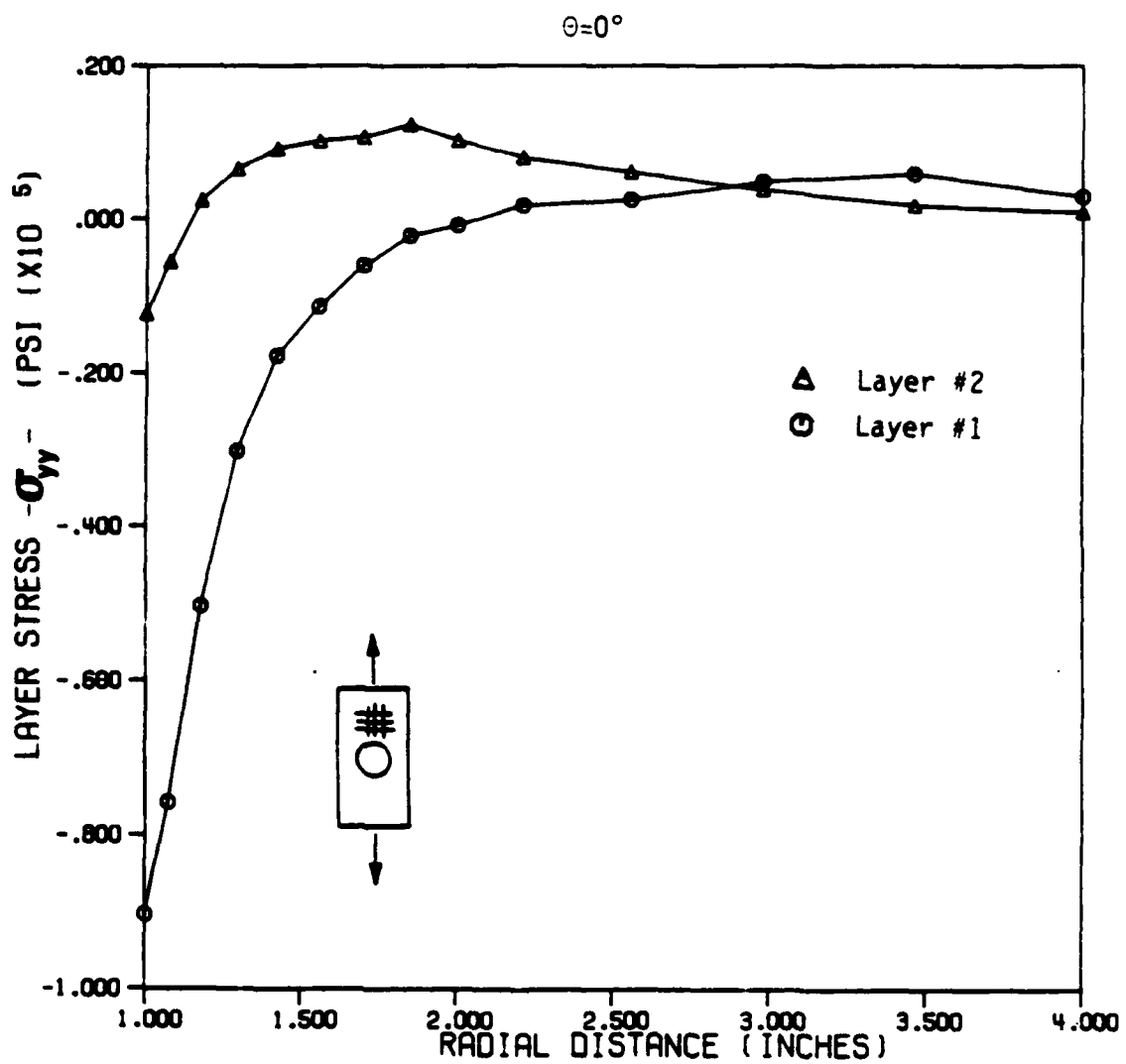


Figure 6.17 ANPLAST residual stresses in each layer for the isotropic laminated sheet with a circular hole subjected to elastic unloading.

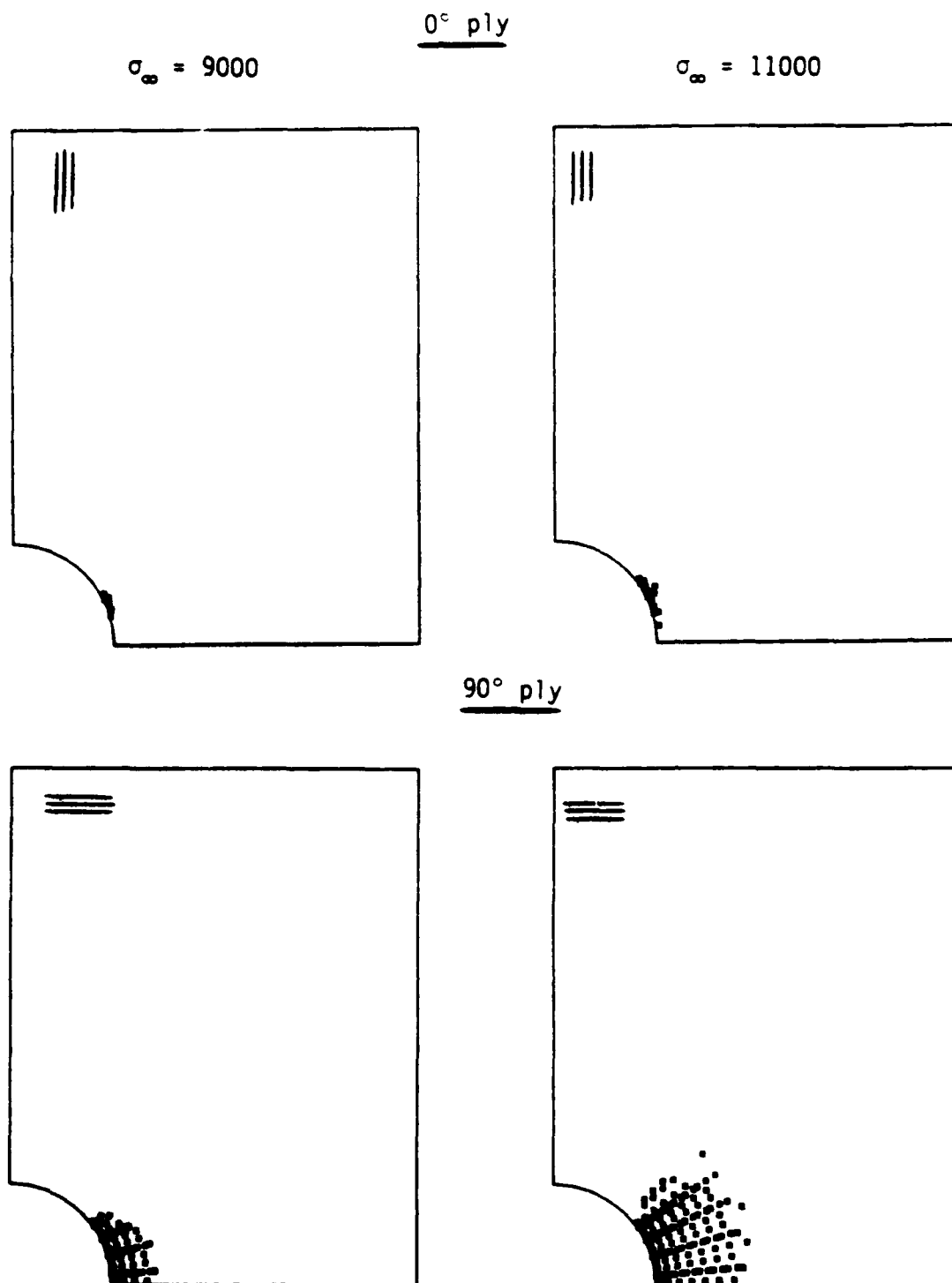


Figure 6.18 Plastic zone growth in each ply for the B-A1 laminated sheet $[0^{\circ}/90^{\circ}]_s$ with a circular hole subjected to elastic-plastic loading.

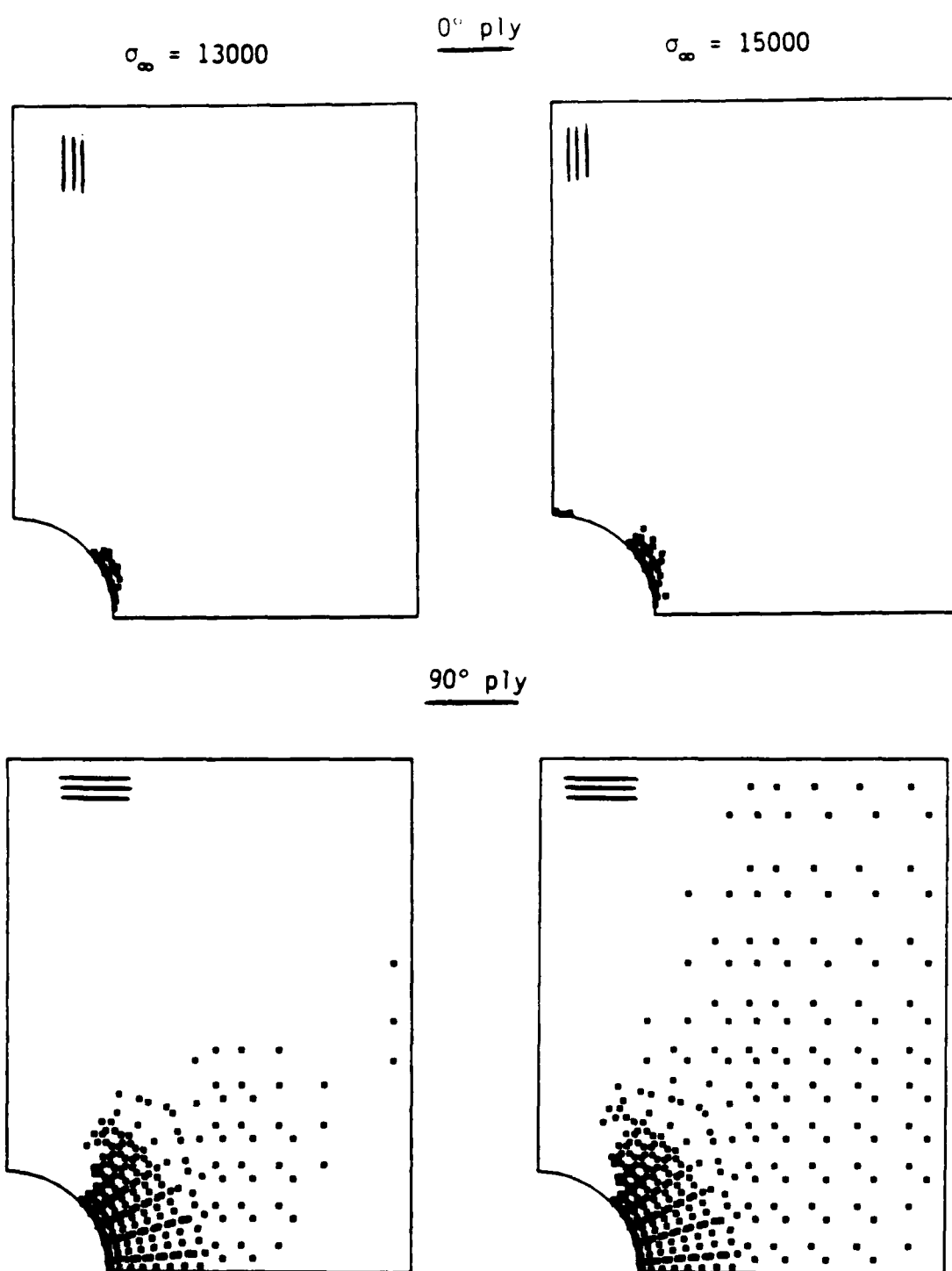


Figure 6.18 continued

layer. Unlike the isotropic laminate results, the initiation of yielding is not caused by the ratio of the layer elastic stiffness. Rather, the very strong plastic anisotropy and ply orientation dominate.

The shape and growth of the plastic zones within each layer parallels the response observed in the orthotropic homogenous problem. The plastic zone in the 90° ply tends to grow across the width of the specimen, while the zone in the 0° ply extends in a more vertical pattern. Note that net section yielding is prevalent in the 90° ply at a remote load of 36000 psi, while at the same time the plastic zone in the 0° ply remains constrained to the vicinity of the hole. Though the plastic zones in each layer take their characteristic shape observed in Section 4, the rate of progression within each layer is controlled by the superposition of the two responses.

The contour of effective stress in Fig. 6.19 clearly demonstrates the much greater magnitude of plastic deformation present in the 90° ply. For the elastic loading increment, the contour of the 0° ply indicates that the initiation of yield did not occur at the symmetry line, but along the hole boundary at approximately $\theta = 10^\circ$. This is consistent with the behavior observed in the analysis of the homogenous orthotropic material.

Dvorak [33] has also analyzed a laminated plate $[0^\circ/90^\circ]_s$ with a circular hole for a FP-aluminum metal matrix composite. The plastic zone visualization for this analysis is illustrated in Fig. 6.20. Note the similarity of plastic zone shape, especially at the lower load. It is interesting to note that Dvorak models the composite as a micromechanical structure, in contrast to the simpler macroscopic approach taken in this research.

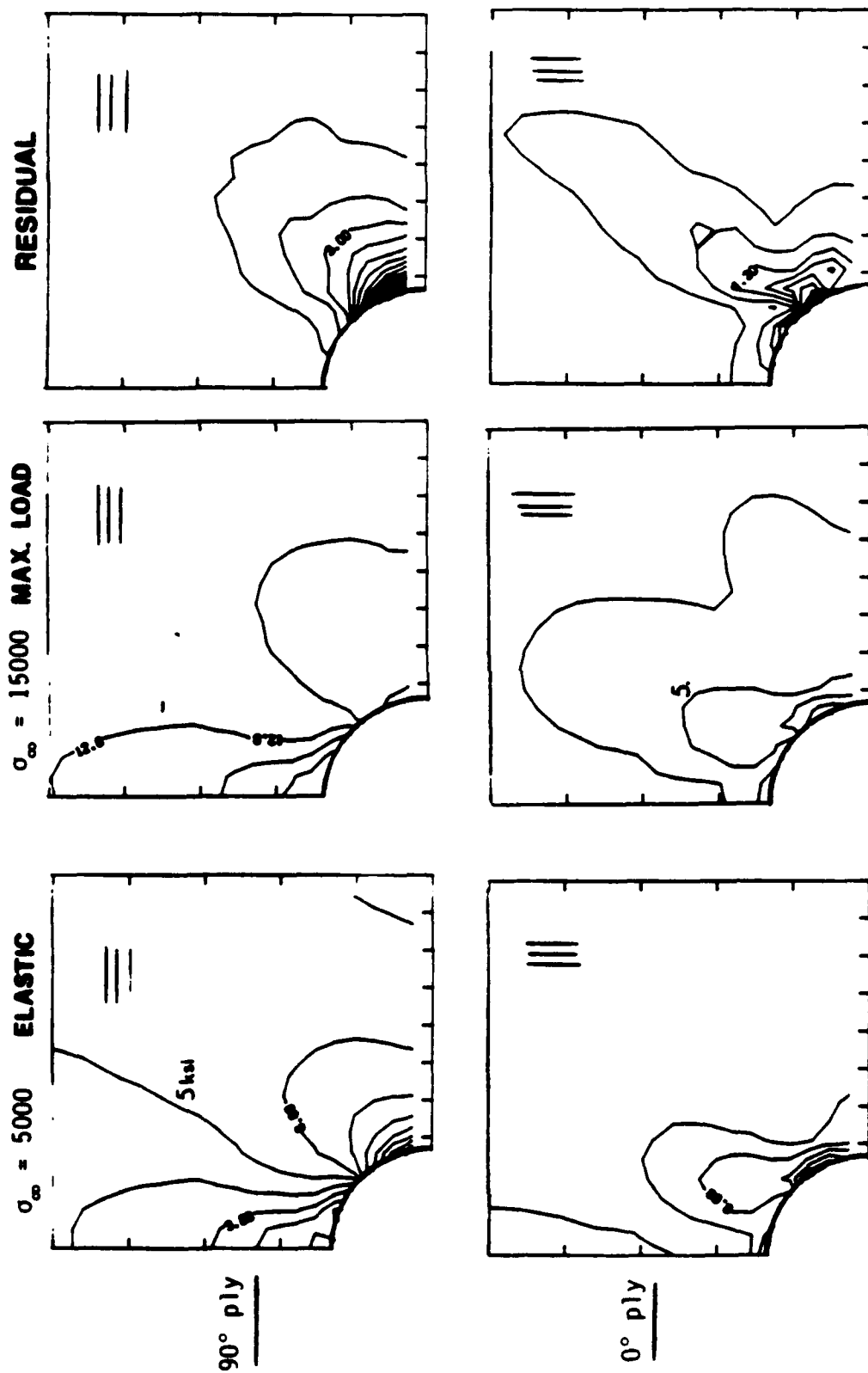


Figure 6.19 Effective stress contours in each ply for the B-A1 laminated sheet subjected to elastic-plastic loading.

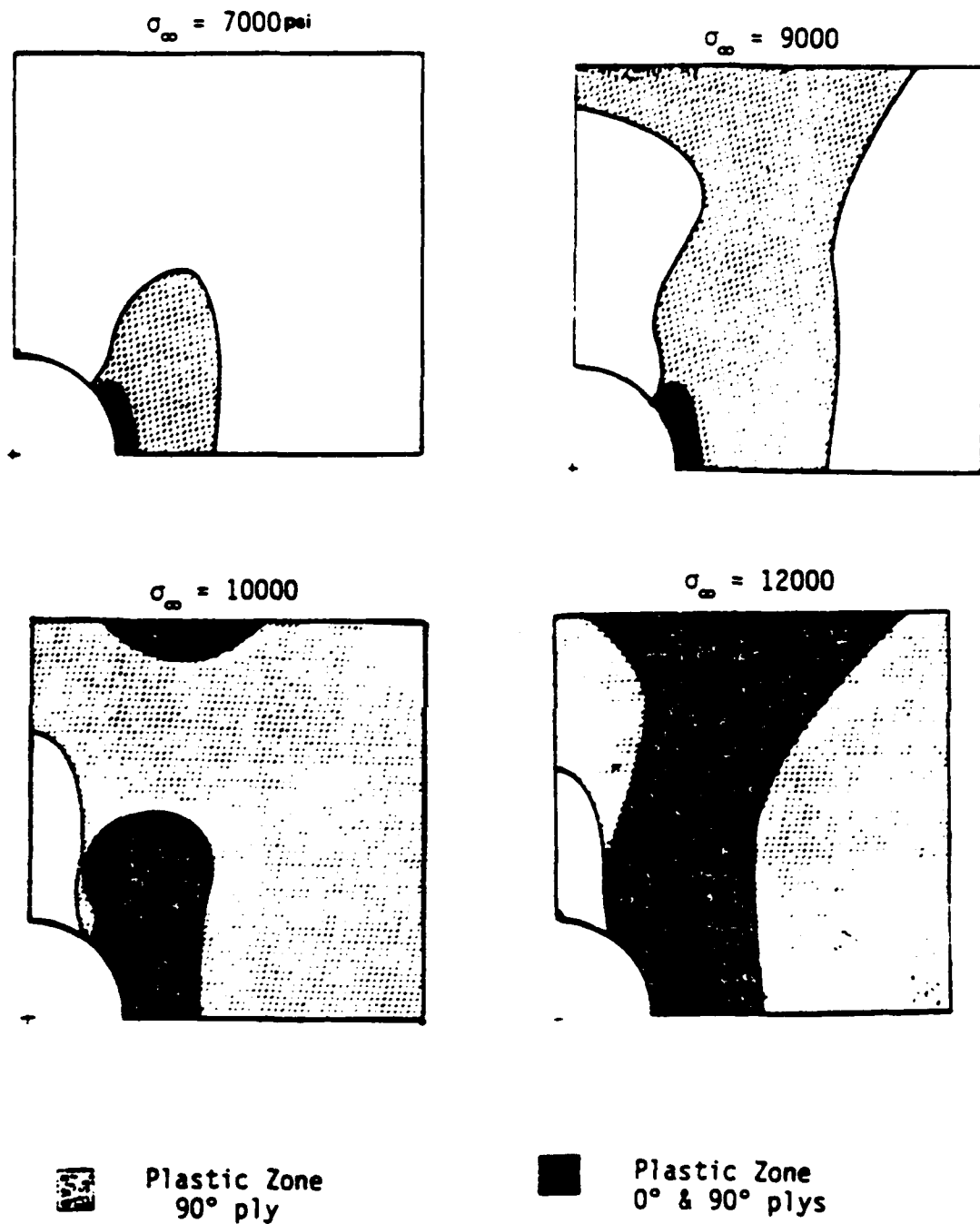


Figure 6.20 Plastic zone growth calculated by Dvorak [33] for an orthotropic FP-Al laminated sheet $[0^\circ/90^\circ]$ with a circular hole subjected to elastic-plastic loading.

A Study of Residual Stresses and Strains Due to Unloading

The B-A1 laminate was unloaded in the same fashion as the isotropic laminate, a small unloading step followed by ten equal unloading increments. After the first unloading step, both layers became elastic and remained elastic until the end of the last loading increment when 4 elements, in proximity to the hole boundary, re-yielded.

The residual stress (σ_{yy}) distributions are illustrated in Fig. 6.21. The typical compressive residual stress exists in the 90° ply, but a residual tensile stress is present in the 0° ply. Since σ_{xx} is also tensile in the 0° ply, these results suggest that crack initiation due to cyclic loading may be prevalent in this ply.

Experience and intuition are not sufficient in analyzing these complex elastic-plastic laminates. As the geometries and loadings become even more complex, the need for a practical computational tool, such as ANPLAST, becomes obvious.

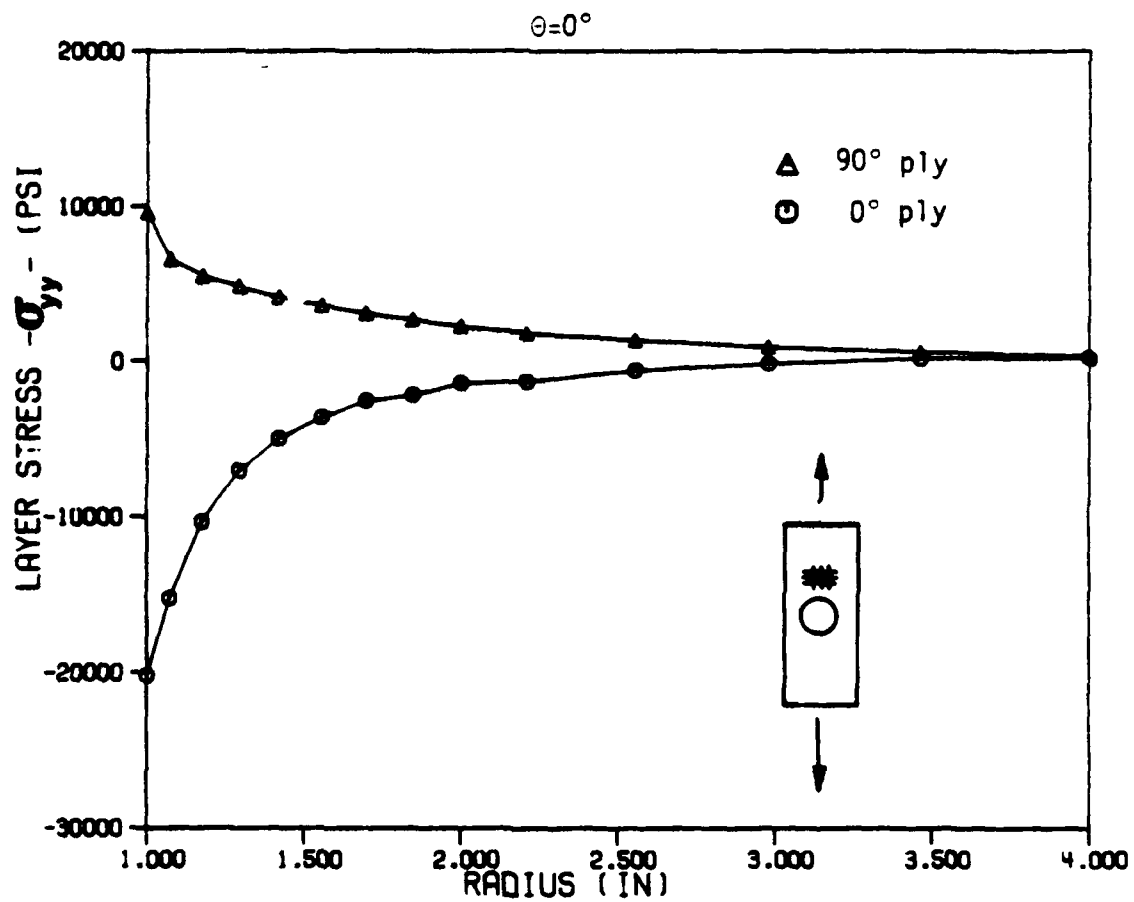


Figure 6.21 ANPLAST residual stresses in each ply for the B-A1 laminated sheet with a circular hole subjected to elastic unloading.

SECTION 7

CONCLUSIONS

The purpose of this research was to develop a numerical tool to investigate the role of anisotropy in the elastic-plastic behavior of structural components.

The plane stress incremental orthotropic plasticity relations for macroscopic deformation of thin sheets have been properly formulated. The plasticity coefficients (r_{11} , r_{12} , r_{66}), effective yield stress ($\bar{\sigma}_y$) and particular work-hardening law (\bar{e}^P vs $\bar{\sigma}$) control the shape and growth of the yield surface as well as the associated plastic flow. The incremental formulation provides the necessary flexibility to analyze nonproportional loading, including unloading.

The orthotropic plasticity flow rule was formulated so that it is compatible with the finite element method and directly implemented into the program ANPLAST. Both the constant strain triangle and isoparametric quadrilateral elements provide satisfactory results. The non-linear problem is solved in an incremental manner which allows complete non-proportionality of loading. The pre-processing and post-processing software provides an efficient complement to the overall ANPLAST analysis capabilities.

The analysis of the sheet with a circular hole provides a benchmark for the elastic and isotropic elastic-plastic capabilities of ANPLAST. The isotropic and orthotropic elastic capability of ANPLAST demonstrates excellent agreement with the theoretical solution. The

isotropic elastoplastic performance of ANPLAST compares well with available theoretical and experimental solutions. Close concordance with the experimental results of Rizzi [24] for a strongly anisotropic B-Al metal-matrix composite verifies the adequacy of the anisotropic formulation and demonstrates the practicality of applying ANPLAST.

The elastic analysis of the cracked panel illustrates the convenience of utilizing an energy method for stress intensity calibration of an anisotropic material. An elastoplastic analysis reveals that plastic flow in the vicinity of the crack is strongly influenced by the amount of anisotropy and the orientation of the principal material direction. This suggests that the mechanisms which control crack propagation are firmly linked to material directionality and the resulting plasticity.

A number of strong similarities exist between the elastoplastic results for the hole and crack. The progression of the plastic zone and related plastic flow is controlled by the same parameters. In both cases a strong compressive longitudinal residual stress is evident at the perimeter of each discontinuity, regardless of the degree of anisotropy.

The response of elastoplastic laminated materials exhibits extremely complex behavior. The study of both isotropic and orthotropic layers leads to the conclusion that global laminate response is a non-linear superposition of individual elastic and elastic-plastic lamina properties. A laminate consisting of orthotropic layers exhibits an initial yield surface which is quite different from that of each lamina. Loading of either laminate construction beyond its

initial yield results in a translation and distortion of the yield surface. When the laminate is loaded between fixed load limits, the yield surface eventually stabilizes after a number of load cycles. It is clear that it is difficult to apply classical elastoplasticity theory to the global deformation of laminates. But it is shown that the most straightforward approach to the solution of these problems is the characterization of elastic-plastic behavior at the mini-level and superposition of the lamina responses via a legitimate lamination theory.

The analysis of the laminated sheet with a circular hole exemplifies the usefulness of the implementation of the incremental lamination theory into ANPLAST. The results demonstrate the significantly different plastic deformation occurring within each layer.

Anisotropy can have a very complex influence on the elastoplastic response of structures. But with aid of a numerical tool such as ANPLAST they can be made tractable and their interesting aspects conveniently elucidated.

LIST OF REFERENCES

- [1] Timoshenko, S.P. and Goodier, J.N., Theory of Elasticity, McGraw-Hill, 1970, pp. 1-31, 84-98.
- [2] Johnson, W. and Mellor, P.B., Engineering Plasticity, Van Nostrand Reinhold Company, London, 1978.
- [3] Mellor, P.B., "Experimental Studies of Plastic Anisotropy in Sheet Metal", Publication Origin Unknown, Postgraduate School of Manufacturing Systems Engineering, University of Bradford.
- [4] Dillamore, I.L., Hazel, R.J., and Watson, T.W., "An Experimental Study of the Mechanical Anisotropy of Some Common Metals", Int. J. Mech. Sci., 1971, Vol. 13, pp. 1049-1061.
- [5] Pearce, R., "Some Aspects of Anisotropic Plasticity in Sheet Metals", Int. J. Mech. Sci., 1968, Vol. 10, pp. 995-1005.
- [6] Dorn, J.E., "Stress-Strain Rate Relations for Anisotropic Plastic Flow", J. of Applied Physics, 1949, Vol. 20, pp. 15-20.
- [7] Hu, L.W., "Studies on Plastic Flow of Anisotropic Metals," J. of Applied Mechanics, 1956, Vol. 23, Trans ASME, pp. 444-450.
- [8] Kachanov, L.M., Fundamentals of the Theory of Plasticity, Mir Publishers, Moscow, 1974, pp. 60-97.
- [9] Gotah, M., "A Theory of Plastic Anisotropy Based on a Yield Function of Fourth Order", Int. J. Mech. Sci., 1977, Vol. 19, pp. 505-512.
- [10] Frederking, R.M.W., and Sidebottom, O.M., "An Experimental Evaluation of Plasticity Theories for Anisotropic Metals", J. of Applied Mechanics, May 1969, Trans ASME.
- [11] Kobayashi, S., Caddel, R.M., and Hosford, W.F., "Examination of Hill's Latest Yield Criterion Using Experimental Data for Various Anisotropic Sheet Metals", Int. J. Mech. Sci., 1985, Vol. 27, pp. 509-517.
- [12] Kenaga, D.W., "Elastic-Plastic Material Characterization and Fatigue Crack Growth in Unidirectional Metal-Matrix Composites", Master's Thesis, School of Aeronautics and Astronautics, Purdue University, August 1984.

- [13] Jones, R.M., Mechanics of Composite Materials, Scripta Book Company, Washington, D.C., 1975, pp. 32-54.
- [14] Marcal, P.V., and King, I.P., "Elastic-Plastic Analysis of Two-Dimensional Stress Systems by the Finite Element Method", J. Mech. Sci., 1967, Vol. 9, pp. 143-155.
- [15] Segerlind, L.J., Applied Finite Element Analysis, John Wiley & Sons, New York, 1976.
- [16] Pinella, D.F., "Finite Element Analysis of Cracks in Orthotropic Elastic-Plastic Materials", Master's Thesis, School of Aeronautics and Astronautics, Purdue University, August 1984.
- [17] Gallagher, R.H., Finite Element Analysis Fundamentals, Prentice-Hall, Englewood Cliffs, New Jersey, 1975, pp. 108-134.
- [18] Yang, T.Y., Finite Element Structural Analysis, Prentice-Hall, Englewood Cliffs, New Jersey, 1986, pp. 254-307, 354-394.
- [19] Cook, R.D., Concepts and Applications of Finite Element Analysis, John Wiley & Sons, New York, 1981.
- [20] Budiansky, B., and Vidensek, R.J., "Analysis of Stresses and Strains in the Plastic Range Around a Circular Hole Subjected to Uniaxial Tension, NACA Tech. Note 3542, Washington, October 1955.
- [21] Theocaris, P.S., and Marketos, E., "Elastic-Plastic Analysis of Perforated Thin Strips of Strain-Hardened Material", J. Mech. Phys. Solids, 1964, Vol. 12, pp. 377-390.
- [22] Thomson, R.A., and Frocht, M.M., "Studies in Photoplasticity", Reprinted from Proceedings of the Third U.S. National Congress of Applied Mechanics by M.M. Frocht in Photoelasticity, Pergamon Press Inc., 1969.
- [23] Nagtegaal, J.C., Parks, D.M., and Rice, J.R., "On Numerically Accurate Finite Element Solutions in the Fully Plastic Range", Comp. Meth. in Applied Mech. & Engr., 1974, Vol. 4, pp. 153-177.
- [24] Rizzi, S.A., "Fatigue Crack Growth in Boron-Aluminum Metal Matrix Composites", Master's Thesis, School of Aeronautics and Astronautics, Purdue University, December 1985.
- [25] Leewood, A.R., and Nagtegaal, J.C., "Design and Analysis Methodology for Fabric Structures", Owens-Corning Fiberglas Technical Report 82-T-347, Granville, Ohio, December 1982.
- [26] Broek, D., Elementary Engineering Fracture Mechanics, Martinus Nijhoff Publishers, Boston, 1982.

- [27] Cherepanov, G.P., Mechanics of Brittle Fracture, McGraw-Hill International, New York, 1977, pp. 71-78.
- [28] Sih, G.C., "Application of Strain Energy Density Theory to Fundamental Fracture Problems", Engineering Fracture Mechanics, 1973, Vol. 5, pp. 365-377.
- [29] Fuchs, H.O., and Stephens, R.I., Metal Fatigue in Engineering, John Wiley & Sons, New York, 1980.
- [30] Bahei-El-Din, Y.A., and Dvorak, G.J., "Plasticity Analysis of Laminated Composite Plates", J. of Applied Mechanics, 1982, Vol. 49, Trans of ASME, pp. 740-746.
- [31] Monilo, M.M., "Three-Dimensional Elastoplastic Finite Element Analysis of Laminated Composites", Ph.D. Thesis, Department of Mechanical Engineering, University of Wyoming, December 1980.
- [32] Sova, J.A., and Peo, C.C., "Tensile Stress-Strain Behavior of Boron/Aluminum Laminates", NASA Technical Paper 1117, 1978.
- [33] Bahei-El-Din, Y.A., and Dvorak, G.J., "Plastic Deformation of a Laminated Plate With A Hole", J. of Applied Mechanics, 1980, Vol. 47, pp. 827-832.

General References

- [34] Owen, D.R.J., and Hinton, E., Finite Elements in Plasticity, Pineridge Press Limited, Swansea, U.K., 1980.
- [35] Bathe, K.J., Finite Element Procedures in Engineering Analysis, Prentice Hall, Englewood Cliffs, N.J., 1982.
- [36] Mishra, S.C., and Parida, B.K., "A Study of Crack Tip Plastic Zone by Elastoplastic Finite Element Analysis", Engineering Fracture Mechanics, 1985, Vol. 22, No. 6, pp. 951-956.
- [37] Chiang, W.T., and Miller, K.J., "Elastic-Plastic Finite Element Analysis of Short Cracks", Fatigue of Engineering Materials and Structures, 1982, Vol. 5, No. 3, pp. 249-263.
- [38] Leewood, A.R., "Compliance Method Investigation", AAE 664 Special Project, Purdue University, Fall 1984.